João Pedro de Sousa Oliveira
Mestre em Ciência e Engenharia de Materiais

Laser Welding of Shape Memory Alloys

Dissertação para obtenção do Grau de Doutor em
Ciência e Engenharia de Materiais

Orientador: Francisco Manuel Braz Fernandes
Professor Associado com Agregação
Faculdade de Ciências e Tecnologia
Universidade Nova de Lisboa

Co-orientador: Rosa Maria Mendes Miranda
Professora Associada com Agregação
Faculdade de Ciências e Tecnologia
Universidade Nova de Lisboa

Júri:

Presidente	Prof. Doutor Rodrigo Ferrão de Paiva Martins
Arguentes	Prof. Doutora Maria Teresa Freire Vieira
	Prof. Doutor Altino de Jesus Roque Loureiro
Vogais	Prof. Doutora Maria Luísa Coutinho Gomes de Almeida
	Prof. Doutor Norman Zhou
	Prof. Doutor Francisco Manuel Braz Fernandes
	Prof. Doutora Rosa Maria Mendes Miranda
	Prof. Doutor Rui Jorge Cordeiro Silva

FACULDADE DE CIÊNCIAS E TECNOLOGIA
UNIVERSIDADE NOVA DE LISBOA

Junho de 2016

João Pedro de Sousa Oliveira
Mestre em Ciência e Engenharia de Materiais

Laser Welding of Shape Memory Alloys

Dissertação para obtenção do Grau de Doutor em
Ciência e Engenharia de Materiais

Orientador: Francisco Manuel Braz Fernandes
Professor Associado com Agregação
Faculdade de Ciências e Tecnologia
Universidade Nova de Lisboa

Co-orientador: Rosa Maria Mendes Miranda
Professora Associada com Agregação
Faculdade de Ciências e Tecnologia
Universidade Nova de Lisboa

Júri:

Presidente	Prof. Doutor Rodrigo Ferrão de Paiva Martins
Arguentes	Prof. Doutora Maria Teresa Freire Vieira
	Prof. Doutor Altino de Jesus Roque Loureiro
Vogais	Prof. Doutora Maria Luísa Coutinho Gomes de Almeida
	Prof. Doutor Norman Zhou
	Prof. Doutor Francisco Manuel Braz Fernandes
	Prof. Doutora Rosa Maria Mendes Miranda
	Prof. Doutor Rui Jorge Cordeiro Silva

FACULDADE DE CIÊNCIAS E TECNOLOGIA
UNIVERSIDADE NOVA DE LISBOA

Junho de 2016

Laser Welding of Shape Memory Alloys

To my parents

If at first you don’t succeed you try and try again

Acknowledgements

Along this path that ends with the writing of this document I crossed myself with several people which, one way or the other, had some influence to the out coming results here presented.

First I must thank my supervisors, Professor Francisco Braz Fernandes and Professor Rosa Miranda, who have accepted to enter this adventure, which started by applying for a scholarship from the Portuguese Foundation for Science and Technology.

To Professor Braz Fernandes I thank for the numerous hours spent with me for discussion of results and for always be available to discuss matters non-related with my work, which arise from my scientific curiosity.

To Professor Rosa Miranda, always available to present ways to improve the work and for the countless hours arguing with me about my work and other non-related situations. Additionally, her expertise in welding technologies was fundamental to me throughout this work. I will not forget her support during my stay in Canada when the experimental procedure appeared not to work either way I tried.

To both Professor Braz Fernandes and Professor Rosa Miranda I express my gratitude for trusting me their students, which I was allowed to co-supervise with them. Also, they allowed me to go after different scientific interests which I came across during my thesis.

To Professor Norman Zhou, director of the Center for Advanced Materials Joining of the University of Waterloo, Canada, I thank him to open his micro joining lab for me and for providing me all the required means to successfully achieve all the purposed tasks.

During my at the University of Waterloo I meet other people which had significant importance in this work. I will always be grateful to my friend Boyd Panton for his help in the laser welding experiments and for our discussions regarding our works. To Zhi Zeng, another colleague, for his help and insights on the best way to optimize the welding procedure. Additionally, I must thank both Boyd and Zhi for trusting me to give them support for their experiments. To Carmen Andrei from the Brockhouse Institute for Material Research at McMaster University for the useful discussions during the transmission electron microscopy measurements.

I also must acknowledge Professor Jose Luis Ocaña, director of the Centro Laser of Universidad Politécnica de Madrid for his availability and support during the similar laser welding trials of NiTi. At the Centro Laser, during welding experiments, the technical support provided by Alberto Cuesta and Alejandro Tur Gil was very welcomed.

Synchrotron X-ray diffraction was deeply used during this work. I acknowledge Dr. Norbert Schell for his availability to receive us at Deutsche Electron Synchrotron (DESY) and for his technical support during the experiments.

I also want to thank to André Cavaleiro for his help during the beam times at the DESY synchrotron. We spent several long nights discussing results for our works. Additionally, his useful scripts were very appreciated to facilitate data analysis.

To my friend and colleague Patrícia Freitas for always be the positive person in our lab.

I acknowledge also the technical support by the staff of the Mechanical and Industrial Engineering Department of Faculdade de Ciências e Tecnologias, Universidade Nova de Lisboa, Portugal, for their help.

Financial support provided by Fundação para a Ciência e Tecnologia, under PhD grant SFRH/BD/85047/2012 is acknowledged as well as support from Project No 612585 "MIDAS—Micro and Nanoscale Design of Thermally Actuating Systems" Marie Curie Actions, FP7-PEOPLE-2013-IRSES

To Professor Toshihiro Omori, from the Tokohu University, Japan, I'm grateful for providing the superelastic Cu-Al-Mn alloy used in this work and for his useful indications during writing of the related papers.

To Professor Luca Lutterotti, from Università degli Studi di Trento, Italia, developer of MAUD for his useful tips for determining the residual stresses from synchrotron data.

To Professor Teresa Vieira, from Universidade de Coimbra, Portugal, for her suggestions as a member of the advisory board of this thesis.

I have to thank also to my parents, Maria and Jorge, for all their love and support throughout the years. Without them I wouldn't be here, that is for sure.

Finally, but not least, I must express my gratitude towards Susana. For her love and companionship, for her everlasting support, for dealing with my exquisite schedules, for really understand my ambitions and to always be there for me when I need to even if there is an ocean between the two of us. If that is not true love, I don't know what it is then.

Agradecimentos

No decorrer deste caminho que termina com a escrita deste documento, cruzei-me com várias pessoas que, de um modo ou de outro, tiveram alguma influência naquilo que é aqui apresentado.

Primeiramente, tenho de agradecer aos meus orientadores, Professor Francisco Braz Fernandes e Professora Rosa Miranda, que aceitaram entrar nesta aventura que começou pela submissão de uma proposta de financiamento à Fundação para a Ciência e Tecnologia.

Ao Professor Braz Fernandes agradeço as inúmeras horas passas a discutir resultados e por estar sempre disponível para discutir outros assuntos não relacionados com o meu trabalho, que que surgiram da minha natural curiosidade científica.

À Professora Rosa Miranda, por estar sempre disponível para apresentar ideias para melhorar o trabalho desenvolvido e pelas incontáveis horas a discutir comigo sobre o trabalho e outros assuntos não relacionados. Além disso, a sua experiência e conhecimento em tecnologias de soldaduras foi fundamental ao longo deste trabalho. Não irei esquecer o apoio que me deu durante a minha estadia no Canadá quando a parte experimental não apresentava resultados.

A ambos os meus orientadores, agradeço por me confiarem os seus alunos, ao permitirem que os pudesse co-supervisionar durante as suas teses de mestrado. Além disso, permitiram-me seguir diferentes interesses científicos que me foram aparecendo ao longo do trabalho.

Ao Professor Norman Zhou, diretor do Center for Advanced Materials Joining da University of Waterloo, Canada, agradeço por me ter aberto as portas do seu laboratório e por providenciar todos os meios necessário para atingir o sucesso das tarefas propostas.

Durante a minha estadia na Universidade de Waterloo, conheci outras pessoas que tiveram importância no desfecho deste trabalho. Estarei sempre grato ao meu amigo Boyd Panton pela sua ajuda nas experiências de soldadura laser e pelas nossas longas discussões sobre os nossos trabalhos. Ao Zhi Zheng, outro colega, pela sua ajuda e ideias sobre as melhores maneiras de otimizar o processo de soldadura. Tenho ainda de agradecer a ambos por confiarem em mim para os ajudar no seu trabalho. À Carmei Andrei do Brockhouse Institute for Material Research da McMaster University, Canadá, agradeço as muito úteis discussões sobre as análises com microscopia eletrónica de transmissão.

Agradeço igual ao Professor Jose Luis Ocaña, diretor do Centro Laser da Universidad Politécnica de Madrid, Espanha, pela sua disponibilidade e ajuda durante a realização da soldaduras dissimilar de NiTi. No Centro Laser, durante a realização das soldaduras, apoio técnico por parte do Alberto Cuesta e do Alejandro Tur Gil foi bastante apreciado.

Difração de raios-X utilizado radiação de sincrotrão foi bastante utilizada neste trabalho. Agradeço ao Dr. Norbert Schell por nos receber no Deutsche Electron Synchrotron (DESY) e pela sua ajuda durante as experiências.

Tenho igualmente de agradecer ao André Cavaleiro pela sua ajuda durante os tempos de feixe no DESY. Passámos longas noites a discutir resultados nos nossos trabalhos. Além disso, os seus programas foram muito úteis no tratamento dos resultados obtidos.

À minha amiga e colega Patrícia Freitas por ser sempre a pessoa positiva no nosso laboratório.

Agradeço também o suporte técnico do pessoal do Departamento de Engenharia Mecânica e Industrial da Faculdade de Ciências e Tecnologias, Universidade Nova de Lisboa, Portugal, pela sua ajuda.

O suporte financeiro providenciado pela Fundação para a Ciência e Tecnologia, bolsa SFRH/BD/85047/2012, é agradecido assim como o apoio do projeto No 612585 "MIDAS—Micro and Nanoscale Design of Thermally Actuating Systems" Marie Curie Actions, FP7-PEOPLE-2013-IRSES.

Ao Professor Toshihiro Omori, da Tokohu University, Japão, agradeço por fornecer as amostras de Cu-Al-Mn superelástico e pelas suas indicações aquando da escrita dos artigos.

Ao Professor Luca Lutterotti, da Università degli Studi di Trento, Itália, criador do MAUD pelos seus comentários sobre a melhor forma de proceder para a determinação de tensões residuais a partir dos dados obtidos no sincrotrão.

À Professora Teresa Vieira, da Universidade de Coimbra, Portugal, agradeço as suas sugestões enquanto membro da comissão de acompanhamento da tese.

Agradeço do fundo do coração aos meus pais, Maria e Jorge, pelo seu amor e suporte ao longo dos anos. Sem eles eu não estaria aqui, isso é certo.

E por último, mas não menos importante, agradeço à Susana. Pelo seu amor e companheirismo, pelo seu apoio incondicional, por lidar com os meus horários peculiares, por realmente compreender as minhas ambições e por estar sempre lá para mim, mesmo quando existe um oceano entre nós. Se isso não é amor verdadeiro, então não sei o que é.

Abstract

Joining of shape memory alloys is of great importance for both functional and structural applications as it can provide an increased design flexibility.

In this work similar NiTi/NiTi, CuAlMn/CuAlMn and dissimilar NiTi/Ti6Al4V joints were produced by Nd:YAG laser.

For the NiTi/NiTi joints the effect of process parameters (namely the heat input) on the superelastic and shape memory effects of the joints was assessed and correlated to its microstructure. Microstructural analysis was performed by means of X-ray diffraction using synchrotron radiation, which allowed for fine probing of the welded material. It was noticed the presence of martensite in the thermally affected regions, while the base material remained fully austenitic. The mechanisms for the formation of martensite, at room temperature, due to the welding procedure are presented and the influence of this phase on the functional properties of the joints is discussed. Additionally, the residual stresses were determined using synchrotron X-ray diffraction.

For the dissimilar NiTi/Ti6Al4V joints, a Niobium interlayer was used to prevent the formation undesired brittle intermetallic compounds. Additionally, it was observed that positioning of the laser beam was of significant importance to obtain a sound joint. The mechanisms responsible for the joint formation are discussed based on observations with advanced characterization techniques, such as transmission electron microscopy. At the NiTi/Nb interface, an eutectic reaction promotes joining of the two materials, while at the Ti6Al4V/Nb interface fusion and, subsequent solidification of the Ti6Al4V was responsible for joining. Short distance diffusion of Nb to the fusion zone of Ti6Al4V was observed. Although fracture of the dissimilar welded joints occurred at a stress lower than the minimum required for the stress induced transformation, an improvement on the microstructure and mechanical properties, relatively to existing literature, was obtained.

Finally, the first weldability study of superelastic CuAlMn alloy was performed. Superelasticity was preserved after welding. Post-weld laser processing improved the damping capability of the welded joint when compared to both as-welded and base materials, aiming for seismic construction.

Keywords: Laser welding; NiTi shape memory alloys; CuAlMn shape memory alloys; NiTi/Ti6Al4V dissimilar joints; synchrotron radiation; functional properties.

Resumo

Promover a ligação de ligas com memória de forma é de grande importância para aplicações funcionais e/ou estruturais uma vez que permite uma maior flexibilidade em termos da conceção do produto.

Neste trabalho foram produzidas ligações similares de NiTi/NiTi, CuAlMn/CuAlMn e dissimilares de NiTi/Ti6Al4V por soldadura laser de Nd:YAG.

Nas ligações NiTi/NiTi, o efeito dos parâmetros de soldadura nos efeitos superelástico e de memória de forma foram analisados e correlacionados com a microestrutura das juntas. A análise microestrutural foi efetuada por difração de raios-X utilizando radiação de sincrotrão. Verificou-se a presença de martensite nas zonas afetadas pelo calor, enquanto o material base era totalmente austenítico. Os mecanismos para a formação de martensite, à temperatura ambiente, devido ao processo de soldadura são apresentados e a sua influência nas propriedades funcionais é discutida. Adicionalmente, as tensões residuais nas juntas soldadas foram determinadas utilizando radiação de sincrotrão.

Nas ligações dissimilares de NiTi/Ti6Al4V foi utilizada uma intercamada de Nióbio de modo impedir a formação de compostos intermetálicos indesejados. Os mecanismos responsáveis pela formação destas juntas foram observados e discutidos com técnicas de caracterização avançadas, como microscopia eletrónica de transmissão. Na interface NiTi/Nb a reação eutéctica promove a ligação dos dois materiais, enquanto que na interface Ti6Al4V/Nb, a fusão e subsequente re-solidificação do Ti6Al4V é responsável pela ligação. Difusão de curta distância do Nb para a zona fundida do Ti6Al4V foi evidenciada. Apesar da fratura das juntas ter ocorrido abaixo da tensão necessária para a ocorrência da transformação induzida por tensão, obteve-se uma melhoria da microestrutura e propriedades mecânicas relativamente ao que se encontra descrito na literatura.

Finalmente, estudou-se a soldabilidade de uma liga superelástica de CuAlMn. Verificou-se que as propriedades superelásticas da junta foram preservadas e que o pós-processamento com laser promoveu a melhoria da capacidade de absorção de energia da junta, quando comparado com o material após soldadura e com o material de base, tendo como objetivo a utilização destes materiais em construções anti-sísmicas.

Palavras-chave: Soldadura laser; Ligas com memória de forma NiTi; Ligas com memória de forma CuAlMn; Soldadura dissimilar NiTi/Ti6Al4V, Radiação de sincrotrão; Propriedades funcionais.

Contents

List of Figures

List of Tables

List of Symbols and Abbreviations

α – Thermal diffusivity [$m^2\ s^{-1}$]

A – Austenite

A_F – Austenite finish temperature

A_S – Austenite start temperature

BM – Base material

BPP – Beam Parameter Product

d – Grain size

D – Wire diameter

ΔT - Undercooling

FZ – Fusion zone

g – Thickness [m]

G – Temperature gradient

HAZ – Heat affected zone

K0 – modified Bessel function of the second kind and zero order

M – Martensite

M_F – Martensite finish temperature

M_S – Martensite start temperature

NOL – Naval Ordnance Laboratory

t – Thickness of welded material [mm]

T – Temperature [K]

T_m – Melting temperature [K]

T_0 – Room temperature [K]

Q – Heat input [$W\ m^{-1}\ K^{-1}$]

φ – Azimuthal angle,

r – is the radial distance [m]

R – Crystal growth rate

σ_{As} – Minimum stress level to start inducing the transformation from martensite to austenite

σ_{Af} – Stress level at which the stress induced transformation from austenite to martensite finishes

σ_{Ms} – Minimum stress level to start inducing the transformation from austenite to martensite

σ_{Mf} – Stress level at which the reverse stress induced transformation from martensite to austenite finishes

σ_X – Residual stresses along the longitudinal direction

σ_Y – Residual stresses along the transversal direction

Θ – Bragg angle

v – Welding speed [m s^{-1}]

Ω – Permanent deformation angle [°]

CAMJ – Center for Advanced Materials Joining

DSC - Differential Scanning Calorimetry

DESY – Deutsche Electron Synchrotron

EDS – Energy Dispersive X-ray Spectroscopy

EELS – Electron Energy Loss Spectra

FIB – Focused Ion Beam

HAADF – High Angle Annular Dark Field

MAUD – Material Analysis Using Diffraction

STEM – Scanning Transmission Electron Microscopy

TEM – Transmission Electron Microscopy

TTT - Time-Temperature-Transformation

1. Introduction

The first chapter of this thesis presents the aims and scope of the work and provides some general information concerning the development of the thesis. The structure and sequence of the different chapters is presented and explained. Additionally, a roadmap is provided for the reader.

Since some of the contents presented in this thesis have already been published, a list of those papers is provided.

1.1 Aims and Scope

Welding of shape memory alloys has attracted significant interest in recent years. The possibility to either obtain complex shaped structures or to combine these functional materials to engineering ones is of great interest.

NiTi/NiTi laser welded joints have already been studied in the literature, however the microstructural modifications induced by the welding procedure and its correlation with both shape memory and superelastic effects still needs to be further clarified. Additionally, up to now there are no studies on the determination of residual stresses in such joints. As such, analysis of the microstructure, functional properties and residual stresses determination was performed.

Production of NiTi/Ti6Al4V joints is a desirable dissimilar combination owing to the properties presented by each material. However, the inherent brittleness of its fusion zone, due to the presence of intermetallic compounds is a considerable setback. Thus, it is of great importance to determine a joining methodology which can either ensure a decreased precipitation or even supress it. To overcome this problem, a Niobium interlayer was used between NiTi and Ti6Al4V, allowing to obtain a sound joint.

Recently, superelastic CuAlMn shape memory alloys have been presented as a prime candidate to replace NiTi. Up to now, there are no reports on the weldability of this material, thus, understanding its laser welding may boost its potential applications. For this, the first weldability tests using a laser were performed and the microstructure and mechanical properties were analysed.

1.2 Location and Duration

The research work for the preparation of this thesis was developed mainly at four locations: Portugal, Canada, Germany and Spain.

The primary location was at CENIMAT/i3N, of Faculdade de Ciências e Tecnologias, Universidade Nova de Lisboa, Portugal. There, thermal, structural and mechanical analysis on the NiTi/NiTi joints were performed. These joints were produced at Centro Laser of Universidad Politécnica de Madrid, Spain. Synchrotron X-ray diffraction data was obtained at Deutsche Electron Synchrotron (DESY), Hamburg, Germany. Finally, NiTi/Ti6Al4V and CuAlMn/CuAlMn joints were produced and structural and mechanically characterized at the Center for Advanced Materials Joining (CAMJ) of the University of Waterloo, Canada.

1.3 Structure of the Thesis

This thesis is composed of five chapters. A critical analysis of existing knowledge is presented in Chapter 2. Chapter 3 details the materials and methods used throughout this investigation. In Chapter 4 the discussion of results is presented, organised in subchapters focused on NiTi/NiTi, NiTi/Ti6Al4V and CuAlMn/CuAlMn laser welds. Finally, in Chapter 5, the most remarkable conclusions as well as potential related areas for research are highlighted.

1.4 Published Results

This thesis contains results that has already been published in scientific journals.

The following papers were published in scientific journals:

- F. M. Braz Fernandes, K. K. Mahesh, C. M. Craciunescu, J. P. Oliveira, N. Schell, R. M. Miranda, L. Quintino, J. L. Ocaña, **In Situ Structural Characterization of Laser Welded Niti Shape Memory Alloys**, European Symposium on Martensitic Transformations 9Th European Symposium on Martensitic Transformations (Esomat 2012), 2012, DOI: 10.4028/www.scientific.net/msf.738-739.338

- J. P. Oliveira, F. M. Braz Fernandes, R. M. Miranda, N. Schell, **On the Mechanisms for Martensite Formation in YAG Laser Welded Austenitic NiTi**, Shape Memory and Superelasticity, vol 2, 114-120, 2016. DOI: 10.1007/s40830-016-0058-z

- J. P. Oliveira, R. M. Miranda, N. Schell, F. M. Braz Fernandes, **High Strain and Long Duration Cycling Behavior of Laser Welded NiTi Sheets**, International Journal of Fatigue, vol. 83, 195-200, 2016. DOI: 10.1016/j.ijfatigue.2015.10.013 (IF: 2.275, 5Y-IF: 2.583)

- J. P. Oliveira, F. M. Braz Fernandes, N. Schell, R. M. Miranda, **Martensite Stabilization During Superelastic Cycling of Laser Welded NiTi Plates**, Materials Letters, vol 171, 273-276, 2016, DOI: 10.1016/j.matlet.2016.02.107 (IF: 2.489, 5Y-IF: 2.466)

- J. P. Oliveira, F. M. Braz Fernandes, N. Schell, R. M. Miranda, **Shape Memory Effect of Laser Welded NiTi Plates**, Functional Materials Letters, vol. 8, 1550069, 2015. DOI: 10.1142/S1793604715500691. (IF: 1.61, 5Y-IF: 1.47) This work was chosen to be the cover page of the December issue of the journal.

- J. P. Oliveira, F. M. Braz Fernandes, R. M. Miranda, N. Schell, J. L. Ocaña, **Residual Stress Analysis in Laser Welded NiTi Sheets Using Synchrotron X-ray Diffraction**, Materials & Design, vol. 100, 180-187, 2016. DOI: 10.1016/j.matdes.2016.03.137. (IF: 3.51, 5Y-IF:3.626)

- J. P. Oliveira, B. Panton, Z. Zeng, C. Andrei, Y. Zhou, R. M. Miranda, F. M. Braz Fernandes, **Laser Joining of NiTi to Ti6Al4V Using a Niobium Interlayer**, Acta Materialia, vol. 105, 9-16, 2016, DOI: 10.1016/j.actamat.2015.12.021. (IF: 4.465, 5Y-IF: 4.869)

- J. P. Oliveira, B. Panton, Z. Zeng, T. Omori, Y. Zhou, R. M. Miranda, F. M. Braz Fernandes, **Laser Welded Superelastic Cu-Al-Mn Shape Memory Alloy Wires**, Materials & Design, vol 90, 122-128, 2016. DOI: 10.1016/j.matdes.2015.10.125. (IF: 3.51, 5Y-IF:3.626)

- J. P. Oliveira, Z. Zeng, T. Omori, N. Zhou, R. M. Miranda, F. M. Braz Fernandes, **Improvement of Damping Properties in Laser Processed Superelastic Cu-Al-Mn Shape Memory Alloys**, Materials & Design, vol 98, 280-284, 2016. DOI: 10.1016/j.matdes.2016.03.032. (IF: 3.51, 5Y-IF:3.626)

2. State of the Art

2.1 Shape Memory Alloys

Shape memory alloys are functional materials that present two very distinct properties: superelasticity and shape memory effect. Among these alloys, NiTi is the most important one, not only because of its functional properties, but also because it presents high strength and ductility [1].

The shape memory effect was first discovered, in the early 1950's, in Au-47.5Cd (at. %) and In-Tl alloys, however it had not attracted significant attention from researchers at that time. Nearly a decade later, in 1963, NiTi alloys became very popular owing to the publicity of Naval Ordinance Laboratory (NOL), where Buehler and co-workers observed this effect. As a tribute to this laboratory and derived from its near equiatomic composition (NiTi), the name NiTiNOL is often used.

The functional properties exhibited by these alloys are due to a reversible martensitic transformation. Before discussing the mechanisms that are responsible for superelasticity and shape memory effect, some key-aspects must be presented first to facilitate the discussion.

Usually shape memory alloys have two stable phases. A low temperature one, known as martensite (M), and a high temperature one, known as austenite (A) or parent phase.

The functional properties exhibited by these alloys are due to a reversible martensitic transformation. SMAs have two phases: a low temperature one, known as martensite (M), and a high temperature one, known as austenite (A) or parent phase.

When cooling the material from the austenitic domain, it starts to transform into martensite at a given M_S temperature. This austenite to martensite transformation (referred in the literature as forward or direct transformation), finishes at the M_F temperature.

Starting with the material in the low temperature phase, by heating it up to a given (A_S) temperature, austenite starts to form. Such transformation from martensite to austenite by heating (referred in the literature as reverse transformation) finishes when the A_F temperature is reached. A_S, A_F, M_S and M_S are designated the transformation temperatures of a given shape memory alloy, where A and M designate the phase (austenite or martensitic) and the subscripts S and F apply for start and finish of transformation, respectively.

Martensitic transformations, as those that take place in shape memory alloys, are diffusionless transformations [2]. When such transformations occur only by effect of temperature, the macroscopic shape change is negligible.

In these alloys, each martensitic crystal has a given different orientation, called variant. An assembly of martensitic variants may exist in two distinct forms: twinned martensite or detwinned martensite. The former is created by the combination of self-accommodated martensitic variants to keep the overall shape when martensite is thermally induced, while in the latter a specific variant is dominant in the system, usually as a result of an applied external load [3].

The reversibility of transformation between austenite and martensite, and vice-versa, is the basis for the peculiar behaviour of this class of alloys.

With the previous presentation of some fundamental aspects related to shape memory alloys it is now possible to discuss the mechanisms of superelasticity and shape memory effect.

Martensitic transformation may also be stress induced giving rise to superelastic effect. Superelasticity occurs by the application of stress when the material is in the temperature range of thermally stable austenite. Such property allows for the material to undergo a significant deformation during loading (up to 10 % strain) with full recovery of its shape upon unloading [4], as shown in Figure 1. Consider a given fixed temperature, above A_F, where the material is tested under an applied uniaxial tensile load. Firstly, there is elastic deformation of austenite (along the A – B path in Figure 1). At B, for a given stress σ_{Ms}, the martensitic transformation starts to occur. Such stress induced transformation from austenite to martensite occurs at an approximately constant stress level, up to a σ_{Mf} stress. When σ_{Mf} is reached, the material is fully martensitic. When the transformation from austenite to martensite occurs, this martensite may turn instantly into detwinned martensite, depending on the relative orientation of the crystallographic variants and the imposed external solicitation. From C to D elastic deformation of the detwinned martensite occurs. If the material is not strained beyond point D, in theory, full recovery of the imposed strain can be obtained. From D to E the martensite elastically unloads. At point E, for a σ_{As} stress level the martensite to austenite transformation starts to occur and proceeds until it is finished (at point F). Complete removal of the imposed stress allows for the elastic unloading of austenite (along the path F – A).

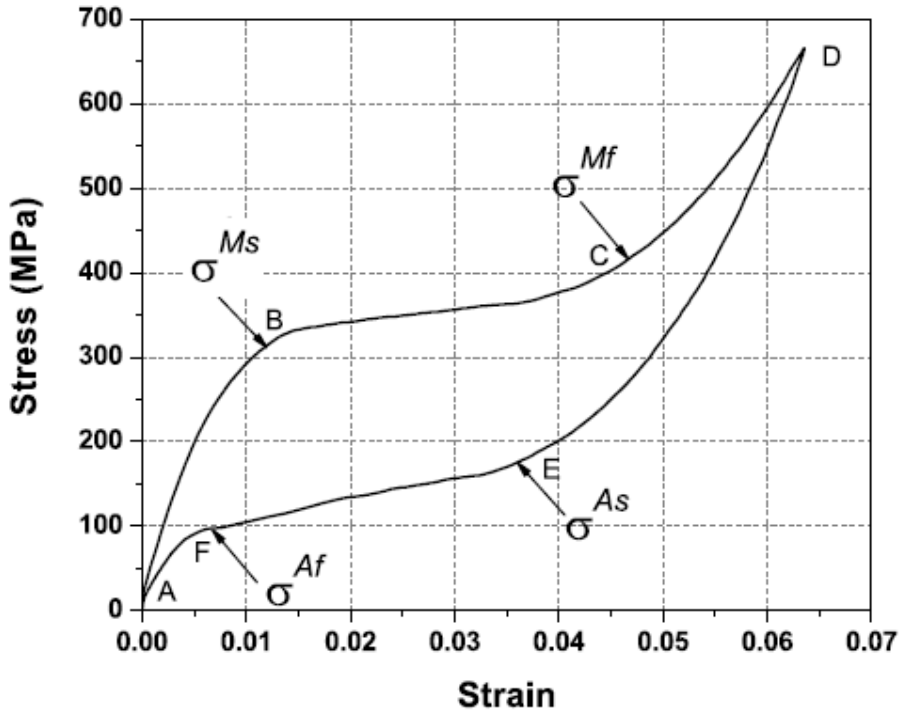

Figure 1 – Typical superelastic behavior of a shape memory alloy [5].

Opposite to superelasticity, shape memory effect occurs starting from the material in the martensitic state [6]. Consider a shape memory alloy with a given form in the austenitic phase.

Cooling it down so that martensite (in the twined state) is stable will not promote any shape alteration in the material. However, if a given deformation is imposed to the material in the martensitic state, it will be retained by the material, as long as it remains in the temperature range where martensite is the stable phase. As a consequence of the applied deformation, martensite detwinning occurs. It is possible to recover the original shape when the material is heated above the A_F temperature. When the A_S temperature is crossed, the shape memory effect starts to occur, that is, the material starts to recover its initial shape, and this proceeds until the A_F temperature is reached, when full recovery of the imposed deformation has occurred. Further cooling back to the martensite domain will occur with no significant macroscopic shape change of the material.

Figure 2 depicts the schema of both superelasticity and shape memory effect in a stress-strain-temperature diagram.

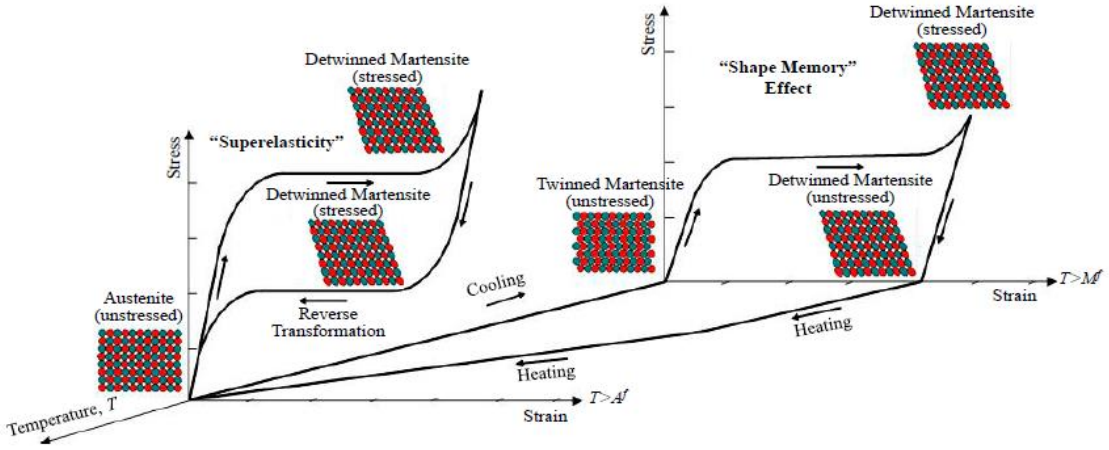

Figure 2 – Stress-strain-temperature plot exhibiting superelasticity and shape memory effect [7].

Though superelasticity and shape memory effect have been discussed separately, they are closely related. The stress-temperature phase diagram for a given shape memory alloy is presented in Figure 3. It is expected that any shape memory alloy exhibits both superelastic and shape memory properties, depending on the temperature at which they are tested and as long as the critical stress for dislocation slip is not reached.

The critical stress for stress-induced martensite follows a Clausius-Clapeyron relationship [8]: $d\sigma/dT = -\Delta S/\varepsilon$, (being σ the applied stress, T the temperature, ΔS the change in entropy and ε the applied strain): with increasing temperature, a higher stress is required to trigger the stress induced transformation. On the other hand, it can be observed (in Figure 3) that the critical stress to induce slip, and therefore plastic deformation, decreases with increasing temperature. As such, it is possible that, at a given temperature, the critical stress for dislocation slip occurs earlier than the superelastic effect, thus inhibiting this property. The temperature above which the stress-induced martensitic transformation is no longer favored is designated by Md However, it is possible to manipulate the critical stress for inducing dislocations slip at a given temperature: by softening or hardening the material, the critical stress for slip decreases or increases, respectively.

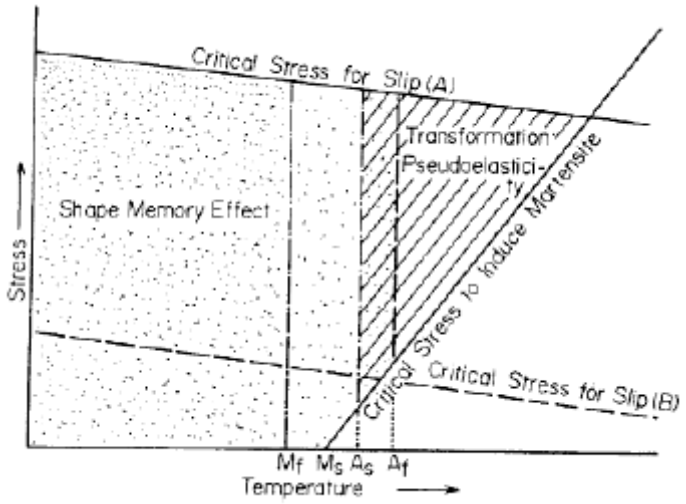

Figure 3 – Stress-temperature diagram for a given shape memory alloy [1].

Another functional property exhibited by these materials is the two-way shape memory effect [3]. When the material is trained to have this property, it remembers a given geometrical shape in the parent phase and another in the martensitic phase. These two shapes are obtained without the help of any mechanical loading.

2.1.1 NiTi Shape Memory Alloys

Ni-Ti-based, Fe-based [9] and Cu-based [10], are the most common classes of shape memory alloys. From these, NiTi, is by far the most studied. Aside from its functional properties and high mechanical resistance, NiTi is also biocompatible, which allows for its use in the biomedical industry. NiTi presents also a good corrosion resistance making it suitable for use in severe mediums.

NiTi may present three distinct phases: austenite, martensite and R-phase. Austenite, with a B2 body centered cubic structure, and martensite, with a B19' monoclinic structure, are the high or (parent) and low temperature phases, respectively. R-phase, with a trigonal structure, may exist between austenite and martensite in special circumstances, as it is discussed latter. The crystal structure of both austenite and martensite are depicted in Figure 4. The crystal structure of R-phase can be viewed as a stretch of the austenite crystal structure along the <111> direction.

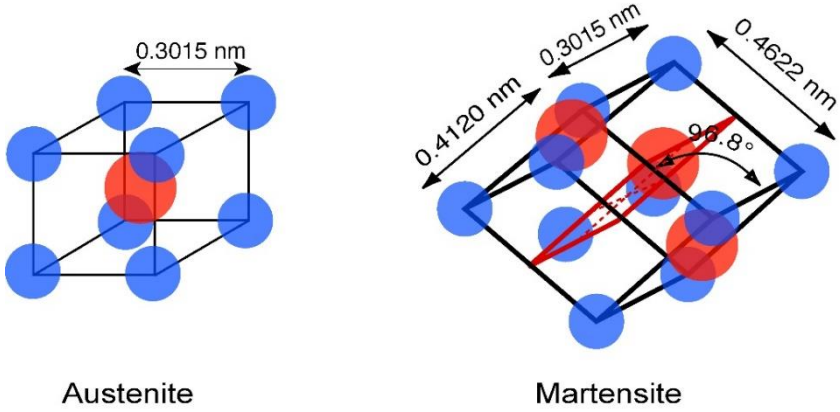

Figure 4 – Crystal structure of austenite and martensite.

The Ti-Ni phase diagram is depicted in Figure 5. It can be seen that NiTi, above a certain temperature, is not a line compound with a fixed composition, but rather has a certain solubility, that is much larger on the Ni side than on the Ti. Other compounds, namely precipitates Ti_2Ni, Ni_3Ti and Ni_4Ti_3 are also observed for this system.

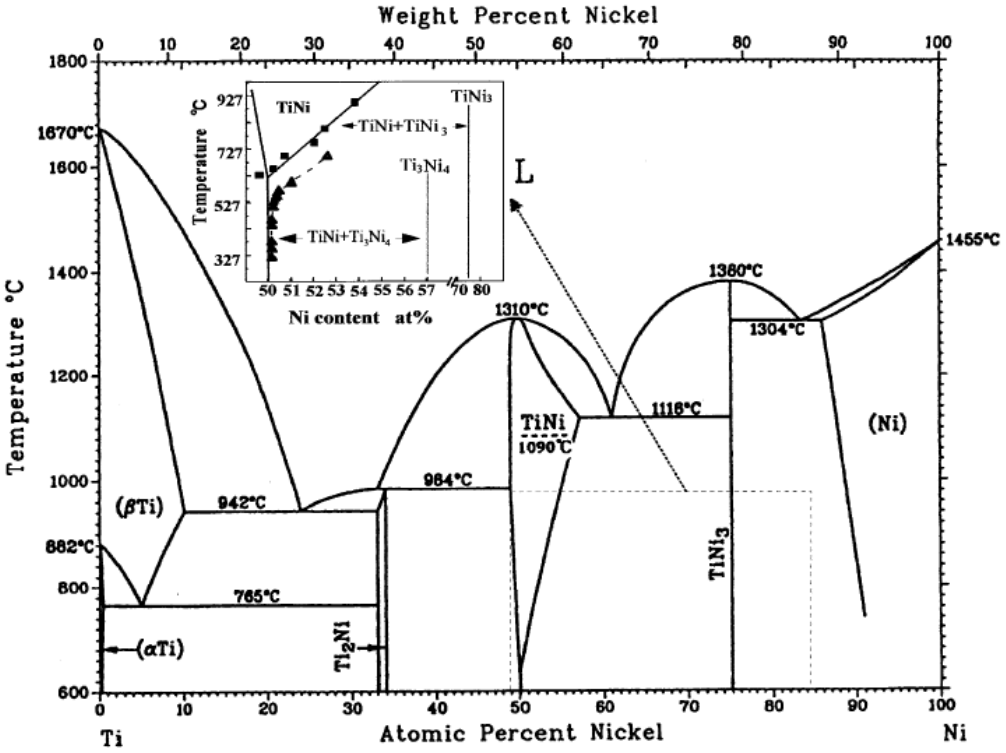

Figure 5 – Phase diagram of Ti-Ni [1].

Extensive studies have been performed studying the precipitation phenomena for NiTi shape memory alloys [11–13]. One time-temperature-transformation (TTT) diagrams is available for this alloy and are shown in Figure 6 a. Preliminary work on this topic allowed for Nishida et al. [14] to present the most detailed TTT diagram for NiTi shape memory alloys (Figure 6 a). More recently, Pelton et al. [15] introduced a diagram exhibiting the time and temperatures required to obtain different transformation temperatures (Figure 6 b) considering significantly shorter permanence times for precipitation phenomena to occur aiming for industrial application involving NiTi.

From Figure 6 a) it can be observed that at lower ageing temperatures and shorter permanence times, Ni_4Ti_3 forms. At higher temperatures and for longer permanence times, Ni_3Ti occurs. In between these conditions, Ni_3Ti_2 is formed. Prolonged ageing leads to the absorption of either Ni_4Ti_3 or Ni_3Ti_2 and increases the content of Ni_3Ti. This is due to the fact that both Ni_4Ti_3 and Ni_3Ti_2 are intermediate phases and Ni_3Ti is the equilibrium phase. The diffusional transformations in this system occur in the following order: $Ni_4Ti_3 \rightarrow Ni_3Ti_2 \rightarrow Ni_3Ti$.

All the aforementioned precipitates (Ni_4Ti_3, Ni_3Ti_2, Ni_3Ti) form when the NiTi alloy used is slightly Ni-rich. In opposition, for Ti-rich NiTi alloys just Ti_2Ni precipitates may exist.

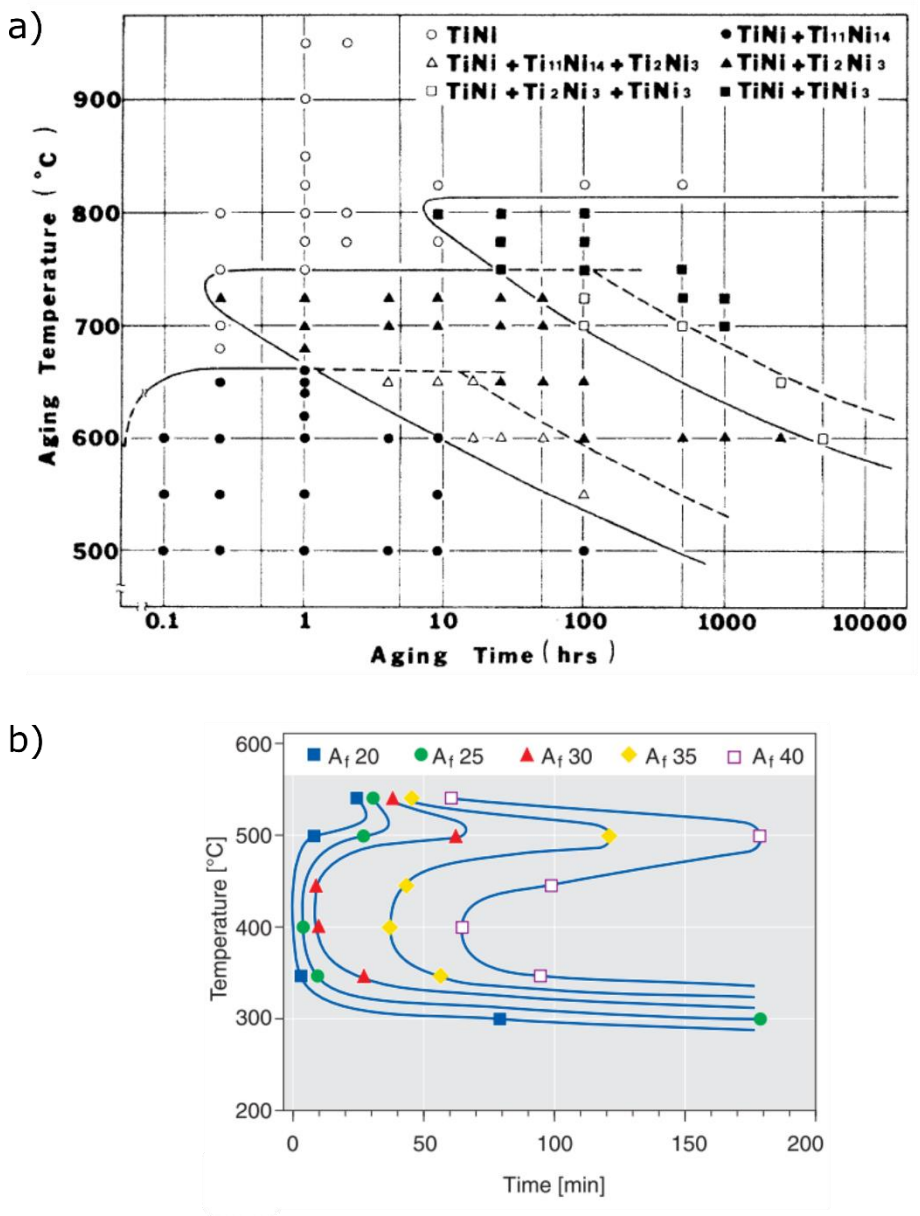

Figure 6 – a) Time-temperature-transformation diagram for NiTi [14]**; b) effect of different time and temperatures to obtain different transformation temperatures** [15]**.**

As a consequence of precipitation phenomena, namely of Ni_4Ti_3, the intermediary phase of the NiTi system, R-phase, can be formed. When Ni_4Ti_3 is coherent with the matrix, or in the presence of dislocation networks, a thermoelastic transformation, which is a transformation that proceeds by changing the stress or temperature, between austenite and R-phase is observed. Such R-phase transformation, when present, is always a step before either the austenite → martensite transformation or vice-versa.

The matrix composition of a given NiTi alloy influences its transformation temperatures and, thus, the functional properties at a given temperature. The influence of the alloy composition on the transformation temperature varies significantly if it is a Ni or Ti-rich NiTi. Figure 7 depicts this variation. It can be observed that for the Ni-rich NiTi the transformation temperatures decrease significantly with increasing Ni content. On the other hand increasing Ti content does not vary significantly the transformation temperatures. Such major difference between Ni and

Ti-rich NiTi alloys is probably due to the fact that solubility limit of NiTi on the Ti-rich side is almost vertical (Figure 5) The transformation temperature of either Ti-rich or equiatomic NiTi are similar. However, for Ni-rich NiTi an increase of 0.1 at. %Ni may decrease the transformation temperatures by 20 K [6].

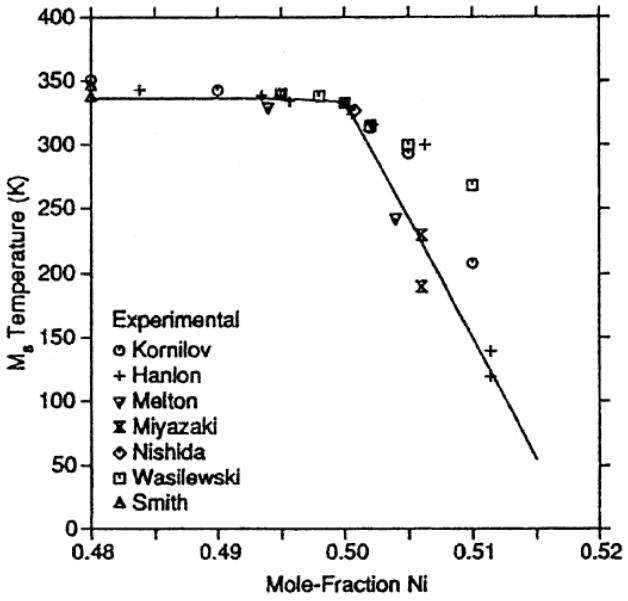

Figure 7 – Variation of the M_S temperature as a function of the Ni content in several NiTi alloys [1].

The incorporation of alloying elements can have distinct effects. The presence of Hydrogen, Nitrogen or Oxygen, for example, is known to affect the transformation temperatures of the NiTi alloys. It is even possible for Ni-rich NiTi to present Ti_2Ni-based precipitates when oxygen is incorporated during thermal processing of the material [16]. For this reason proper atmosphere must be used when thermal processing of these materials is performed. On the other hand, elements such as Copper [17], Iron [18] or Niobium [19] can be alloying elements which form ternary Ni-Ti-X shape memory alloys, being X a given metallic element.

Despite the good corrosion properties of NiTi at room temperature, similarly to other Ti-based alloys, severe oxidation occurs at temperature above 450 °C. Such oxidation is detrimental to the functional properties of the material, hence the need for inert atmospheres when performing heat treatments, for example.

For NiTi shape memory alloys, the tensile curves for both austenitic and martensitic NiTi are similar when subjected to tensile testing, both presenting a constant stress level plateau. However, for austenitic NiTi, this (superelastic) plateau occurs roughly between 300 and 500 MPa, while for martensitic NiTi, this value (where martensite detwinning occurs) lowers to around 200 MPa. During tensile testing, R-phase also exhibits a constant stress plateau at nearly 50 MPa, with a maximum extension of 1 %, which can be fully recovered upon unloading.

2.1.2 Cu-based Shape Memory Alloys

Although NiTi shape memory alloys exhibit the better properties in strength, ductility and corrosion resistance, they are very expensive. For that reason, inexpensive Cu-based shape memory alloys have been studied and developed and they possess advantages in electrical and

thermal conductivities and deformability, when compared to NiTi [20]. Among the large number of shape memory alloys that have been discovered, most are Cu-based. In this group, two sub-groups are dominant in terms of development for practical applications: Cu-Zn- and Cu-Al-based alloys. These can be ternary, where Cu-Zn-Al and Cu-Al-Ni have most often been the object of research and development efforts. For that reason, their phase diagrams, crystal structures and fundamentals on the transformation temperatures are more accurately described [21].

Depending on the composition of the Cu-based alloys they may, or may not, present complete shape memory effect or superelasticity. For example, the Cu-Al-Ni shape memory alloy only presents complete shape memory effect when its composition is very well defined (14 to 14.5 wt% Al and 3 to 4.5 wt% Ni). The same occurs for other Cu-based alloys such as the Cu-Al-Be, Cu-Au-Zn, Cu-Sn or Cu-Zn.

For a range of compositions, the metastable β phase orders during cooling and undergoes a first-order, diffusionless, structural transition into a more close packed phase. This is the basis of the martensitic transformation in Cu-based alloys [22].

Among the different available Cu-based shape memory alloy, a Cu-Al-Mn alloy was studied in the present work. Hence the main focus of this section is related with this particular class of alloys.

Problems arise for Cu-based alloys with high Al content with the β_2 or the β_1 ordered structure. Some of these problems are the excessive brittleness, which limits the amount of cold work, and the very low fatigue strength. The brittle characteristics of these alloy arises from the high degree of order of the parent β phase and tend to cause intergranular fractures [23]. Additionally, the low ductility of Cu-based shape memory alloys, is usually attributed to large grain size, high degree of elastic anisotropy and grain boundary segregation of impurities. For practical applications, these can be a considerable setback for the use of such shape memory alloys.

In 1995 it was first shown that Cu-Al-Mn alloys, with low Al composition (<17 at. %), exhibited excellent ductility, as well as stable superelastic properties [24]. From this moment on, special attention was devoted to these materials. The addition of Mn to the binary Cu-Al alloy was found to stabilize the body centered cubic β phase, widen the single-phase region to lower Al compositions and lower temperatures, and improve the ductility of the low Al alloys by decreasing the degree of order of the parent phase.

The phase diagram for a Cu-Al-Mn alloy is depicted in Figure 8. It is seen that the transition temperatures of order-disorder transitions β (A2) → β_2 (B2) and β_2 → β_1 ($L2_1$) drastically decreases with the Al content. Increasing either the Mn or the Al content of the alloy decreases the transformation temperatures, with a greater sensitivity to modifications in the Mn content. The α phase, which can also appear in these shape memory alloys, has a face centered cubic structure.

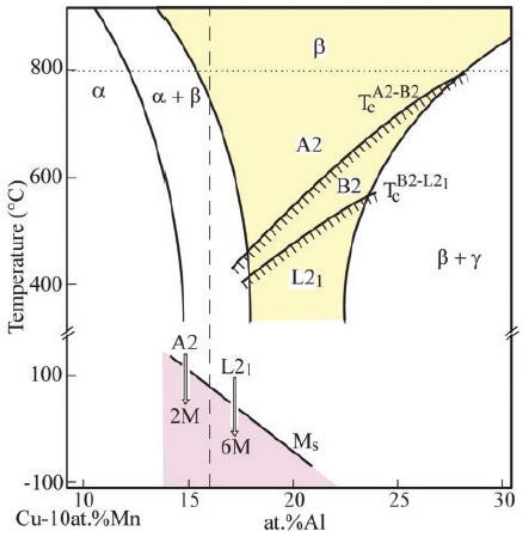

Figure 8 – Cu-Al-Mn phase diagram [25]**. Vertical section in 10 at.% Mn of phase equilibrium for the Cu-Al-Mn system.**

Three different martensite structures can occur depending on the composition of the Cu-Al-Mn alloy: α_1' (3R), β_1' (18R) and γ_1' (2H) [26]. The α_1' phase forms for low Al contents, the γ_1' phase is predominant for high Al contents, while the β_1' exists for intermediate ranges of Al. Sometimes the 18R martensite structure is described as 6M modulated martensite. This is due to the choice of the monoclinic (6M) or orthorhombic (18R) unit cell, which some authors use to describe in a better way the transformation mechanism. In both cases is the stacking sequence that defines one or the other structure [27,28].

The effect of Al content on superelasticity and shape memory effect of Cu-Al-Mn alloys with Al contents below 18 at. % was studied by Kainuma et al. [24,26]. Good ductility and excellent cold-workability due to a lower degree of order in the Heusler ($L2_1$) β_1 parent phase was observed. For Cu-Al-Mn alloys with Al and Mn contents below 18 at. % and of nearly 10 at. %, respectively, the superelasticity and shape memory effect arise from the reverse martensitic transformation from cubic β_1 ($L2_1$) parent phase to monoclinic β_1' (18R) martensite.

From the different Cu-Al-Mn alloys studied, it was observed that the Cu-17Al-11.4Mn (at. %) has the highest performing superelastic properties and can even exceed the recoverable strain achieved by NiTi [4,29].

The stress-strain response of the Cu-17Al-11.4Mn (at. %) alloy wires is extremely dependent on the relative grain size to wire diameter ratio, d/D, where d is the grain size and D the wire diameter [23]. It was observed that an increased recoverable strain was obtained with increasing grain size, due to the decrement of the grain constraint by the surrounding grain boundaries. Additionally, these alloys present a strong dependence of their mechanical characteristics with their crystal orientation. Others factor are influenced by the d/D ratio: the onset for the stress induced transformation, work-hardening rate (defined as the slope of the stress-strain curve after the initial linear behavior of these materials) and stress hysteresis increase with decreasing d/D; the transformation strain and the maximum superelastic recovery decreased with decreasing d/D.

Owing to the aforementioned characteristics, this particular alloy has usually a bamboo-like grain structure with a length of at least 1 mm. However, growing such massive grains it was not easy until Omori et al. [30] find out that these alloys can present abnormal grain grown under appropriate processing conditions. When a given material presents abnormal grain growth, selective growth of a few grains occurs by engulfing the neighboring ones. Some of techniques available to activate this phenomena consist on plastic deformation followed by an annealing heat treatment with a temperature gradient or by plastic deformation at high temperatures. However, these methods can only be applied to wires or sheets, in which fracture occurs by slight plastic deformation. For these Cu-Al-Mn alloys a cyclic heat treatment was sufficient to promote the growth of the grain structure. The heat treatment consisted on the following sequence: slow cooling down from the β-phase region (for example at 850 °C) to the biphasic α + β region (for example at 600 °C) and subsequent heating to the β phase region again. This cyclic heat treatment can be performed several times in order to obtain increasingly larger grains.

Aside from their improved mechanical and functional properties, the Cu-17Al-11.4Mn (at. %) alloy is being considered as a potential lower cost alternative to NiTi for seismic and vibrational damping applications [31,32]. Additionally, this alloy does not present risks to the human body, which have enabled its use in medical devices for ingrown nail correction [29].

2.2 Laser Welding

Welding is, eventually, the most used manufacturing technology since ancient times due to the possibility to produce complex shapes and components in tailored materials. Among the large diversity of welding processes, Laser welding finds increasing applications in industry.

“Laser” is an acronym for light amplification by stimulated emission of radiation. The stimulated emission phenomenon was predicted by Albert Einstein in 1916 but it was demonstrated in practice almost five decades later. As a result of the stimulated emission of radiation all photons have the same wavelength, are in phase (both in space and in time) and travel in the same direction. Thus, the main characteristics of laser radiation are: monochromaticity, directionality low divergence and coherency in both space and time, allowing a good focusability.

The power density of a laser beam can be defined as the power to beam focused diameter ratio. For laser welding the power density is within 10^6 to 10^8 W/cm.

The most commonly used lasers in welding and materials processing (cutting and surface treatments) are: CO_2, Nd/YAG and fibre lasers. Among these, Nd:YAG lasers, and more recently fibre lasers, are quite used in welding, since the output radiation has a wavelength of 1064 nm, which is easily absorbed by metallic materials [33].

Due to the above mentioned characteristics of the laser light, laser welding is a high density energy process, able to weld with low heat input, thus, both the fusion zone and the heat affected zone are narrow and the residual stresses and distortions in the welds are often negligible [34]. Other advantages of laser welding are: there is no physical contact between the heat source and the material; there is no need to have special environments, as a vacuum chamber; it is a flexible and possible to automatize process; it can weld difficult materials in

similar or dissimilar joints; it is a high precision process capable of performing microwelding. However, the major disadvantages are related to: equipment and consumables costs, especially inert shielding gases and the required precision and fit-up prior to welding, especially in butt welding.

When the laser beam produced in the laser source is focused onto the material surface, the photons energy are absorbed and converted into heat that dissipates by conduction. If the energy introduced is higher than the dissipated one, heating and melting occurs in the beam/material interaction volume. At high energy densities, the material is vaporized and heat is transmitted into depth. So a capillary of metallic vapor forms surrounded by the molten walls that are sealed up behind. The shape of this molten pool is similar to a keyhole and, so, it is known as "keyhole welding mode". It is characterized by a very narrow weld with an aspect ratio (width/depth) << 1. The forces exerted on the molten pool determine its shape and stability, namely the gravity and surface tension tend to close the capillary, while the beam pressure, vapor pressure and recoil pressure tend to maintain it open.

If the energy density is not sufficient to form the keyhole, a conduction weld is formed with a width to depth ratio >> 1 and the molten pool undergoes a strong stirring driven by Marangoni forces which result from the variation in surface tension and variations in material density with temperature in the fusion zone [35]. Besides these, a transition mode is commonly observed that is a mixture of conduction welding on the top surface and keyhole at the bottom [36]. Typical fusion zone geometries for conduction and keyhole welding modes are depicted in Figure 9.

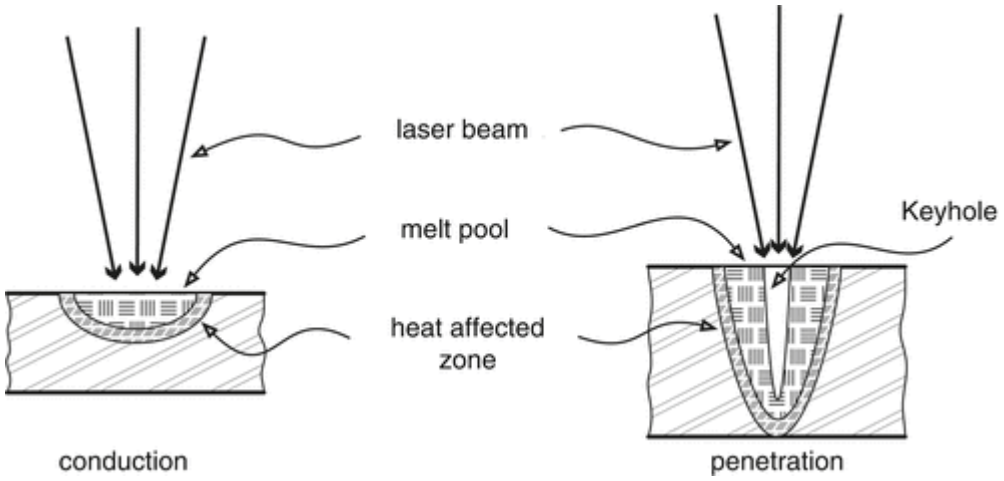

Figure 9 – Typical fusion zone geometries for conduction-limited and keyhole welding modes (from [37]**).**

Process parameters can be related to laser itself (wavelength, output power, operation mode and beam quality), the manipulation system and materials (optical and physical properties as a function of temperature).

Considering the operation mode, it can be pulsed or continuous: in continuous, laser power and welding speed are the main operating parameters to control, while in the pulsed wave mode, the pulse shape, frequency and duration, and the peak energy are the major ones. In all cases a shielding gas is required to minimize evaporation phenomena and oxidation of the molten pool

and the heat affected zones, but also to improve coupling of the laser/material, blowing away the plasma formed above the surface.

The beam quality is a relevant parameter and according to ISO 1146:1999 there are three parameters for assessing the beam quality, that it, the energy distribution along the beam radius, being the most important M^2 and BPP (beam parameter product), where $M^2 = 1$ for a Gaussian beam [38]. The beam quality and its wavelength, as well as, the beam diameter exiting the laser cavity controls the beam spot on the focus plane as well the depth of focus. If the beam quality is poor, the energy density can be insufficient to melt the material and even prevent full penetration.

So, from the characteristics mentioned above laser is considered the most suitable fusion welding process for shape memory alloys, which are known to be very sensitive to oxidation at high temperatures and variation in chemical composition.

2.2.1 Laser Welding of Shape Memory Alloys

Shape memory alloys, especially NiTi, are increasingly applied in industrial applications. However, these materials are very hard to machine, thus difficulties arise when trying to obtain complex shapes. For this reason, joining techniques are used in order to widen the range of applications of this class of functional materials. When correctly applied, such joining techniques may provide an increased design flexibility aiming at both functional and structural applications.

Owing to the functional properties presented by shape memory alloys, it must be ensured that, after joining, these properties are preserved. Otherwise, the intrinsic value of these materials decreases significantly. Amongst the different available joining techniques, laser welding is, by far, the most used for shape memory alloys.

In this section some of the most important studies related to laser welding of NiTi shape memory alloys is presented. For Cu-Al-Mn shape memory alloys no weldability studies have been performed yet, thus this section in devoted only to NiTi.

2.2.1.1 Laser Welding of NiTi Shape Memory Alloys

Similar laser welding of NiTi shape memory alloys dates back to 1989 when Araki et al. [39] welded 3 mm thick Ni-rich NiTi plates, using a CO_2 laser. Due to the high sensitivity of NiTi to high temperatures, laser welding was considered to be an adequate process to minimize the thermal affected regions and to preserve the functional properties of the welds.

Early laser welding studies on NiTi shape memory alloys where performed using CO_2 lasers [39–41] while, nowadays, the primary choice for such studies are the infrared lasers, such as Nd:YAG [42,43] and fibre lasers [44–46].

The microstructure in the fusion zone of the NiTi laser welds can present either a dendrite-like, planar or cellular microstructure or a combination of these. The solidification structure observed can be explained based on rapid solidification theory [47], which establishes four parameters to govern the microstructure found in the fusion zone: temperature gradient (G), undercooling (ΔT), crystal growth rate (R) and alloy composition. The ratio between temperature gradient and crystal growth rate, G⁄R, governs the solidification mode, while the product G.R, represents the cooling rate and controls the crystal growth. As the constitutional supercooling increases, the

solidification structure changes from planar to cellular and from cellular to dendritic. As such, it is possible to observe only one, two or even all three structures in the fusion zone of a laser weld.

Structural characterization of the present phases after welding is of great importance, as the identification of the existing phases in the welded region is crucial to understand, for example, the mechanical behaviour of the welded joints. This type of characterization is usually performed by X-ray diffraction. However, a problem arises when doing this type of analysis on the most common configuration (Bragg-Brentano). In this geometry, the irradiated area decreases with the 2Θ angle [48] and since the extension of both heat affected and fusion zones is reduced, it is difficult to ensure that the analysed region comprehends only one of those regions. That is, it may be difficult to ensure that the analysed region is only either the heat affected zone or the fusion zone of the welded specimen. Nonetheless, it was already reported the use of X-ray diffraction using laboratory sources to perform structural analysis on laser welded NiTi [49]. The authors have shown that while the base material was austenitic, the fusion zone had both austenite and martensite.

The formation of undesired compounds in laser welded NiTi joints was also reported to occur [41,50,51]. Amongst the different precipitates that can form in the Ni-Ti system, Ti_2Ni is the one that is more detrimental to the joints mechanical performance due to its inherent brittleness. The presence of Ti_2Ni-based oxides was identified by Schlobmacher et al. [51], who proposed that its formation in the fusion zone occurred due to the presence of oxygen. This assumption reinforces the need to have the NiTi base material as free of impurities as possible and required good gas protection during welding so that no contaminants, such as hydrogen or oxygen, can be picked-up by the molten metal. Besides Ti_2Ni, Ni_3Ti [44,45,52,53] was also found in the fusion zone of laser welded joints.

The tensile strength, as well as the elongation to fracture of the welded joints are usually below that of the original base material [41,54,55], as depicted in Figure 10. The presence of grain boundary segregation of precipitates in the thermally affected regions and the microstructural differences (grain size and existing phases) between those regions and the base materials, may justify this occurrence.

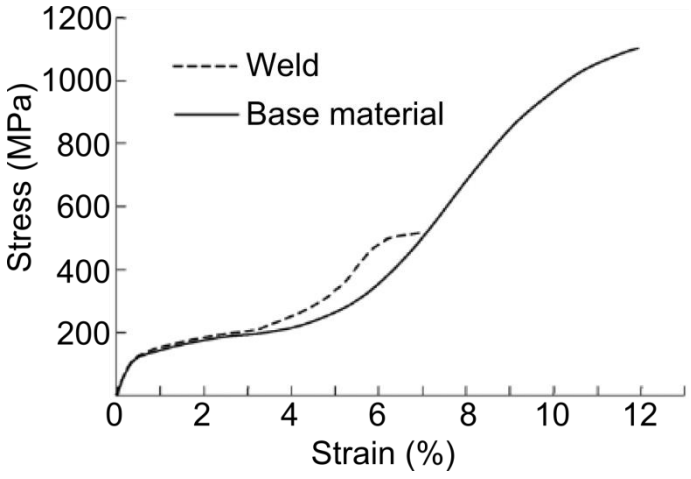

Figure 10 – Stress-strain curve for martensitic NiTi base material and the laser welded joint (adapted from [54]**).**

The superelastic behaviour of a NiTi joint can only be assessed after at least one load/unload cycle. When the material is mechanically tested in the austenitic or martensitic phase, a constant-stress plateau is expected. In the former case, upon unloading, the irrecoverable strain at zero stress should be significantly lower than in the latter. For that reason, although a constant-stress plateau can be observed after welding in tensile tests of NiTi welds, it is not assured that superelasticity is preserved. This is due to the fact that as when the material is loaded in the martensitic state, as soon as it enters the constant stress plateau, an irrecoverable strain (corresponding to the difference between the maximum applied strain and the elastic deformation of martensite) will occur when unloading to a zero stress condition. On the other hand, while loading the material in the austenitic state up to the end of the constant stress plateau should not originate a significant irrecoverable strain upon unloading.

Several studies report the cycling behaviour of NiTi welds [39,40,44,55–58]. However, a significant disparity in the reported experiments is observed. Cycling tests are reported, for a number of cycles ranging from 1 to 100 cycles and for an applied strain between 3 and 8 %.

As a rule of thumb, laser weds presented lower superelastic behaviour (higher irrecoverable strain after unloading) when compared to the base material. Chan et al. [44] subjected laser welds to a load/unload cycle at different strains and observed that increasing the applied strain, the irrecoverable strain upon unloading also increased. Additionally, these values were higher than those of the base material. It was also observed that the critical stress for the stress induced transformation in the welded joint, decreased, when compared to the base material. Similar findings, regarding the decrease of the critical stress for the occurrence of the superelastic plateau, were also reported in [55,57]. It is suggested that this stress reduction occurs due to accommodation by dislocation slip as a result of the heterogeneous microstructure of the welded joint.

Hsu et al. [58], reported that after 50 mechanical load/unload cycles, only 0.19% permanent strain was observed in the laser welds, while for the base material it was of 0.09%. Such small permanent deformation can partially be explained by the total strain imposed during the cycling tests, which was only 3%. Similar results were reported by Gugel et al. [42], when cycling both base material and welded specimens for a total of 10 cycles up to 2.5% strain. Nonetheless, for applications where conventional materials are not able to present such elastic behaviour, NiTi laser welds can definitely be used.

The effect of maximum strain imposed during cycling behaviour was presented by Vieira et al. [55]. When testing both the base material and the welded joint up to 4 and 8% strain for a total of 30 cycles, significant differences were found, as far as the accumulated irrecoverable strain is concerned. While after the cycling tests at 4% the welded material presented an accumulated irrecoverable strain of nearly 0.7%, this value increased significantly up to about 4.4% for 8% strain tests. In both cases, the welded material always had a higher accumulated irrecoverable strain when compared to the base material. Interestingly, the superelastic behaviour of the joints was observed up to applied stresses of 50 MPa below their tensile strength, which may be of significant importance for industrial applications.

Chan et al. [46] analysed the cycling behaviour of NiTi welds up to 100 cycles, with a maximum imposed strain of 4%. Stress kinks which were attributed to a local stress induced transformation

of the thermal affected regions were only observed in the first loading cycle. The absence of those stress kinks in the following cycles suggests that local plastic deformation of those regions has occurred, thus, not contributing for the superelastic effect and leading to an increase in the irrecoverable strain.

Fatigue behaviour analysis of laser welded NiTi is reported in [58, 59]. In [59] Yan et al. studied the rotating-bending fatigue of laser welded NiTi. The effect of the imposed strain amplitude with the number of cycles to failure presented by the laser welds was compared to the base material. Is was observed a decrease on the fatigue properties of NiTi after laser welding, which was attributed to segregation of solute and impurities upon solidification of the weld metal and to the existence of a coarse grain and dendritic structures in the same region. When the imposed strain amplitude was below 0.4%, which is still within the elastic limit of the material, the welded joints were able to withstand up to 10^6 cycles without rupture. However, when the strain amplitude was of 1.0%, the fatigue life of the NiTi joint was reduced to about 10^3 cycles, while the base material was able to sustain a total of 10^4 cycles. It was observed that the differences between the base material and welded material increased when increasing the strain amplitude.

The fatigue resistance under rotating-bending solicitation of laser welded NiTi was also analysed by Chan et al. [60]. Similarly to [59], it was reported a decrease of the fatigue resistance after welding. In this study, the authors also analysed the influence of the bending frequency and reported a decrease of the fatigue resistance when increasing the bending frequency. During the stress induced transformation of austenite to martensite the sample temperature increases [61]. As such, when the frequency increased the generated heat also increased. With increasing temperature the plateau for stress induced transformation raises, requiring a higher stress to occur. It is even possible to overcome the M_d temperature, at which the stress for dislocation slip is lower than the starting of the stress induced transformation. All these factors explain the lower fatigue resistance of the NiTi base material and laser welds with increasing frequency. Fracture analysis of the welded samples after fatigue tests, revealed that cracks were originated in the fusion zone due to higher roughness, when compared to the base material, coming from solidification after laser impingement. In NiTi, it is reported that increasing surface roughness, as usually found in the fusion zone, may decrease the fatigue-crack growth resistance [62], justifying the decrease in the fatigue resistance of the welded material. Brittle-like features in the fracture surface were reported in [59], while in [60] the welded material fractured in a ductile mode.

Nevertheless, laser welded NiTi joints revealed a lower fatigue resistance when compared to the base material, though these joints were still capable to withstand a significant number of cycles, which is of significant importance for applications in micro-electro-mechanical systems [63], for example.

Aside from studies on the superelasticity of laser welded NiTi joints, the effect of this fusion-based technique on the shape memory effect was also assessed by several authors.

The shape memory effect on laser welded NiTi was first reported in early studies on laser welding of NiTi [39,40], and it was stated that full recovery of the imposed strain was achieved when the samples were heated to the austenitic phase.

From the functional properties presented by NiTi, the shape memory effect appears to be the less affected by laser welding. Several authors reported that at least 90% of the imposed deformation is recovered when the shape memory effect is triggered [41,56–58]. Evidence of the shape memory effect in laser welded NiTi was investigated by tensile testing [39,41,56–58]: the samples are pulled, in the martensitic phase, up to a certain strain and unloaded to a 0 stress condition, presenting a significant deformation. Then, the welded specimens were heated above the A_F temperature and the shape memory effect occurs allowing for a significant strain recovery of the imposed deformation.

For NiTi, the shape memory recovery is dependent of the applied strain. As such, it is important to known how the applied strain affects the shape memory recovery of the welded joint and compare to the base material. Schlobmacher et al. [56] tested NiTi joints up to 6% strain with subsequent unloading to 0 stress and heating above A_F. They reported that the irrecoverable strain after martensite → austenite transformation increased with the applied strain, as it was expected. Although the irrecoverable strain of the welded joints was small (bellow 0.1% for a 4% strain and 0.3% for 6% strain), these were less performing than the base material.

The effect of imposed strain on the shape memory recovery for Ti-rich laser welded NiTi was also evidenced by Falvo et al. [54]. It was observed that the maximum strain recovery of the welded joint was of 4% for an imposed strain of 5%, while for the base material, the maximum strain recovery achieved 5.2% for a total strain of 7.3%. The reason for this difference between the weld and base material is related to the development of dislocation slip, leading to plastic deformation. The authors attributed the earlier development of slip in the welded material to the lower resistance of the joint when compared to the base material.

Only one study addressed the problem of the two-way shape memory effect after welding [64]. In their work, Ti-rich NiTi, 1.2 mm thick plates, martensitic at room temperature, were butt welded using an Nd:YAG laser. After welding, the residual stresses resulting from previous cold working of the base material and laser welding itself were relaxed by heat treatment. A load/unload cycle, up to 3.5% strain was performed to compare the mechanical response of the base material and the welded joint, and the main difference observed was on the stress for the onset of martensite detwinning, which was found to be higher in the welded specimen. This effect was attributed to the grain growth and the occurrence of precipitates due to weld thermal cycle of laser welding.

Several techniques can be used to determine the transformation temperature of any shape memory alloy. Differential scanning calorimetry [65,66], dilatometry [67] or electrical resistivity [68,69] are the most used ones.

For laser welded NiTi, the transformation temperatures of the thermal affected regions are always determined by differential scanning calorimetry, despite the fact that these are very narrow. This problem was reported by [56] and, to overcome it, the minimum required dimension of the sample to be tested was remolten by the laser to simulate the fusion zone. However, it is very difficult to ensure that a given sample for thermal analysis has only one of the thermal affected regions [70].

Hsu et al. observed a decrease in the transformation temperatures of the fusion zone when compared to the equiatomic NiTi base material [58]. The oxygen content was measured in both regions and it was found to be significantly higher in the fusion zone, hence justifying the change in the transformation temperatures. For NiTi, the increase in oxygen content is known to decrease the transformation temperatures [16], and this reinforces the need for a good shielding protection, so that the contamination in the fusion zone is not detrimental to the joints properties.

Tuissi et al. [57] performed differential scanning calorimetry measurements in both base material, heat affected zone and fusion zone. Their findings showed that in both base material and heat affected zone only one transformation peak is identified in both cooling and heating. However, in the fusion zone a partially overlapped two-step transformation was observed and was attributed to the presence of R-phase due to the imposed residual stresses after welding.

Laser processing of NiTi was performed by Khan et al. [71]. Although this is not a laser welding research, some interesting findings can still be applicable. In the laser processed material, full penetration of 0.37 mm thick NiTi with a pulse overlap of 80% was attained. This can be then compared to bead on plate welding, which is normally used to determine the best range of parameters for butt welding. Differential scanning calorimetry of the processed region, where fusion occurred, revealed the presence of extra peaks at high temperatures when compared to the one-stage transformation observed, in both cooling and heating, in the base material. These extra peaks were due to a variation in the microstructure of the material after laser processing: while the base material was fully austenitic, the processed region had both austenite and martensite (observed by X-ray diffraction). As such, a good agreement between the thermal analysis and the microstructural characterization by X-ray diffraction was obtained. The existence of martensite in the processed region was explained based on preferential volatilization of Ni in the fusion zone [72], as previously suggested by [73]. In fact, Ni depletion increases the transformation temperatures of NiTi [16]. So, the austenitic base material at room temperature prior to laser processing, experienced an increase in its transformation temperatures that allowed for martensite to be stable at room temperature, replacing austenite as the equilibrium phase.

Post-weld heat treatments are usually used for stress relief of residual stress due to the thermal gradient inherent to fusion welding [74] or optimization of the tensile properties of the welded material by obtaining a more suitable microstructure [75,76]. Accordingly, by choosing appropriate heat treatment parameters (temperature and time) the mechanical properties of the welds can be improved.

In NiTi laser welded joints, post-weld heat treatments were seen to promote Ni_4Ti_3 precipitation [46,77–79]. The presence of Ni_4Ti_3 may improve the mechanical properties of NiTi as it can resist the plastic flow by acting as effective barriers to dislocation motion [46].

For Ni-rich NiTi, the heat treatments promote a raise in the transformation temperatures, due to Ni depletion of the matrix surrounding the Ni-rich precipitates [1]. This was observed by Chan et al. [46]. In opposition, for Ti-rich welded NiTi, precipitates formed during heat treatments can promote a decrease in the transformation temperatures. However, the effect of post-weld heat treatment on Ti-rich NiTi joints was not yet reported.

In Chan et al. work [46] a two-step transformation took place after the post-weld heat treatments (350 and 450 °C for 60 minutes), as depicted in Figure 11. This is an indication that R-phase should exist as an intermediate phase during austenite ←→ martensite transformation. Similar results were observed by Yan et al. [79]. The presence of Ni_4Ti_3 precipitates, which are known to promote the existence of coherency stress fields, favours the formation of the R-phase [80].

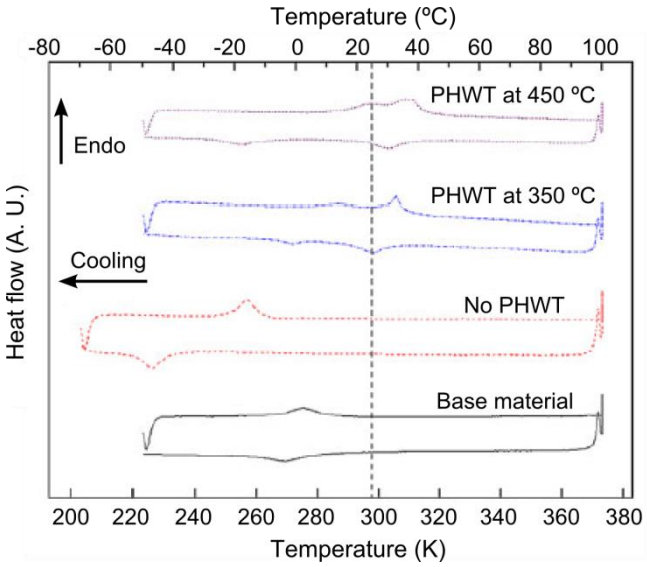

Figure 11 – Differential scanning calorimetry curves for the base material and fusion zone of NiTi welds with and without post-weld heat treatments (PHWHT). The dashed line represents room temperature (adapted from [46]**).**

When a proper selection of the parameters for the post-weld heat treatment was made, it was possible to obtain higher elongation to fracture of the joints when compared to as-welded material [46]. Additionally, the onset for the stress induced transformation decreases with the post-weld heat treatment due to a softening effect (Figure 12) [79].

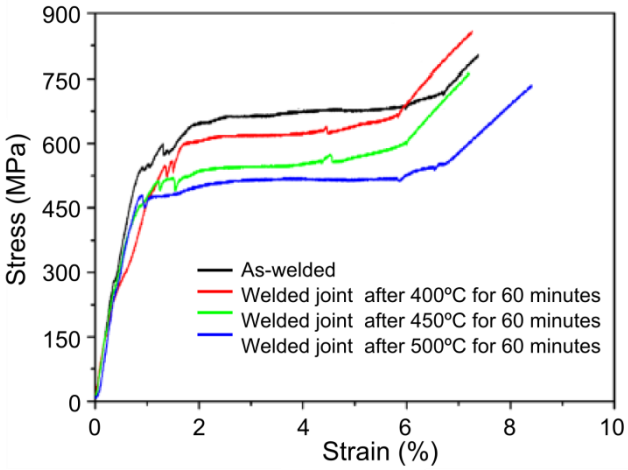

Figure 12 – Effect of post-weld heat treatments on the mechanical properties of laser welded NiTi joints (adapted from [79]**).**

The cycling behavior of post-welded NiTi joints was studied by Chan et al. [46]. It was observed that low temperature heat treatments (350 °C for 60 minutes) preserved the superelastic properties of the welded joints. However, if higher post-weld heat treatments temperatures

were used (450 °C for 60 minutes), massive Ni_4Ti_3 precipitation would occur allowing for martensite to be stable at room temperature, replacing austenite and thus the superelastic effect was inhibited.

Ni_4Ti_3 grain size was also seen to affect the fatigue behavior of post-weld heat treated NiTi joints. When these were of only 10 nm, an improvement on the rotating-bending fatigue behavior, compared to the base material was observed. However, when the grain size increased to 300 nm the fatigue resistance decrease significantly, when compared to the base material. The reason for this behavior is related to the fact that, with the increased grain size of the precipitates, introduction of dislocations to relax the misfit with the surrounding matrix is required to attenuate the stress fields.

In opposition to similar joining of NiTi, dissimilar combinations involving this functional material presents significant additional welding problems.

One of the attempted dissimilar joints was of NiTi to Ti6Al4V. Significant metallurgical problems arise when welding NiTi to Ti6Al4V. Assessment of the weldability of NiTi to Ti6Al4V was investigated by Miranda *et al*. [81]. Regardless of the heat input introduced during welding, to control the cooling rate upon solidification, cracking was always observed in the fusion zone. SEM analysis of fracture surfaces revealed the presence of brittle Ti_2Ni which caused transgranular cracking upon cooling. The formation of Ti_2Ni is promoted by the migration of Nickel, from NiTi, to the liquid Titanium. As such, it is apparent that the solution for overcoming the embrittlement of NiTi/Ti6Al4V welded joints can be made by introducing an element that either inhibits or decreases the amount of brittle intermetallics formed in the fusion zone.

The insertion of an interlayer was tried by Zoeram et al. [82,83] using Cu. The embrittlement of the welded joint was reduced, as the amount of Ti_2Ni decreased when compared to the joint without interlayer. Nonetheless, some other Cu-based intermetallics were formed due to the presence of the Cu interlayer, namely Ti_2Cu, Cu_2Ti, Cu_3Ti and Cu_4Ti. Hardness measurements on the fusion zone revealed higher values than both base materials, despite a significant decrease when compared to the fusion zone of the joint welded without the Cu interlayer. The thickness of the interlayer used, and thus the amount of Cu introduced into the fusion zone, has been seen to play a significant role on the properties of the joints. As the thickness of the interlayer increased (up to 75 µm), the Cu-rich areas also increased in the fusion zone. However, further increase of the interlayer thickness promoted formation of shrinkage cavities and increasing the interlayer thickness was found to be detrimental to the joints properties due to the formation of brittle Cu-based intermetallics. An optimum interlayer thickness was found to be of 75 µm, and the correspondent welded joint experienced rupture at 300 MPa and 3.3% strain, without any indication of superelastic plateau.

It is apparent that despite the use of interlayer provided better mechanical properties of the dissimilar joint, no interlayer was yet found to inhibit the formation of undesired intermetallics compounds. As such, determining the correct interlayer or combination of interlayers may be of great importance to obtain sound NiTi/Ti6Al4V joints.

Detailed analysis of the existing literature of welding of NiTi shape memory alloys reveals that for similar laser welded joints the effects of laser welding parameters on the microstructural

alterations are not yet clear. Additionally, the effect of those microstructural modifications on the functional properties still need to be address. Up to know, no residual analysis of welded NiTi joints was performing, hence an important gap is evident. For the dissimilar combination of NiTi to Ti6Al4V, it is necessary to found laser welding strategies that allow to obtain sound joints, so that the formation of brittle intermetallics, which are known to impair the mechanical properties of the joints, is decreased or even supressed. As no welding studies exist for CuAlMn shape memory alloys it was also considered of significant importance to address this issue.

3. Materials and Methods

In this section, the materials and characterization techniques used in this investigation are described. Initially, the raw materials used for similar and dissimilar welding are presented. The welding equipment is described based on the laser type used (continuous or pulsed-wave mode). Based on the laser used, similar and dissimilar (when applicable) welding parameters and configuration used involving shape memory alloys are specified.

Several characterization techniques were used throughout the investigation: tensile testing, hardness measurements, indentation-load measurements, optical microscopy, scanning electron microscopy, transmission electron microscopy, X-ray diffraction using synchrotron radiation. However, some of those techniques were only used for a given type of welded joint (i.e. for NiTi/NiTi or NiTi/Ti6Al4V joints, for example). As such, all characterization techniques are presented without specifying for which joints they were used (unless strictly necessary). During the discussion of the results (Results and Discussion section), it is clear which techniques were used for each welded joint.

3.1 Materials

3.1.1 Similar laser welding

For NiTi/NiTi welds, Ni-rich (50.8 at. %) NiTi sheets, 1.00 ± 0.05 mm thick, supplied in the flat-annealed condition from Memory (Connecticut, United States of America), were used.

For similar CuAlMn laser welding, Cu-17Al-11.4 Mn (at. %) wire, 0.5 ± 0.005 mm in diameter. The CuAlMn alloy was prepared by induction melting under Argon atmosphere. The ingot was hot forget and cold-drawn to make 0.5 mm in diameter wires. To obtain the superelastic properties, the wires were subjected to a solution treatment at 900 ^{o}C for 5 minutes and quenched in water. The material was then subsequently aged at 200 ^{o}C for 20 minutes [30].

3.1.2 Dissimilar laser welding

For NiTi/Ti6Al4V dissimilar laser welding, aside from the NiTi sheets described previously, Ti6Al4V sheet, 1.05 ± 0.05 mm thick, from Titanium Joe (Ontario, Canada), were also used.

All materials were cut with a precision cut-off machine equipped with a diamond wheel. After cutting to the desired dimensions, the materials were cleaned with acetone and ethanol to remove impurities prior to welding.

3.2 Laser Welding

Laser welding was performed using continuous and pulsed-wave mode Nd:YAG lasers with a wavelength of 1.064 nm.

For similar NiTi/NiTi butt joints a DY033 Nd:YAG laser power source from Rofin-Sinar (Centro Láser de Madrid, Spain), operating in a continuous wave mode was used. The following welding parameters were varied: laser power and welding speed. The laser beam was focused to 0.45 mm diameter at the top surface of NiTi and Ar was used as shielding gas at 45 l/min. No gap between opposite plates (of 30 x 30 mm) was left prior to welding. Table 1 depicts the welding parameters for the NiTi/NiTi laser butt joints.

Table 1 – Laser welding parameter for similar laser welding of NiTi to NiTi.

Sample	Power	Welding speed	Heat input
A	990	25	396
B	990	20	495
C	990	15	660
D	1485	30	495
E	1485	25	594
F	1485	20	743

For both dissimilar NiTi/Ti6Al4V joints and similar CuAlMn welds, a Miyachi Unitek LW50A pulsed Nd:YAG laser system (University of Waterloo, Canada) was used. A top-hat type spatial profile was used to ensure that the near-Gaussian incident beam was transformed into a uniform-intensity round spot of 400 or 600 µm in diameter, respectively.

For the NiTi/Ti6Al4V joints, the pulse profile had a 20 ms duration, with a 3 ms upslope and 15 ms downslope. The peak power was set at 3.0 kW. Laser spot welds, along the joining interfaces, were performed with an overlap of 25% so that a continuous weld could be obtained. Argon was used as shielding gas and the flow rate was set at 16.5 l/min.

Preliminary welding trials to joint NiTi to Ti6Al4V were performed to determine the optimum welding parameters to obtain full penetrating welds. Cracks were observed after cooling to room temperature preventing any mechanical analysis of the welded joints. The effect of laser positioning was also tested: when impinging directly NiTi or Ti6Al4V base materials, or at the contact interface of the base materials, crack formation was not avoided.

Niobium was placed in between the two base materials so that is could act as a diffusion barrier to prevent solidification cracking in the fusion zone. Niobium was selected as interlayer as it form an eutectic with NiTi and has full solubility in Ti, and vice-versa. The schema of the experimental set-up used for welding NiTi to Ti6Al4V is depicted in Figure 13. The laser beam was positioned on the Ti6Al4V joint (250 µm from the contact interface between the two base materials), so that 60% of the laser diameter was on the Ti6Al4V top surface. It was chosen to position the laser on the Ti6Al4V alloy, because NiTi suffers a more severe degradation of its properties at high temperatures. Additionally, focusing the laser on the NiTi side did not promote the formation of a joint to the Ti6Al4V side.

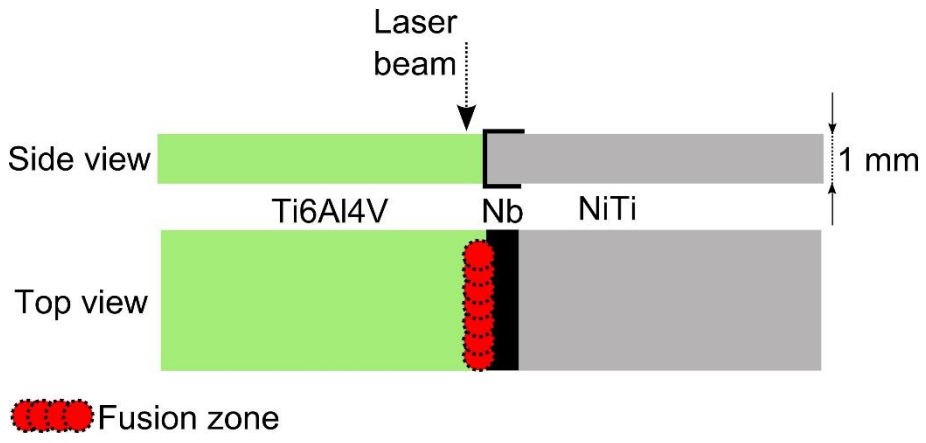

Figure 13 – Schematic of the set-up used for welding NiTi to Ti6Al4V.

For the Cu-Al-Mn welds, the pulse profile had a 6 ms duration, with a 1 ms up and downslopes. Argon was used as shielding gas and the flow rate was set at 9.5 l/min. Due to reduced amount of material, the welding process was developed to obtain full penetration welds with a symmetric contour, using a minimum heat input. To remove joint fit-up from the variables in study, bead on plate welds were produced with a peak power of 1.5 kW. An in-house custom built fixture was used to ensure that the base material wires were straight prior to welding (Figure 14).

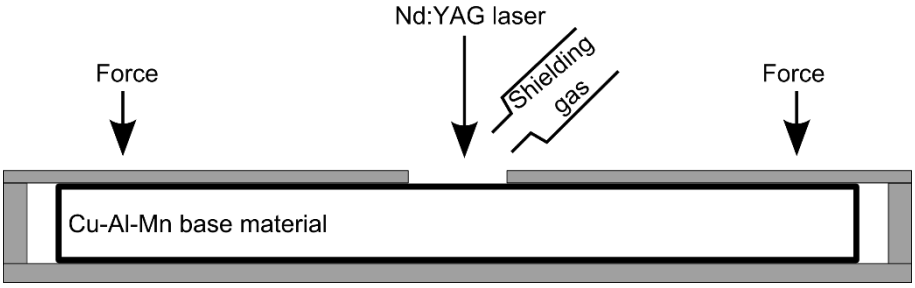

Figure 14 – Fixture, laser and shield gas position for welding the CuAlMn shape memory alloy.

Also, two distinct batches were used: “wire 1” was used for microstructural characterization and tensile testing of both base material and weld; “wire 2” was used to assess the mechanical cycling behavior of both base material and weld.

3.2.1 Post-weld heat treatments

3.2.1.1 Conventional furnace heat treatments

Post-weld heat treatments were performed on similar laser welded NiTi joints in order to evaluate the microstructural changes induced in the different regions (base material, heat affected and fusion zones). The post-weld heat treatments were performed at 350, 400 and 450 °C, at a constant holding time of 60 minutes.

3.2.1.2 Laser post-weld treatments

Laser post-weld heat treatments were performed on the similar laser welding CuAlMn joints. Based on the optimum welding parameters obtained for similar CuAlMn laser welds, a post-weld laser processing comprised by a total of 48 laser spots, with an overlap of 65% of the beam spot diameter (600 μm) was performed. This laser processing was performed on the central region of the specimen along about 1/3 of the total wire length, keeping the remaining 2/3 in the original microstructural condition Figure 15.

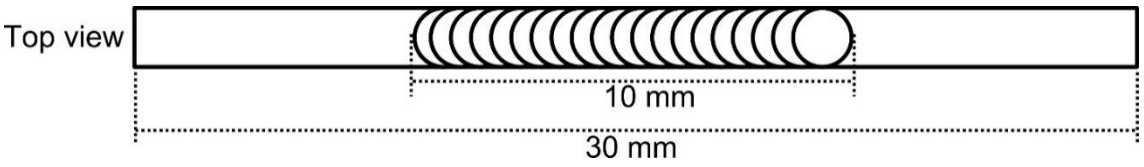

Figure 15 – Set-up for laser processing of the CuAlMn alloy (not to scale).

Laser processing was performed on both the original base material and on the laser welded samples to understand the feasibility of post-weld laser heat treatment to improve the mechanical properties of the joints.

3.3 Thermal analysis

Differential scanning calorimetry (DSC) was used to characterize the structural transformation temperatures of the NiTi base material and of the fusion zone of similar NiTi welds. Due to the reduced dimensions of the specimens required) for DSC analysis (less than 3 mm in length) a precision cutting machine was used to carefully separate the fusion zone from the remaining material. However, as the extension of either the heat affected or fusion zones are within the range of a few millimeters, it is not possible to ensure that the analyzed material comprised only the fusion zone. That is, the DSC sample from the fusion zone could also have some parts of the adjacent heat affected zone. A DSC 204 F1 Phoenix from Netzsch was used. The temperature range was set between -160 to + 70 °C. Both heating and cooling rates were set at 10 K/min.

The DSC curve of the base material is depicted in Figure 16 [84]. Upon cooling, the existence of two exothermic peaks indicates a two-step transformation from austenite to R-phase and, later, to martensite. Upon heating, only one endothermic peak is observed corresponding to the transformation of martensite into austenite. At room temperature, the base material is fully austenitic.

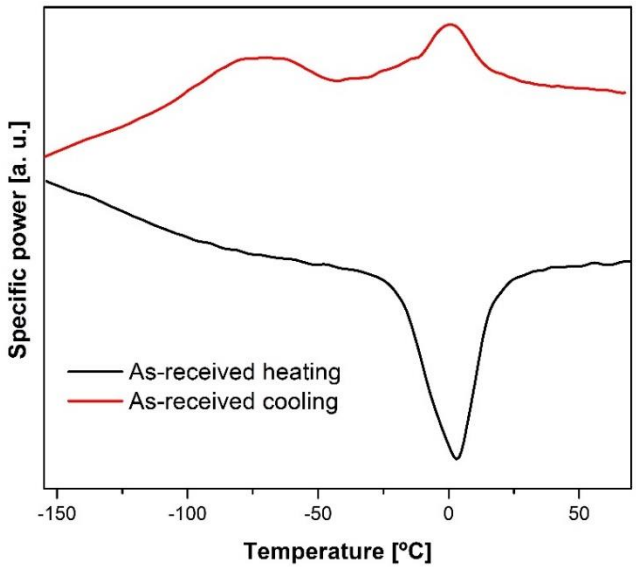

Figure 16 – Differential scanning calorimetry of the base material.

3.4 Microscopy analysis

3.4.1 Optical microscopy

For microstructural observation, the welded specimens were mounted in epoxy resin and mechanically polished up to 2500 fine SiC paper. To reveal the microstructure of the base material and thermally affected zones etching solutions were used: $HF:HNO_3:H_2O$ (1:5:10 in volume) for joints with NiTi; $FeCl_3$ (10 g) + HCl (25 ml) + H_2O (100 ml) for CuAlMn welded joints. Optical microscopy was carried out using an Olympus BX51M and a Leica DMI5000M optical microscopes.

3.4.2 Scanning electron microscopy

Scanning electron microscopy was used for analyzing both the microstructure of the welded joints and the fracture surfaces after mechanical testing. Two different scanning electron

microscopes were used: a ZEISS DSM 962 ESM (available at CENIMAT/i3N, Portugal) at an acceleration voltage of 15 kV and JEOL JSM-6460SME (available at the University of Waterloo, Canada) at an acceleration voltage of 20 kV. In the latter, energy dispersive X-ray spectroscopy (EDS) was performed with an INCA Energy 350 EDS microanalysis system to quantify the compositional changes of the thermally affected regions in the CuAlMn similar welds.

3.4.3 Transmission electron microscopy

From the Ti6Al4V/NiTi dissimilar welding using Nb interlayer, specimens for transmission electron microscopy (TEM) were prepared by focused ion beam (FIB), using a Zeiss NVision 40. The FIB lift-out technique, which consisted on a series of FIB cuts adjacent to the region of interest to be analyzed by TEM, was used [85]. With such technique it is possible to obtain cross-sections up to 150 µm. Additionally, it allows for the preparation of TEM specimens for a given desired location of the samples to be analyzed. In order to protect the surface of the region of interested to be analyzed, a tungsten protective layer was deposited prior to FIB milling. After cutting the sample to the desired dimensions, while reducing its thickness so that the material can be analyzed by TEM, a micromanipulator is used to promote the "lift-out" of the sample.

Transmission electron microscopy was performed using a JEOL 2010F TEM/STEM operated at 200 kV (available at McMaster University, Canada). This electron microscope was equipped with an Oxford Inca energy dispersive X-ray system and a Gatan imaging filter system for the acquisition of the electron energy loss spectra (EELS). EELS was used to acquire an energy loss spectrum at each pixel of a given selected area. Scanning TEM (STEM) EDS maps were obtained using a probe with 1 nm in diameter.

3.5 X-ray diffraction analysis

X-ray diffraction using conventional Cu K-alpha radiation was previously performed [86] to determine the structural transformations of the NiTi base material as a function of temperature from +120 to -180 °C (Figure 17). Similarly to what was observed from the DSC measurements, it can be depicted a two-step transformation from austenite to R-phase and from this to martensite. It was also confirmed that the base material was fully austenitic at room temperature.

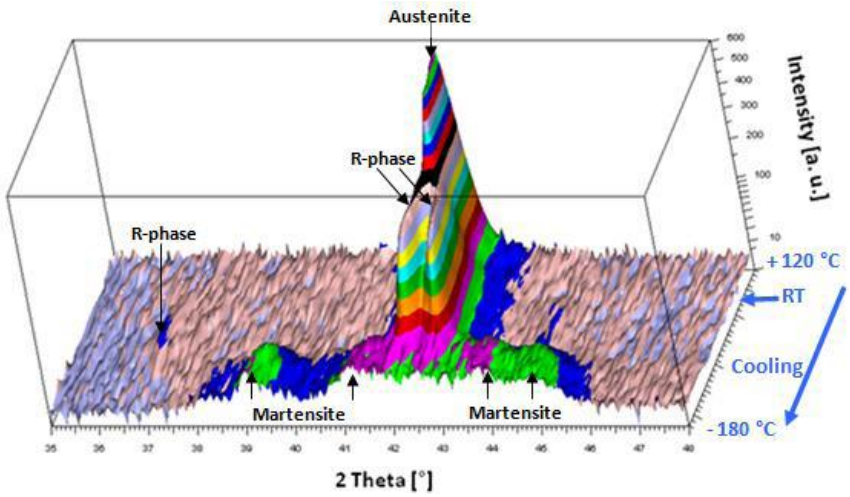

Figure 17 – X-ray diffraction patterns of the base material as function of temperature. Analysis performed from +120 to -180 °C [86]**.**

Structural characterization, using synchrotron radiation, was performed, in beamline P07 of Petra III/DESY using wavelengths that ranged from 0.12525 Å (100 keV) to 0.1426 Å (87 keV). The sample to detector distance also varied from 1.04 to 1.41 m. All X-ray diffraction analyzes based on synchrotron radiation, were performed on transmission mode and the Debye-Scherrer rings were captured using 2D detectors from either PerkinElmer or MAR 345.

The experimental set-up used during the synchrotron X-ray diffraction measurements is depicted in Figure 18. The azimuthal angle, φ, was defined as equal to 0º in the longitudinal direction of the weld bead and equal to 90º for the transversal direction (perpendicular to the weld bead).

Structural characterization, performed at room temperature, probed a total of 6 mm in length of the welded material. The analysis started on the base material, through the heat affected zone and the weld bead and finishing in the base material again. Beam spot dimensions were of 200 x 200 µm and the distance between consecutive spots was of 200 µm.

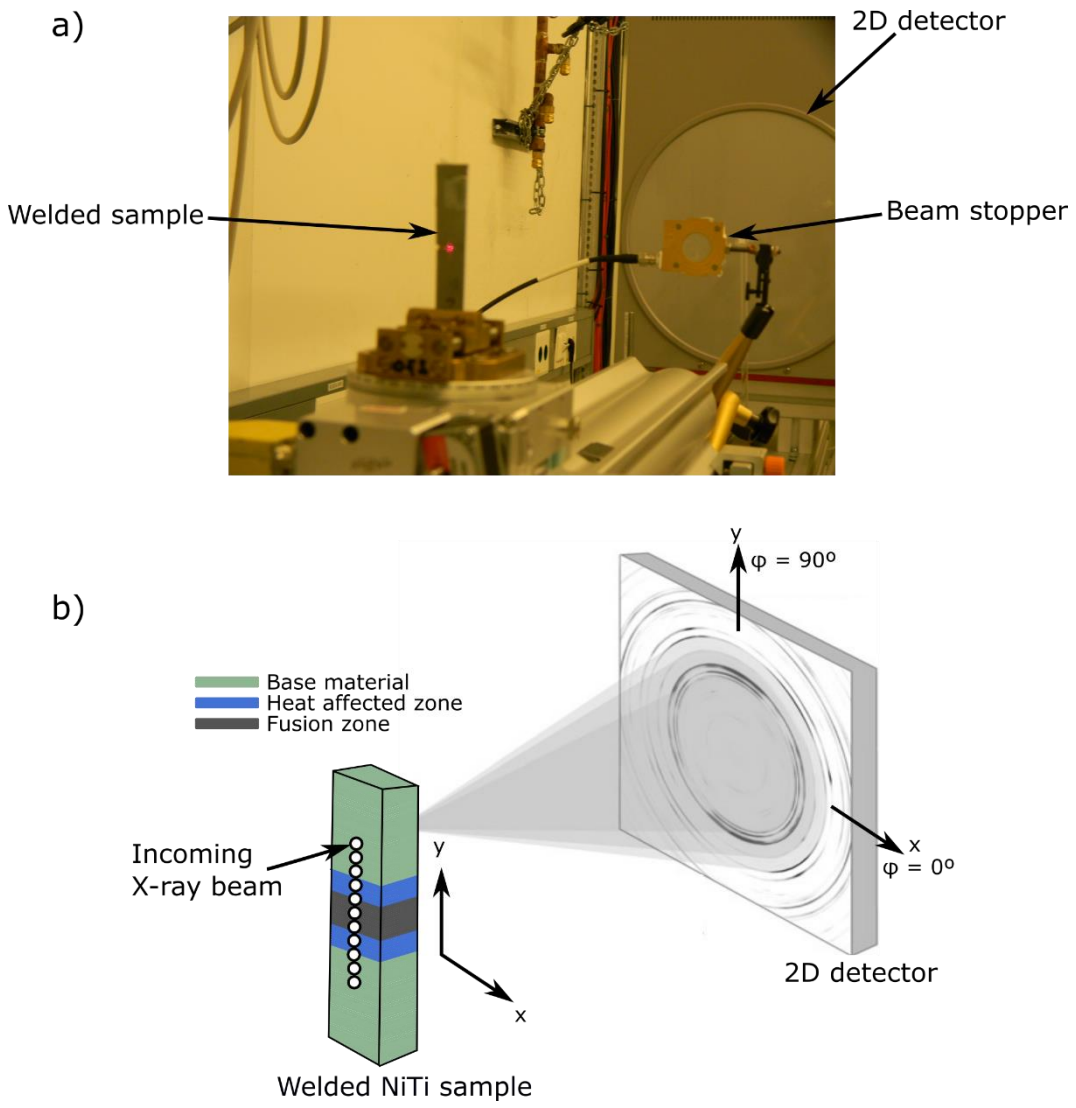

Figure 18 – a) Experimental set-up for the X-ray diffraction analysis performed when no dilatometer was used; b) schematic representation (not to scale).

When such synchrotron-based X-ray diffraction characterization was performed at non-ambient temperatures, a modified dilatometer Bähr DIL 805 A/D was used (Figure 19). The induction coils were specially designed (Figure 19 b) to allow for the X-ray beam to pass through the equipment without hitting any metallic part that could add extra diffraction peaks to the 2D detector. This equipment allowed heating the samples up to a given temperature at a chosen heating rate. This way, in-situ, structural characterization could be performed. These in-situ tests were performed for a select batch of samples. The probing line started in the base material, going through the heat affected zone and fusion zone and finished slightly after the weld centerline. During the in-situ measurement, the welded samples were subjected to the following thermal cycle: heating the sample to 150 ^{o}C; hold for 5 minutes; cooling to room temperature. The aim of these structural characterization tests was to determine the origin of the microstructural modifications observed in the thermally affected regions after welding. Additionally, some samples were subjected to post-weld heat treatments and the welded material was probed in conditions similar to those aforementioned.

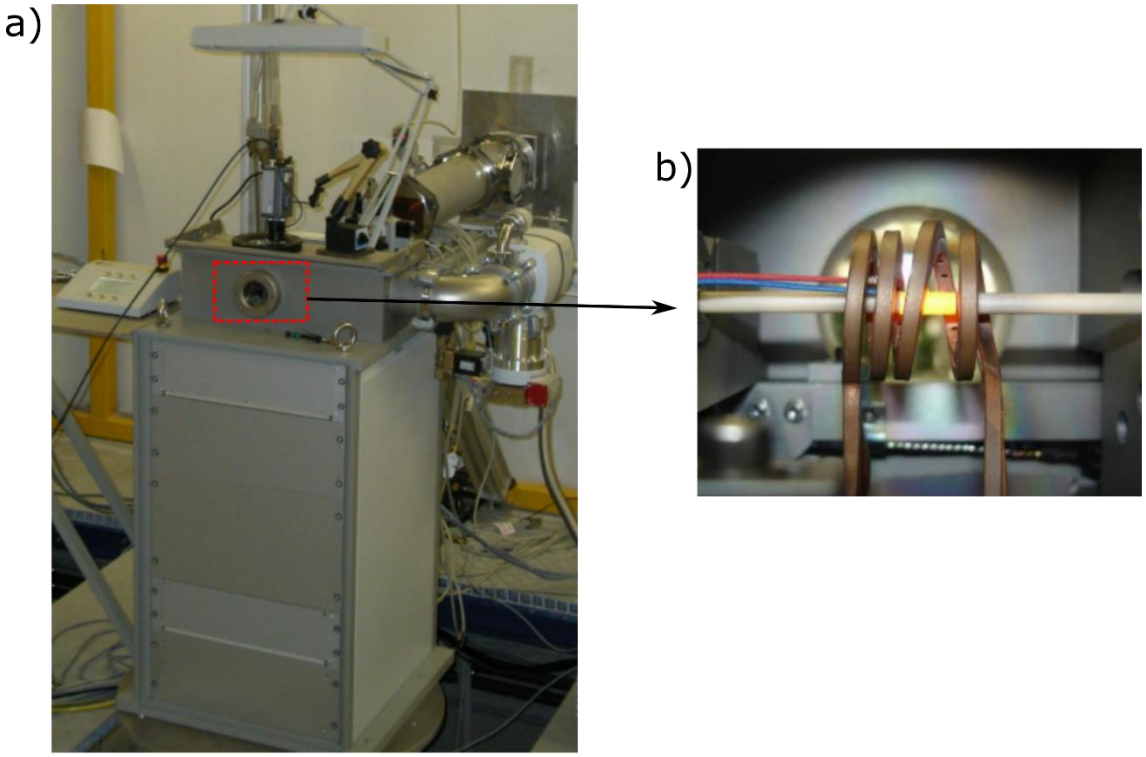

Figure 19 – a) Overview of the Bähr DIL 805 A/D dilatometer; b) close up of dilatometer with the coils used for heating the sample.

All data acquired in synchrotron facilities was treated using the program Fit2D [87]. It was possible to convert the Debye-Scherrer rings into conventional diffractograms (intensity vs interplanar spacing plots).

To analyze the microstructure of the welded joints, the integration was carried on along the full azimuthal angle.

For determining the residual stresses, Rietveld code implemented in MAUD (Material Analysis Using Diffraction) [88] was used in a similar way as described in [89]. During Rietveld refinement, parameters such as background, intensity, profile shape, unit cell, texture and stress model were

refined. For the Rietveld analysis, four austenite peaks were considered: (100), (110), (111) and (200). When both austenite and martensite were present, five additional martensite peaks were considered: (101), (110), $(1\bar{1}1)$, (020) and (211). During Rietveld analysis performed with MAUD, integration in 5° steps along the azimuthal angle was performed. The mechanical properties of both phases used in the stress model are described in [90,91].

Following other authors that have made similar assumptions when performing residual stress analysis with high energy synchrotron radiation [92], a plane-stress condition was assumed owing to reduced thickness of the material under study. As such, and according to the configuration presented in Figure 18 b) used in the diffraction experiments, the principal directions of the system are:

- x component, along the longitudinal direction of the weld bead;
- y component, perpendicular to the weld bead;
- z component, normal to the material surface.

As a plane-stress condition is assumed, the principal stresses along the principal direction z, σ_Z, are assumed to be close to zero. Based on this assumption, it is possible to determine the remaining principal stresses, σ_X and σ_Y, calculated through Rietveld refinement.

3.6 Hardness measurements

Conventional hardness measurements were performed using a micro-Vickers hardness tester, from Shimadzu Corporation (University of Waterloo, Canada). Indentations were made along the cross-section of the weld and compared to those on the base material. The load for each indentation was of 300 g and the hold time was kept at 20 s.

Additionally, indentation load vs indentation depth measurements were made, using a Nanovea M1 hardness tester (University of Waterloo, Canada). Three sets of loads of 20, 30 and 38 N were applied in the fusion zone and base material. Both loading and unloading rates were set at 60, 85 and 120 N/min for each applied load, respectively. A flat tip head with 100 µm diameter was used as indenter.

3.7 Mechanical testing

3.7.1 Tensile tests

Tensile tests to rupture of the welds were conducted at room temperature using an Autograph Shimadzu AG50kNG machine (CENIMAT/i3N, Portugal), equipped with a load cell type SFL-50 kN AG, for the similar NiTi joints. An Instron model 5548 micro-tensile tester (University of Waterloo, Canada) was used for the dissimilar joints of NiTi to Ti6Al4V and for the similar CuAlMn welds. The measurement accuracy is of ± 1 µm and of ± 0.5 µm, respectively. The gauge length of the specimens varied from 20 (to NiTi/Ti6Al4V and CuAlMn welds) to 30 mm (for NiTi/NiTi joints). Uniaxial tensile tests of the similar NiTi butt welded joints were performed with single loading until rupture in a previous work [93]. From these, the ultimate tensile strength and deformation to rupture were recorded. All these tests were performed at displacement speed of 2 mm/min.

3.7.2 Cycling tests

Cycling behavior of the welded joints was also assessed using the same equipment described before. For the NiTi/NiTi joints, a total of 600 mechanical cycles alternating between 8 and 10% strain (as depicted in Table 2) was imposed, while for the CuAlMn joints a total of 10 load/unload cycles up to 5% strain was chosen.

Table 2 – Alternated cycling routine imposed to the NiTi laser welded samples

Stage number	Maximum imposed strain [%]	Number of cycles
1	10	60
2	8	60
3	10	60
4	8	60
5	10	360
Number of cycles if the sample did not break: 600		

3.7.3 Shape memory effect evaluation

The shape memory effect of the laser welded NiTi butt joints was assessed by means of bending tests. A special device, built in AISI 316L stainless steel, allowed bending of the samples to 180º [93]. The curvature radius was of 12.5 mm and the sample was positioned in such a way that the weld bead was in the mid part of the bent region (as shown in Figure 20). In these conditions, the welded samples were bent up to 4% strain. Prior to bending, the material, alongside with the device, were placed in liquid nitrogen to ensure that, bending of the samples occurred in the martensitic condition. After bending, the sample was removed from liquid nitrogen and left to freely recover to ambient conditions. The permanent deformation angle, Ω, was measured under a binocular magnified using a protractor with a resolution of 0.5º, when the samples were in equilibrium with the room temperature. This procedure was repeated four times, alternating the surface of the weld facing the bending device. This means that the weld face and root were under compressive and tensile stress conditions alternately. A schema of the shape memory effect bending tests is depicted in Figure 20. Samples A, B, D and E were analyzed.

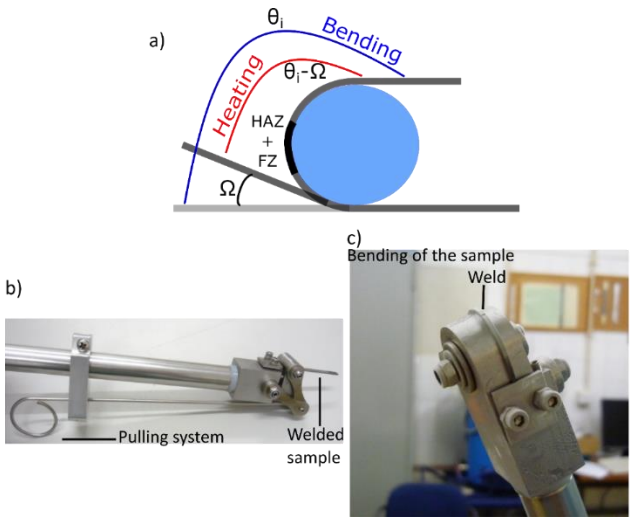

Figure 20 – a) Schematic illustration of the shape memory effect tests performed on laser welded NiTi plates; b) device for bending the samples; c) sample being bent.

4. Results and Discussion

4.1 Similar Laser Welding of NiTi Shape Memory Alloys

In this section, the effects of laser welding on the microstructure of similar laser welded NiTi joints are presented and discussed. The mechanisms that justify observed microstructural features are discussed. Additionally, the mechanical and functional properties, namely the shape memory effect and superelasticity, presented by the welded joints are also analyzed and correlated to the microstructure of the welded materials. Residual stresses created by the weld thermal cycle were also measured using synchrotron radiation based diffraction and are discussed.

4.1.1 Microstructural Characterization by Optical Microscopy

Figure 21 depicts the optical macrographs of samples A and C. While the base material has a fine grain structure, in the heat affected zone and, especially, in the fusion zone, a coarse grained structure is observed. While the heat affected zone presents coarse equiaxed grains, in the fusion zone columnar grains are observed. The effect of the heat input on the extension of the thermally affected regions is notorious: higher heat input (sample C) leads to a higher extension of both heat affected and fusion zones. It can be also observed that the width of the face of the fusion zone is significantly larger than its root. This suggests that both conduction and keyhole modes occurred during welding. Other authors have also observed mixed welding modes occurring in laser welding [36].

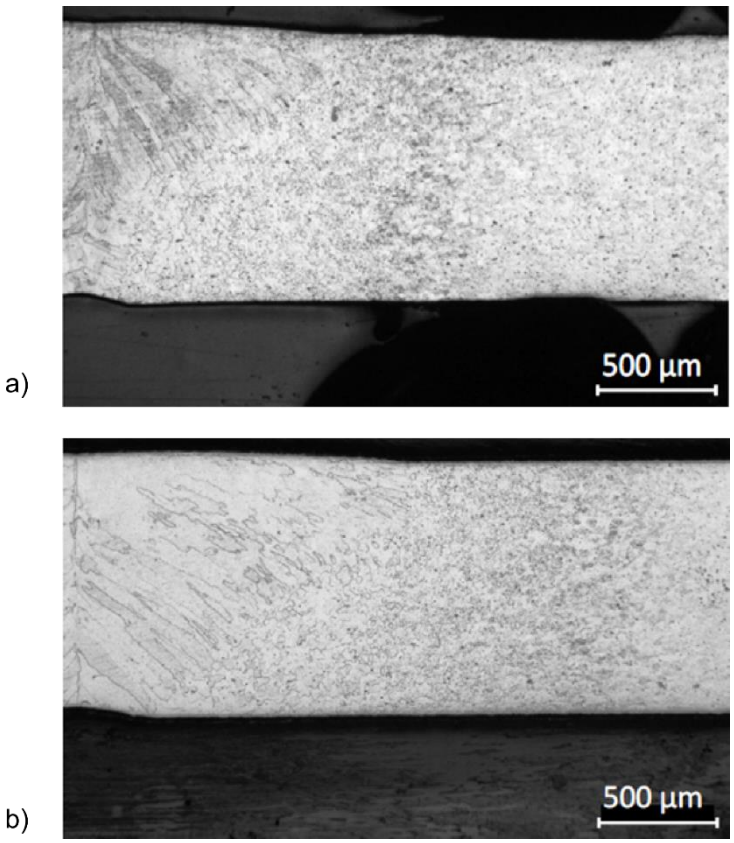

Figure 21 – Optical microscopy of laser welded NiTi joints: a) sample A; b) sample C.

The effect of the heat input introduced during welding is clear in these macrographs: higher heat input (sample C), leads to a higher extension of both heat affected and fusion zones, when compared to sample A, which had lower heat input.

Owing to the characteristics of laser welding, the thermally affected regions have reduced extensions, when compared to other welding techniques such as Tungsten Inert Gas (TIG).

4.1.2 Microstructural Characterization by Differential Scanning Calorimetry and Dilatometry Measurements

Differential scanning calorimetry (DSC) and dilatometry measurements are often used to determine the transformation temperatures of shape memory alloys.

Figure 22 depicts the DSC curve of the fusion zone of sample D. Similarly to the base material, upon cooling a two-step transformation is observed. However, the second transformation peak, usually associated with R-phase to martensite transformation, is shifted to higher temperatures. Additionally, the temperature range where this peak occurs is smaller in the fusion zone than in the base material (-50 and -25 °C for the fusion zone vs -110 and - 50 °C for the base material). Upon heating, a two-step transformation is clearly observed, in opposition to the one-step transformation which occurred for the base material. In can also be observed that the high temperature peaks in both cooling and heating ramps are asymmetric. If the fusion zone had fixed transformation temperatures, symmetrical and well-defined peaks would be expected. However, this is not the case, as observed in Figure 22. Thus, such feature may be associated to a gradient of transformation temperatures in the fusion zone, thus contributing to the observed asymmetry.

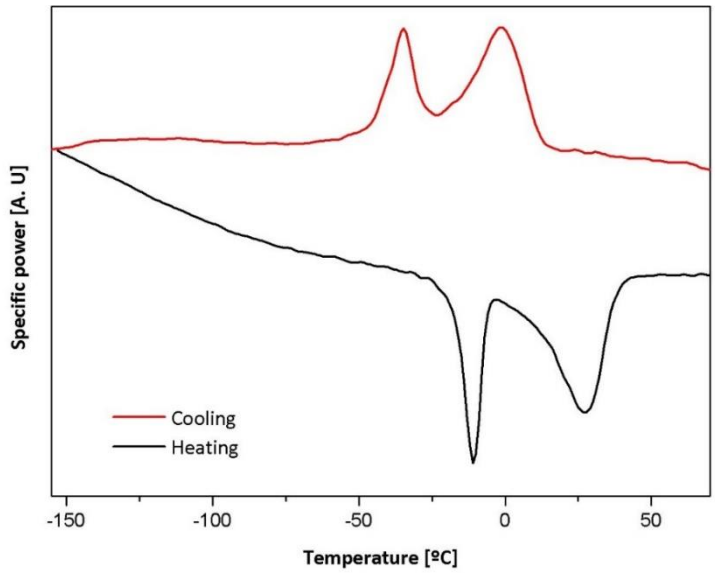

Figure 22 – Differential scanning calorimetry of the fusion zone of sample D.

What can be perceived from these DSC measurements it that the thermal behavior of the fusion zone itself cannot provide information regarding the transformation temperatures of this region. This is due to the presence of a gradient of transformation temperatures, which arise from a gradient of chemical compositions, within the fusion zone. This gradient contributes to

the asymmetric peaks obtained by DSC, preventing to perform a correct analysis of the transformation temperatures of the fusion zone.

Similar information can be obtained from the dilatometry measurements (Figure 23) obtained during the use of the dilatometer for the in-situ X-ray diffraction measurements. It can be observed that the variation of the length is not a linear function of temperature as it would be expected if a single phase existed within that temperature range. As a matter of fact, small variations in the linearity of the length vs temperature of the welded samples are observed throughout the tested temperature range. This means that multiple transformations, from martensite presented in both heat affected and fusion zones to austenite, are occurring. Such results are in line with what was observed from the DSC measurements.

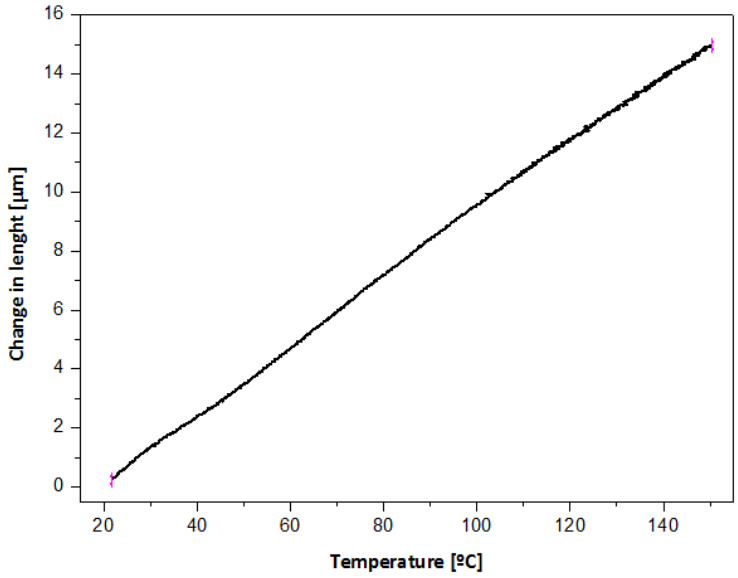

Figure 23 – Dilatometry measurements of sample B.

4.1.3 Microstructural Characterization using Synchrotron-based X-ray Diffraction [1]

From the DSC and dilatometer measurements presented previously it can be inferred that a microstructural gradient is present in these laser welded NiTi joints. Both these techniques are not able to provide a localized analysis of a given region of the welded material. As such, in order to obtain a detailed characterization of the microstructure in the different regions of the joints advanced characterization techniques, which have high spatial resolution, are required. To have a complete microstructural characterization of both heat affected and fusion zones, and compare them with the base material, synchrotron-based X-ray diffraction was performed. In the configuration used, it was possible to fine probe the different regions of the welded material as it is presented next.

[1] *The below results (section 4.1.3) were already published in a paper in the journal Shape Memory and Superelasticity, entitled On the Mechanisms for Martensite Formation in YAG Laser Welded Austenitic NiTi.*

Figure 24 a) depicts three diffractograms of different regions of the welded material: base material, heat affected and fusion zones. Figure 24 b) shows the superimposition of the diffractograms, at room temperature, of a laser welded NiTi joint. A clear districting between the base material and the thermally affected regions is noticed: while the base material is fully austenitic, both the heat affected and fusion zones present a mixture of austenite and martensite. Broadening of the austenite peak, which may be associated with the presence of precipitates is marked with an arrow.

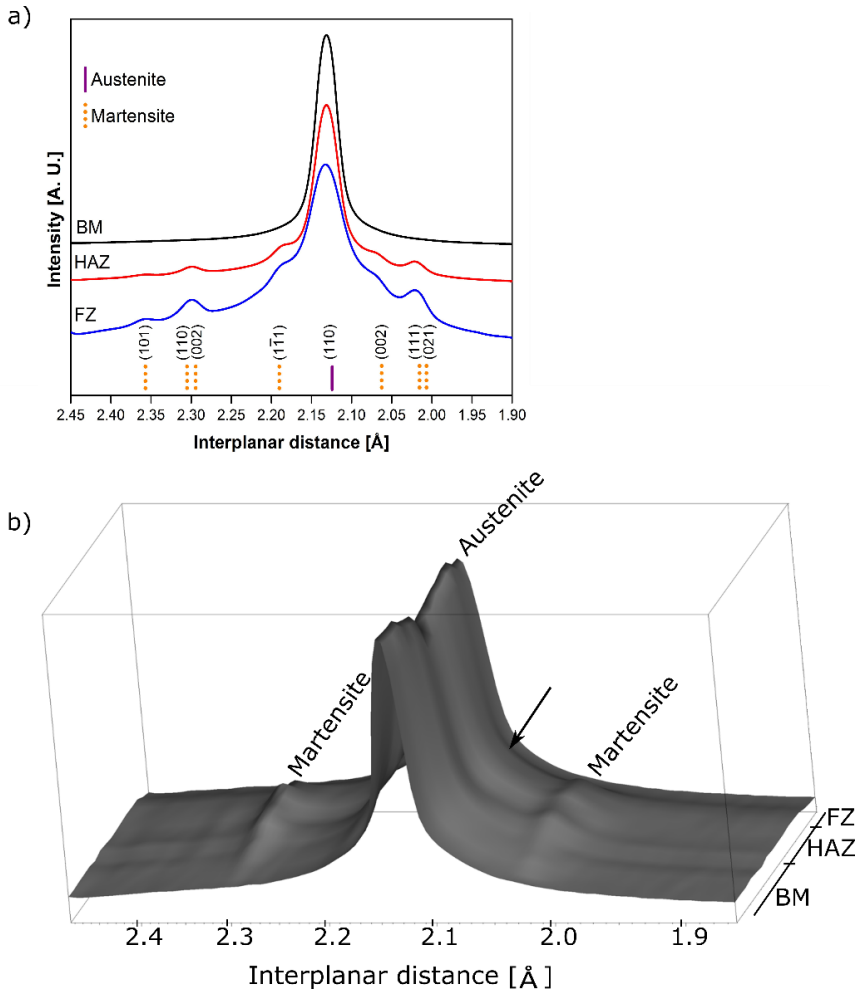

Figure 24 – a) Typical diffractograms of the base material (BM), heat affected zone (HAZ) and fusion zone (FZ) of a laser welded NiTi joint; b) Superimposition of diffractograms of sample B at room temperature, showing the base material, heat affected zone and fusion zone.

In order to understand the mechanisms responsible for the formation of martensite, at room temperature, in the heat affected and fusion zone, while the base material remains fully austenitic, the discussion is carried on analyzing separately each region. Such separation is needed as the mechanisms that are responsible for this microstructural modifications have different origins, despite leading to the same final results: thermal stabilization of martensite in the thermally affected regions.

4.1.3.1 Existence of Martensite in the Heat Affected Zone

The superimposition of the diffractograms at the different regions of sample B, at room temperature, is depicted in Figure 24 b). Only one sample is analyzed as the structural

modifications which occurred due to the weld thermal cycle is similar in all welded samples. As such, the formation mechanisms of martensite in the heat affected zone will also be similar on different welds.

From Figure 24 b), it can be observed that, aside from the presence of martensite peaks in the heat affected and fusion zones, with an intensity decrease in the austenite peak in these regions, a broadening of the (110) austenite peak can be noticed on the right-hand side of this peaks. This broad peak, marked with an arrow in Figure 24 b), occurs in a strip of powder patterns corresponding to the heat affected zone only.

In the neighborhood of the (110) austenite peak several martensite peaks are expected to occur. However, aside from martensite, precipitates from the Ti-Ni system, such as Ni_4Ti_3, are also expected to exist. Either one of these phases, martensite and/or Ni_4Ti_3, might justify this singularity.

In order to confirm which one of these hypotheses – presence of martensite or precipitates – was responsible for the broad peak observed near the austenite peak, the sample was heated up to 150 °C and in-situ X-ray diffraction was performed in a similar way as in Figure 24 b). The reason for such approach is that 150 °C is well above the A_f temperature of the base material. As such, any remaining martensite, in the heat affected and fusion zone, will transform to austenite. However, 150 °C is not enough to promote the dissolution of the Ti-Ni-based precipitates, meaning that if the broad peak is not present at that temperature it can be assigned to martensite. Otherwise it must be assigned to a given precipitate.

The superimposition of the diffractograms obtained at 150 °C is depicted in Figure 25. It can be observed that the martensite peaks in both the heat affected and the fusion zone have completely disappeared, while the broad peak on the right-hand side of the austenite peak is still present (marked with a black arrow in Figure 25). As such, the only possibility to explain this feature is by the occurrence of precipitation phenomena in the heat affected zone.

For Ni-rich NiTi, precipitation of Ni_4Ti_3, Ni_3Ti_2 and Ni_3Ti is possible to occur. Ni_4Ti_3 and Ni_3Ti_2 are metastable precipitates [94,95], while Ni_3Ti is the equilibrium precipitate [96]. It is also known that Ni_4Ti_3 is the first precipitate to occur, at lower temperatures and shorter permanence times.

The Time-Temperature-Transformation (TTT) diagrams for NiTi are scarce. A detailed TTT diagram was presented by Nishida et al. [14]. However, the effect of different temperatures on the precipitation phenomena occurring for short periods of time (magnitude of few minutes or less) was not considered. Pelton et al. [15] presented a more recent TTT diagram for NiTi with focus on shorter required times for the onset of the precipitation phenomena. Additionally, Pelton et al. used an alloy with the same composition as the one used as base material for this investigation. In both TTT diagrams available, it is possible to infer that Ni_4Ti_3 precipitation may occur. In Pelton's diagram it is more clearly depicted that Ni_4Ti_3 precipitation may occur while crossing a temperature range from 350 to 500 °C, in a short elapsed time, of a couple of seconds.

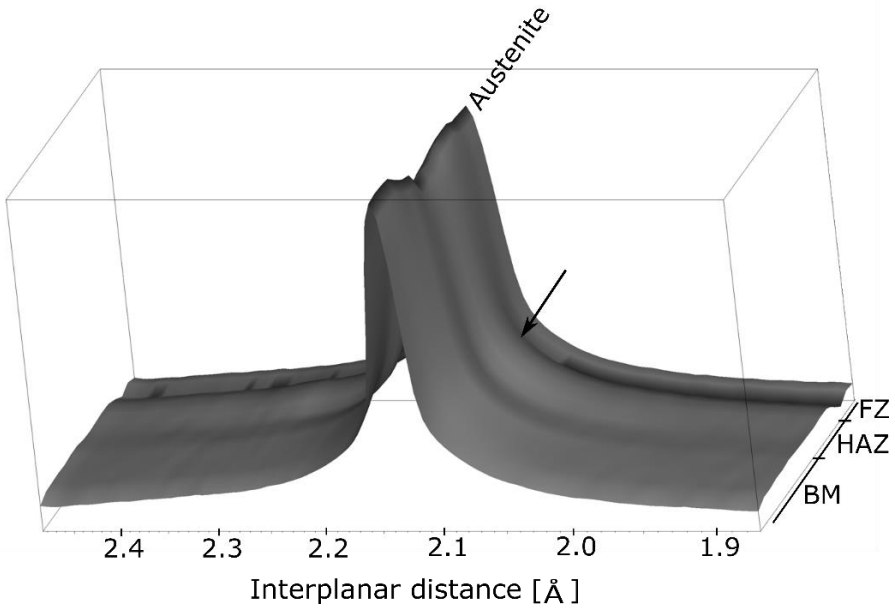

Figure 25 – Superimposition of diffractograms of sample B at 150 °C, showing the base material (BM), heat affected zone (HAZ) and fusion zone (FZ).

Owing to the weld thermal cycle at which the joints are subjected, it is expected that only Ni_4Ti_3 precipitates should be formed, as for the formation of Ni_3Ti_2 and Ni_3Ti longer permanence times are required.

In order to simulate the temperature gradient in the material due to the welding operation, the 2D solution from the Rosenthal equation (Eq. 1) was used. The 2D solution can be used in the situations of single-pass welding of thin materials or when full penetration keyhole occurs [33].

$$T - T_0 = \frac{Q}{2\pi\, k\, g} e^{(v\, x/2\alpha)} K0\left[\frac{v\, r}{2\alpha}\right] \dots\dots\dots\

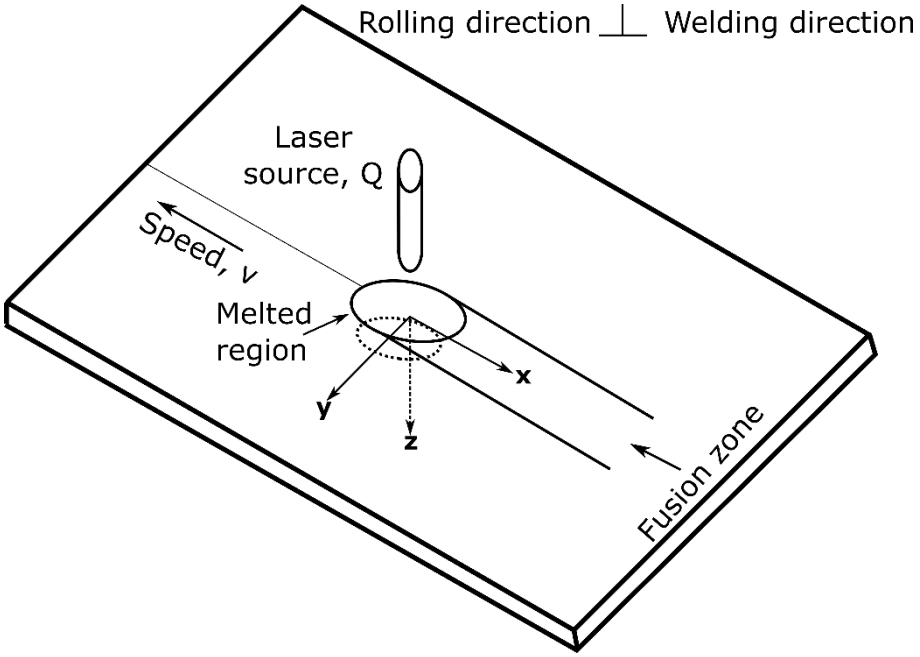

Figure 26 – Reference system used to determine the temperature gradient in the welded joint (adapted from [47]**).**

The temperatures reached for sample B in the heat affected zone, computed using the welding parameters chosen for this sample and the physical properties of NiTi, are depicted in Figure 27. It is also possible to compute the permanence time that the material takes to cross the temperature range between 350 and 500 °C where Ni_4Ti_3 precipitation may occur. This time, in seconds, is presented in Figure 28. It can be observed that the permanence time for such precipitation phenomena is within the time interval determined by Pelton et al. [15] in their experiments. Due to the characteristics of laser welding, the holding time at temperatures where precipitation phenomena can occur is within the magnitude of a few seconds.

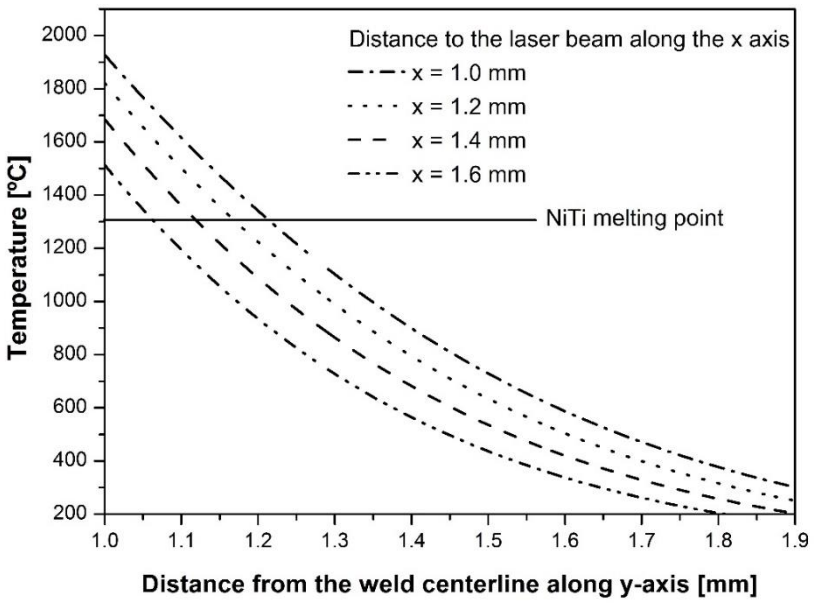

Figure 27 – Evolution of the surface temperature as a function of the distance of the weld beam along the y-axis, for sample B.

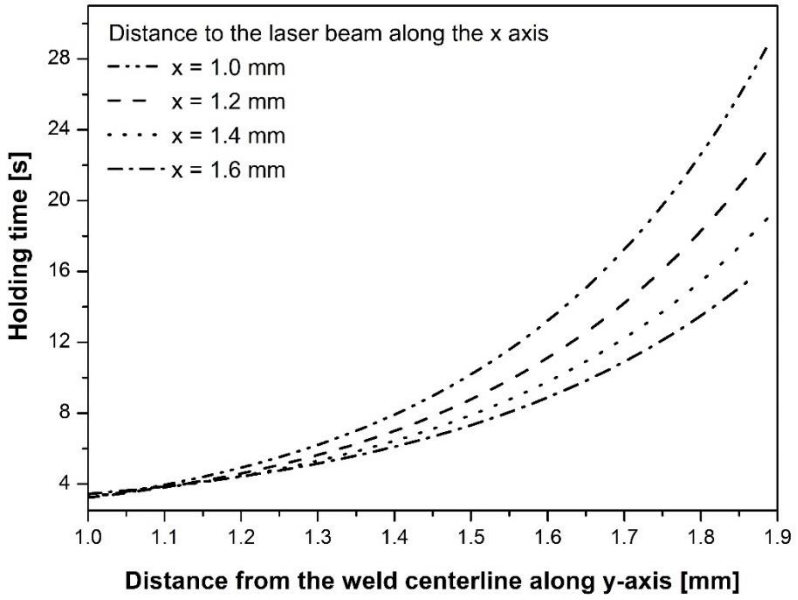

Figure 28 – Holding time, in the heat affected zone, at a temperature range of 350 to 500 °C where Ni_4Ti_3 precipitation may occur, for sample B.

As Ni_4Ti_3 is a minority phase, its intensity in the diffractograms is expected to be very low when compared to the observed martensite and austenite. Additionally, the most intense peak for this precipitate, according to 39-1113 JCPDF card, occurs for an interplanar distance of 2.092 Å, which is very close to the austenite peak and therefore can be partially overlapped by its tail. The remaining peaks of Ni_4Ti_3 have a maximum intensity ranging from 15 to 30 % of the most intense one.

In order to clarify if the Ni_4Ti_3 peaks were present in the diffractograms of the heat affected zone, a post-weld heat treatment at a temperature of 450 °C, during 60 minutes, was performed in sample B. The objective of such post-weld heat treatment was to induce a more significant Ni_4Ti_3 precipitation so that more peaks of this precipitate could be distinguished. After a longer period in the temperature range for Ni_4Ti_3 precipitation, these precipitates should be clearer in the X-ray diffraction patterns, as their intensity is higher due to a higher fraction in the analyzed regions. Also, their appearance should be consistent with the peak positions identified in the heat affected zone of the as-welded material (Figure 24 b and Figure 25), giving then a clear indication that these precipitates were well indexed.

Figure 29 a) and c) depicts the diffractograms of the heat affected zone of sample B, at room temperature and 150 °C, respectively. Both martensite (M) and austenite (A) can be clearly observed at room temperature, but at 150 °C very narrow Ni_4Ti_3 (N) peaks can be depicted, aside from the austenite peak.

After heat treatment at 450 °C for 60 minutes, R-phase (R), as well as austenite and martensite, are observed at room temperature (Figure 29 c). The diffractograms of sample B at room temperature and at 150 °C (to avoid the presence of any martensite or R-phase peaks), after the post-weld heat treatment, is shown in Figure 29 d). The broadening of the (110) austenite peak is still visible and three extra peaks, corresponding to Ni_4Ti_3, are observed. All these three peaks were indexed using the same 39-1113 JCPDF card corresponding to Ni_4Ti_3.

As it can be depicted, the Ni_4Ti_3 peaks located on the left-hand side of the austenite peak have still very low intensity after the heat treatment. So, the fact that these peaks have extremely reduced intensity at 150 °C in the as-welded sample is understandable, as the permanence time in the temperature range from 350 to 500 °C after welding is not sufficient for a significant precipitation phenomena to occur.

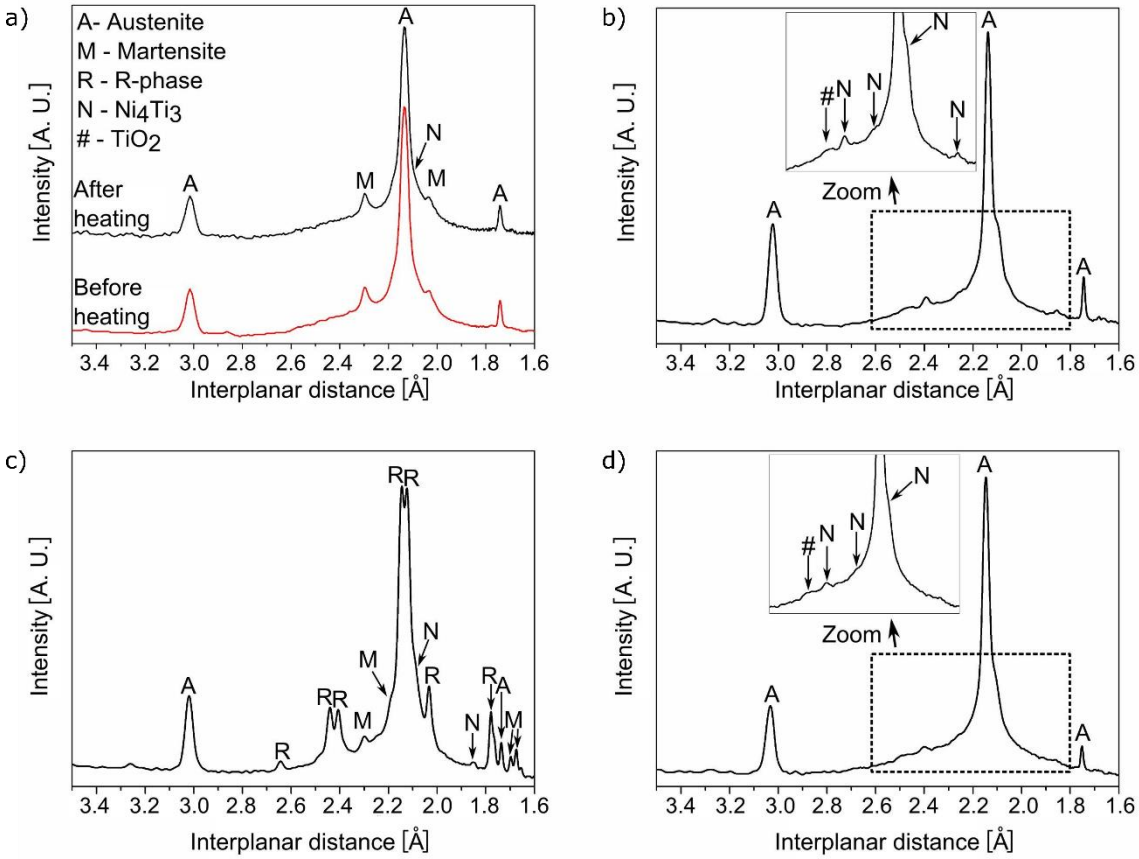

Figure 29 – Diffractograms of heat affected zone of sample B: a) at room temperature (before and after heating to 150 °C), as-welded; b) at 150 °C, as-welded; c) at room temperature, after post-weld heat treatment at 450 °C for 60 minutes; d) at 150 °C after post-welded heat treatment at 450 °C for 60 minutes.

Due to the occurrence of Ni-rich precipitates, in this case Ni_4Ti_3, there is a Ni depletion in the surrounding matrix [1]. This Ni depletion raises the transformation temperatures. As a consequence of this local compositional variation of the matrix, martensite can be formed at room temperature.

No changes were observed in the X-ray diffraction patterns of the as-welded sample at room temperature and 150 °C (Figure 29 a). As such, it can be concluded that the observed martensite is not originated by thermal stresses from welding. If martensite was originated due to the thermal stresses, it would be expected that the intensity of these peaks, at room temperature, would have decreased after heating to 150 °C.

4.1.3.2 Existence of Martensite in the Fusion Zone

The fusion zone also exhibits martensite at room temperature, as depicted in Figure 24. It was stated by Hyungson et al. [97] that, within the keyhole, the temperature may exceed the boiling

point of the material, thus causing an intense evaporation. At those temperature, Ni and/or Ti volatilization may occur.

In order to understand which of these elements, Ni or Ti, was more prone to evaporation at high temperatures (above Ni and Ti melting point), the vapor pressure for each element was computed. For such calculation, Equation 2 was used:

$$\log p = -\frac{A}{T} + B + C\log(T) \ldots\ldots\ldots\

Although martensite is observed in both the heat affected and fusion zones after welding, while the base material is fully austenitic, the mechanisms that explain the formation of this phase at room temperature are quite distinct. In the heat affected zone, precipitation phenomena, namely of Ni_4Ti_3, originates a Ni depletion of the surrounding matrix. In the fusion zone preferential Ni volatilization also causes Ni depletion. As such, this compositional variation is responsible for a change in the transformation temperatures, allowing for martensite to be stable at room temperature.

4.1.4 Functional Properties of the Similar Laser Welded NiTi Joints

The tensile behavior of these joints was previously studied in [93]. The ultimate tensile strength of these NiTi joints ranged between 482 and 637 MPa, while the elongation to fracture ranged between 10.6 and 12.1 %.

Shape memory alloys attract significant attention owing to their functional properties: superelasticity and shape memory effect. As such, when joining NiTi it is expected that the welded joints are able to preserve these properties so that they can be used in functional applications. In the following sections, the superelastic behavior and shape memory effect of the NiTi joints is assessed and discussed.

4.1.4.1 Superelastic Behavior of NiTi Laser Welded Joints Subjected to High Strain and Long Duration Cycling [2]

Despite the superelastic behavior of NiTi welds was studied previously, such studies have only analyzed a low number of mechanical cycles and low applied strains [44,99,100]. Understanding the influence of laser welding on the functional fatigue in terms of the superelastic effect is of major importance, as may boost the application of these joints to both structural and functional applications. Additionally, for structural applications, it is often required that the selected materials are able to withstand severe conditions, that is, high applied strains and/or high number of cyclic solicitations.

The superelastic behavior of these joints was analyzed for a total of 600 load/unload cycles up to 10% strain, which are, up to now, the most demanding conditions found in the literature.

The cycling behavior of samples A, B and C is evidenced in Figure 31, showing only a selected set of load/unload cycles. Sample A fractured after 303 cycles in the base material due to a pre-existing defect in this region. As such, the welding procedure did not have any influence on the fracture behavior of this sample.

It can be noticed the great resistance of the welded joints when subjected to a load/unload cycling with very large alternating strains (8 and 10 %). In particular, samples B and C were able to withstand the entire programmed cycling test without fracture.

[2] *The below results (section 4.1.4.1) were already published in a paper in the journal International Journal of Fatigue, entitled High Strain and Long Duration Cycling Behavior of Laser Welded NiTi Sheets.*

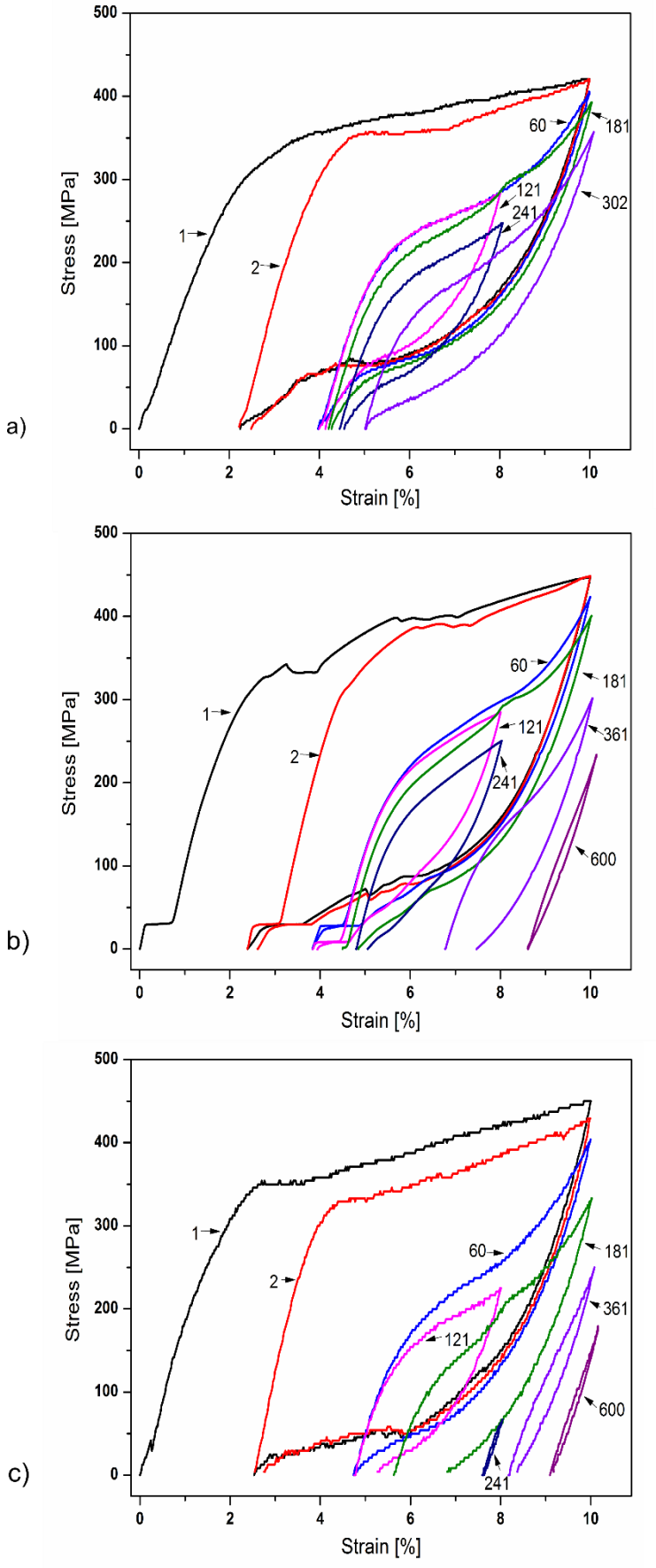

Figure 31 – Cycling behavior of: a) sample A; b) sample B; c) sample C.

The superelastic plateau on the first cycle occurs at roughly 350 MPa, similar to that of the base material. Additionally, samples B and C were successfully cycled 600 times, at a stress level 110 to 130 MPa below their ultimate tensile strength. In sample B a very small plateau at low stress level (≈ 30 MPa) detected at the initial stages of the cycling protocol. Such feature is attributed to the presence of residual R-phase. However, as the cycling test proceeded, the R-phase transformation was suppressed.

It is known that in an ideal superelastic behavior, a complete strain recovery could be obtained in NiTi for strains up to 10 % [1]. However, both testing conditions and materials parameters may give raise to a non-complete ideal superelastic behavior. For example, the temperature at which the tests are performed, the strain rate imposed [101,102], the maximum applied strain [103], the effect of thermo-mechanical treatments [104] and the grain size of the material are all known to influence the superelastic response of this material.

The superimposition of the X-ray diffraction patterns of samples A, B and C are depicted in Figure 32. As it was already shown, the base material is fully austenitic, while the thermally affected zone has both austenite and martensite. The effect of the heat input on the extension of these thermally affected regions is evidenced: higher heat input leads to a more significant extension of both heat affected and fusion zones. Some large variations of the diffraction peaks intensity can be observed and are the result of the coarse grain structure in the heat affected and fusion zones.

As superelasticity is dependent on the amount of austenite available for the stress induced transformation to occur, the presence of martensite at room temperature will have implication on the functional behavior of these joints upon mechanical cycling. It is expected that the superelastic recovery of the joints decreases with increasing martensite fraction in the thermally affected regions.

The presence of martensite in both the heat affected and fusion zones of the welds brings particular features to the cyclic response of the material. As the individual presence of each phase is responsible for a unique contribution regarding the strain recovery upon unloading during cyclic solicitation, the presence of both phases in the welded material must be considered when analyzing these mechanical cycling tests.

For the martensitic phase, it is well known that the cyclic behavior is extremely dependent on the applied strain [105,106]. In this phase, as soon as the plateau for the detwinning of martensite is reached, an irrecoverable strain is expected to occur. This irrecoverable strain should correspond to the difference between the applied strain and elastic deformation of martensite. However, one must notice that, as long as the applied stress is not enough to promote dislocation slip, a significant, if not full, recovery of the applied deformation can occur by heating the material above A_f, triggering the shape memory effect.

Previously, Tuissi et al. [57] suggested that the thermally affected regions of their NiTi laser welds had a softening effect, lowering the stress level of the plateau exhibited by the welded material. Despite the base material was fully austenitic at room temperature, in the thermally affected regions austenite was not yet fully transformed, similarly to what was observed in this work. For this reason, the strain recovery of the welds was lower than that of the base material.

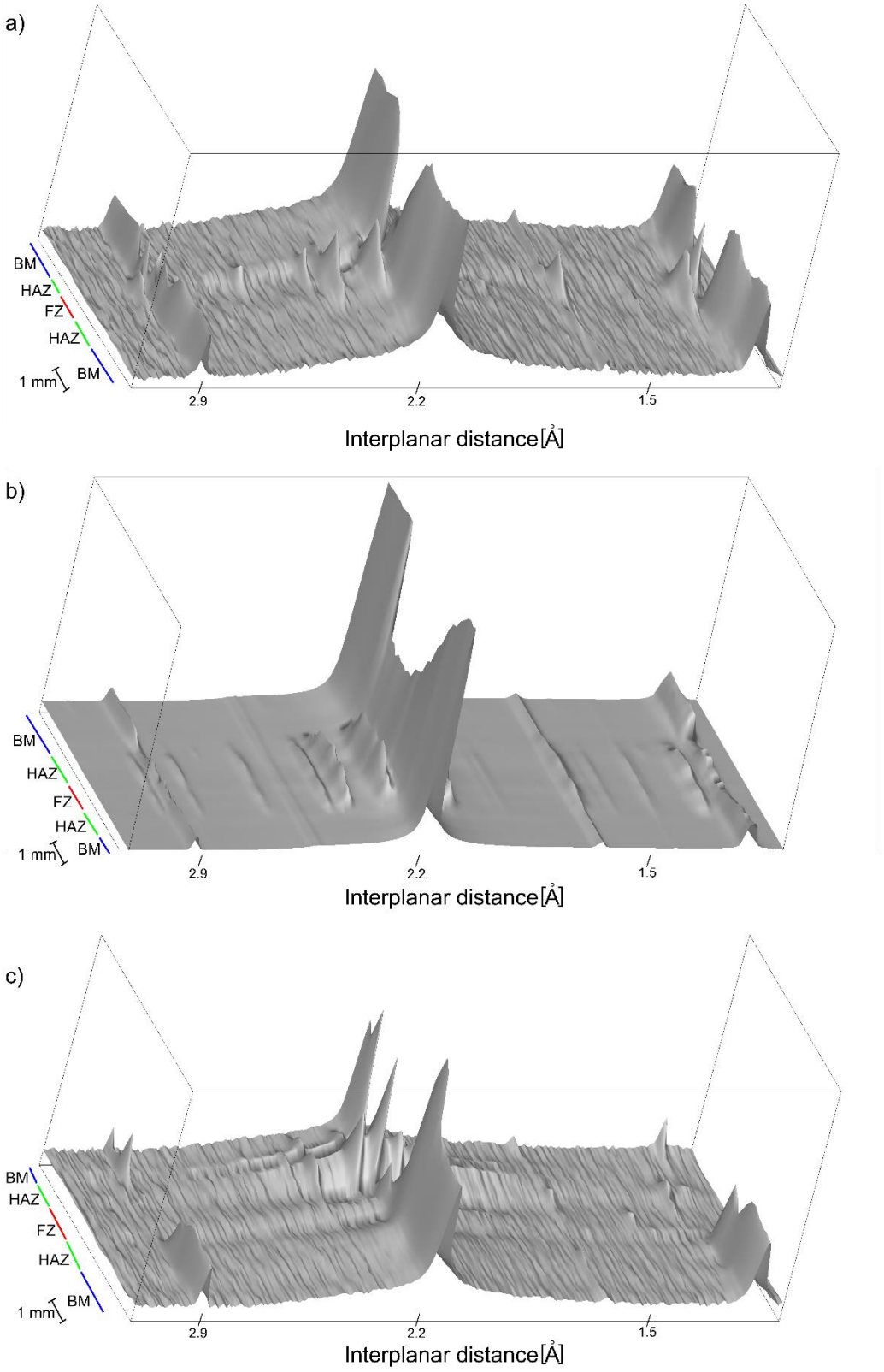

Figure 32 – X-ray diffraction patterns of NiTi joints: a) sample A; b) sample B; c) sample C. BM – base material; HAZ – heat affected zone; FZ – fusion zone.

During the cyclic solicitation at high applied strains used in this investigation, the existing martensite in both the heat affected and fusion zones are detwinned and upon unloading a significant irrecoverable strain is observed.

The evolution of the accumulated irrecoverable strain for the analyzed samples is exhibited in Figure 33. It can be observed that a significant amount of accumulated irrecoverable strain occurs at the end of the first cycle of load/unload. This feature can be explained by the presence of martensite in the heat affected and fusion zones and is explained in more detail further into this section of Results and Discussion.

Load/unload tensile tests performed by Wada and Liu [106] on martensitic NiTi evidenced that, for applied strains of 8 %, the recoverable strain upon unloading to a zero stress condition, was about 1 %, corresponding to the elastic deformation of martensite. Deformation beyond 8 % strain would result in dislocation slip. In the laser welds tested during this investigation with the presence of martensite, aside from austenite, the evolution of the accumulated irrecoverable strain can be explained as follows: for the sample with higher heat input (sample C), a higher amount of martensite is present. Thus, a higher irrecoverable strain will occur for this sample associated to the detwinning of the existing martensite, as well as some dislocation slip due to high strain imposed. For samples with lower heat input, the irrecoverable strain tends to be, correspondingly, lower.

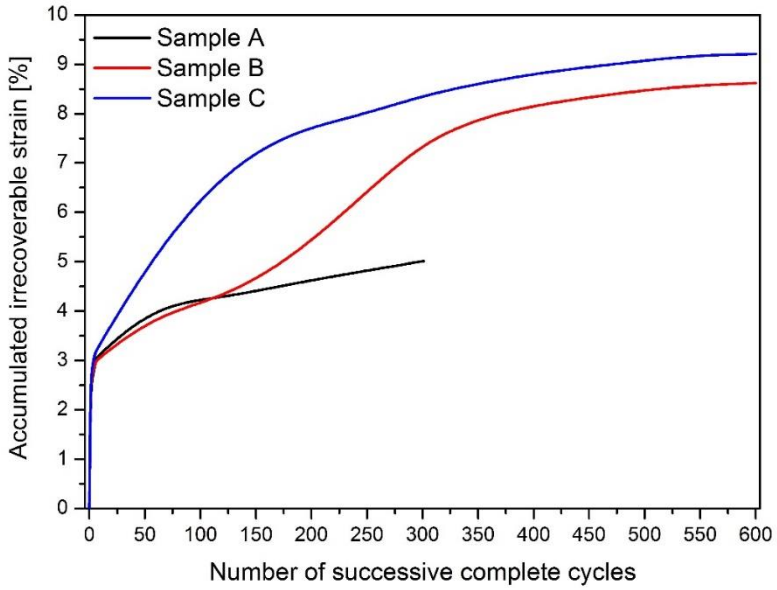

Figure 33 – Evolution of the accumulated irrecoverable strain with the number of cycles for each analyzed sample.

Miyazaki et al. [107] showed that under superelastic cycling of NiTi, dislocations and other lattice defects are introduced during the stress induced transformation and tend to pile-up with increasing number of cycles. As a consequence, an increase in the accumulated irrecoverable strain after each cycle occurs. For these cycling tests it can be assumed that part of the accumulated irrecoverable strain is due to the introduction of dislocations during the stress induced transformation. These defects do not allow for the stress induced martensite to revert

to austenite upon unloading leading to a stabilization effect of martensite. This stabilization effect phenomena is dealt in a separate section to clarify its origin and mechanisms.

It can also be noticed that the superelastic plateau slope changed significantly due to strain-hardening and corresponding increased dislocation defects occurring during the cycling tests. With increasing number of mechanical cycles, the accumulated irrecoverable strain increases up to a point where a stabilization plateau is reached as observed in Figure 33 for samples B and C.

The great resistance of the welds under superelastic cycling at high strains, is also inferred from the fact that the joints were cycled close to their ultimate tensile strength (110 to 130 MPa below).

The effect of the grain size in the different regions of the welds cannot be neglected, especially in the thermally affected regions. Compared to the base material, both the heat affected and the fusion zones exhibit a coarse grain structure as evidenced previously in Figure 21. For NiTi, it is known that the larger the grain size, the lower the superelastic recovery [108]. This means that the grain structure in the thermally affected regions also contribute to the accumulated irrecoverable strain presented by the laser welded NiTi joints.

4.1.4.1.1 Martensite Stabilization During Superelastic Cycling [3]

In the previous sub-section, the superelastic behavior of the NiTi joints was presented and discussed based on their microstructure. As stated before, the accumulated irrecoverable strain increases significantly in the early stages of cyclic deformation and onwards it tends to stabile to a fixed value.

The presence of martensite, alongside with austenite, in both the heat affected and fusion zones, with the remaining material austenitic, may justify this feature. In particular, the martensite formed in the as-welded material should undergo detwinning as a consequence of the imposed deformation of 10 %, thus contributing significantly to the accumulated irrecoverable strain. On the other hand, it is expected that due to the introduction of the dislocations, which are known to occur during cycling solicitation of austenitic NiTi, some of the stress induced martensite may not transform back to austenite upon unloading. The formation of this retained martensite would be due to the blockage of the reverse martensitic transformation upon unloading. Also, with increasing amount of retained martensite, less austenite is available to ensure superelasticity, thus the strain recovery of the material would reduce as the number of successive number of load/unload cycles increases.

In either case, martensite detwinning or formation of retained martensite, the same phenomenon occurs: martensite stabilization. The difference is that in the former it occurs from thermal martensite by reorientation of martensite variants [109]. In the latter case, the introduction of dislocations during mechanical cycling, makes the reverse transformation to require an increased driving force [110], thus preventing the return to austenite upon unloading.

[3] *The below results (section 4.1.4.1.1) were already published in a paper in the journal Materials Letters, entitled Martensite Stabilization During Superelastic Cycling of Laser Welded NiTi Plates.*

Usually both these two effects are studied separately. However, owing to the microstructure of these laser joints it is reasonable to assume that both effects contribute to martensite stabilization and to the increase of the accumulated irrecoverable strain exhibited by the welds.

In order to analyze the martensite stabilization effect, three different welded NiTi joints were analyzed by means of synchrotron X-ray diffraction. These samples were welded with the same parameters as sample B to keep consistency between the observed results. One sample was as-welded (sample reference W0, where W = weld, 0 = number of mechanical cycles); one sample had a total of 4 load/unload cycles at 10 % strain (sample reference W4); one sample sustained the entire cycling routine presented previously (sample reference W600).

The diffractograms of all samples are shown in Figure 34. Comparing samples W0 and W4 a notorious microstructural evolution is observed: the intensity of the martensite peaks, in the thermally affected regions, greatly increases in the latter sample. As a result of the augmented intensity of the martensite peaks in these regions, the austenite peak intensity decreases. Additionally, the base material starts to present some evidence of martensite peaks.

After 600 mechanical cycles Figure 34 c), there are no significant differences in the microstructure of the heat affected and fusion zones when compared to the sample cycled 4 times. Only a slight increase in the martensite peak intensity was observed. The most significant change occurs in the base material, near the heat affected zone, where martensite is now clearly visible. Such evidence is more clear when analyzing the evolution of the net height of the austenite and martensite peaks (the latter located at d = 2.17 Å) along the welded material, as depicted in Figure 35.

From the analysis of both Figure 34 and Figure 35, it is observed that prior to any mechanical solicitation, the welded material presents a mixture of both martensite and austenite in the thermally affected regions. Such martensite is thermally stabilized due to the weld thermal cycle as explained previously. Despite austenite can undergo a reversible stress induced transformation up to 10 % strain [1], the same does not occur with martensite. In the martensitic state, any applied stress/strain after the onset of the detwinning plateau will generate a given irrecoverable strain [111]. As mechanical cycling of the welds was performed up to 10 %, as far as thermal martensite is concerned, no recovery upon unloading would be expected.

As was also referred before, aside from the stabilization of thermal martensite during mechanical cycling, another stabilization phenomenon occurs: stabilization of the stress-induced martensite [111,112]. Previously, Delville et al. [113], showed that, during superelastic cycling of austenitic NiTi, significant accumulated irrecoverable strain could occur as a consequence of the introduction of dislocations along the cycling path. Later, Sedmak et al. [114] used in-situ X-ray diffraction analysis with synchrotron radiation on the same material as Delville. It was observed that the accumulated irrecoverable strain increased at each load/unload cycle, but only after the 4^{th} cycle evidence of retained martensite was found. In an ideal superelastic behavior, upon unloading, the stress induced martensite would fully transform back to austenite with no irrecoverable strain. As the residual martensite starts to accumulate (or being stabilized), build-up of the residual stresses and generation of dislocations during mechanical cycling starts to decrease.

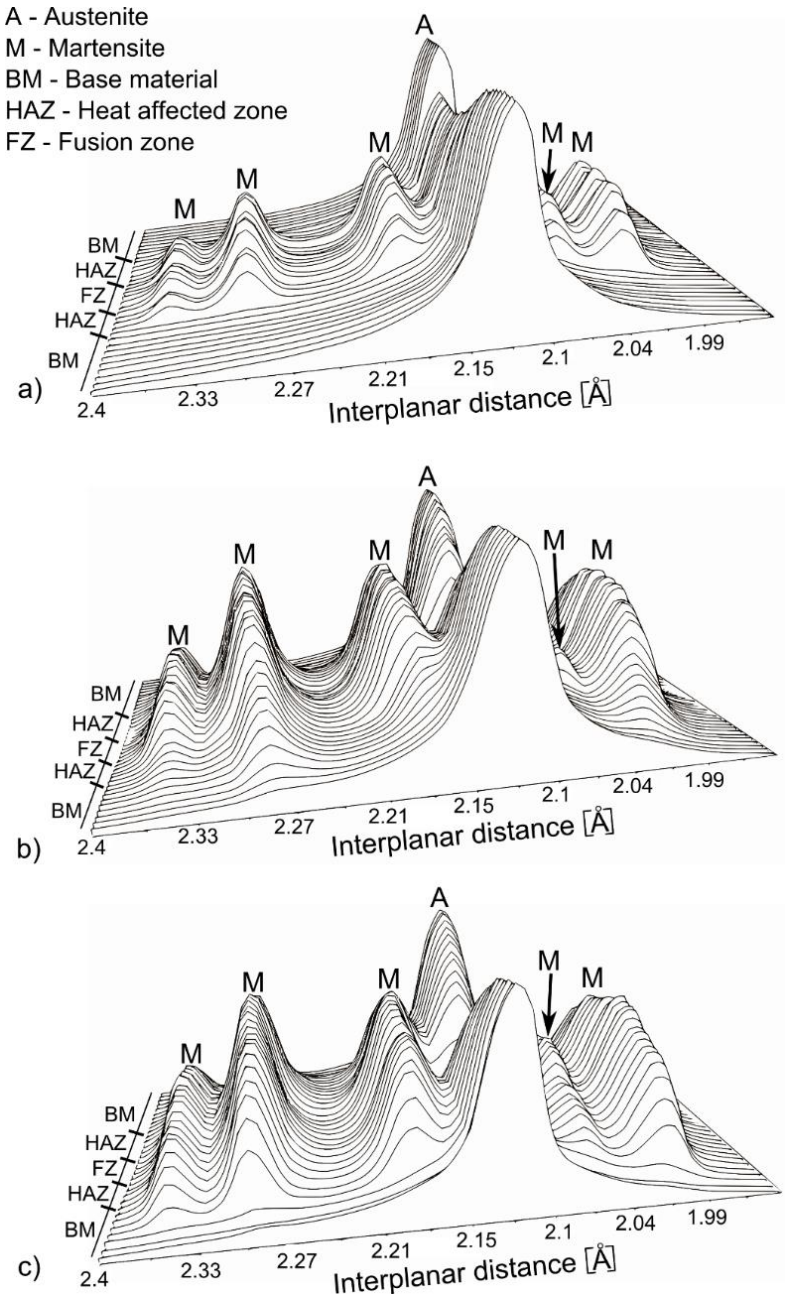

Figure 34 – X-ray diffractograms of sample B: a) as-welded; b) after 4 cycles at 10 % strain; c) after the full cycling routine (600 cycles). Intensity in log scale.

Analyzing Figure 35 it can be observed the main difference between samples W4 and W600: in the base material, close to the heat affected zone, more stabilized martensite in found in sample W600. Moving into the base material, away from the fusion zone, this stabilization effect decreases and finally ceases to exist.

Despite the gauge length of the samples used for the cycling tests was of 30 mm, only a length of 6 mm was probed by means of X-ray diffraction. However, within the probed length it is possible to obtain detailed information on the microstructural evolution of the welded joints as a result of the cycling tests. With such information, it was possible to highlight the two different mechanisms of stabilization of martensite, which are relevant to further understand the mechanical cycling behavior presented by the welds.

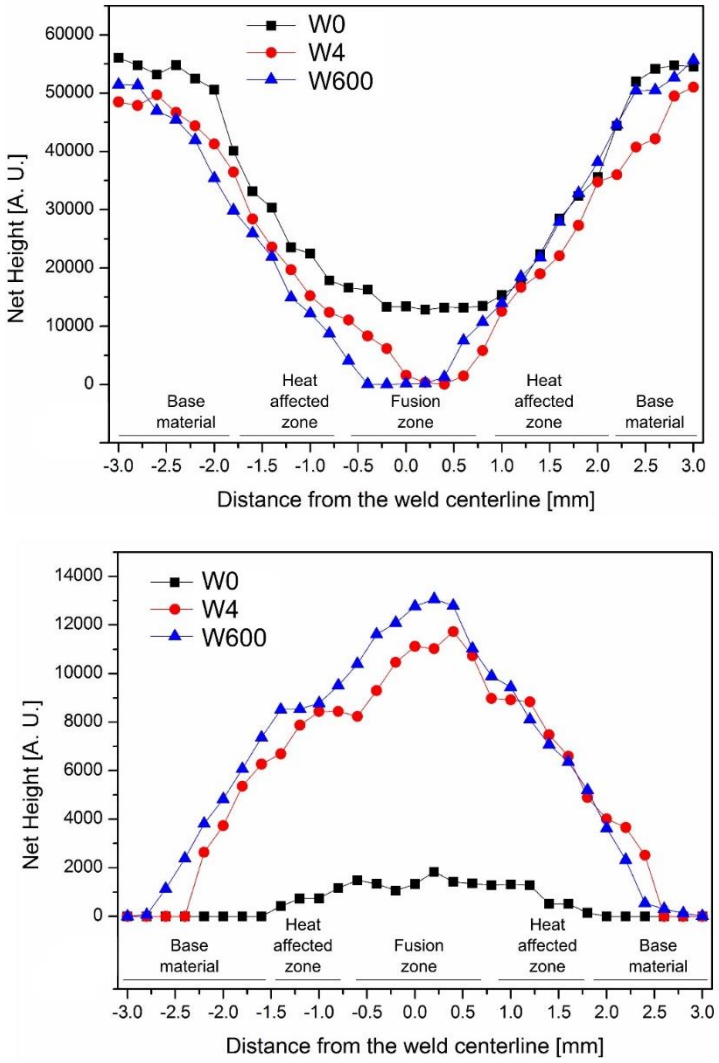

Figure 35 – Evolution of the net height from the austenite peak (top) and for the martensite peak located at d = 2.17 Å (bottom) along sample B.

One must take in consideration that, in theory, it is possible to reverse this stabilization effect by triggering the shape memory effect, enabling the transformation of martensite to austenite. Up to now no other study have evidenced simultaneously both types of martensite stabilization occurring within the same material.

4.1.4.2 Shape Memory Effect of the Similar Laser Welded NiTi Joints [4]

The shape memory effect is other functional property typical of shape memory alloys. Similarly to superelasticity, when processing these materials is of major importance to ensure that this propriety is preserved. In this section the shape memory effect exhibited by laser welded NiTi joints is presented and discussed.

Despite some martensite was found in the thermally affected regions, the remaining base material was fully austenitic. For this reason it was necessary to cool down the welds so that

[4] *The below results (section 4.1.4.2) were already published in a paper in the journal Functional Materials Letters, entitled Shape memory effect of laser welded NiTi plates.*

only martensite was present in the material. To promote this phase transformation the welds were dipped in liquid nitrogen and bent 180 °, as explained in the Materials and Methods section. Samples A, B, D and E, with different values of heat input were analyzed.

The ability for martensitic NiTi to recover its initial shape through shape memory effect varies between 8 and 10 %. The strain of 4 % applied during bending was clearly below the maximum possible range for the shape memory effect to be fully activated, hence it would be expected that these welded joints fully recover their initial shape upon heating to austenite.

As heating of the sample was made only up to room temperature some martensite existent in the thermally affected regions after the welding procedure would not transform into austenite. However, the presence of martensite at room temperature in these regions was not enough to prevent the complete recovery of the initial shape of all the laser welded specimens. This means that the permanent deformation angle, Ω, which was previously defined in the Materials and Methods section, was of 0° for all the analyzed welds. Thus, the austenite that coexisted with martensite in the heat affected and fusion zones was responsible to ensure that these regions did not contribute to a permanent deformation of the material.

It is worth noting that the welds were able to fully resist to a sequence of four different bending/recovery cycles, during which the shape memory effect was evaluated, causing alternating tensile/compressive stresses in the weld.

During the free recovery of the welded samples to room temperature, two different angles were recorded over time. One, δ, related to the overall recover of the samples (designated as “Global” angle), and another, ψ, related to the recovery of the heat affected and fusion zones (designated as “HAZ + FZ” angle). These angles were measured by taking two straight lines, tangents to the regions of interest as depicted in Figure 36.

These results, over time, for sample A, are shown in Figure 37. It should be noticed that the measurement of both angles only started roughly 15 second after taking the samples out of the liquid nitrogen and place them over a table to freely recover. For that reason the dashed lines represent an extrapolation of the shape memory behavior over that lapse of time, taking in consideration that, immediately after the samples are removed from the liquid nitrogen, they are bent at a 180 ° angle. Of particular interest is that both the heat affected and fusion zones recover faster their initial shape than the base material.

Despite it is known during the shape memory effect dislocations can be introduced [115], it is apparent that during the evaluation of this property, these dislocations were not sufficient to promote a degradation of this functional property.

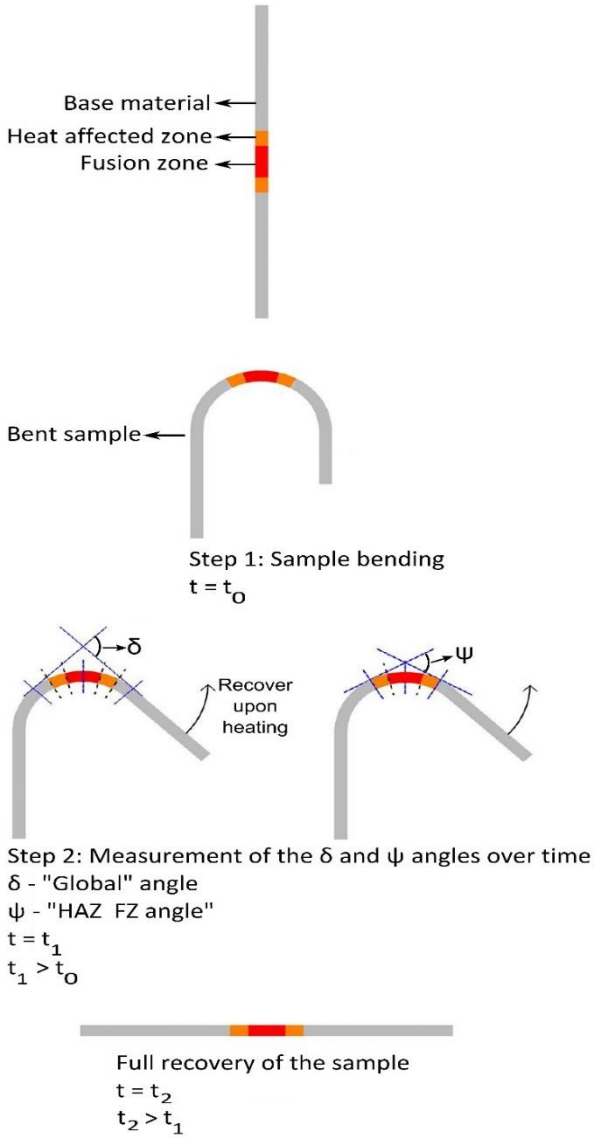

Figure 36 – Schema for determination of the angles in the different regions of the welded material as different times (not to scale).

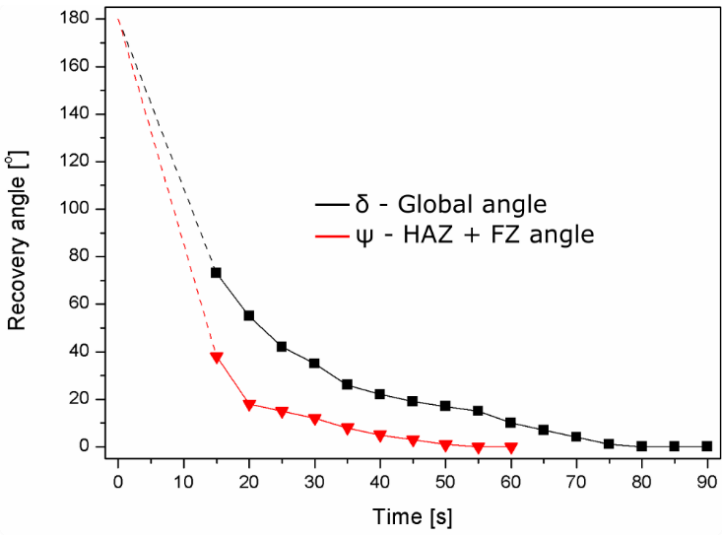

Figure 37 – Evolution of recovery angle over time for sample A.

From these results, it can be concluded that the laser welds present excellent shape memory recovery properties, which is defined by a permanent deformation angle of 0 ° after freely recover to room temperature. The welding parameters did not had any influence on the shape memory effect of the analyzed welds. Even the presence of martensite, at room temperature, in the thermally affected regions, did not inhibited the complete recovery of initial shape. This is especially relevant for possible industrial applications that may require the use of laser welded NiTi joints.

4.1.5 Residual Stress Analysis in Similar Laser Welded NiTi Joints [5]

Due to localized heating, during welding thermal stresses are known to occur. These thermal stresses can then origin residual stresses in the welded joint and distortions or even premature failure of the weld can occur.

In fusion based processes, such as laser welding, the gradient of peak temperature followed by a variation in heating and cooling rates along a weld will originate residual stresses in the weld region and its neighborhood [116,117]. A wide variety of factor affects the welding residual stress field: materials properties, welding process parameters, pre-heating temperature (if any) and dimensions of the structure to be welded as well as imposed external restrain conditions are some examples [118].

Residual stresses can occur due to a structural mismatch or by an uneven distribution of nonelastic strains. The aforementioned thermal stresses caused by the localization of the heating source originates non uniform temperature distributions in the weld itself and surrounding medium [119]. Additionally, the molten zone shrinks during solidification and this shrinkage is constrained by the surrounding cooler material [120]. In the presence, during cooling, of any phase transformations with associated volume change, it is possible to compensate the tensile contraction stresses that occur in the fusion zone, as long as the phase transformation is associated with a volume expansion and not contraction.

Residual stresses are always present after welding. However, post-weld heat treatments are usually performed to decrease their magnitude and increase the joints mechanical performance.

Measuring residual stresses can be performed by destructive, like the hole drilling method, or non-destructive methods using X-ray diffraction methods. Residual stress measurements by means of X-ray diffraction analysis can be performed using laboratorial sources, which have low energy X-rays, or in dedicated facilities, known as storages rings. Using laboratorial sources only allows for the determination of residual stresses in a restrict thickness of the welded material, usually in the order of the dozen of micrometers, owning to the low energy X-rays. In opposition, in synchrotron facilities, such analysis can be performed throughout the material, as the available energy of the X-rays is considerably higher: up to 300 keV, allowing for the analysis of samples up to 10 mm thick.

[5] The below results (section 4.1.5) were already published in a paper in the journal Materials & Design, entitled Residual Stress Analysis in Laser Welded NiTi Sheets Using Synchrotron X-ray Diffraction

As described in the Materials and Methods section, Rietveld refinement was used to determine the σ_X and σ_Y residual stresses. Samples A and F were chosen to be analyzed as they had significantly different values of heat input.

The variation of the 2Θ peak positions of the (110) austenite peak, which is the most intense for the NiTi system, in both analyzed welds is depicted in Figure 38 for three distinct regions of the welded material (base material, heat affected zone and fusion zone). Figure 38 a) and d) correspond to the base material and show that the 2Θ peak position of the (110) austenite peak does not vary significantly along the azimuthal angle. In the heat affected (Figure 38 b) and e) the variation is more notorious and is impaired in the fusion zone (Figure 38 c) and f). It must be noticed that in the thermally affected regions has high intensity peaks due to the coarse grain structure in these regions.

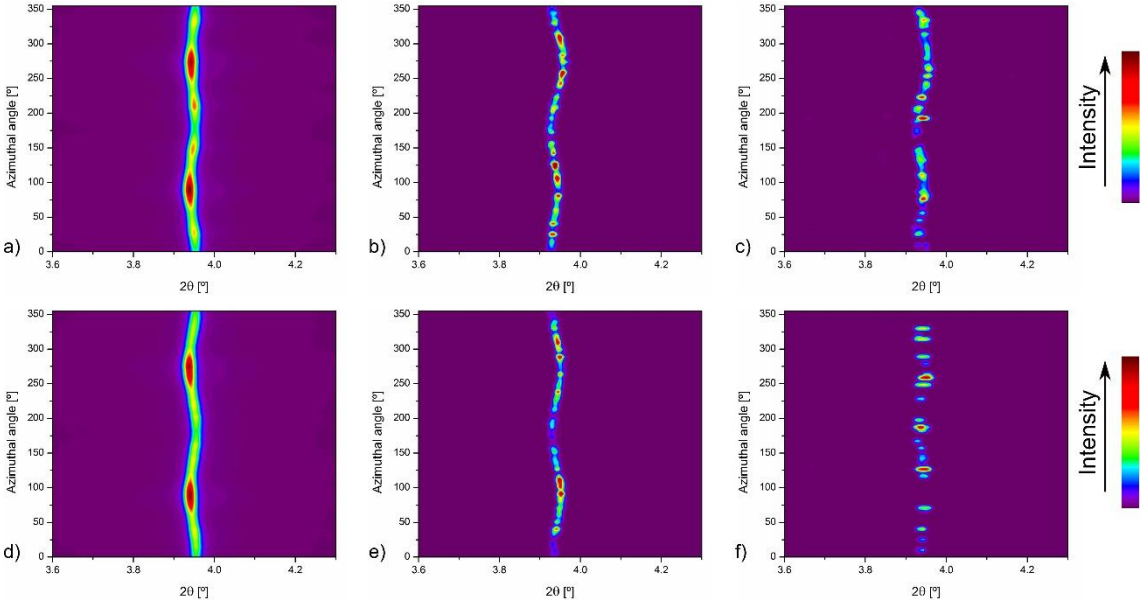

Figure 38 – Variation of the 2Θ peak position of the (110) austenite peak along the azimuthal angle φ, for sample A (top) and F (bottom). a) and d) correspond to the base material; b) and e) correspond to the heat affected zone; c) and f) correspond to the fusion zone.

After performing Rietveld refinement, good agreement in position, width and intensity between in the calculated and experimental patterns was observed (Figure 39), indicating a good fitting.

The calculated principal residual stresses of the austenitic phase, σ_X and σ_Y, for the analyzed welded samples are depicted in Figure 40. Considering both samples, it can be observed that the σ_X residual stresses in the heat affected zone range from approximately 10 to 105 MPa. In the fusion zone, these tensile residual stresses reach up to 135 MPa, for the sample F.

An inversion of the stress state is noticed when approaching the fusion zone from the heat affected zone: the σ_Y residual stresses are always compressive in the heat affected zone, but changed to a tensile state, ranging from 20 and 60 MPa, in the fusion zone.

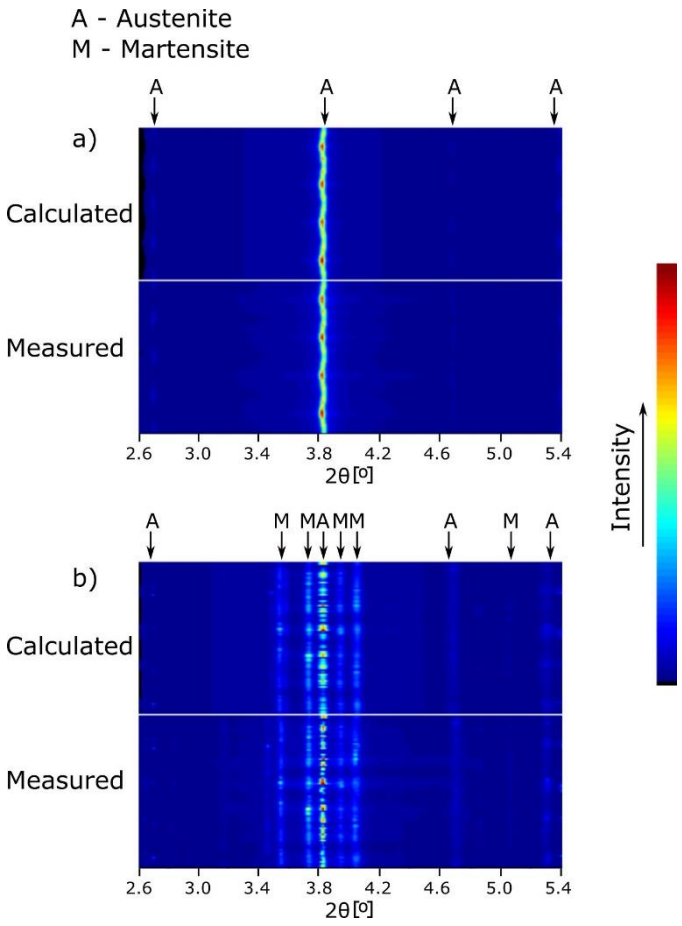

Figure 39 – Calculated and measurement diffraction patterns: a) in the base material, where only austenite (A) is present; b) in the fusion zone, where both austenite and martensite (M) are present.

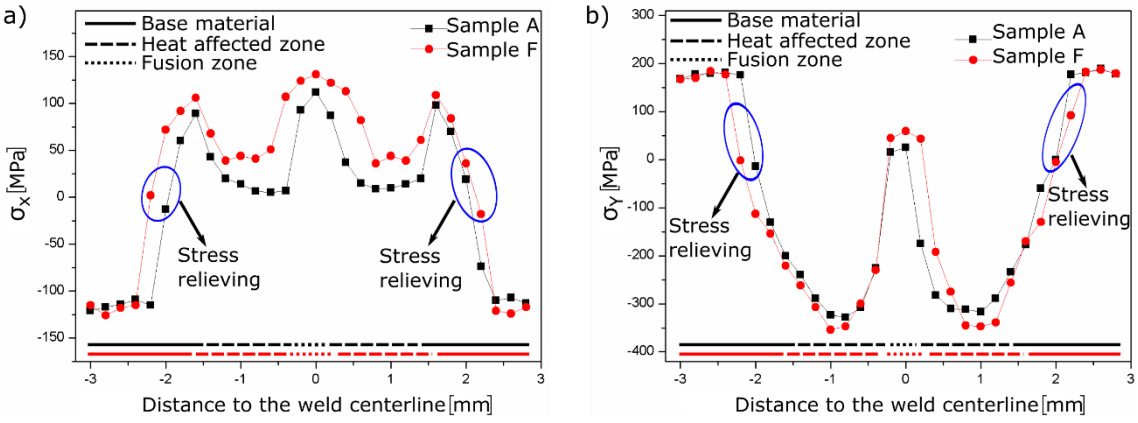

Figure 40 – Calculated residual stresses for samples A and F: a) σ_X; b) σ_Y.

Comparing the residual stresses along the principal directions of the same welded sample, it can be observed that the absolute value of the residual stresses is higher along the y axis than along the x axis. Such feature occurs due to the fact that, during welding, a constraint was applied along this direction in order to guarantee a good fit-up throughout the full weld length. As such, the material was not able to move freely, generating residual thermal stresses along this direction.

Of particular interest is the stress relief phenomenon marked with an arrow in Figure 40. Such stress relief occurs in both the principal directions of the system. Due to this stress relief phenomenon, along the longitudinal direction an inversion from compressive to tensile residual stresses in the base material is observed. Along the transversal direction, the opposite occurs: the tensile residual stresses in the base material change to a compressive state. This inversion of this stress states can be justified due to the fact that no distortions were observed after welding, meaning that an overall equilibrium was achieved in the welded material.

The stress relief effect observed in the base material occurs in the regions that have been heated up to temperatures below 350 °C. As such, the residual stresses magnitude in these regions decreases due to the fusion welding process, reverting the effects of work hardening with no change on the grain structure of the material.

The effect of higher heat input in sample F, gives rise to a higher magnitude of the residual stresses in the different regions of the weld (heat affected and fusion zones), in either the principal directions, when compared to sample A. Such effect of the heat input on the magnitude of the residual stresses was also identified by other authors [121].

Another consequence of the higher heat input introduced in sample F is that the stress relief phenomena in the base material occurs at a longer distance from the weld centerline, when compared to sample A. Such feature is evident in Figure 40, where the stress relief phenomenon is seen to occur in a region about 0.2 mm wider than in sample A.

The von Mises stresses can be obtained from the principal stresses determined using Rietveld analysis. The evolution of the von Mises stresses along the welded materials is depicted in Figure 41. For sample F, in a localized region of the heat affected zone, the von Mises stress reaches a maximum value of 357 MPa. This value is within the range of the critical stress for the martensitic transformation of these joints, which varies between 335 and 375 MPa. However, in the remaining regions of the material, the von Mises stresses are below this range.

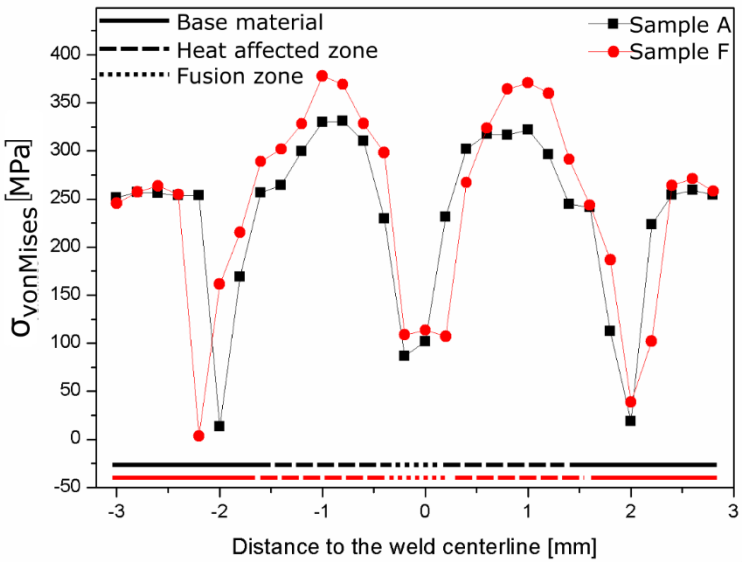

Figure 41 – Evolution of the von Mises stresses for samples A and F.

The residual stresses were also determined for the martensite in both the heat affected and fusion zones. However, the calculated residual stresses for this phase ranged between - 6 and + 8 MPa, which can be negligible considering the magnitude of the residual stresses found for the austenitic phase. The reason for this to occur is related to the mechanical properties of austenitic and martensitic NiTi. The former has a higher Young's modulus than the latter. As such, the load is predominantly transferred to the "harder" material, which is austenite. Additionally, the martensite in the Ni-Ti system has a lower constant stress plateau than austenite, which enables stress relaxation of the neighboring austenite.

As the maximum residual stresses found for the austenite are below the stress required for the stress induced transformation it can be inferred that the existing martensite occurs due to thermal factors and not due to mechanical ones.

Rietveld analysis performed on the synchrotron radiation based X-ray diffraction data enable to determine the residual stress of NiTi laser welded joints along two of the principal direction of the system. The higher heat input of sample F gave origin to a higher magnitude of the residual stresses, when compared to sample A. Additionally, a stress relief effect was seen to occur in the work hardened base material, as a consequence localized heating below 350 °C in this region.

4.1.6 Effect of Laser Welding on the Phase Fraction of Austenite and Martensite in the Thermally Affected Regions

Aside from the determination of residual stresses, Rietveld refinement can also be used for phase quantification [122]. Owing to the presence of both martensite and austenite in the thermally affected regions, while the base material is fully austenitic, it is important to determine the amount of each phase in the different regions of the weld.

Figure 42 depicts the evolution of both austenite and martensite phase fractions in the heat affected and fusion zones of samples A and F. It can be observed a clear difference between the austenite phase fraction in the heat affected zone and in the fusion zone. While in the former the austenite phase fraction ranges between 80 and 96 % (corresponding to a range between 4 and 20 % for martensite), in the latter, a significant decrease of the volume fraction to austenite is observed (close to 50 %).

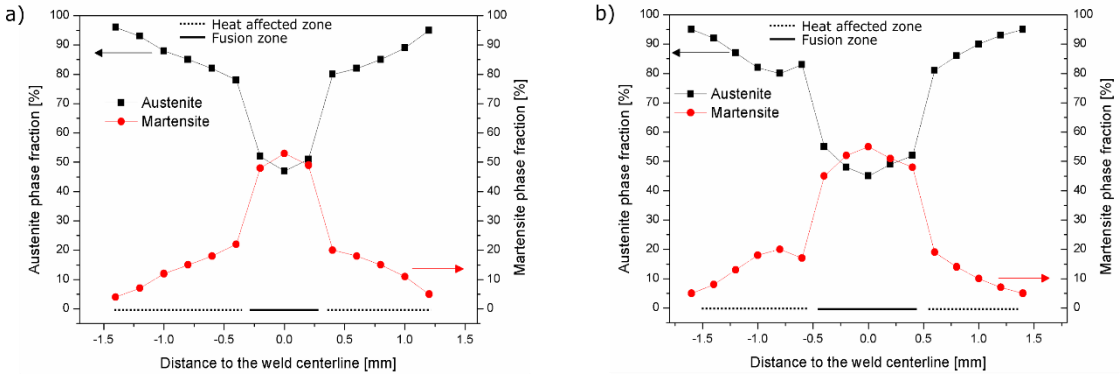

Figure 42 – Austenite and martensite phase fractions in the thermally affected regions of samples A (a) and F (b). HAZ – heat affected zone; FZ – fusion zone.

The reason for this abrupt variation in both the austenite and martensite phase fractions is related to the mechanisms that originate martensite, which were presented previously. In the fusion zone, the Ni depletion due to preferential Ni evaporation over Ti is significantly more important than the Ni depletion caused by Ni_4Ti_3 precipitation in the heat affected zone. For this reason, the transformation temperatures in the fusion zone were higher than in the heat affected zone, allowing for a more massive presence of martensite, when comparing both regions.

The differences in martensite and austenite phase fractions between the two analyzed samples were not significant, with those differences ranging around 5 % between them.

4.1.7 Effect of Post-weld Heat Treatments on the Microstructure of the Similar Laser Welded NiTi Joints

As stated previously, post-weld heat treatments are a common method to change the microstructure of welded structures in order to improve their mechanical performance, reduce the residual stresses or change the stable microstructure of the material.

Figure 43 depicts the superimposition of the diffraction of the laser welded NiTi joints after three distinct post-weld heat treatments. These were performed at 350, 400 and 450 °C for 60 minutes. It can be observed that the post-weld heat treatments promoted a more uniform distribution of the existing phases (which are shown in Figure 44) throughout the welded samples. The uniformity of this distribution is evident by the non-existence of a clear distinction between the base material and the thermally affected regions.

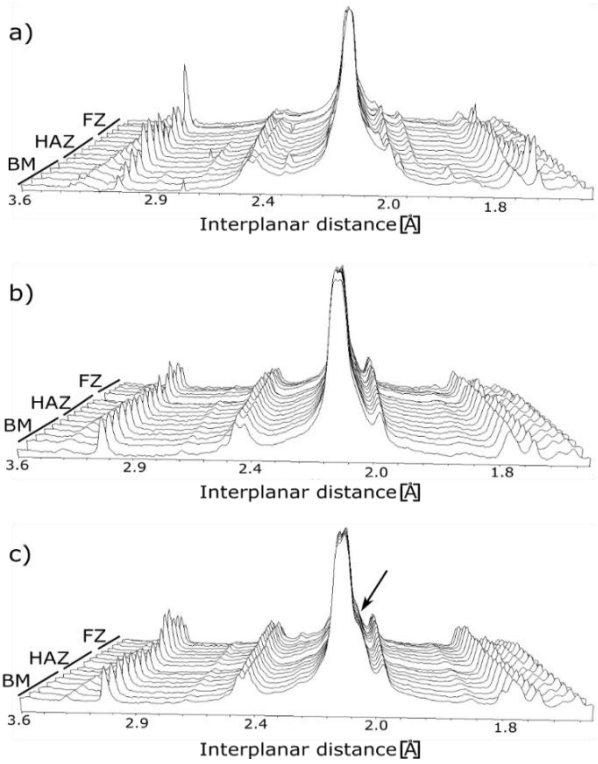

Figure 43 – Superimposition of diffractograms of laser welded NiTi joints after post-weld heat treatments at: a) 350 °C, for 60 minutes, in sample C; b) 400 °C, for 60 minutes, in sample B; c) 450 °C, for 60 minutes, in sample E. BM – base material; HAZ – heat affected zone; FZ – fusion zone.

The existing phases after the aforementioned post-weld heat treatments are austenite, martensite, R-phase and Ni_4Ti_3 (Figure 44).

The existence of R-phase in the base material, as well as in the thermally affected regions, can be justified by the presence of Ni_4Ti_3 precipitates, which are known to assist the formation of this phase [12]. Additionally, the presence of these precipitates can be beneficial because particle hardening increases the yield strength of austenite, which in turn contributes to better functional stability, as less dislocations are formed during mechanical and/or thermal cycling [13] The presence of Ni_4Ti_3 precipitates is more evident after the post-weld heat treatment at 450 °C, as evidenced by broadening of the peak, which is marked by an arrow in Figure 43 c).

The presence of martensite in the base material has occurred due to Ni depletion of the matrix caused by Ni_4Ti_3 precipitation, which raised the transformation temperatures. Nonetheless, such Ni depletion was not yet sufficient to inhibit the presence of austenite at room temperature

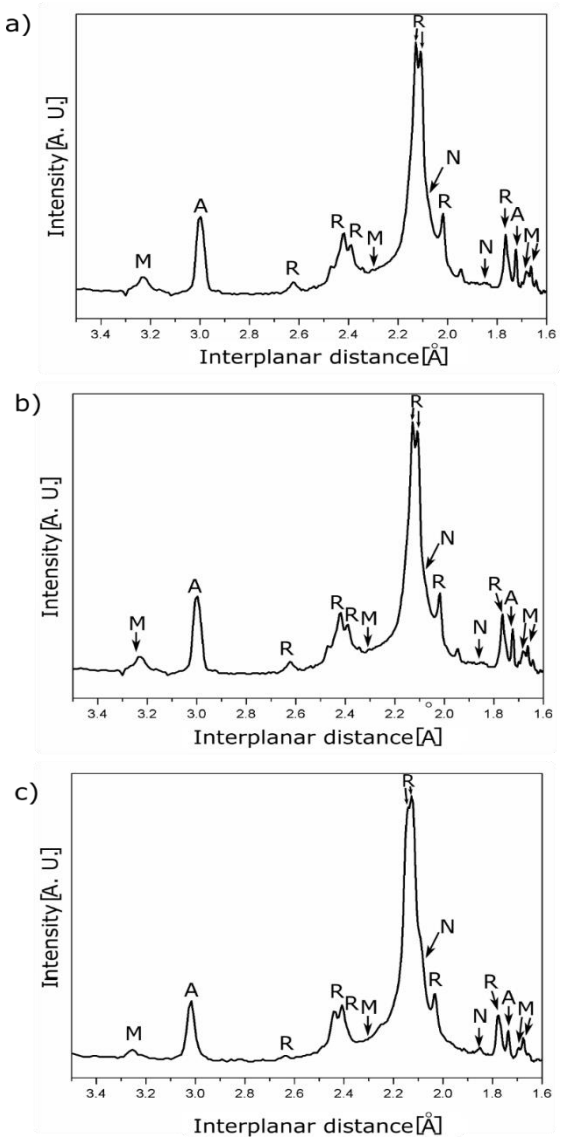

Figure 44 – Diffractograms obtained after post-weld heat treatments at 350 °C (a), 400 °C (b) and 450 °C (c) for 60 minutes.

4.2 Dissimilar Laser Welding of NiTi to Ti6Al4V Using Niobium Interlayer [6]

In this section the mechanisms that allow joining between NiTi and Ti6Al4V using a Nb interlayer are presented and discussed. Microstructural analysis of the two joining interfaces (NiTi/Nb and Ti6Al4V/Nb) is presented in order to assess the effect of laser welding on the originated microstructures. Finally, the mechanical behavior of the dissimilar joints is analyzed.

4.1.1 Microstructural Characterization

In order to obtain sound NiTi/Ti6Al4V joints, two key factors were essential: use of the Nb interlayer and positioning of the laser beam. When no interlayer was used solidification cracking occurred regardless of the laser beam positioning. That is, impinging the laser beam either on the NiTi or Ti6Al4V base materials or at the contact interface had no influence on minimizing the risk of solidification cracking phenomena observed after welding. The reason for the occurrence of the cracks is due to the formation of brittle intermetallics compounds, such as Ti_2Ni [81].

It was thus apparent that, reducing or avoiding the formation of these undesired phases was of major importance to succeed in obtaining sound NiTi/Ti6Al4V welds. When the Nb interlayer was placed in between the two base materials, it was chosen to position the laser in the Ti6Al4V base material. The reason for such a choice is based on the fact that NiTi suffers a more pronounced degradation of its properties at high temperatures than the Ti6Al4V base material. However, the relative position of the laser beam was also of great influence: when it was placed too close to the Nb interlayer the beam was reflected and no joint was formed; when it was positioned far away from the interface the heat was not enough to promote joining between NiTi and Niobium, although joining between Ti6Al4V and Nb was observed.

Only when the laser beam was positioned at 250 µm from the joint interface on the Ti6Al4V base material, joining was achieved. Cross section of the weld during FIB milling is shown in Figure 45. With the Niobium interlayer correctly positioned and with proper welding parameters, defect-free joints were obtained (Figure 46). Some porosity is observed in Figure 45, but this was created during FIB of the specimens as there was no porosity prior to the preparation by FIB.

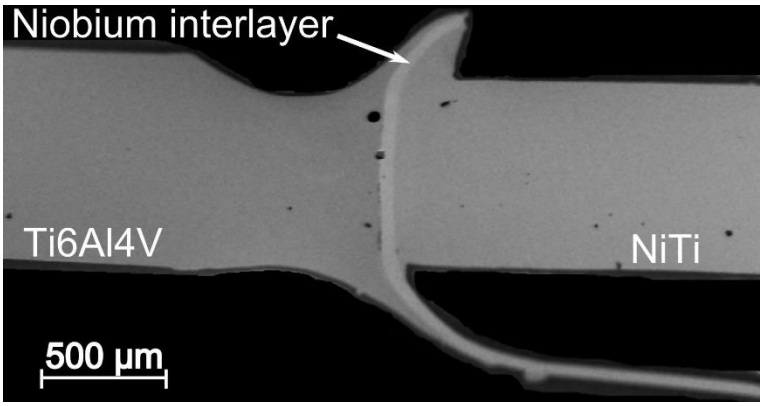

Figure 45 - Scanning electron image of the dissimilar NiTi/Ti6Al4V joint using Nb interlayer.

[6] The below results (section 4.2) were already published in a paper in the journal Acta Materialia, entitled Laser Joining of NiTi to Ti6Al4V Using a Niobium Interlayer.

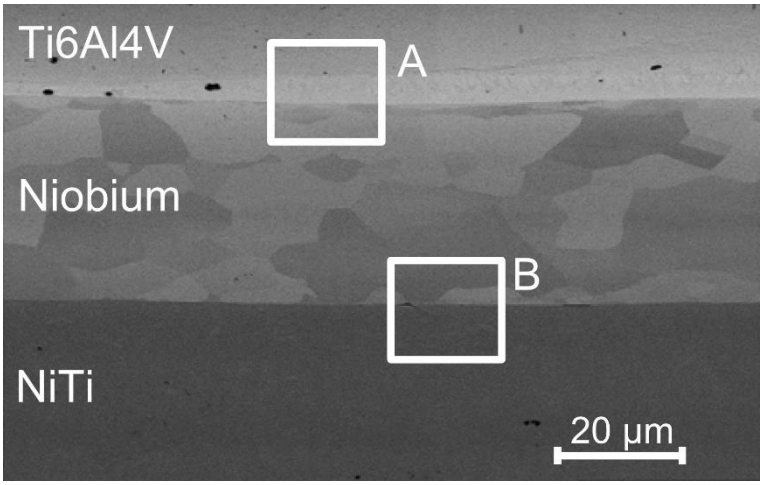

Figure 46 - Scanning electron microscopy of the interface between Niobium and the two base materials. The white squares mark the areas prepared by FIB for TEM analysis.

Owing to the significant difference in the melting temperature of the base materials involved (1310, 1660 and 2477 ^{o}C for NiTi, Ti6A4lV and Niobium, respectively), this laser welding procedure resulted in melting of only NiTi and Ti6Al4V. The bulk Nb interlayer remained in the solid state.

Necking was observed in the fusion zone of the Ti6Al4V side (Figure 45). Wetting of the Niobium by the Ti base material, evidenced in Figure 45, may be the principal contributing factor to the observed necking. Other authors have also reported similar non-symmetrical weld pools when welding Ti6Al4V to Niobium by laser or electron beam welding. The reason pointed out for this occurrence is related to the higher melting point and thermal conductivity of Niobium (52.3 W m^{-1} K^{-1} [98], vs 18 [123] and 6.6 W m^{-1} K^{-1} [124] of NiTi and Ti6Al4V, respectively). One final factor that explains the necking is related to the material loss by vaporization, as the laser beam was directly impinging this region of the base material.

The remaining of the discussion is now focused at analyzing, separately, each one of the two regions identified in Figure 46. That is, the microstructural features observed in region A, corresponding to the Ti6Al4V/Nb interface are first analyzed and discussed, followed by the NiTi/Nb interface, in region B.

4.1.1.1 Ti6Al4V/Nb interface

As a result of the good wettability of the liquid Ti on the Niobium, the liquid phases were able to incorporate Niobium and promote its diffusion as a result of convection currents. As β-Ti and Niobium have full solubility in one another, solid state diffusion of Ti into the Niobium also occurred, as observed in Figure 47.

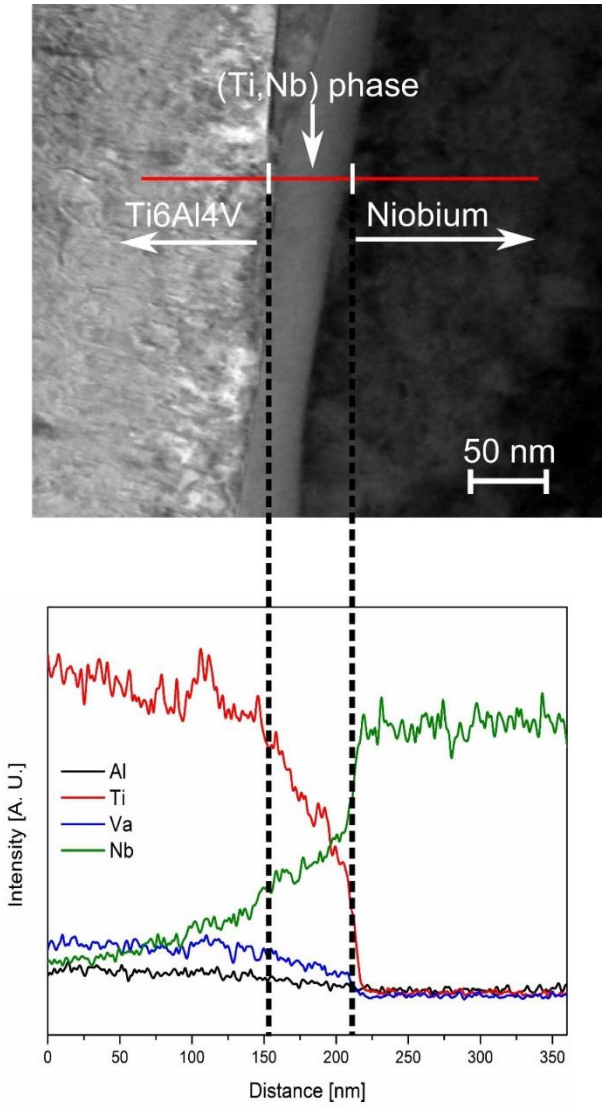

Figure 47 – STEM image and EDS line scan across the Ti6Al4V/Nb interface (top). The red line depicts the EDS line scan performed and the results are shown on the bottom.

A (Ti, Nb) region, with a width of 30 nm, was formed at the interface of the fusion zone and the Niobium interlayer. Diffusion of Niobium into the liquid Ti was seen to occur at a distance of at least 200 nm. Mixing occurred thoroughly in the melt due to convection currents and the Marangoni effect [35]. The content of Ti, Al and V in this (Ti, Nb) region were seen to decrease when compared to the Ti base material. The overall composition in the (Ti, Nb) region, determined by point EDS, was of 47.7Ti-46.2Nb-2.9Al-3.3V (wt. %).

The addition of Nb in Ti-based alloys acts as a β-stabilizer and promotes solid-solution strengthening [125]. A minimum of 36 wt. % of Nb is required to stabilize the β phase at room temperature [91]. Computing the Al and Mo equivalency [91] (equations 3 and 4, respectively) of the region formed between the liquid Ti and the Nb interlayer, indicates that it should be β metastable at room temperature. Ti-based alloys with Al equivalency below 3.0 wt.% and Mo equivalency above 11.7 wt.% are considered to be of the β-type.

$$[Al]_{eq} = [Al] + \frac{[Zr]}{6} + \frac{[Sn]}{3} + 10[Al] = 2.9\ wt.\% \ldots\ldots\ldots\ldots\ldots\ldots\ldots\ldots\ldots\ldots Eq.3$$

$$[Mo]_{eq} = [Mo] + \frac{[Ta]}{5} + \frac{[Nb]}{3.6} + \frac{[W]}{2.5} + \frac{[V]}{1.5} + 1.25[Cr] + 1.25[Ni] + 1.7[Mn] + 1.7[Co] + 2.5[Fe] = 15.0\ wt.\% \ldots\ldots\ldots\ldots\ldots Eq.4$$

Electron energy loss spectroscopy (EELS) was performed on the Ti6Al4V/Nb interface (Figure 48). With such technique it is possible to obtain a finer spatial distribution of the elements at the interface. The mean free path of diffusion of each element into a given region is limited by the temperature achieved during welding and the available time for diffusion to occur [33]. The difference in composition and the high heating and cooling rates characteristic of the pulsed laser welding process have contributed to the lack of mixing in the (Ti, Nb) region with the bulk of the fusion zone. At the interface of the (Ti, Nb) region and the Nb interlayer, a sharp discontinuity in the Ti content is observed. This indicates that no significant diffusion of Ti into the interlayer has occurred due to the short time of the joining process.

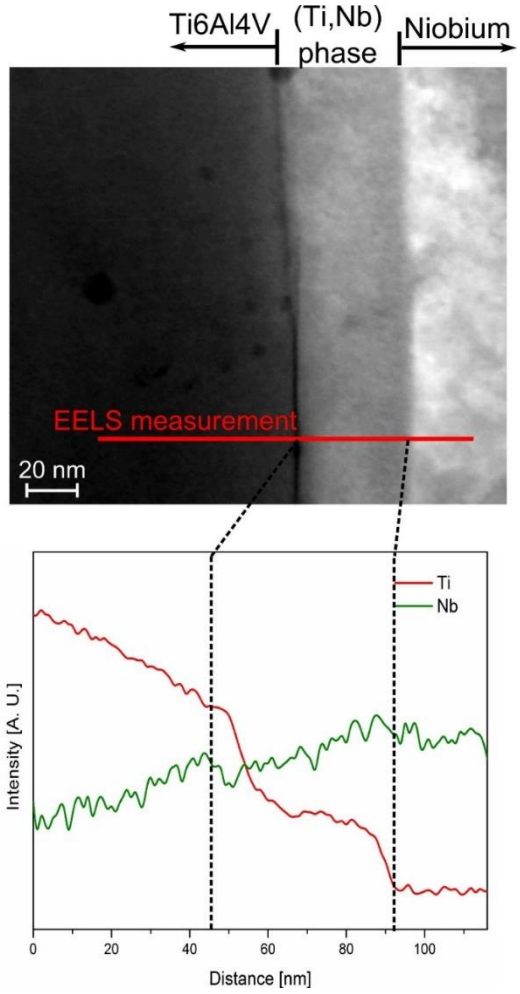

Figure 48 – STEM image and EELS line scan across the Ti6Al4V/Nb interface (top). The red line depicts the EELS line scan performed and the results are shown on the bottom.

4.1.1.2 NiTi/Nb interface

A typical eutectic microstructure is observed at the NiTi-Nb interface (Figure 49). Similar NiTi-Nb eutectic microstructure was previously observed by Grummon et al. when brazing NiTi to pure Niobium [126]. The authors have suggested that a quasi-binary isopleth exists between the intermetallic NiTi and pure Niobium. In the Ni-Ti-Nb ternary phase diagram, the eutectic isotherm is 140 °C below the congruent melting point of NiTi (1310 °C). Spontaneous melting occurred with the pure Niobium being in intimate contact with the NiTi base material at high temperatures. Upon solidification two distinct phases were formed: austenitic NiTi and bcc-Nb [127].

From the quasi-binary NiTi-Nb phase diagram (Figure 49) it is expected that, in conditions close to equilibrium, the first liquid to form has a composition similar to the eutectic point at $Ni_{38}Ti_{36}Nb_{24}$. However, the fast heating and cooling characteristic of pulsed laser welding prevent the occurrence of equilibrium conditions. Region A from Figure 49 was identified as the un-melted NiTi base metal. Near this region, a proeutectic zone (region B) which terminated in bulbous projections was observed. Selected area diffraction (SAD) was performed in these regions and indexing the SAD image confirmed the presence of the austenitic NiTi phase (Figure 50).

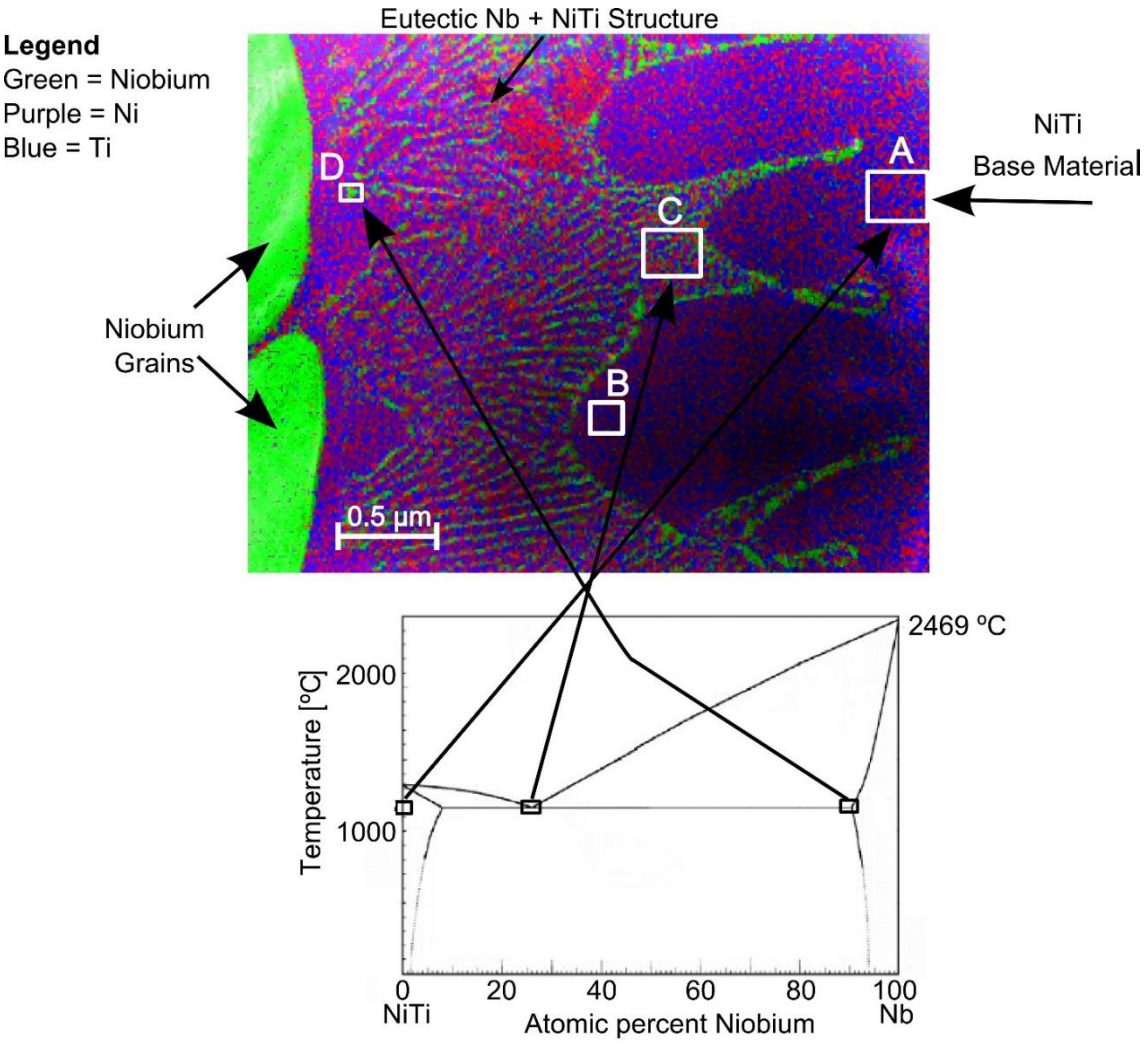

Figure 49 – EDS mapping of the NiTi/Nb interface (top) and correlation with the NiTi-Nb phase diagram (bottom).

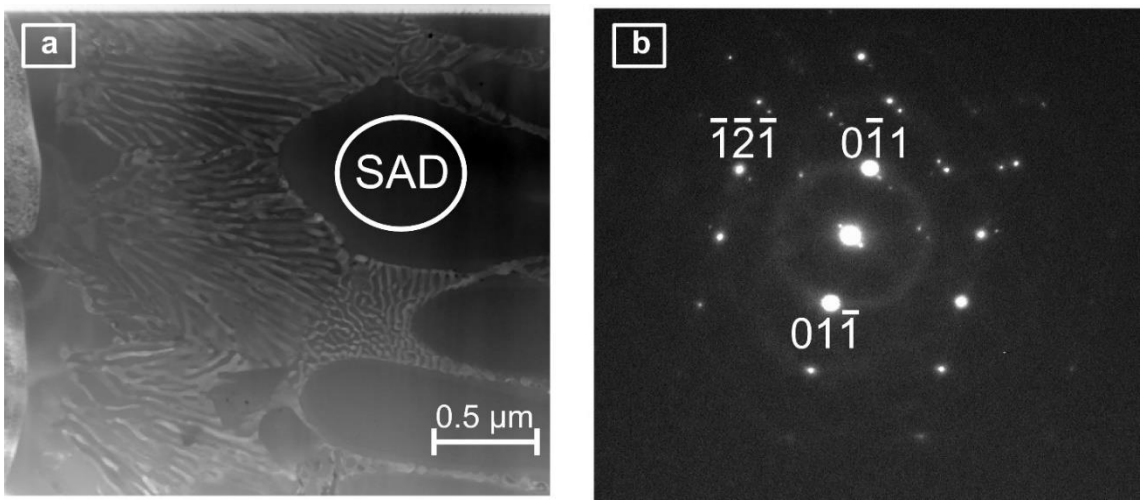

Figure 50 – a) High angular annular dark field image of the NiTi-Nb interface with a region where selected area diffraction (SAD) was performed; b) Indexed SAD image.

The majority of the joint was composed by a lamellar eutectic solidification structure as seen in region C of Figure 49. With the use of STEM in High Angle Annular Dark Field (HAADF) mode it is possible to distinguish between light (i.e. NiTi) and heavy (such as Nb) elements [128]. EDS mapping of eutectic microstructure confirmed that the dark regions in Figure 51 were Nb lean, while the light regions were Nb rich.

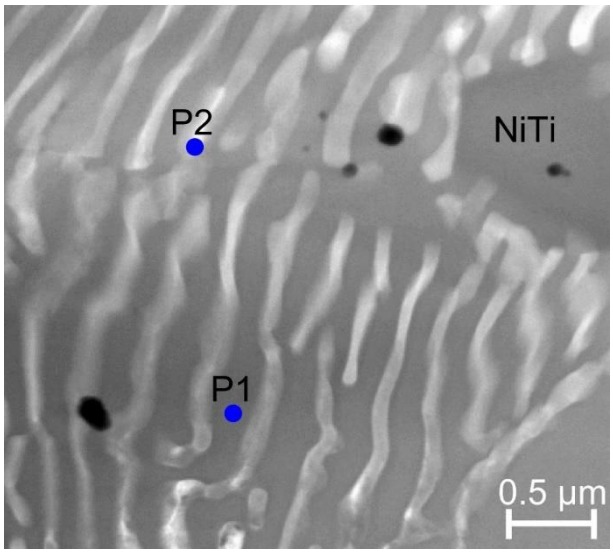

Figure 51 – High angular annular dark field image of the eutectic microstructure with EDS analysis point indicated. The black spots were identified as impurities.

Table 4 – Results of EDS analysis on the NiTi + Nb eutectic microstructure, with positions indicated on Figure 51.

Point	Atomic content (%)		
	Ni	Ti	Nb
P1	51.7	38.1	10.2
P2	12.5	22.8	64.7

On the left-hand side of Figure 49 un-melted Niobium grains were identified. Significant grain boundary penetration around these Niobium grains was also observed and is presented in more detail in Figure 52. The faster diffusion along these paths resulted in the eutectic reaction

propagating along the grain boundaries instead of through the bulk. Other binary systems have shown similar behavior: in the Ni-W system, Tungsten has a significantly higher melting point than Nickel, resulting in grain boundary penetration of Ni-W eutectic along the W grain boundaries [129].

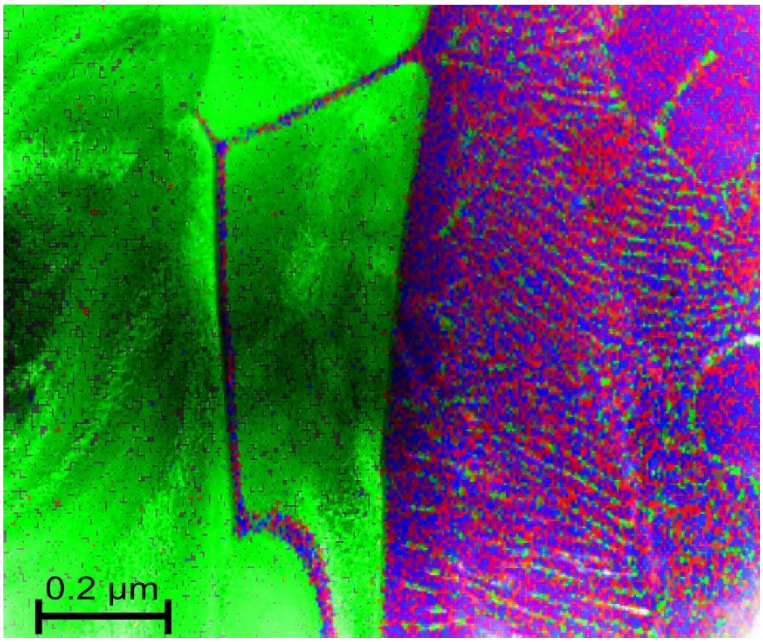

Figure 52 – Grain boundary penetration of NiTi into the Niobium grains. Color legend: green – Nb purple – Ni; Red – Ti.

Two different joint mechanisms were identifies for the NiTi/Nb/Ti6Al4V joint. Fusion welding was used to join Ti6Al4V to Nb. Niobium experienced dilution and was incorporated into the Ti6Al4V weld pool. A (Ti, Nb) region was formed upon solidification as a thin layer along the Nb interface to the minimal mixing with the bulk fusion zone. The Nb interlayer acted as heat sink as a consequence of its high thermal conductivity, absorbing a significant amount of energy from the Ti6Al4V side of the joint and transferring it to the NiTi side. This heat transfer was enough to promote a temperature raise to at least 1170 °C so that contact melting between NiTi and Niobium occurred and a joint between these two materials was formed.

Dissimilar joining between NiTi and Ti6Al4V did not occur when no interlayer was present, further suggesting that the eutectic reaction was responsible for joining at the NiTi/Nb interface. As expected from the NiTi-Nb phase diagram, no intermetallic compounds were observed in the solidified joint. The high melting point of the Niobium interlayer ensured that the bulk of the Nb remained in the solid state during welding, successfully stopping mixture of the two base materials.

4.1.2 Mechanical behavior of the welded joint

Tensile tests were performed on the joints made with the Niobium interlayer, with the laser offset into the Ti6Al4V base material, to assess its tensile strength. A typical stress-strain curve of these joints is depicted in Figure 53. As mentioned previously, dissimilar joining between NiTi and Ti6Al4V did not occur when no interlayer was used, even when the laser was offset into the NiTi base material. Additionally, when using a Nb interlayer, sound joints are only obtained when the laser is offset to the Ti6Al4V side.

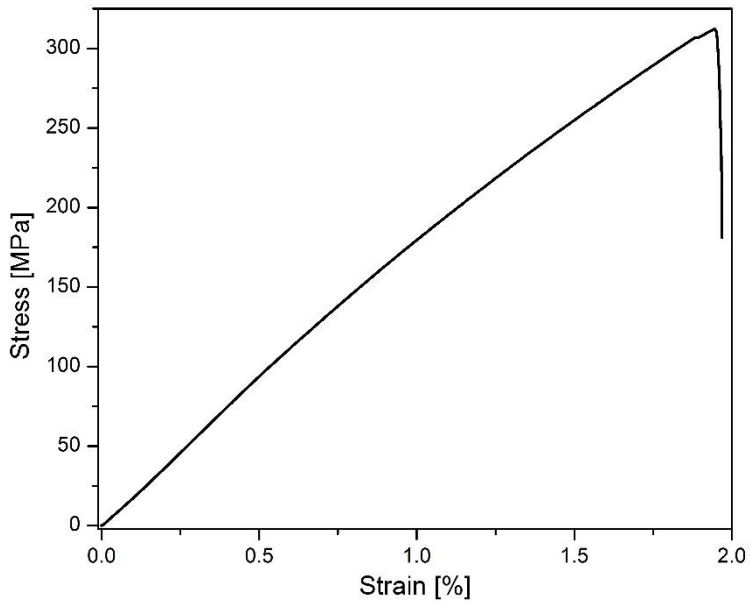

Figure 53 – Stress-strain curve of NiTi to Ti6Al4V weld using Niobium interlayer.

An average tensile strength of 300 MPa and an elongation to fracture of nearly 2.0 % was measured. These results were a significant improvement on the joints made without the Niobium interlayer, which were unable to be tested because fracture occurred during removal from the welding fixture. The tensile strength of pure Niobium ranges between 250 and 350 MPa, so the joint strength matched the maximum theoretical strength of the interlayer.

Other authors have shown similar values of tensile strengths [82], despite using a Copper interlayer, which has better mechanical properties than Niobium. However, the tensile strength of the Niobium interlayer was below the critical stress for the stress-induced martensitic transformation in NiTi (usually around 400 MPa).

The joint strength can be improved through further optimization of the joining parameters, including joint fit-up, laser peak power and pulse width. This work shows that a high melting point interlayer can be used to achieve a defect-free joint between NiTi and Ti6Al4V. If a similar interlayer was identified as possessing a higher ultimate tensile strength, then the joint strength could be increased to accommodate the superelastic effect typical of austenitic NiTi shape memory alloys.

Fracture surfaces of the welded specimens revealed a mostly brittle fracture morphology on the Ti6Al4V fusion zone (Figure 54). The Niobium interlayer was torn during fracture, leading to the Ti6Al4V and the NiTi fracture surfaces having both the fusion welded and eutectic bonded regions of the joint.

The NiTi side of the joint had more ductile dimples from the eutectic phases formed, while the Ti alloy side had more brittle cleavage features from the fusion zone. Hydrogen or oxygen pick-up by the Ti6Al4V weld pool could have contributed to the brittle characteristics of the fracture surfaces [130,131]. The grain boundary penetration of the Niobium interlayer by the eutectic reaction with NiTi can reduce the ductility of these regions, thus contributing to the observed brittle crack formation [132].

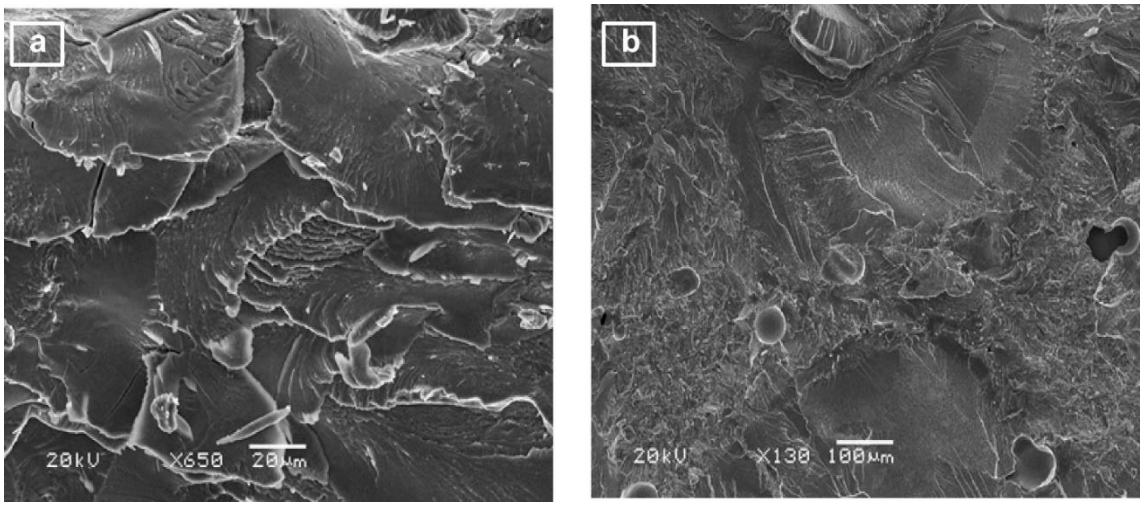

Figure 54 – Fracture surface on the Ti6Al4V side (a) and on the NiTi side (b) of the welded joint.

In summary, defect-free dissimilar laser welding of NiTi to Ti6Al4V was achieved using a Niobium interlayer. The following are the major conclusions that can be drawn:

- Niobium acted as a barrier to mixing of the two base materials, preventing thus the formation of brittle intermetallics, while ensuring joining at both interfaces. When no interlayer was used dissimilar joint between NiTi and Ti6Al4V did not occur;

- The average tensile strength and elongation of the joints with the Nb interlayer was 300 MPa and 2%, respectively. This tensile strength matched that of the Niobium interlayer;

- At the Ti6Al4V/Nb interface, dissolution of Nb into the liquid Titanium occurred. A thin (Ti, Nb) region with an average chemical composition of 47.7Ti-46.2Nb-2.9Al-3.3V (in wt. %) was identified at the interface of the Niobium interlayer and the fusion zone.

- At the NiTi/Nb interface, intimate contact between NiTi and Niobium promoted joining due to a eutectic reaction;

- To obtain a sound joint precise control of the position of the laser with respect to the interlayer was crucial. If the beam was positioned far away from the interlayer, eutectic melting in the NiTi/Nb interface did not occur. On the other hand, when the beam was positioned too close to the interlayer, no joint was formed because the laser beam was reflected by the Niobium interlayer.

4.3 Similar Laser Welding of CuAlMn Shape Memory Alloys

In this section, the effect of laser welding parameters on the microstructure and mechanical properties of superelastic Cu-17Al-11.4Mn (at. %) alloy is discussed. Additionally, post-weld laser treatment was performed and its effect on the processed material is compared to both non-processed and as-welded materials.

4.3.1 Microstructural Characterization by Optical Microscopy

For the selected welding parameters used for the CuAlMn alloy (described in section 3.2), full penetration was attained and no welding defects were observed (Figure 55). Microstructural analysis by optical microscopy of the welded material, revealed that the base material had a bamboo-like microstructure (Figure 56), with grain size ranging from 1 to 2 mm in length. The fusion zone was constituted by fine columnar (near the base material) and equiaxed grains (in the center of this region). In this latter region, the grain size ranged from 15 to 80 µm (Figure 57). The different colors observed in the base material grains and inside the fusion zone are related to differences in grain orientation.

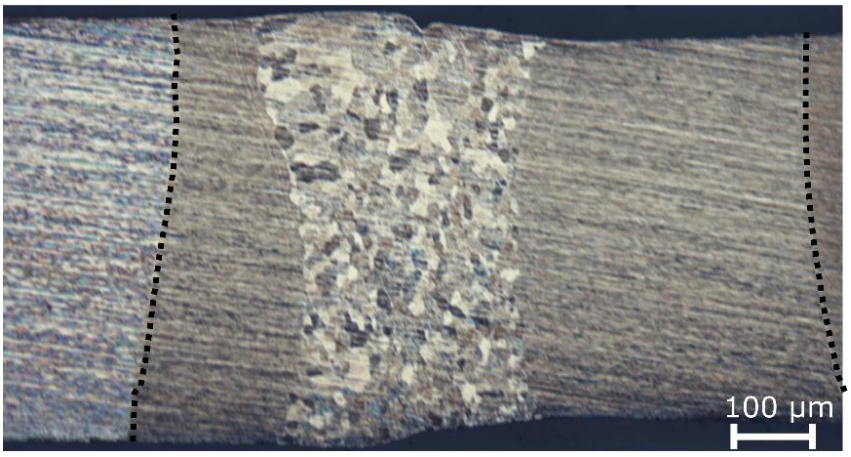

Figure 55 – Optical micrograph of the microstructure of the laser welded CuAlMn alloy. The dotted lines indicate the base material grain boundaries.

Figure 56 – Optical micrograph of base material. The dotted lines indicate the base material grain boundaries.

No heat affected zone was observed after welding. Similar observations were previously reported in laser welded NiTi [50,58]. The absence of this thermal affected region was attributed to the effect of higher temperature heat treatments performed on the base material prior to welding. As such, the weld thermal cycle was not enough to promote any further microstructural modification when compared to the base material.

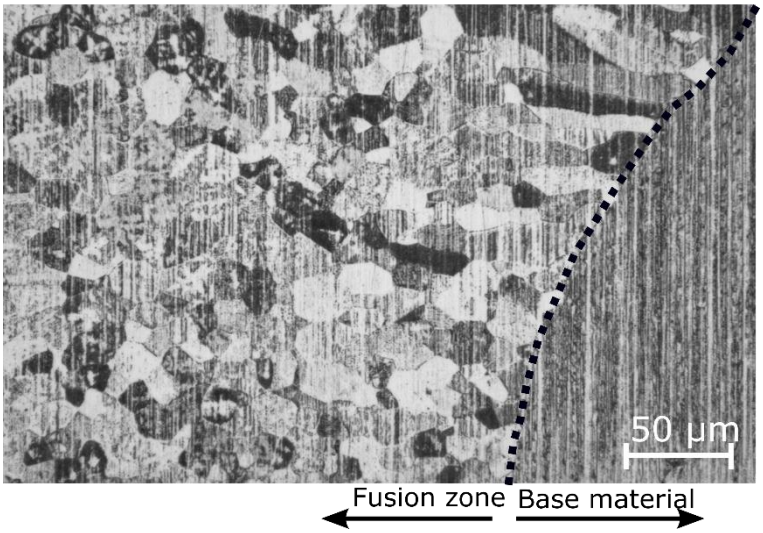

Figure 57 – Optical micrograph of the fusion zone. The dotted line indicate the fusion boundary.

No precipitates were observed in the base material and the fusion zone with the magnifications used for the optical microscopy performed. The high cooling rates associated to laser welding [33] ensured that any possible precipitation phenomena, namely of the α phase, were suppressed. For the CuAlMn alloy, the presence of the α phase is detrimental for the superelastic effect, as this phase does not exhibit superelasticity. As such, to take advantage of the superelastic effect after welding, α phase free welds must be ensured.

4.3.2 Microstructural Characterization by Energy Dispersive X-ray Spectroscopy, Conventional Hardness Measurements and Indentation vs Load Measurements [7]

To characterize the compositional variation within the base material and in the fusion zone, energy dispersive spectroscopy measurements were performed at 1/3 and 2/3 of the wire thickness. A total of 12 duly spaced spots in each line were analyzed, with 4 of them in the fusion zone. No significant compositional changes were observed. In fact, the average chemical composition of the fusion zone did not differ significantly from that of the base material composition. These results are presented in Table 5. Although, it is known that, for NiTi shape memory alloys, laser welding can promote preferential volatilization of certain elements, this was not the case for the welding parameters chosen to weld the CuAlMn alloy.

Table 5 – Average EDS measurements in both base material and fusion zone of the laser welded CuAlMn alloy.

Region	Cu [%]	Al [%]	Mn [%]
Base material	72.48 ± 2.21	16.16 ± 1.89	11.37 ± 1.31
Fusion zone	71.92 ± 2.65	16.44 ± 2.31	11.64 ± 1.71

Hardness measurements were performed at half thickness of the welded wire, starting in the base material, going through the fusion zone and finishing on the base material again. Some scattering on the hardness measurements was observed (Figure 58), but the average values within each zone are similar. In the base material the average hardness was of 263.9 ± 6.5 HV, while in the fusion zone this value slightly dropped to 258.4 ± 8.1 HV. Hardness measurements

[7] The below results (sections 4.3.1, 4.3.2 and 4.3.3) were already published in a paper in the journal Materials & Design, entitled Laser Welded Superelastic Cu-Al-Mn Shape Memory Alloy Wires.

performed on the superelastic CuAlMn alloy by other authors have shown similar results [133]. From our measurements it was also confirmed that no heat affected zone existed after welding of the material, as expected from microstructural observation performed by optical microscopy.

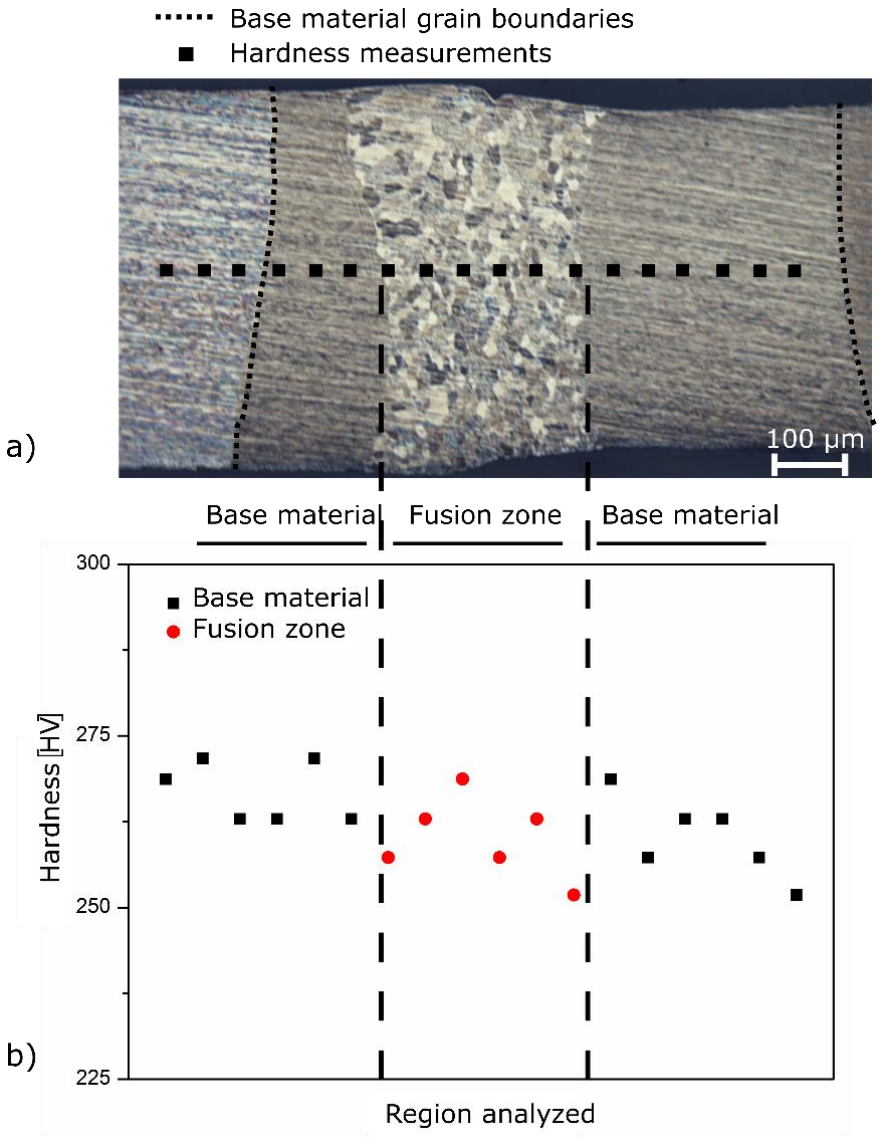

Figure 58 – Hardness measurement along the welded material (total of 18 analyzed spots).

To get a more clear mechanical characterization of both base material and fusion zone, load-displacement indentation tests were performed (Figure 59). As the indenter tip was of 100 µm, when the measurements were made in the fusion multiple grains were captured at each indentation. However, in the base material, only one grain was analyzed during each indentation.

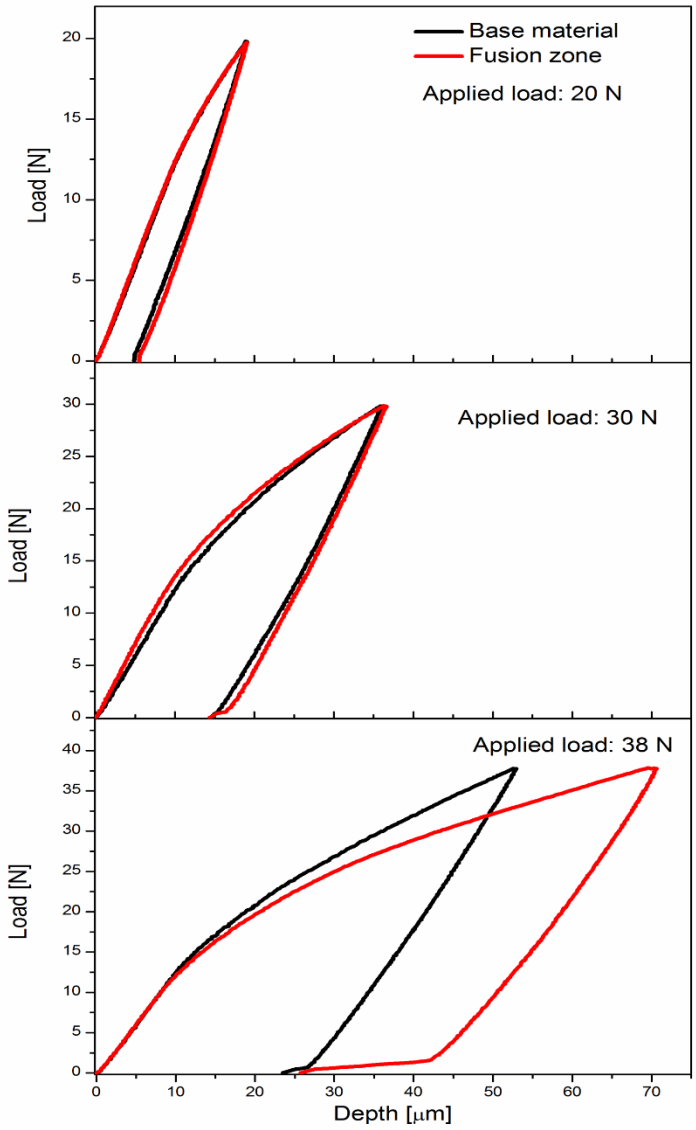

Figure 59 – Indentation curves in the fusion zone and in the base material for different applied loads.

When the applied loads were of 20 and 30 N, similar behavior was exhibited by both base material and fusion zone: the penetration depth for the applied load was similar and, upon unloading, the same residual penetration depth was recorded. When the maximum applied load was increased to 38 N, the fusion zone revealed a softer behavior, that is, the penetration depth for the maximum applied load was higher than for the base material. The increased ductility observed in the fusion zone, for the applied load of 38 N, occurred due to the reduction in grain size from the bamboo-like original microstructure to the fine grained one of this region. Upon unloading, the residual penetration depth was similar for both regions.

4.3.3 Characterization of the Mechanical Properties

The stress-strain curves of both base material and welded wire are depicted in Figure 60. These tensile curves are similar to one another, with both specimens requiring the same average stress for the onset of the stress induced transformation.

Usually, when welding other shape memory alloys like NiTi, there is a decrease in either the onset for the stress-induced transformation and/or in the tensile strength or elongation at

fracture [134–136]. This occurs due to grain growth phenomena in both heat affected and fusion zones. However, in the laser welded CuAlMn alloy that was not the case. Due to the massive grain size of the base material, obtained using high temperature heat treatments, only the fusion zone had its microstructure changed (to micrometer range sized grains). As a consequence of the aforementioned heat treatment, no heat affected zone was evidenced as a consequence of the weld thermal cycle. As such, the microstructural differences between base material and weld are restricted to the fusion zone of the weld, hence no significant differences were observed in the tensile behavior of both base material and welded joints.

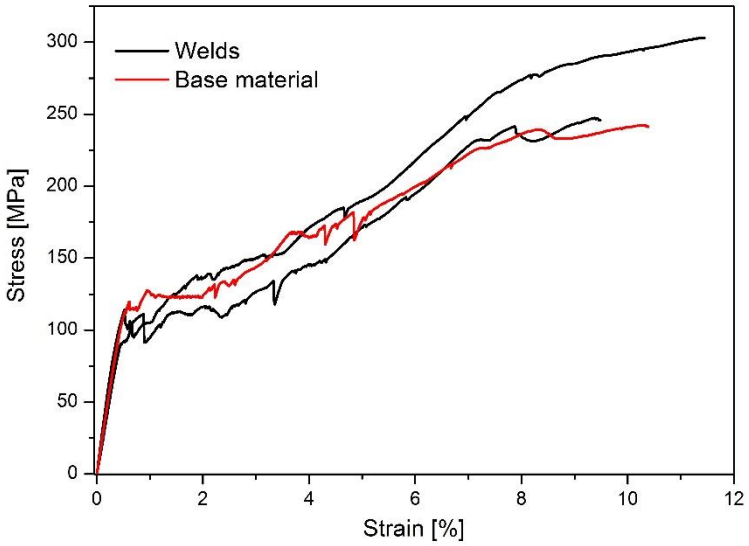

Figure 60 – Stress-strain curves of both base material and welded wires.

The superelastic strain is defined as the macroscopic strain from which the elastic contribution was subtracted [137] assuming no plastic deformation exists. In the superelastic CuAlMn alloy, the superelastic strain increases with the increase of the d/D ratio (where d is the grain size and D the wire diameter). Additionally, with increasing d/D, there is also an increase in the free surface grain boundary area, thus reducing the constraining strain imposed by the neighboring grains. In the fusion zone, the average number of grains per unit volume was considerably higher than in the base material, which lead to an increase in the constraint strain. Nonetheless, no significant changes were observed in the tensile properties of the welded wires. This phenomena is probably due to the reduced extension of the fusion zone relatively to the remaining non-affected base material. That is, volume fraction ratio between fusion zone and base material is very small, thus no significant differences in the superelastic strain were observed.

During tensile testing, necking of the fusion zone was observed. However, fracture occurred in the coarse grained base material far away from the possible influence of the weld heat input. The occurrence of necking in the fusion zone but, with fracture in the base material, may be related to the grain structure of the base material. It is known that Cu-Al-base shape memory alloys are prone to intergranular cracking [23]. As the grain boundaries of the base material are predominantly perpendicular to the direction of solicitation during tensile testing, any crack that forms will propagate in a catastrophic manner inside this region. On the other hand, the fine grained microstructure in the fusion zone is less prone to intergranular cracking. A schematic

representation, depicting the region where fracture occurred in the welds, is shown in Figure 61.

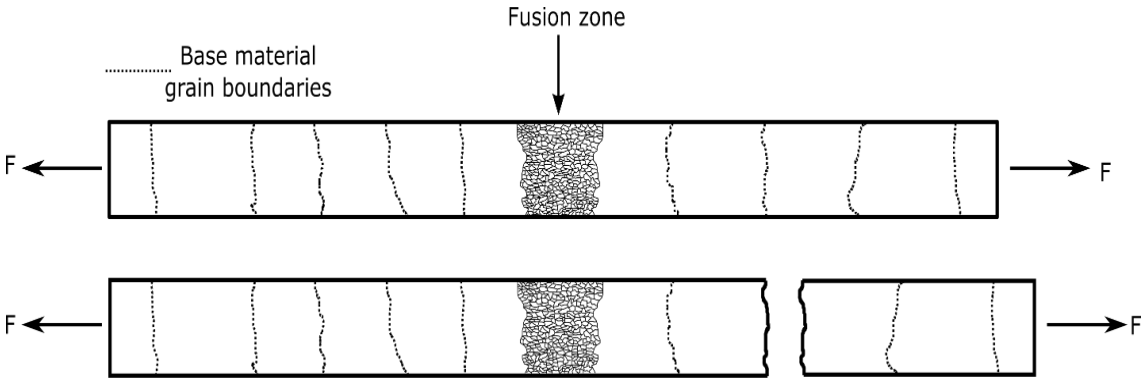

Figure 61 – Schematic representation the fracture along a grain boundary in the base material of the laser welded CuAlMn alloy (not to scale).

Analysis of the fracture surfaces of both base material and welded specimens revealed the same characteristics as fracture occurred in the same region (non-affected base material for the welds). Ductile-like fracture, with presence of dimples is depicted in Figure 62, corresponding to the fracture surface of a welded specimen. As such, no influence of the welding process was observed on the fracture characteristics of the laser welded specimens.

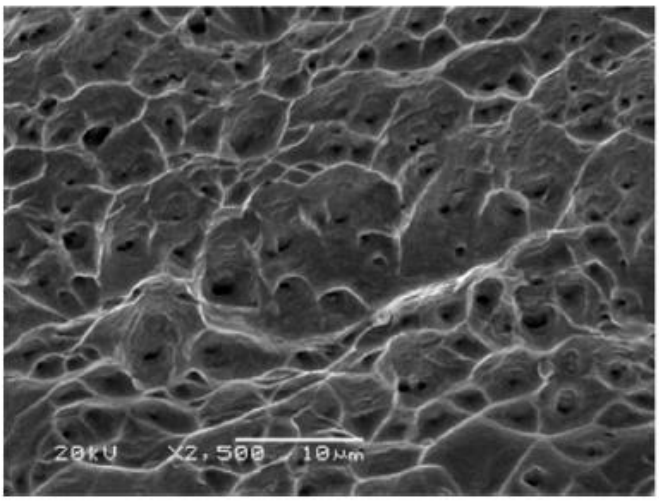

Figure 62 – Fracture surface of the welded specimen observed by scanning electron microscopy. Fracture occurred in the base material.

In NiTi laser welds, fracture occurs in the thermal affected regions as a consequence of the localization of strain in the softened material [57]. However, that was not the case for this singular CuAlMn alloy

The analysis of the cycling behavior of both base material and welds was performed. A total of 10 load/unload cyclic solicitations, up to 5% strain, were imposed to the specimens. As the superelastic CuAlMn alloy is intended to be used in systems subjected to load variations, such as in seismic structural applications or in biomedical components that move with the body, it is required to understand their behavior under cycling loading/unloading.

The cycling behavior of the base material and weld are depicted in Figure 63. From these results it is observed that the start of the martensitic transformation had higher values than those recorded during tensile tests. These cycling tests were performed with “wire 2”, as explained in the Materials and Methods Section (section 3.2), while “wire 1” was used for the tensile tests. As the stress to induce the martensitic transformation is dependent on the ratio of the grain size to wire diameter and on the crystallographic orientation of the grains, any slight change in the base material original microstructure will give raise to a change in the mechanical behavior of the material. This is the reason why higher stress values for the start of the martensitic transformation are observed in both base material and welded specimen during cycling tests.

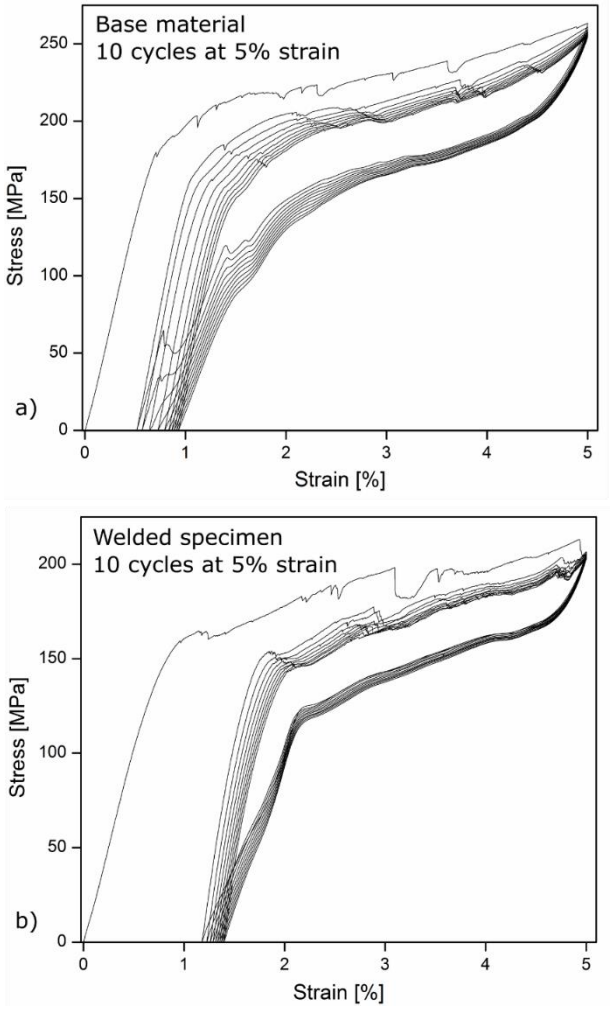

Figure 63 – Cycling behavior of: a) base material; b) weld.

The most significant difference between base material and weld during the cycling tests was the evolution of the irrecoverable strain and the absorbed energy for each cycle, which is related to the hysteretic loop (Figure 64). The use of the superelastic effect in applications, usually requires that the cycling behavior along a given load/unload path is stabilized after a given number of cycles. This stabilization effect occurs in shape memory alloys due to dislocation motion inhibition, which occurs as a results of a microstructural evolution. Both base material and welded specimen converged to a stabilized superelastic response after a low number of cycles, with the latter converging faster. The welded specimen tends to stabilize faster than the base material due to rapid plastic buildup, which is related to the constriction of the transformation

by the surrounding grains. In terms of design of applications, it is of major importance to understand when a given welded material presents a stabilized mechanical response. As such, it is clear that, for damping applications (for example), where joining technologies for the superelastic CuAlMn are required, laser welding is a suitable choice owing to the mechanical properties presented by these joints.

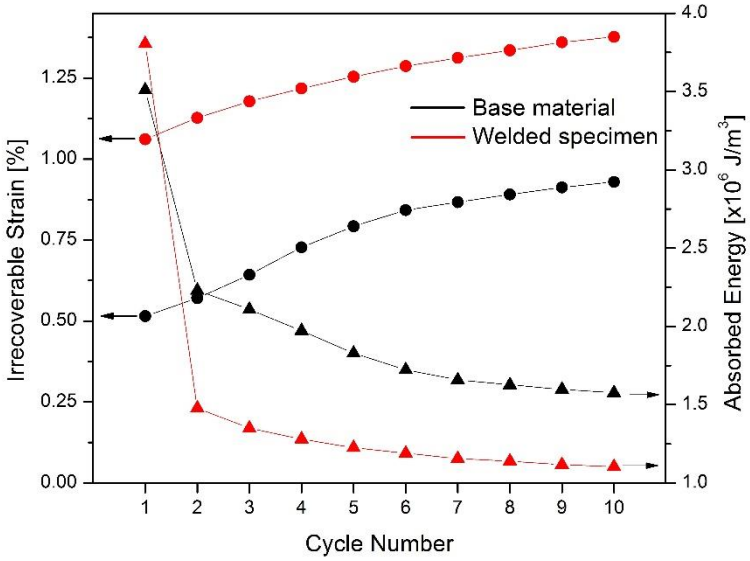

Figure 64 – Evolution of the irrecoverable strain and absorbed energy with the number of cycles for the base material and weld.

Kato *et al*. also analyzed the cycling behavior of Cu-Al-Mn single crystals [138]. Similarly to the cycling deformation behavior of these laser welded CuAlMn alloys, the single crystals convergence to a stabilized irrecoverable strain response occurred in the early cycles of deformation. Additionally, the majority of the plastic strain occurred in the first load/unload cycle and the onset stress for the stress induced transformation decreased with the number of successive cycles.

From this first investigation on laser welding of the CuAlMn alloy some conclusions can be drawn:

- The superelastic CuAlMn alloy presents excellent weldability. As such, new possibilities for the use of complex shaped component of this material in damping applications (or others) may be envisaged;

- The tensile properties of the welded material were similar to those of the base material;

- During tensile tests, fracture of the welds occurred always in the base material. Fracture occurred in a ductile way. No influence of the laser procedure was evidenced on the fracture of the material;

- Some significant differences were observed when comparing the cycling behavior of the base material to the laser welds: the irrecoverable strain of the weld in the first load/unload cycle is more than twice that of the base material; the absorbed energy of the weld is smaller than that of the base material;

- The laser welds tended to stabilize to a fixed value of the irrecoverable strain after a smaller number of cycles than that of the base material. This is of major importance for applications where a controlled actuation is required.

4.3.4 Effect of Post-weld Laser Processing on Superelastic Cu-Al-Mn Shape Memory Alloy [8]

Post-weld heat treatments are a recurring practice in order to improve the mechanical properties and/or the microstructure of welded joints. Following laser welding of the superelastic Cu-Al-Mn shape memory alloy, post-weld laser processing was performed. The aim of such post-weld treatment was to improve the mechanical properties and damping capacity of the as-welded material. This is especially important as these materials are currently being studied for possible application in seismic devices [139]. As such, welding can be an effective joining method to obtain complex shaped structures and these must possess excellent mechanical properties, so that they can withstand the imposed solicitations in service.

As referred in section 3.2.1, post-weld laser processing was performed using the same welding parameters as for the welding experiments. A total of 48 spots, corresponding to 10 mm in length, were laser spot processed with a formation of a fusion zone at each one of those spots. Aside from the as-welded material, laser processing was also performed on the original base material to compare the differences with the post-weld laser processes samples.

Tensile curves of the base material (BM), as-welded (AW), as-processed (AP) and post-weld laser processed (PWP) are depicted in Figure 65. The most remarkable observation is the significantly higher tensile strength presented by samples AP and PWP when compared to BM and AW ones. Also, the critical stress for the stress-induced transformation in the laser processed samples increased to nearly 200 MPa, in opposition to the 100 MPa at which the martensitic transformation starts for the base material and welded samples.

The reason for this significant increase of the critical stress for the onset of martensitic transformation is related to the microstructural changes induced by the laser processing on both AP and PWP samples. Similarly to the microstructure of the fusion zone in the CuAlMn laser welded joints, the laser processed region presents the same microstructural features, with micrometer sized grains (15 to 80 μm, as observed in Figure 66). This is understandable, as the parameters for laser processing matched those used for laser welding, so in each place where the laser impinged the CuAlMn alloy, the microstructure would resemble that of the fusion zone of the CuAlMn laser welds. On the non-affected base material the grain size ranged between 1 and 2 mm in length. As a result of the significant increase in grain density in the laser processed samples, an increase in the transformation stresses occurred. Other Cu-based shape memory alloys have been found to present a similar behavior [140].

[8] The below results (section 4.3.4) were already published in a paper in the journal Materials & Design, entitled Improvement of Damping Properties in Laser Processed Superelastic Cu-Al-Mn Shape Memory Alloys.

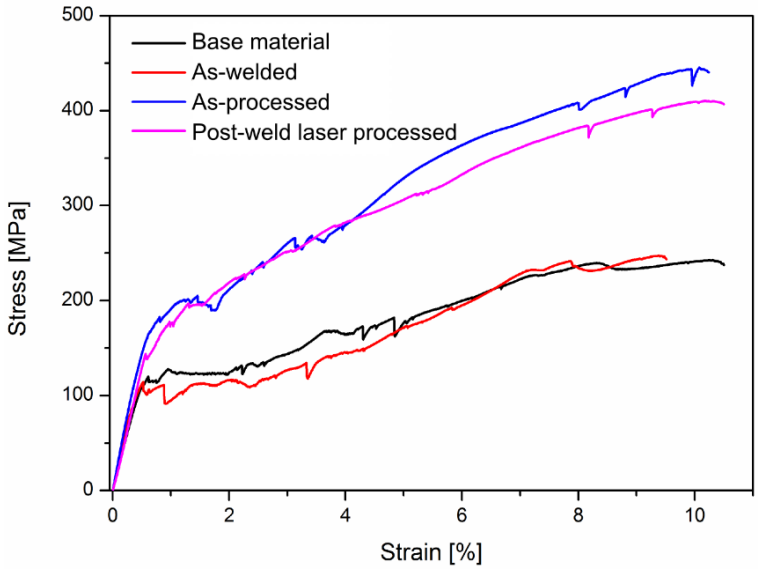

Figure 65 – Tensile curves of base material, as-welded, as-processed and post-weld laser processed CuAlMn samples.

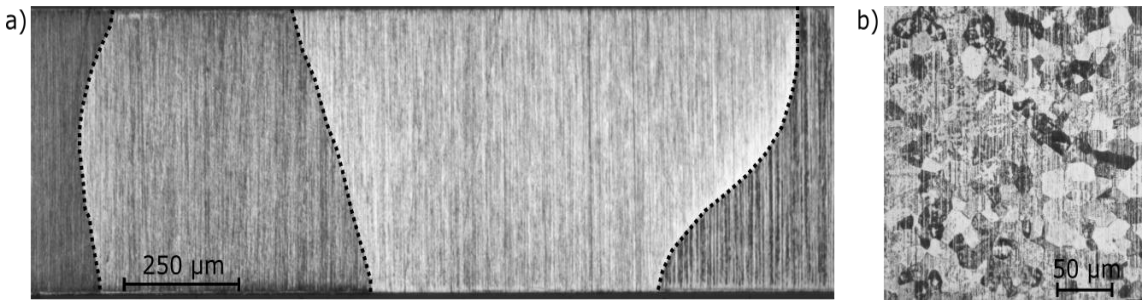

Figure 66 – Optical micrographs of: a) non-affected base material; b) laser processed region. The dotted lines indicate the base material grain boundaries.

What can be also observed from the tensile tests is that there are no significant differences between both AP and PWP samples. During these tensile tests, fracture of the AP and PWP samples have been seen to occur in the base material, similarly to what has happened in the as-welded samples. Fracture in the base material has typical ductile-like characteristics, characterized by a massive presence of dimples, as shown previously (Figure 62).

In order to analyze the fracture surface of the laser processed region, another PWP sample was tested to failure. However, in this case, the gauge length was set so that fracture could only occur in this region. The fracture surface morphology of the PWP sample is shown in Figure 67, and similarly to what was observed in BM and AW samples, ductile-like characteristics are observed.

Laser processing of the CuAlMn shape memory alloy replaces the originally massive bamboo structure by and equiaxed grain structure in the regions where the laser impinges the material. In fact, the AP and PWP have exactly the same microstructure throughout the laser processed region, hence the similar mechanical behavior observed during tensile tests to fracture. For this reason, only the cycling behavior of the PWP sample was assessed and compared to both the base material and as-welded samples. (Figure 68).

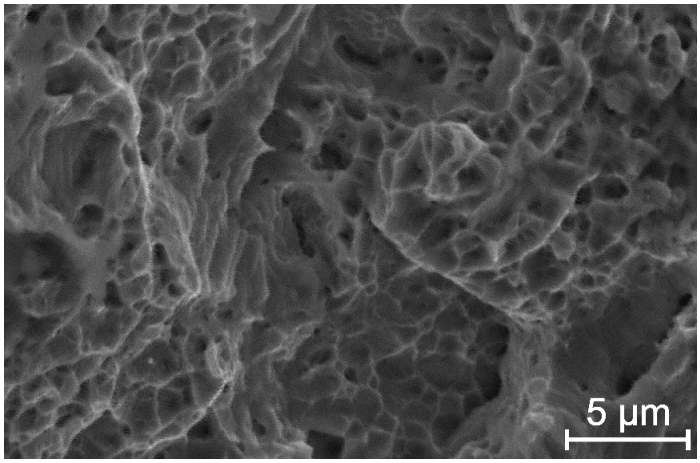

Figure 67 – Fracture surface of the post-weld laser processed sample.

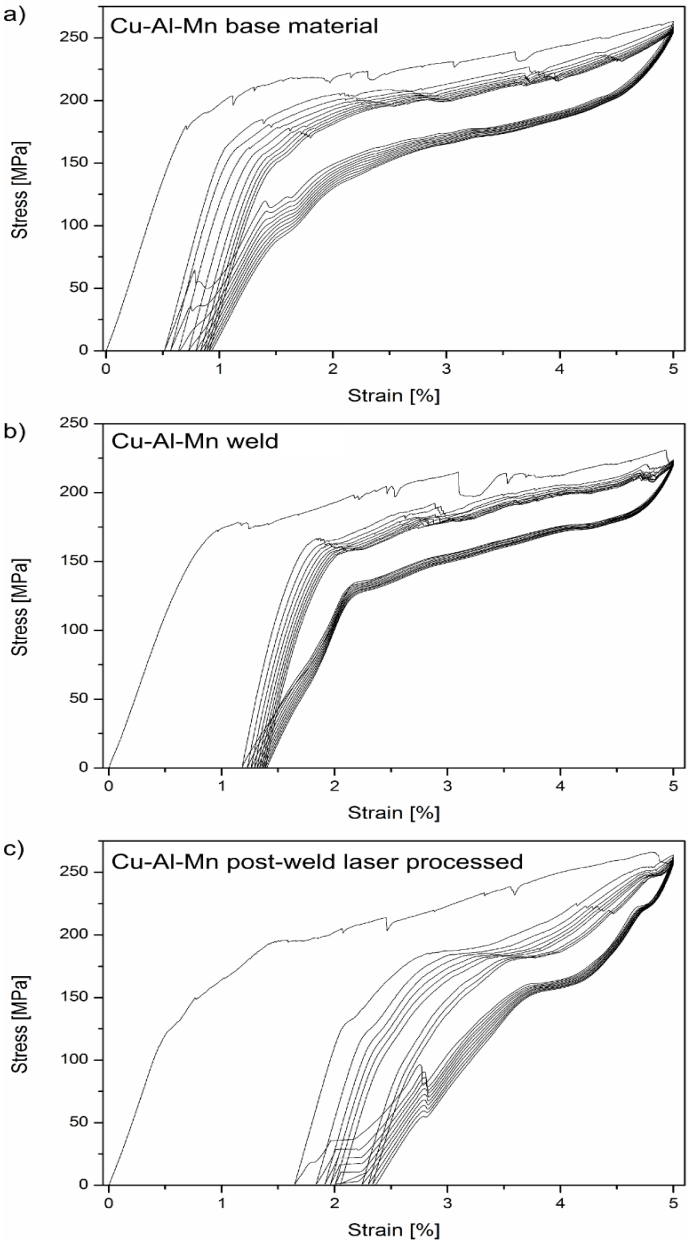

Figure 68 – Cycling behavior of: a) base material; b) as-welded; c) post-weld laser processed CuAlMn samples.

It can be observed that the PWP sample presented a stabilized hysteretic response after the second load/unload mechanical cycle: the shape of the stress-strain curve did not differ significantly from the second cycle onwards. A similar effect was also identified in the BM and AW samples.

As a consequence of the laser processing, it can be assumed that two distinct regions exist in a given sample: the non-affected base material, which possesses a significantly large bamboo-like grain size, and the processed region, constituted by a micrometer sized grains. As referred in the Introduction section, the superelasticity of the CuAlMn alloy is dependent on the grain size, d, and wire diameter, D. It is the intentionally massive grain size of the original base material which provides the best superelastic properties for this material. Accordingly, the two different regions in the laser processed sample will bring a distinct overall mechanical behavior. Figure 69 depicts the expected mechanical behavior of the two regions: the original bamboo structure and the fine grain structure resulting from laser processing. The effect of smaller grain size on the Cu-Al-Mn alloy is evidenced by a raise in the critical stress for the martensitic transformation. Also, the superelastic strain recovery of this region is lower. As such, then both processed and non-processed regions are loaded individually, it is expected that a large superelastic strain is accommodated by the bamboo structure, before the finer grained laser processed region starts to be strained extensively.

As a result of the lower stress of the beginning of the superelastic plateau, and due to significant ability to deform at constant stress level, the non-processed base material is relaxing the imposed stresses on the material.

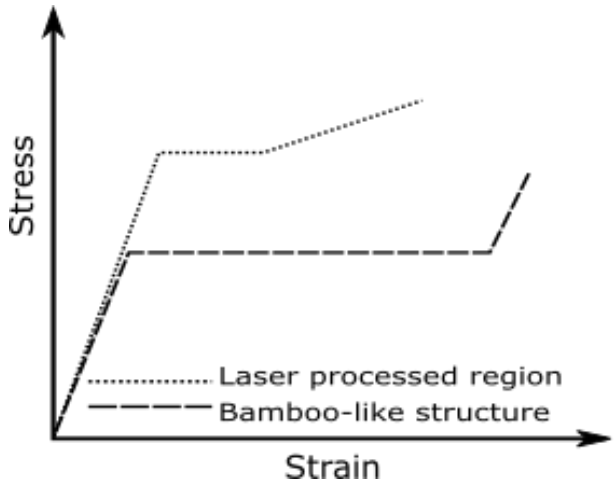

Figure 69 – Schematic representation of the expected mechanical behavior of the processed and non-processed regions in the CuAlMn alloy (not to scale and with arbitrary values).

Similarly to what was observed for the welded CuAlMn alloy, the decrease in grain size in the laser processed zone, and thus in the overall d/D ratio of the processed material, leads to a decrease in the superelastic properties, namely by an increase in the accumulated irrecoverable strain after unloading. The accumulated irrecoverable strain of the PWP sample was found to be significantly higher than for BM and AW ones (Figure 70). This occurs as a consequence of the smaller d/D ratio, which resulted in a more significant constriction of the transformation, thus justifying the larger plastic strain measured.

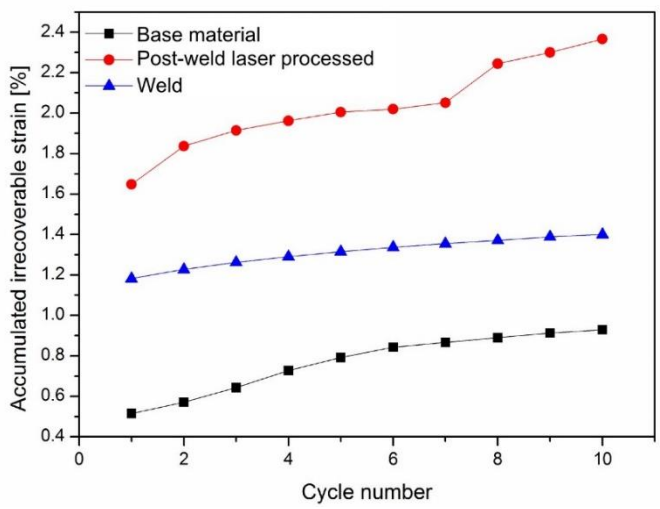

Figure 70 – Evolution of the accumulated irrecoverable strain with the number of cycle for base material, as-welded and post-weld laser processed CuAlMn alloy.

As a consequence of the significantly higher irrecoverable strain after the first complete load/unload cycle, the ability to absorb energy (determined from the area inside the load/unload stress-strain curve after each full cycle) during mechanical cycling sharply decreased (Figure 71), but remained almost constant in subsequent cycles. This means that, in the first load/unload cycle, the higher ability for energy absorption presented by the PWP sample is obtained, in part, at the expenses of a higher irrecoverable strain upon unloading. Nevertheless, the difference of the absorbed energy between PWP and BM samples is less than 10% after the second cycle.

As a result of the higher stress required for the start of the martensitic transformation, the PWP sample, exhibited a higher ability for energy absorption, despite the higher irrecoverable strain during mechanical cycling, than the AW samples. Thus, an improvement of this property was obtained after laser processing of the welded material. This means that, although laser welded superelastic CuAlMn wires present interesting properties, these can be improved by a proper post-weld laser processing.

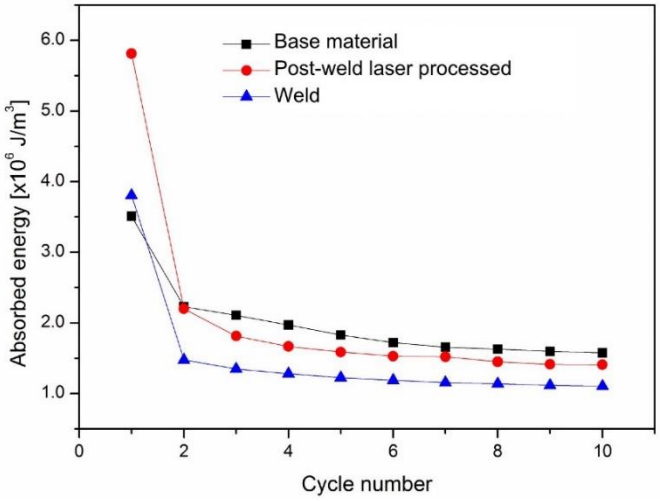

Figure 71 – Evolution of the absorbed energy with the number of cycles for base material, as-welded and post-weld laser processed CuAlMn alloy.

As the superelastic CuAlMn alloys are intended to be used in seismic devices, the significantly high damping capacity in the first load/unload cycle is of major importance. As such, the use of laser processed CuAlMn wires could be of great importance in such applications, as they exhibit an ability to absorb higher energies than the base material in the first load/unload cycle, while in the proceeding ones no significant differences between the processed and non-processed base material are observed. Furthermore, the ability for the PWP material for energy absorption is always higher than that of the AW material. Thus, it would be feasible to obtain complex shaped welded joints by laser with improved mechanical properties providing a post-weld laser processing was performed.

From the cycling tests, it was also observed that the onset for the stress-induced martensitic transformation decreased with the number of cycles. This is known to occur for shape memory alloys due to two possible reasons: the development of defects, such as dislocations; and/or retention of martensite nuclei, which will assist the austenite to martensite transformation in the following cycles, thus requiring lower external stresses.

As a results of dislocation slip occurring during the stress-induced transformation, a change in the stress-strain curves of the laser processed material was observed: after the first cycle it is noticed a variation on the slope of the superelastic plateau after 3.5% strain. This variation is related to the occurrence of plastic deformation during mechanical cycling, leading to strain-hardening of the processed material. This effect is more evident in the PWP sample due to the significantly higher density of fine grains, which have a larger contribution to the plastic deformation of the material when compared to the base material or the as-welded samples.

Some conclusions on the effect of post-weld laser processing on the mechanical properties of the CuAlMn alloy can be drawn:

- The tensile strength of the post-weld laser processed material increased to about twice that of the base material and as-welded samples;

- The absorbed energy and thus the damping capacity of the post-weld laser processed material in the first load/unload cycle, increase by 1.7 times when compared to that of the original base material;

- Despite the increased irrecoverable strain during mechanical cycling, the processed material was able to show similar damping properties to those of the base material after the second cycle, remaining constant in further cycling.

As such, the use of laser processing on these alloys may be of great interest, even when these have already been subjecting to welding.

5. Conclusions and Future Work

Shape memory alloys are functional materials which are difficult to machine, thus limiting their use in complex shaped applications. Joining methods must then be employed in order to allow for a greater design flexibility when using these materials.

In this work similar joints of NiTi/NiTi and CuAlMn/CuAlMn and dissimilar joints of NiTi/Ti6Al4V were produced by laser welding.

For NiTi/NiTi similar joints the following conclusions can be drawn:

- The laser welding procedure is responsible for inducing microstructural changes in the thermally affected regions: while the base material is fully austenitic, the remaining regions have a mixture of austenite and martensite.

- The mechanisms responsible for the formation of martensite, at room temperature, in the welded joints were presented: in the fusion zone preferential Ni volatilization, increased the transformation temperatures; on the heat affected zone, Ni_4Ti_3 precipitation had a similar effect.

- As a results of the presence of martensite in the thermally affected regions, the superelastic behavior of the joints was affected. Higher heat input, corresponding to higher amount of martensite, lead to a lower superelastic recovery of the joints when subjected to high strain cycling.

- Shape memory effect of the laser welded joints was not inhibited by the laser welding procedure. The joints exhibited full recovery of the imposed strain (up to 4 %).

- The residual stresses were determined by Rietveld refinement and these were found to be influenced by the constraints imposed during welding. Additionally, the heat input introduced promoted a stress-relief effect in the cold worked base material.

For the NiTi/Ti6Al4V dissimilar joints the following can summarize this work:

- Only when a Niobium interlayer is placed between NiTi and Ti6Al4V sounds joints can be obtained. Otherwise, solidification cracking occurs in the fusion zone.

- The Niobium interlayer act as an active barrier to the mixing of the molten metals, thus preventing the formation of brittle intermetallics.

- Positioning of the laser beam was fundamental to obtain a sound joint: only when placed impinging the Ti6Al4V base material, and at a given distance from the contact interface, the eutectic reaction between NiTi and Niobium took place.

As for the similar CuAlMn laser joints the following are the main conclusions:

- The superelastic CuAlMn alloy presents excellent weldability and fracture of the joints during tensile tests occurred in the base material due to its peculiar microstructure.

- The mechanical behavior, under cycling solicitation, of these joints is similar to that of the base material after the second load/unload cycle.

- Post-weld laser processing of the joints was found to improve the damping ability of the material, thus allowing its use in energy absorption applications.

Based on the experiments performed, other works might be of particular interest to conduct in the future:

- Development of a method to determine the phase quantification and residual stress magnitude in the post-weld heat treatment samples. Owing to the severe overlapping of the existing peaks it was found to be very difficult to separate the peaks of different phases.

- It would be interesting to study the effect of low-temperature post-weld heat treatments (≈ 200 °C) on the existing phases, so that the base material was still fully austenitic after these post-processing.

- The influence of different testing temperatures on the mechanical behavior of both NiTi/NiTi and CuAlMn/CuAlMn joints would be interesting to be analyzed;

- Analysis of the effects of different laser welding parameters on the mechanical behavior of the similar CuAlMn joints.

- Comparing the residual stresses measured by synchrotron radiation with other methods (micromechanics);

- Determination of the residual stresses in both CuAlMn/CuAlMn and NiTi/Ti6Al4V joints should also be attempted.

- Development of an energy absorption device based on CuAlMn joints.

- Development of system to carefully control the laser positioning for the dissimilar NiTi/Ti6Al4V joints;

- Study of others high temperature interlayers for the NiTi/Ti6Al4V joints. Specially, those who have a tensile strength above the threshold for the stress induced transformation.

6. References

[1] Otsuka K, Ren X. Physical metallurgy of Ti-Ni-based shape memory alloys. Prog Mater Sci 2005;50:511–678. doi:10.1016/j.pmatsci.2004.10.001.

[2] Bram M, Ahmad-Khanlou A, Heckmann A, Fuchs B, Buchkremer HP, Stöver D. Powder metallurgical fabrication processes for NiTi shape memory alloy parts. Mater Sci Eng A 2002;337:254–63. doi:10.1016/S0921-5093(02)00028-X.

[3] Liu Y, Liu Y, Van Humbeeck J. Two-way shape memory effect developed by martensite deformation in NiTi. Acta Mater 1998;47:199–209. doi:10.1016/S1359-6454(98)00325-5.

[4] Dolce M, Cardone D. Mechanical behaviour of shape memory alloys for seismic applications 2. Austenite NiTi wires subjected to tension. Int J Mech Sci 2001;43:2657–77. doi:http://dx.doi.org/10.1016/S0020-7403(01)00050-9.

[5] Lagoudas DC. Shape Memory Alloys: Modeling and Engineering Applications. New York: Springer; 2008. doi:10.1007/978-0-387-47685-8.

[6] Allafi JK, Ren X, Eggeler G. The mechanism of multistage martensitic transformations in aged Ni-rich NiTi shape memory alloys. Acta Mater 2002;50:793–803. doi:10.1016/S1359-6454(01)00385-8.

[7] Seo J, Kim Y, Hu J. Pilot Study for Investigating the Cyclic Behavior of Slit Damper Systems with Recentering Shape Memory Alloy (SMA) Bending Bars Used for Seismic Restrainers. Appl Sci 2015;5:187–208. doi:10.3390/app5030187.

[8] Liu Y, Mahmud A, Kursawe F, Nam TH. Effect of pseudoelastic cycling on the Clausius-Clapeyron relation for stress-induced martensitic transformation in NiTi. J Alloys Compd 2008;449:82–7. doi:10.1016/j.jallcom.2006.02.080.

[9] Kajiwara S. Characteristic features of shape memory effect and related transformation behavior in Fe-based alloys. Mater Sci Eng A 1999;273-275:67–88. doi:10.1016/S0921-5093(99)00290-7.

[10] Sutou Y, Omori T, Wang JJ, Kainuma R, Ishida K. Characteristics of Cu-Al-Mn-based shape memory alloys and their applications. Mater Sci Eng A 2004;378:278–82. doi:10.1016/j.msea.2003.12.048.

[11] Khalil-Allafi J, Eggeler G, Dlouhy A, Schmahl WW, Somsen C. On the influence of heterogeneous precipitation on martensitic transformations in a Ni-rich NiTi shape memory alloy. Mater Sci Eng A 2004;378:148–51. doi:10.1016/j.msea.2003.10.335.

[12] Khalil-Allafi J, Dlouhy A, Eggeler G. Ni4Ti3-precipitation during aging of NiTi shape memory alloys and its influence on martensitic phase transformations. Acta Mater 2002;50:4255–74. doi:10.1016/s1359-6454(02)00257-4.

[13] Wagner MFX, Dey SR, Gugel H, Frenzel J, Somsen C, Eggeler G. Effect of low-temperature precipitation on the transformation characteristics of Ni-rich NiTi shape memory alloys during thermal cycling. Intermetallics 2010;18:1172–9. doi:10.1016/j.intermet.2010.02.048.

[14] Nishida M, Wayman CM, Honma T. Precipitation processes in near-equiatomic TiNi shape

memory alloys. Metall Trans A 1986;17:1505–15. doi:10.1007/BF02650086.

[15] Pelton AR, Dicello J, Miyazaki S. Optimisation of processing and properties of medical grade Nitinol wire. Minim Invasive Ther Allied Technol 2000;9:107–18. doi:10.3109/13645700009063057.

[16] Frenzel J, George EP, Dlouhy A, Somsen C, Wagner MF-X, Eggeler G. Influence of Ni on martensitic phase transformations in NiTi shape memory alloys. Acta Mater 2010;58:3444–58. doi:10.1016/j.actamat.2010.02.019.

[17] Miller D a, Lagoudas DC. Thermomechanical characterization of NiTiCu and NiTi SMA actuators: influence of plastic strains. Smart Mater Struct 2000;9:640–52. doi:10.1088/0964-1726/9/5/308.

[18] Lemanski JL. A Low Hysteresis NiTiFe Shape Memory Alloy Based Thermal Conduction Switch. AIP Conf Proc 2006;824:3–10. doi:10.1063/1.2192327.

[19] Ying C, Hai-Chang J, Li-Jian R, Li X, Xin-Qing Z. Mechanical behavior in NiTiNb shape memory alloys with low Nb content. Intermetallics 2011;19:217–20. doi:10.1016/j.intermet.2010.08.011.

[20] Otsuka K, Wayman CM. Shape Memory Materials. Cambridge. Cambridge Press; 1998. doi:10.1016/S1369-7021(10)70128-0.

[21] Funakubo H. Shape Memory Alloys. New York: J.B. Kennedy Gordon and Breach Science Publishers; 1986.

[22] Obradó E, Frontera C, Mañosa L, Planes A. Order-disorder transitions of Cu-Al-Mn shape-memory alloys. Phys Rev B 1998;58:14245–55. doi:10.1103/PhysRevB.58.14245.

[23] Sutou Y, Omori T, Yamauchi K, Ono N, Kainuma R, Ishida K. Effect of grain size and texture on pseudoelasticity in Cu–Al–Mn-based shape memory wire. Acta Mater 2005;53:4121–33. doi:10.1016/j.actamat.2005.05.013.

[24] Kainuma R, Takahashi S, Ishida K. Ductile Shape Memory Alloys of the Cu-Al-Mn System. J Phys IV 1995;05:C8–961 – C8–966. doi:10.1051/jp4/199558961.

[25] Sutou Y, Omori T, Kainuma R, Ishida K. Ductile Cu–Al–Mn based shape memory alloys: general properties and applications. Mater Sci Technol 2008;24:896–901. doi:10.1179/174328408X302567.

[26] Kainuma R, Takahashi S, Ishida K. Thermoelastic Martensite and Shape Memory Effect in Ductile Cu-Al-Mn Alloys. Metall Mater Trans A 1996;27.

[27] Gigla M, Szczeszek P, Krzelowski M, Paczkowski P, Prusik K, Morawiec H. Martensite Structures in Shape Memory β Phase Alloys. Appl. Crystallogr., WORLD SCIENTIFIC; 2004, p. 134–7. doi:10.1142/9789812702913_0025.

[28] Kaufmann S, Niemann R, Thersleff T, Rößler UK, Heczko O, Buschbeck J, et al. Modulated martensite: why it forms and why it deforms easily. New J Phys 2011;13:053029. doi:10.1088/1367-2630/13/5/053029.

[29] Araki Y, Endo T, Omori T, Sutou Y, Koetaka Y, Kainuma R, et al. Potential of superelastic Cu-Al-Mn alloy bars for seismic applications. Earthq Eng Struct Dyn 2011;40:107–15. doi:10.1002/eqe.1029.

[30] Omori T, Kusama T, Kawata S, Ohnuma I, Sutou Y, Araki Y, et al. Abnormal Grain Growth Induced by Cyclic Heat Treatment. Science (80-) 2013;341:1500–2. doi:10.1126/science.1238017.

[31] Shrestha KC, Araki Y, Nagae T, Omori T, Sutou Y, Kainuma R, et al. Effectiveness of superelastic bars for seismic rehabilitation of clay-unit masonry walls. Earthq Eng Struct Dyn 2013;42:725–41. doi:10.1002/eqe.2241.

[32] Gencturk B, Araki Y, Kusama T, Omori T, Kainuma R, Medina F. Loading rate and temperature dependency of superelastic Cu-Al-Mn alloys. Constr Build Mater 2014;53:555–60. doi:10.1016/j.conbuildmat.2013.12.002.

[33] Steen WM, Mazumder J. Laser Material Processing. London: Springer London; 2010. doi:10.1007/978-1-84996-062-5.

[34] Katayama S. Handbook of laser welding technologies. Oxford: Woodhead Publishing Limited; 2013.

[35] Mills KC, Keene BJ, Brooks RF, Shirali A. Marangoni effects in welding. Philos Trans R Soc A Math Phys Eng Sci 1998;356:911–25. doi:10.1098/rsta.1998.0196.

[36] Sibillano T, Ancona A, Berardi V, Schingaro E, Basile G, Lugarà PM. Optical detection of conduction/keyhole mode transition in laser welding. J Mater Process Technol 2007;191:364–7. doi:10.1016/j.jmatprotec.2007.03.075.

[37] Wang Q, Chung Y. Encyclopedia of tribology. vol. 150. New York: Springer; 2013. doi:10.1016/0043-1648(91)90333-P.

[38] Quintino L, Costa A, Miranda R, Yapp D, Kumar V, Kong CJ. Welding with high power fiber lasers - A preliminary study. Mater Des 2007;28:1231–7. doi:10.1016/j.matdes.2006.01.009.

[39] Araki T, Hirose A, Uchihara M, Kohno W, Honda K, Kondoh M. Characteristics and fracture morphology of Ti-Ni type shape memory alloy and its laser weld joint. J Soc Mater Sci Japan 1989;38:478–83. doi:10.2472/jsms.38.478.

[40] Hirose A, Araki T, Uchihara M, Honda K, Kondoh M. Laser Welding of Ti-Ni Type Shape Memory Alloy. J Japan Inst Met Mater 1990;54:262–9.

[41] Tuissi A, Bassani P, Gerosa M, Mauri D, Pini M, Capello E, et al. CO2 Laser Welding of NiTi/Ni-based alloys. In: Pelton A, Duerig T, editors. Proc. Int. Conf. Shape Mem. Superelastic Technol., 2004, p. 229–38. doi:10.1361/cp2003smst229.

[42] Gugel H, Schuermann A, Theisen W. Laser welding of NiTi wires. Mater Sci Eng A 2008;481-482:668–71. doi:10.1016/j.msea.2006.11.179.

[43] Sevilla P, Martorell F, Libenson C, Planell JA, Gil FJ. Laser welding of NiTi orthodontic archwires for selective force application. J Mater Sci Mater Med 2008;19:525–9. doi:10.1007/s10856-007-0164-8.

[44] Chan CW, Man HC, Yue TM. Effects of process parameters upon the shape memory and pseudo-elastic behaviors of laser-welded NiTi thin foil. Metall Mater Trans A Phys Metall Mater Sci 2011;42:2264–70. doi:10.1007/s11661-011-0623-1.

[45] Chan CW, Man HC. Laser welding of thin foil nickel–titanium shape memory alloy. Opt

Lasers Eng 2011;49:121–6. doi:10.1016/j.optlaseng.2010.08.007.

[46] Chan CW, Man HC, Yue TM. Effect of Postweld Heat Treatment on the Microstructure and Cyclic Deformation Behavior of Laser-Welded NiTi-Shape Memory Wires. Metall Mater Trans A 2012;43:1956–65. doi:10.1007/s11661-011-1062-8.

[47] Kou S. Welding Metallurgy. 2nd ed. Hoboken: John Wiley & Sons, Inc.; 2002. doi:10.1002/0471434027.

[48] Dinnebier R, Billinge S. Powder Diffraction: Theory and Practice. 1st ed. Cambridge: Royal Society of Chemistry; 2008. doi:10.1039/9781847558237.

[49] Iijima M, Brantley WA, Yuasa T, Muguruma T, Kawashima I, Mizoguchi I. Joining characteristics of orthodontic wires with laser welding. J Biomed Mater Res Part B Appl Biomater 2008;84B:147–53. doi:10.1002/jbm.b.30856.

[50] Schlossmacher P, Haas T, Ussler AS. Laser-Welding of a Ni-Rich TiNi Shape Memory Alloy: Mechanical Behavior. J Phys IV 1997;07:C5–251 – C5–256. doi:10.1051/jp4:1997539.

[51] Schlossmacher P, Haas T, Schussler A. Laser welding of Ni-Ti Shape Memory Alloys. Proc. Int. Conf. Shape Mem. Superelastic Technol., 1994, p. 85–90.

[52] Zhao X, Wang W, Chen L, Liu F, Huang J, Zhang H. Microstructures of cerium added laser weld of a TiNi alloy. Mater Lett 2008;62:1551–3. doi:10.1016/j.matlet.2007.09.021.

[53] Zhao X, Wang W, Chen L, Liu F, Chen G, Huang J, et al. Two-stage superelasticity of a Ce-added laser-welded TiNi alloy. Mater Lett 2008;62:3539–41. doi:10.1016/j.matlet.2008.03.042.

[54] Falvo A, Furgiuele FM, Maletta C. Laser welding of a NiTi alloy: Mechanical and shape memory behaviour. Mater Sci Eng A 2005;412:235–40. doi:10.1016/j.msea.2005.08.209.

[55] Vieira LA, Fernandes FMB, Miranda RM, Silva RJC, Quintino L, Cuesta A, et al. Mechanical behaviour of Nd:YAG laser welded superelastic NiTi. Mater Sci Eng A 2011;528:5560–5. doi:10.1016/j.msea.2011.03.089.

[56] Schlossmacher P. Laser welding of Ni-Rich TiNi Shape Memory Alloy- Pseudoelastic properties. Proc. Int. Conf. Shape Mem. Superelastic Technol., 1997, p. 137–42.

[57] Tuissi a, Besseghini S, Ranucci T, Squatrito F, Pozzi M. Effect of Nd-YAG laser welding on the functional properties of the Ni–49.6at.%Ti. Mater Sci Eng A 1999;273-275:813–7. doi:10.1016/S0921-5093(99)00422-0.

[58] Hsu YT, Wang YR, Wu SK, Chen C. Effect of CO2 laser welding on the shape-memory and corrosion characteristics of TiNi alloys. Metall Mater Trans A 2001;32:569–76. doi:10.1007/s11661-001-0073-2.

[59] Yan XJ, Yang DZ, Qi M. Rotating–bending fatigue of a laser-welded superelastic NiTi alloy wire. Mater Charact 2006;57:58–63. doi:10.1016/j.matchar.2005.12.009.

[60] Chan CW, Man HC, Cheng FT. Fatigue behavior of laser-welded NiTi wires in small-strain cyclic bending. Mater Sci Eng A 2013;559:407–15. doi:10.1016/j.msea.2012.08.119.

[61] Mukherjee K, Sircar S, Dahotre NB. Thermal effects associated with stress-induced martensitic transformation in a Ti-Ni alloy. Mater Sci Eng 1985;74:75–84. doi:10.1016/0025-5416(85)90111-9.

[62] McKelvey AL, Ritchie RO. Fatigue-crack growth behavior in the superelastic and shape-memory alloy Nitinol. Metall Mater Trans a-Physical Metall Mater Sci 2001;32:731–43. doi:DOI 10.1007/s11661-001-0089-7.

[63] Pan Q, Cho C. The Investigation of a Shape Memory Alloy Micro-Damper for MEMS Applications. Sensors 2007;7:1887–900. doi:10.3390/s7091887.

[64] Falvo A, Furgiuele FM, Maletta C. Functional behaviour of a NiTi-welded joint: Two-way shape memory effect. Mater Sci Eng A 2008;481-482:647–50. doi:10.1016/j.msea.2006.11.178.

[65] Bradley TG, Brantley W a, Culbertson BM. Differential scanning calorimetry (DSC) analyses of superelastic and nonsuperelastic nickel-titanium orthodontic wires. Am J Orthod Dentofacial Orthop 1996;109:589–97. doi:10.1016/S0889-5406(96)70070-7.

[66] Shaw JA, Churchill CB, Iadicola MA. Tips and Tricks for Characterizing Shape Memory Alloy Wire: Part 1-Differential Scanning Calorimetry and Basic Phenomena. Exp Tech 2008;32:55–62. doi:10.1111/j.1747-1567.2008.00410.x.

[67] Uchil J, Mahesh KK, Kumara KG. Dilatometric study of martensitic transformation in NiTiCu and NiTi shape memory alloys. J Mater Sci 2001;36:5823–7. doi:10.1023/A:1012908222409.

[68] Uchil J, Mahesh KK, Kumara KG. Electrical resistivity and strain recovery studies on the effect of thermal cycling under constant stress on R-phase in NiTi shape memory alloy. Phys B Condens Matter 2002;324:419–28. doi:10.1016/S0921-4526(02)01462-X.

[69] Novák V, Šittner P, Dayananda GN, Braz-Fernandes FM, Mahesh KK. Electric resistance variation of NiTi shape memory alloy wires in thermomechanical tests: Experiments and simulation. Mater Sci Eng A 2008;481-482:127–33. doi:10.1016/j.msea.2007.02.162.

[70] Song YG, Li WS, Li L, Zheng YF. The influence of laser welding parameters on the microstructure and mechanical property of the as-jointed NiTi alloy wires. Mater Lett 2008;62:2325–8. doi:10.1016/j.matlet.2007.11.082.

[71] Khan MI, Zhou Y. Effects of local phase conversion on the tensile loading of pulsed Nd:YAG laser processed Nitinol. Mater Sci Eng A 2010;527:6235–8. doi:10.1016/j.msea.2010.06.025.

[72] Khan MI, Pequegnat A, Zhou YN. Multiple Memory Shape Memory Alloys. Adv Eng Mater 2013;15:386–93. doi:10.1002/adem.201200246.

[73] Yan XJ, Yang DZ. Corrosion resistance of a laser spot-welded joint of NiTi wire in simulated human body fluids. J Biomed Mater Res - Part A 2006;77:97–102. doi:10.1002/jbm.a.30378.

[74] Cho JR, Lee BY, Moon YH, Van Tyne CJ. Investigation of residual stress and post weld heat treatment of multi-pass welds by finite element method and experiments. J Mater Process Technol 2004;155-156:1690–5. doi:10.1016/j.jmatprotec.2004.04.325.

[75] Krishnan KN. The effect of post weld heat treatment on the properties of 6061 friction stir welded joints. J Mater Sci 2002;37:473–80. doi:10.1023/A:1013701104029.

[76] Elangovan K, Balasubramanian V. Influences of post-weld heat treatment on tensile properties of friction stir-welded AA6061 aluminum alloy joints. Mater Charact

2008;59:1168–77. doi:10.1016/j.matchar.2007.09.006.

[77] Chan CW, Man HC, Yue TM. Effect of post-weld heat-treatment on the oxide film and corrosion behaviour of laser-welded shape memory NiTi wires. Corros Sci 2012;56:158–67. doi:10.1016/j.corsci.2011.11.020.

[78] Yan XJ, Yang DZ, Liu XP. Influence of heat treatment on the fatigue life of a laser-welded NiTi alloy wire. Mater Charact 2007;58:262–6. doi:10.1016/j.matchar.2006.05.001.

[79] Yan X, Ge Y. Influence of Post-Weld Annealing on Transformation Behavior and Mechanical Properties of Laser-Welded NiTi Alloy Wires. J Mater Eng Perform 2014;23:3474–9. doi:10.1007/s11665-014-1156-8.

[80] Sitepu H, Schmahl W., Allafi J., Eggeler G, Dlouhy a, Toebbens D., et al. Neutron diffraction phase analysis during thermal cycling of a Ni-rich NiTi shape memory alloy using the Rietveld method. Scr Mater 2002;46:543–8. doi:10.1016/S1359-6462(02)00032-5.

[81] Miranda RM, Assunção E, Silva RJC, Oliveira JP, Quintino L. Fiber laser welding of NiTi to Ti-6Al-4V. Int J Adv Manuf Technol 2015. doi:10.1007/s00170-015-7307-8.

[82] Shojaei Zoeram A, Akbari Mousavi SAA. Laser welding of Ti–6Al–4V to Nitinol. Mater Des 2014;61:185–90. doi:10.1016/j.matdes.2014.04.078.

[83] Shojaei Zoeram A, Akbari Mousavi SAA. Effect of interlayer thickness on microstructure and mechanical properties of as welded Ti6Al4V/Cu/NiTi joints. Mater Lett 2014;133:5–8. doi:10.1016/j.matlet.2014.06.141.

[84] Oliveira J. Correlation Between the Mechanical Cycling Behavior and Microstructure in Laser Welded Joints Using NiTi Memory Shape Alloys. MSc thesis. 2012.

[85] Stevie FA, Vartuli CB, Giannuzzi LA, Shofner TL, Brown SR, Rossie B, et al. Application of focused ion beam lift-out specimen preparation to TEM, SEM, STEM, AES and SIMS analysis. Surf Interface Anal 2001;31:345–51. doi:10.1002/sia.1063.

[86] Oliveira JP. Correlation Between the Mechanical Cycling Behavior and Microstructure in Laser Welded Joints Using NiTi Memory Shape Alloys. MSc Thesis in Materials Science and Engineering, Faculdade de Ciências E Tecnologia Universidade Nova de Lisboa, Portugal: 2012.

[87] Hammersley AP, Svensson SO, Hanfland M, Fitch AN, Hausermann D. Two-dimensional detector software: From real detector to idealised image or two-theta scan. High Press Res 1996;14:235–48. doi:10.1080/08957959608201408.

[88] Lutterotti L, Matthies S, Wenk H-R, Schultz AS, Richardson JW. Combined texture and structure analysis of deformed limestone from time-of-flight neutron diffraction spectra. J Appl Phys 1997;81:594. doi:10.1063/1.364220.

[89] Wenk H-R, Lutterotti L, Kaercher P, Kanitpanyacharoen W, Miyagi L, Vasin R. Rietveld texture analysis from synchrotron diffraction images. II. Complex multiphase materials and diamond anvil cell experiments. Powder Diffr 2014;4:1–13. doi:10.1017/S0885715614000360.

[90] Šittner P, Heller L, Pilch J, Curfs C, Alonso T, Favier D. Young's Modulus of Austenite and Martensite Phases in Superelastic NiTi Wires. J Mater Eng Perform 2014;23:2303–14.

doi:10.1007/s11665-014-0976-x.

[91] Boyer R, Welsch G, Collings E. Materials Properties Handbook: Titanium Alloys. 1st ed. Ohio: ASM International; 1994.

[92] Korsunsky AM, Collins SP, Alexander Owen R, Daymond MR, Achtioui S, James KE. Fast residual stress mapping using energy-dispersive synchrotron X-ray diffraction on station 16.3 at the SRS. J Synchrotron Radiat 2002;9:77–81. doi:10.1107/S0909049502001905.

[93] Vieira LA. Laser welding of shape memory alloys. MSc Thesis in Mechanical Engineering, Faculdade de Ciências E Tecnologia Universidade Nova de Lisboa, Portugal: 2010.

[94] Ke CB, Cao SS, Ma X, Zhang XP. Modeling of Ni4Ti3 precipitation during stress-free and stress-assisted aging of bi-crystalline NiTi shape memory alloys. Trans Nonferrous Met Soc China 2012;22:2578–85. doi:Doi 10.1016/S1003-6326(11)61503-3.

[95] Otsuka K, Ren XB. Recent developments in the research of shape memory alloys. Intermetallics 1999;7:511–28. doi:10.1016/s0966-9795(98)00070-3.

[96] Otsuka K, Ren X. Physical metallurgy of Ti-Ni-based shape memory alloys. Prog Mater Sci 2005;50:511–678. doi:DOI 10.1016/j.pmatsci.2004.10.001.

[97] Ki H, Mazumder J, Mohanty PS. Modeling of laser keyhole welding: Part II. simulation of keyhole evolution, velocity, temperature profile, and experimental verification. Metall Mater Trans A 2002;33:1831–42. doi:10.1007/s11661-002-0191-5.

[98] Gale W, Totemeir T. Smithells Metals Reference Book. 8th ed. Oxford: Elsevier; 2004. doi:10.1017/CBO9781107415324.004.

[99] Vieira LA, Fernandes FMB, Miranda RM, Silva RJC, Quintino L, Cuesta A, et al. Mechanical behaviour of Nd:YAG laser welded superelastic NiTi. Mater Sci Eng A 2011;528:5560–5. doi:10.1016/j.msea.2011.03.089.

[100] Mirshekari GR, Kermanpur A, Saatchi A, Sadrnezhaad SK, Soleymani AP. Microstructure, Cyclic Deformation and Corrosion Behavior of Laser Welded NiTi Shape Memory Wires. J Mater Eng Perform 2015;24:3356–64. doi:10.1007/s11665-015-1614-y.

[101] Nemat-Nasser S, Guo W-G. Superelastic and cyclic response of NiTi SMA at various strain rates and temperatures. Mech Mater 2006;38:463–74. doi:10.1016/j.mechmat.2005.07.004.

[102] Tobushi H, Shimeno Y, Hachisuka T, Tanaka K. Influence of strain rate on superelastic properties of TiNi shape memory alloy. Mech Mater 1998;30:141–50. doi:10.1016/S0167-6636(98)00041-6.

[103] Lin PH, Tobushi H, Tanaka K, Hattori T, Makita M. Pseudoelastic Behaviour of TiNi Shape Memory Alloy Subjected to Strain Variations. J Intell Mater Syst Struct 1994;5:694–701. doi:10.1177/1045389X9400500514.

[104] Saburi T, Nenno S, Nishimoto Y, Zeniya M. Effects of Thermo-mechanical Treatment on the Shape Memory Effect and the Pseudoelasticity of Ti-50.2Ni and Ti-47.5Ni-2.5Fe Alloys. Iron Steel Inst Japan 1986;72:571–8.

[105] Tan G, Liu Y, Sittner P, Saunders M. Lüders-like deformation associated with stress-induced martensitic transformation in NiTi. Scr Mater 2004;50:193–8.

doi:10.1016/j.scriptamat.2003.09.018.

[106] Wada K, Liu Y. Shape recovery of NiTi shape memory alloy under various pre-strain and constraint conditions. Smart Mater Struct 2005;14:S273–86. doi:10.1088/0964-1726/14/5/016.

[107] Miyazaki S, Imai T, Igo Y, Otsuka K. EFFECT OF CYCLIC DEFORMATION ON THE PSEUDOELASTICITY CHARACTERISTICS OF Ti-Ni ALLOYS. Metall Trans A, Phys Metall Mater Sci 1986;17 A:115–20.

[108] Saburi T, Yoshida M, Nenno S. Deformation behavior of shape memory Ti-Ni alloy crystals. Scr Metall 1984;18:363–6. doi:10.1016/0036-9748(84)90453-8.

[109] Liu Y, Favier D. Stabilisation of martensite due to shear deformation via variant reorientation in polycrystalline NiTi. Acta Mater 2000;48:3489–99. doi:10.1016/S1359-6454(00)00129-4.

[110] Liu Y, Tan GS. Effect of deformation by stress-induced martensitic transformation on the transformation behaviour of NiTi. Intermetallics 2000;8:67–75. doi:10.1016/S0966-9795(99)00079-5.

[111] Tan G, Liu Y. Comparative study of deformation-induced martensite stabilisation via martensite reorientation and stress-induced martensitic transformation in NiTi. Intermetallics 2004;12:373–81. doi:10.1016/j.intermet.2003.11.008.

[112] Wang S, Tsuchiya K, Wang L, Umemoto M. Martensitic stabilization and defects induced by deformation in TiNi shape memory alloys. Int J Miner Metall Mater 2011;18:66–9. doi:10.1007/s12613-011-0401-5.

[113] Delville R, Malard B, Pilch J, Sittner P, Schryvers D. Microstructure changes during non-conventional heat treatment of thin Ni-Ti wires by pulsed electric current studied by transmission electron microscopy. Acta Mater 2010;58:4503–15. doi:10.1016/j.actamat.2010.04.046.

[114] Sedmák P, Šittner P, Pilch J, Curfs C. Instability of cyclic superelastic deformation of NiTi investigated by synchrotron X-ray diffraction. Acta Mater 2015;94:257–70. doi:10.1016/j.actamat.2015.04.039.

[115] Scherngell H, Kneissl A. Influence of the microstructure on the stability of the intrinsic two-way shape memory effect. Mater Sci Eng A 1999;273-275:400–3. doi:10.1016/S0921-5093(99)00306-8.

[116] Teng T-L, Lin C-C. Effect of welding conditions on residual stresses due to butt welds. Int J Press Vessel Pip 1998;75:857–64. doi:10.1016/S0308-0161(98)00084-2.

[117] Rahman Chukkan J, Vasudevan M, Muthukumaran S, Ravi Kumar R, Chandrasekhar N. Simulation of laser butt welding of AISI 316L stainless steel sheet using various heat sources and experimental validation. J Mater Process Technol 2015;219:48–59. doi:10.1016/j.jmatprotec.2014.12.008.

[118] Deng D, Murakawa H, Liang W. Numerical and experimental investigations on welding residual stress in multi-pass butt-welded austenitic stainless steel pipe. Comput Mater Sci 2008;42:234–44. doi:10.1016/j.commatsci.2007.07.009.

[119] Lienert A, Siewert T, Babu S, Acoff V. ASM handbook, Volume 6A, Welding Fundamentals

and Processes. 1st ed. Ohio: ASM International; 2011.

[120] Coelho RS, Corpas M, Moreto JA, Jahn A, Standfuß J, Kaysser-Pyzalla A, et al. Induction-assisted laser beam welding of a thermomechanically rolled HSLA S500MC steel: A microstructure and residual stress assessment. Mater Sci Eng A 2013;578:125–33. doi:10.1016/j.msea.2013.04.039.

[121] Akbari D, Sattari-Far I. Effect of the welding heat input on residual stresses in butt-welds of dissimilar pipe joints. Int J Press Vessel Pip 2009;86:769–76. doi:10.1016/j.ijpvp.2009.07.005.

[122] Qiu S, Krishnan VB, Padula SA, Noebe RD, Brown DW, Clausen B, et al. Measurement of the lattice plane strain and phase fraction evolution during heating and cooling in shape memory NiTi. Appl Phys Lett 2009;95:95–8. doi:10.1063/1.3245308.

[123] Shaw JA. Simulations of localized thermo-mechanical behavior in a NiTi shape memory alloy. Int J Plast 2000;16:541–62. doi:Doi 10.1016/S0749-6419(99)00075-3.

[124] Ezugwu EO, Da Silva RB, Bonney J, MacHado Á R. Evaluation of the performance of CBN tools when turning Ti-6Al-4V alloy with high pressure coolant supplies. Int J Mach Tools Manuf 2005;45:1009–14. doi:10.1016/j.ijmachtools.2004.11.027.

[125] Zhang R, Acoff VL. Processing sheet materials by accumulative roll bonding and reaction annealing from Ti/Al/Nb elemental foils. Mater Sci Eng A 2007;463:67–73. doi:10.1016/j.msea.2006.06.144.

[126] Grummon DS, Low K-B, Foltz J, Shaw J a. A New Method for Brazing Nitinol Based on the Quasibinary TiNi-Nb System. 48th AIAA/ASME/ASCE/AHS/ASC Struct. Struct. Dyn. Mater. Conf., 2007, p. 1–7.

[127] Kwo J, Hong M, Nakahara S. Growth of rare-earth single crystals by molecular beam epitaxy: The epitaxial relationship between hcp rare earth and bcc niobium. Appl Phys Lett 1986;49:319–21. doi:10.1063/1.97155.

[128] Heidelbach F, Riekel C, Wenk H-R. Quantitative texture analysis of small domains with synchrotron radiation X-rays. J Appl Crystallogr 1999;32:841–9. doi:10.1107/S0021889899004999.

[129] Glebovsky V, Straumal B, Semenov V, Sursaeva V, Gust W. Grain Boundary Penetration of a Ni-Rich Melt in Tungsten Polycrystals. High Temp Mater Process 1995;14. doi:10.1515/HTMP.1995.14.2.67.

[130] Wang RR, Welsch GE. Joining Titanium Materials with Tungsten Inert-Gas Welding, Laser-Welding, and Infrared Brazing. J Prosthet Dent 1995;74:521–30.

[131] Li X, Xie J, Zhou Y. Effects of oxygen contamination in the argon shielding gas in laser welding of commercially pure titanium thin sheet. J Mater Sci 2005;40:3437–43. doi:10.1007/s10853-005-0447-8.

[132] Chaturvedi MC. Welding and Joining of Aerospace Materials. Cambridge: Woodhead Publishing Limited; 2012.

[133] Sutou Y, Koeda N, Omori T, Kainuma R, Ishida K. Effects of ageing on bainitic and thermally induced martensitic transformations in ductile Cu-Al-Mn-based shape memory alloys. Acta Mater 2009;57:5748–58. doi:10.1016/j.actamat.2009.08.003.

[134] Tuissi A, Besseghini S, Ranucci T, Squatrito F, Pozzi M. Effect of Nd-YAG laser welding on the functional properties of the Ni–49.6at.%Ti. Mater Sci Eng A 1999;273-275:813–7. doi:10.1016/S0921-5093(99)00422-0.

[135] Maletta C, Falvo A, Furgiuele F, Barbieri G, Brandizzi M. Fracture Behaviour of Nickel-Titanium Laser Welded Joints. J Mater Eng Perform 2009;18:569–74. doi:10.1007/s11665-009-9351-8.

[136] Khan MI, Panda SK, Zhou Y. Effects of Welding Parameters on the Mechanical Performance of Laser Welded Nitinol. Mater Trans 2008;49:2702–8. doi:10.2320/matertrans.MRA2008243.

[137] Vaidyanathan R, Bourke MAM, Dunand DC. Phase fraction, texture and strain evolution in superelastic NiTi and NiTi-TiC composites investigated by neutron diffraction. Acta Mater 1999;47:3353–66. doi:10.1016/S1359-6454(99)00214-1.

[138] Kato H, Ozu T, Hashimoto S, Miura S. Cyclic stress–strain response of superelastic Cu–Al–Mn alloy single crystals. Mater Sci Eng A 1999;264:245–53. doi:10.1016/S0921-5093(98)01095-8.

[139] Araki Y, Maekawa N, Shrestha KC, Yamakawa M, Koetaka Y, Omori T, et al. Feasibility of tension braces using Cu-Al-Mn superelastic alloy bars. Struct Control Heal Monit 2014;21:1304–15. doi:10.1002/stc.1644.

[140] Montecinos S, Cuniberti a., Sepúlveda a. Grain size and pseudoelastic behaviour of a Cu–Al–Be alloy. Mater Charact 2008;59:117–23. doi:10.1016/j.matchar.2006.11.009.

7 Appendices

7.1 Peer-review accepted for publications papers

7.1.1 On the Mechanisms for Martensite Formation in YAG Laser Welded Austenitic NiTi,

This paper was submitted and accepted in Shape Memory and Superelasticity.

Shap. Mem. Superelasticity
DOI 10.1007/s40830-016-0058-z

On the Mechanisms for Martensite Formation in YAG Laser Welded Austenitic NiTi

J. P. Oliveira[1] · F. M. Braz Fernandes[1] · R. M. Miranda[2] · N. Schell[3]

Abstract Extensive work has been reported on the microstructure of laser-welded NiTi alloys either superelastic or with shape memory effect, motivated by the fact that the microstructure affects the functional properties. However, some effects of laser beam/material interaction with these alloys have not yet been discussed. This paper aims to discuss the mechanisms for the occurrence of martensite in the heat-affected zone and in the fusion zone at room temperature, while the base material is fully austenitic. For this purpose, synchrotron radiation was used together with a simple thermal analytic mathematical model. Two distinct mechanisms are proposed for the presence of martensite in different zones of a weld, which affects the mechanical and functional behavior of a welded component.

Keywords NiTi · Laser welding · Synchrotron radiation · Martensite · X-ray diffraction · Precipitation phenomena · Ni_4Ti_3

✉ J. P. Oliveira
jp.oliveira@campus.fct.unl.pt

[1] CENIMAT/I3N, Departamento de Ciências dos Materiais, Faculdade de Ciências e Tecnologia, FCT, Universidade Nova de Lisboa, 2829-516 Caparica, Portugal

[2] UNIDEMI, Departamento de Engenharia Mecânica e Industrial, Faculdade de Ciências e Tecnologia, FCT, Universidade Nova de Lisboa, 2829-516 Caparica, Portugal

[3] Helmholtz-Zentrum Geesthacht, Institute of Materials Research, 21502 Geesthacht, Germany

Introduction

Ni–Ti shape memory alloys (SMAs) are known to exhibit superelasticity, shape memory effect, and biocompatibility, which make them a good candidate for several types of applications [1]. Due to the low formability of these alloys, a suitable joining technique must be used to obtain devices and components with complex geometries [2].

Laser welding of these SMAs is being studied in the last years in order to fully understand the effects of this joining technique on the microstructure and functional properties of these materials.

Literature can be found about the microstructure [3–5] and the effects of laser welding on the functional properties of the joints [2, 6–8]. However, some consequences of the interaction between the laser beam and these materials were not yet fully discussed despite the effects observed and reported. One of those effects is the existence of a different phase from the base material at room temperature in the heat-affected zone (HAZ) and in the fusion zone (FZ) after the welding.

It is a well-known fact that, in Ni–Ti SMAs, the transformation temperatures are composition dependent. A minor change in its composition significantly modifies the transformation temperatures of these materials [1]. In particular, for a Ni-rich alloy, a depletion in Ni causes a significant raise on the transformation temperatures, while for Ti-rich alloys, an enrichment in Ni does not significantly change these temperatures.

In this work it was observed that the base material was fully austenitic at room temperature and the heat-affected zone and fusion zone had both martensite and austenite after welding. Understanding the cause for this microstructural change is of great importance as it brings significant changes in the mechanical behavior of the welded NiTi joints.

Published online: 04 March 2016

A change in the transformation temperatures in the laser welding region has been reported in other works [2, 7, 9, 10]. More recently, Khan et al. [11] have studied the laser processing of a NiTi shape memory alloy that was austenitic at room temperature, in order to obtain, in a controlled manner, an increase of the transformation temperatures that they related to the differential volatilization of Ni and Ti from the liquid pool. This way, the authors were able, depending on the process parameters, to obtain martensite at room temperature in the laser-processed region. The same reasoning may be applied to laser welding. But, in our study, we have identified two different mechanisms operating in different regions of the weld: differential volatilization of Ni and Ti in the fusion zone and Ni_4Ti_3 precipitation in the heat-affected zone.

The small dimensions of the HAZ and FZ, characteristic of laser welding, make it difficult to ensure that only one or the other region is being analyzed by DSC, even when using precision cutting for the sample preparation, as it is recognized by other authors [7, 9, 12].

So, in the present work, synchrotron radiation was used for a detailed microstructural analysis along the weld, in parallel with a simple thermal model based on the work of Rosenthal [13] that was used to estimate the thermal cycle during laser welding.

Experimental Procedure

Near-equiatomic (50.8 at % Ni) Ni–Ti plates, 1.0 mm thick, supplied in the condition of flat annealed, were butt-welded with a Nd:YAG laser source from Rofin-Sinar, operating in continuous wave mode. The samples to be welded were positioned, so that the weld was performed perpendicular to the base material rolling direction. Helium and Argon were used to create an inert atmosphere in the weld area, both on the top and on the weld root. Table 1 summarizes the welding parameters used. The welding parameters were chosen in order to produce sound welds, thus the heat input necessary has a small admissible range. Though it is known that an increase in the heat input originates lower cooling rates, this effect is negligible for the range of heat inputs tested.

Differential Scanning Calorimetry (DSC) was used to characterize the structural transformation temperatures of the base material. Liquid nitrogen was used to cool down the system to −160 °C. Upon heating, the maximum temperature was of about 70 °C. The cooling and heating rates were set at 10 °C/min.

X-Ray Diffraction was performed at HEMS—High Energy Materials Science beamline (PETRA III, DESY, Hamburg, Germany). It used a wavelength of 0.1426 Å (87 keV). A 2D detector was used and the tests were held at room temperature (21 °C). Several scans were recorded starting in the base material, passing through the heat-affected zone and the fusion zone and finishing again in the base material. A length of approximately 6.0 mm was analyzed, with the weld center line positioned at half distance, in steps of 0.1 mm. The beam spot was of 0.2 × 0.2 mm and the exposure time was kept between 5 and 10 s. A post-weld heat treatment was performed on sample A for 60 min at 450 °C in order to induce precipitation phenomena. The structural characterization by synchrotron X-ray diffraction of this sample was also performed.

Results and Discussion

Phase transformation temperatures measured by DSC in the base material revealed, upon cooling, the existence of two exothermic peaks indicating a two-step transformation from austenite to R-phase and, later, to martensite. Upon heating, only one endothermic peak is observed corresponding to the transformation of martensite into austenite (Fig. 1).

Three X-ray diffractograms corresponding to the base material, heat-affected zone, and fusion zone of sample B, at room temperature, are depicted in Fig. 2. For an interplanar distance, d, ranging from 1.90 to 2.45 Å, where the most relevant peaks of the NiTi system can be found, there is a clear distinction between the base material, the heat-affected zone, and the fusion zone. The base material is fully austenitic, but in the heat-affected zone and the fusion zone extra martensite peaks are detected, while the austenite peak still remains.

Explaining the mechanisms that lead to the presence of the observed microstructure, namely the martensitic phase, in the heat-affected zone and in the fusion zone, while the base material is fully austenitic, is the focus of this work.

As the mechanisms that explain the existence of martensite in the heat-affected zone and in the fusion zone

Table 1 Welding parameters of the analyzed samples

Sample reference	Power (W)	Welding speed (mm/s)	Heat input (J/cm)	Focused beam diameter (mm)
A	990	20	495	0.45
B	1485	25	594	

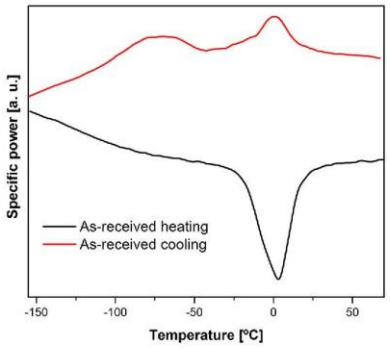

Fig. 1 Differential scanning calorimetry measurements of the base material

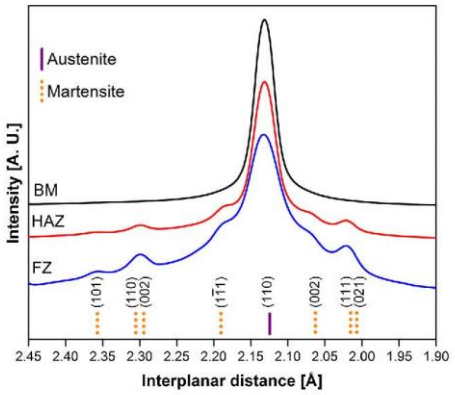

Fig. 2 Diffractograms of base material (BM), heat-affected zone (HAZ), and fusion zone (FZ) of sample B

are different, the subsequent analysis is divided in order to analyze each region separately.

Existence of Martensite in the Heat-Affected Zone

Since martensite was observed in both samples (as observed in Fig. 2 for sample B), results and discussion will be presented for sample A. In fact, the variation of structural modifications due to the weld thermal cycle is similar in both samples, as well as the formation mechanisms of martensite in the heat-affected zone.

Overlaying, in a continuous way, the diffractograms of sample A (Fig. 3), aside from the presence of martensite peaks in the heat-affected zone and fusion zone with a minor decrease in the austenite peak intensity, a broad peak can be noticed on the right-hand side of the (110) austenite peak in the strip of powder patterns corresponding to the heat-affected zone. This feature is marked with an arrow in Fig. 3. Martensite peaks are expected to occur in the neighborhood of the (110) austenite peak, meaning that the existence of martensite in the heat-affected zone can originate this singularity. Aside from martensite, for interplanar spacings near the (110) austenite peak, precipitates, such as Ni_4Ti_3, are also expected to occur.

Sample A was heated up to 150 °C and in situ x-ray diffraction was performed in a similar way as shown in Fig. 3. The reason for this approach is that 150 °C is well above the A_f temperature of the base material, so any remaining martensite, in the heat-affected zone and in the fusion zone, will transform to austenite. However, that temperature is not enough to dissolve any precipitates that can be formed in the Ni–Ti system, meaning that if the broad peak is not present at 150 °C, than it can be assigned to martensite. Otherwise it must be assigned to a given precipitate.

Figure 4 depicts a superposition of the diffractograms of the sample A heated at 150 °C. The martensite peaks have completely disappeared, while the broad peak on the right-hand side of the austenite peak is still present (marked with an arrow). The only possibility to explain the observed feature is by the occurrence of precipitation phenomena in the heat-affected zone.

For Ni-rich NiTi shape memory alloys, precipitation of Ni_4Ti_3, Ni_3Ti_2, and Ni_3Ti may occur. Ni_4Ti_3 and Ni_3Ti_2 are metastable precipitates [14, 15] while Ni_3Ti is the equilibrium precipitate [1]. It is also known that Ni_4Ti_3 precipitation is the first to occur and happens for lower temperatures and shorter permanence times, when compared to Ni_3Ti_2 and Ni_3Ti.

A detailed TTT diagram for NiTi SMAs was presented by Nishida et al. [16]. Recently, Pelton et al. [17] published another TTT diagram for NiTi SMAs but with short times for the onset of the precipitation phenomena. Pelton et al. tested a NiTi SMA with the same composition as the base material of the samples used in this study. From both TTT diagrams it is possible to infer that Ni_4Ti_3 precipitation may occur in small time scale (a few seconds). In Pelton's diagram it is depicted more clearly that Ni_4Ti_3 precipitation may occur while crossing the temperature range of 350 to 500 °C in a short elapsed time, of a couple of seconds.

Modeling of Temperatures and Permanence Times for Precipitation in the Heat-Affected Zone

To simulate the temperature gradient in the material due to the welding operation, the simple 2D solution from the Rosenthal equation (Eq. 1) was employed. It can be used in

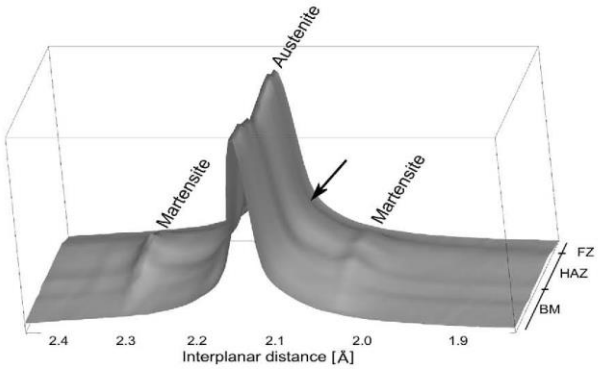

Fig. 3 Superposition of the diffractograms of sample A, at room temperature

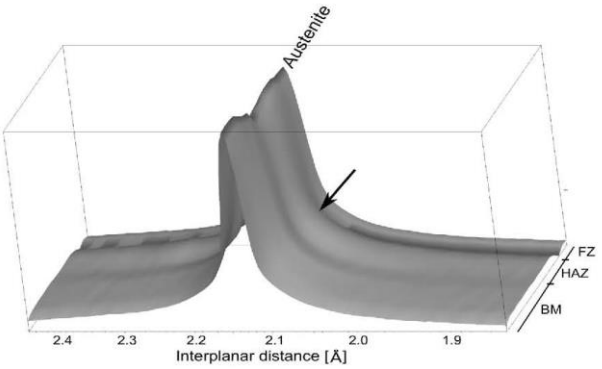

Fig. 4 Superposition of the diffractograms of sample A, at 150 °C

the situation of the single-pass welding in thin materials or for a full penetration keyhole weld [18]. The temperature is given by Eq. 1:

$$T - T_0 = \frac{Q}{2\pi kg} e^{(v\,x/2\alpha)} K0\left[\frac{v\,R}{2\alpha}\right], \quad (1)$$

where T, is a given temperature for point in the (x,y) space, in K; T_0, is the room temperature, in K; Q, is the heat input in W; k, is the thermal conductivity, in W m^{-1} K^{-1}; g, is the plate thickness, in m; v, is the welding speed, in m s^{-1}; α, is the thermal diffusivity, in m^2 s^{-1}; K0, is a modified Bessel function of the second kind and zero order; R, is the radial distance $\left(R = \sqrt{x^2 + y^2}\right)$, in m.

The reference system used for calculating the temperature gradient is depicted in Fig. 5, where the laser spot advances in the negative direction of the x-axis.

The temperatures reached for sample A, in the heat-affected zone, computed from Eq. 1 with the welding parameters tested, and the physical properties of NiTi, are depicted in Fig. 6. According to this equation, the time, in seconds, that the material takes to cross the temperature range from 350 to 500 °C is within the time interval of Pelton et al. experiments (see Fig. 7). Due to the laser welding characteristics, the holding time at temperatures where precipitation can occur is within the magnitude of a few seconds.

As a consequence of Ni_4Ti_3 being a minority phase, its intensity in the diffractograms is expected to be very low. Aside from that aspect, the most intense peak for this precipitate, according to 39-1113 JCPDF card, occurs for an interplanar spacing of 2.092 Å, very close to the austenite peak and therefore can be partially overlapped by its tail. All other peaks have a maximum intensity ranging

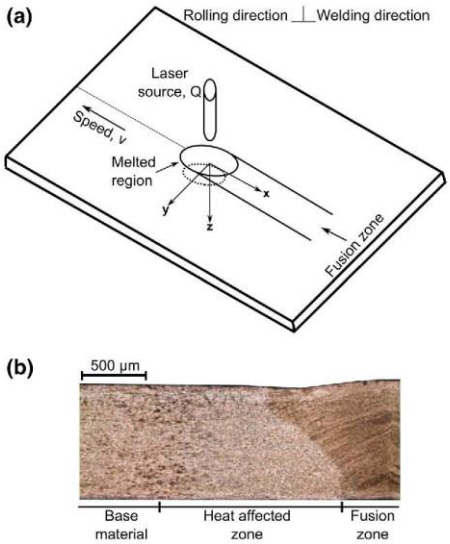

Fig. 5 **a** Reference system used to determine the temperature gradient in the joint (Adapted from [13]). **b** Macrograph of a NiTi laser-welded joint

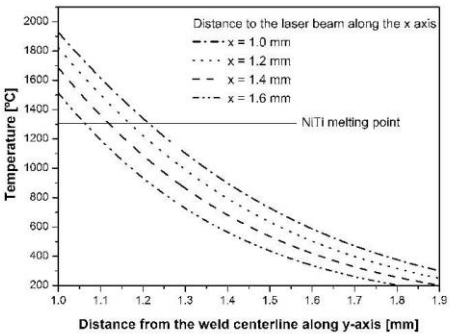

Fig. 6 Evolution of the surface temperature as a function of the distance to the weld beam along the y-axis, for sample A

from 15 to 30 %. For this reason, a post-weld heat treatment at a temperature of 450 °C, during 60 min, was performed. The objective of the post-weld heat treatment is to induce a more significant Ni_4Ti_3 precipitation so that more peaks of this precipitate can be observed. After a longer period in the temperature range for Ni_4Ti_3 precipitation occur, these precipitates are clearer in the X-ray diffraction patterns, as their intensity is higher due to a

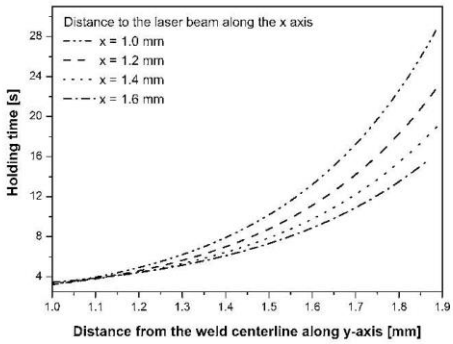

Fig. 7 Holding time, in the heat-affected zone, at an interval temperature of 350–500 °C where Ni_4Ti_3 precipitation may occur, for sample A

higher fraction in the analyzed region. Also, their appearance should be consistent with the positions identified in the heat-affected zone of the as-welded material, giving then a clear indication that these precipitates were well indexed.

Figure 8a, c depict the diffractograms of the heat-affected zone of the as-welded sample A, at RT and 150 °C. Both martensite and austenite can be clearly observed at room temperature, but at 150 °C very narrow Ni_4Ti_3 peaks can be depicted, aside from the austenite peak. After the heat treatment, R-phase can be observed at room temperature, as well as austenite and martensite. The diffractograms of the sample at room temperature and at 150 °C (to avoid the presence of any martensite or R-phase peaks), after the post-welding heat treatment at 450 °C for 60 min, are depicted in Fig. 8b, d, respectively. The broad peak in the neighborhood of the (110) austenite peak is still visible and three extra peaks corresponding to Ni_4Ti_3 are again observed. All these three peaks were indexed using the same 39-1113 JCPDF card corresponding to Ni_4Ti_3. As it can be depicted, the Ni_4Ti_3 peaks located on the left-hand side of the austenite peak have very low intensity after the heat treatment. So, the fact that they have very low intensity, for the X-ray diffraction analysis performed at 150 °C, is understandable as the permanence time in the temperature range from 350 to 500 °C during cooling, after welding, is not sufficient for a massive/significant precipitation phenomena to occur.

Due to the occurrence of Ni-rich precipitates, in this case Ni_4Ti_3, there is a Ni depletion in the surrounding matrix [19]. This Ni depletion raises the transformation temperatures. This local composition variation on the matrix allows martensite to be formed at room temperature. As no changes in the diffraction patterns were observed, at

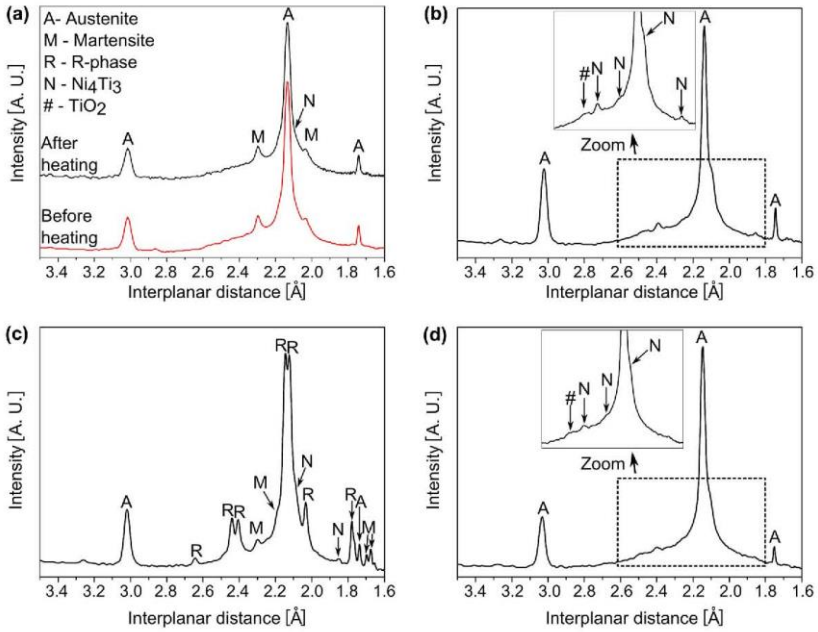

Fig. 8 Diffractograms of the heat-affected zone: **a** at room temperature (before and after heating up to 150 °C), as-welded; **b** at 150 °C, as-welded; **c** at room temperature, after post-weld heat treatment at 450 °C for 60 min; **d** at 150 °C after post-weld heat treatment at 450 °C for 60 min

room temperature, before and after heating to 150 °C it can be concluded that the observed martensite is not due to thermal stresses from welding.

Existence of Martensite in the Fusion Zone

The fusion zone, as depicted in Figs. 3 and 4, also exhibits a martensitic phase. Hyungson et al. [20] state that, within the keyhole, the temperature may exceed the boiling point of the material, which causes an intense evaporation. At those temperatures, Ni and Ti volatilization can occur. Considering Fig. 9, the vapor pressure of Ni is about two times higher than that of Ti. For this reason, in case of evaporation, a Ni depletion occurs in the fusion zone. Figure 9 was made taking into consideration the equation $\log p = -\frac{A}{T} + B + C \log T$, for temperatures above the melting temperature (T_m) of Ni and Ti, where p is the vapor pressure (in Pa), T is the temperature (in K), and A, B, and C are constants (given in Table 2) [21].

Despite the presence of a shielding gas to prevent oxidation, evaporation of elements with high pressure vapor can occur during welding. Though these losses are very small they can be sufficient to locally change the chemical composition in the fusion zone. Due to different vapor pressures of Ti and Ni, a Ti enrichment is expected which

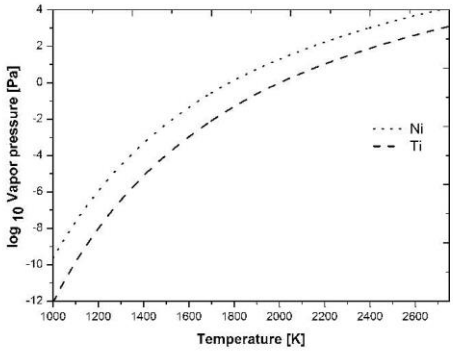

Fig. 9 Vapor pressure as a function of temperature for Ni and Ti

Table 2 Constant parameters for calculating the vapor pressure of Ni and Ti [21]

Temperature range	Element	Constant values		
		A	B	C
Above T_m	Ni	22,400	16.95	−2.01
	Ti	23,200	11.74	−0.66

is consistent with the existence of martensite at room temperature after welding as shown by our X-ray diffraction results.

Conclusions

The mechanisms responsible for the existence of martensite at room temperature after laser welding of austenitic NiTi were discussed using a detailed X-ray diffraction analysis.

Two different mechanisms were identified. Besides the preferential volatilization of the Ni, which had been identified as responsible for the increase of the transformation temperatures in the fusion zone, it was also possible to identify a precipitation mechanism in the heat-affected zone as giving rise to the occurrence of martensite at room temperature. In both cases the compositional variation of the matrix greatly changes the transformation temperatures when compared to the base material.

Despite the existence of martensite in the heat-affected zone and in the fusion zone at room temperature after welding, austenite is still present. This change in the existing phases of laser-welded joints may be of great importance to understand the mechanical behavior of a welded component.

Acknowledgments JPO and FBF acknowledge funding by FEDER funds through the COMPETE 2020 Programme and National Funds through FCT—Portuguese Foundation for Science and Technology under the project UID/CTM/50025/2013. RMM acknowledges UID/EMS/00667/2013. JPO acknowledges FCT/MCTES for funding PhD Grant SFRH/BD/85047/2012. The authors acknowledge DESY and HZG for beamtime and travel reimbursement under proposal I-20120563 EC FP7/2007-2013 Grant agreement no. 312284. The authors acknowledge the helpful discussion with Professor Yinong Liu from the University of Western Australia.

References

1. Otsuka K, Ren X (2005) Physical metallurgy of Ti-Ni shape memory alloys. Prog Mater Sci 50:511–678
2. Falvo A, Furgiuele FM, Maletta C (2005) Laser welding of a NiTi alloy: mechanical and shape memory behavior. Mater Sci Eng, A 412:235–240
3. Sevilla P, Martorell F, Libenson C, Planell JA, Gil FJ (2008) Laser welding of NiTi orthodontic archwires for selective force application. J Mater Sci Mater Med 19:525–529
4. Gugel H, Schuermann A, Theisen W (2008) Laser welding of NiTi wires. Mater Sci Eng, A 481–482:668–671
5. Chen Y, Ke L, Liu Y, Xu S (2010) Laser butt welding of TiNi shape memory alloy sheet. Adv Mater Res 97–101:3936–3939
6. Falvo A, Furgiuele FM, Maletta C (2006) Functional behaviour of a NiTi-welded joint: two-way shape memory effect. Mater Sci Eng, A 481–482:647–650
7. Khan M, Zhou Y (2010) Effects of local phase conversion on the tensile loading of pulsed Nd:YAG laser processed Nitinol. Mater Sci Eng, A 527:6235–6238
8. Oliveira JP, Braz Fernandes FM, Schell N, Miranda RM (2015) Shape memory effect of laser welded NiTi plates. Funct Mater Lett 8(6), 1550069
9. Tuissi A, Besseghini S, Ranucci T, Squatrito F, Pozzi M (1999) Effect of Nd-YAG laser welding on the functional properties of the Ni–49.6at.%Ti. Mater Sci Eng, A 273–275:813–817
10. Hsu YT, Wang YR, Wu SK, Chen C (2001) Effect of CO_2 laser welding on the shape-memory and corrosion characteristics of TiNi alloys. Metall Mater Trans A 32A:569–576
11. Khan MI, Pequegnat A, Zhou YN (2013) Multiple memory shape memory alloys. Adv Eng Mater 15:386–393
12. Song YG, Li WS, Li L, Zheng YF (2008) The influence of laser welding parameters on the microstructure and mechanical property of the as-jointed NiTi alloy wires. Mater Lett 62:2325–2328
13. Kou S (2003) Welding metallurgy. Wiley Interscience
14. Ke C, Cao S, Ma X, Zhang X (2012) Modeling of Ni4Ti3 precipitation during stress-free and stress-assisted aging of bi-crystalline NiTi shape memory alloys. Trans Nonferrous Metals Soc China 22:2578–2585
15. Otsuka K, Ren X (1999) Recent developments in the research of shape memory alloys. Intermetallics 7:511–528
16. Nishida M, Wayman CM, Honma T (1986) Precipitation processes in near-equiatomic TiNi shape memory alloys. Metall Trans A 17A:1505–1515
17. Pelton AR, DiCello J, Miyazaki S (2000) Optimisation of processing and properties of medical grade Nitinol wire. Minim Invasive Ther Allied Technol 9:107–118
18. Steen W, Mazumder J (2010) Laser material processing. Springer
19. Neves F, Cunha A, Martins I, Correia JB, Oliveira M, Gaffet E (2008) Ni4Ti3 precipitation during ageing of MARES NiTi shape memory alloys studied by FEG-SEM. Microsc Microanal 14:13–16
20. Hyungson K, Mohanty P, Mazumder J (2002) Modeling of laser keyhole welding: part II. simulation of keyhole evolution, velocity, temperature profile, and experimental verification. Metall Mater Trans A 33A:1831–1842
21. Gale WF, Totemeir TC (2004) Smithells metals reference book. Elsevier

7.1.2 High Strain and Long Duration Cycling Behavior of Laser Welded NiTi Sheets

This paper was submitted and accepted in International Journal of Fatigue.

International Journal of Fatigue 83 (2016) 195–200

Contents lists available at ScienceDirect

International Journal of Fatigue

journal homepage: www.elsevier.com/locate/ijfatigue

High strain and long duration cycling behavior of laser welded NiTi sheets

J.P. Oliveira [a,*], R.M. Miranda [b], N. Schell [c], F.M. Braz Fernandes [a]

[a] CENIMAT/i3N, Faculdade de Ciências e Tecnologia, Universidade Nova de Lisboa, Portugal
[b] UNIDEMI, Faculdade de Ciências e Tecnologia, Universidade Nova de Lisboa, Portugal
[c] Institute of Materials Research, Helmholtz-Zentrum Geesthacht, Max-Planck-Str. 1, D-21502 Geesthacht, Germany

ARTICLE INFO

Article history:
Received 10 August 2015
Received in revised form 30 September 2015
Accepted 8 October 2015
Available online 22 October 2015

Keywords:
NiTi
Shape memory alloys
Laser welding
High strain cycling
Superelasticity

ABSTRACT

The use of NiTi in complex shaped components for structural applications is limited by the material cost and machinability and adequate joining techniques have been investigated to minimize the thermal cycle effect on the superelastic and shape memory effects exhibited by NiTi. Laser welding is the most used joining process for this material. However, existing studies mainly address the functional properties of laser welded NiTi wires, and the superelastic cycling tests are limited to either a low number of cycles (maximum 100) or to low strains (below 6%). This paper discusses the results of the cycling behavior exhibited by laser butt welded 1 mm thick NiTi plates, when tested to high strains (up to 10%) and for a large number of cycles (600). The superelastic effect was observed and the microstructural changes induced by the laser welding procedure, namely the extension of the thermal affected regions, were seen to influence the evolution of the accumulated irrecoverable strain. Thus, it is possible, by controlling the heat input introduced during welding, to tune the maximum superelastic recovery presented by NiTi laser welds.

1. Introduction

In the past years we have seen an increasing use of NiTi shape memory alloys in applications, such as: biomedical [1], automotive [2] and aerospace [3]. Some of these applications require the use of complex shapes, which are not easy to obtain due to the difficult machinability of NiTi. For this, intensive research has been devoted to join NiTi aiming to minimize thermal effects of welding on the material functional properties, that is: shape memory effect and superelasticity.

Amongst the welding processes studied, laser welding is the most used since the laser beam can be focused into a small spot diameter, reducing the extension of the fusion and the heat affected zones. As upon sequence, the welded NiTi joints exhibit mechanical properties below those of the as-received material, namely lower ultimate tensile strength and elongation to fracture.

Understanding the influence of laser welding on the functional fatigue (as defined by Eggeler et al. [4]) in terms of the shape memory effect or superelasticity, is of major importance. The effect of laser welding on the functional properties of NiTi joints was studied by several authors [5–10] and it is, nowadays, well established that the welding thermal cycle, originates a microstructural gradient from the fusion zone toward the base material with coarse grains in the molten and solidified region.

The shape memory effect was seen to be preserved in the fusion and heat affected zones after welding [10], even if there is a change in the transformation temperatures of these regions when compared to the base material.

Superelasticity of the welded NiTi joints has also been studied, but for a low number of cycles and at low strains [9,11,12]. Up to now the maximum cyclic deformation imposed to a laser welded NiTi joint was 8% for a total of 10 cycles and with a low strain-rate [12] which is known to affect, for example, the superelastic recovery upon unloading of NiTi [13,14]. Chan et al. studied the fatigue behavior of laser welded NiTi wires in small strain cyclic bending tests [15]. Previously, Chan et al. [16] analyzed the effect of post-weld heat treatments on the cyclic behavior of laser welded NiTi wires by testing samples up to a maximum of 100 cycles at a maximum imposed strain of 4%.

Additionally, most of the existing studies focus on the analysis of the effect of laser welding on NiTi thin sheets or wires (below 0.5 mm in thickness/diameter) [12,15–19]. Studies on the superelastic effect presented after laser welding of NiTi is scarce for sheets with more than 0.5 mm thickness [9,20]. Vieira et al. [9] studied the superelastic behavior of laser welded NiTi sheets by

* Corresponding author.
E-mail address: jp.oliveira@campus.fct.unl.pt (J.P. Oliveira).

http://dx.doi.org/10.1016/j.ijfatigue.2015.10.013
0142-1123/

analyzing the mechanical behavior of the welds at a 6% strain during 30 cycles. Hsu et al. [20] applied a total of 50 cycles up to 3% strain to 2 mm thick NiTi plates welded by laser.

While thin wires are mostly used for biomedical and microelectromechanical systems, sheets or large diameter wires are often required for structural applications. Thus, the analysis of the cyclic behavior in more severe conditions (high applied strains and/or high number of cycles) is required to understand the feasibility of the use of laser welded NiTi in such structures. That is, concerning the superelasticity of laser welded NiTi, there is an area that was not yet addressed: the study of the behavior of welded joints when cycled at high strains and for a high number of cycles.

The authors have previously studied the effect of laser welding parameters on one of the functional characteristics: the shape memory effect of laser welded NiTi plates [10]. The present paper presents a study performed to assess the functional fatigue in terms of the superelastic behavior of laser butt joints in NiTi plates at high strains (up to 10%) and for 600 cycles. A structural analysis by X-ray diffraction supports the discussion of the superelastic behavior observed in the welds. This will open up the possibility of designing and manufacturing complex shaped structural devices using fusion welding by laser.

2. Experimental procedure

NiTi plates, with a nominal composition of 50.8 at.% Ni–49.2 at.% Ti, supplied in the flat annealed condition, 1 mm thick, were used. Specimens were cut with a diamond wheel on a precision cut-off machine ATM Brilliant from as-received plates to 30 × 30 mm samples for butt welding. Surfaces to join were inspected and hand finished in order to ensure the best surface contact along all the joint length. Surface oxides were removed by chemical etching in a HF: HNO_3:H_2O solution with a dilution of 1:5:10.

A DY033 Nd:YAG laser power source from Rofin-Sinar, operating in a continuous wave mode, was used with a gas protection of Argon injected in a special chamber built *in situ*. Table 1 summarizes welding speed and laser power selected to verify the influence of the welding parameters on the mechanical properties. The beam was focused to 0.45 mm diameter and the focal point position (FPP) was set on the upper surface. Butt welding was performed with zero gap between opposite plates.

A precision cutting machine was used to prepare the tensile specimens from the butt-welded NiTi plates with the following dimensions: length 60 mm, thickness 1 mm, width 3 mm (Fig. 1). All the mechanical tests were conducted at room temperature with an Autograph Shimadzu AG50kNG machine, using a load cell type SFL-50 kN AG. The cross-head displacement speed of 2 mm/min and an average gauge length of 30 mm were selected for the mechanical tests. Uniaxial tensile tests of similar laser welded butt joints in NiTi were performed with single loading until rupture. From the tensile tests, the ultimate tensile strength (UTS) and deformation to rupture were registered and those results were taken into account to fix the conditions for the cyclic loading tests using the same cross-head displacement speed (2 mm/min) and gauge length (30 mm) as before. Cycling tests were performed in the following sequence: stage 1: 60 cycles at 10% of strain; stage 2: 60 cycles at 8%; stage 3: 60 cycles at 10%; stage 4: 60 cycles at 8%; stage 5: 360 cycles at 10%.

Table 1
Welding parameters for butt joining 1 mm thick plates.

Power (W)	Welding speed (mm/s)	Heat input (J/cm)	Sample reference
990	25	396	A
990	20	495	B
990	15	660	C

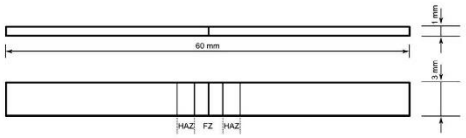

Fig. 1. Dimensions of the tensile specimens. The heat affected (HAZ) and fusion zones (FZ) are not to scale as they depend on the laser welding parameters.

Table 2
Strength and ductility parameters of the samples analyzed, obtained from tensile tests to rupture.

Sample reference	Ultimate tensile strength (MPa)	Elongation to fracture (%)
A	537	12.1
B	511	10.6
C	530	11.1

Structural analysis was performed on all samples in beamline P07 of Petra III/DESY using a wavelength of 0.1426 Å (87 keV). A length of about 6 mm was analyzed, starting in the base material, through the heat affected zone and the weld bead and finishing in the base material again. The distance between shots was of 200 μm and the beam dimensions were 200 × 100 μm.

The data acquired was treated using the program Fit2D [21], and it was possible to obtain the diffractograms in the different regions of the welds: base material, heat affected and fusion zones.

3. Results and discussion

Table 2 presents the strength and ductility parameters for the welded samples studied (Fig. 2). The NiTi base material had an UTS of 1530 MPa with an elongation to fracture of 20.1%. The superelastic plateau of the base material was at 350 MPa. All uniaxial-tensile tests until rupture of the laser welds fractured in the fusion zone.

The mechanical cycling tests for the welded samples A, B and C, are depicted in Fig. 3(a), (b) and (c), respectively. For all samples a selected set of load/unload cycles are shown. Sample A fractured at cycle number 303 in the base material due to a pre-existing defect in this region. So, the welding procedure did not have an influence on the fracture of this sample.

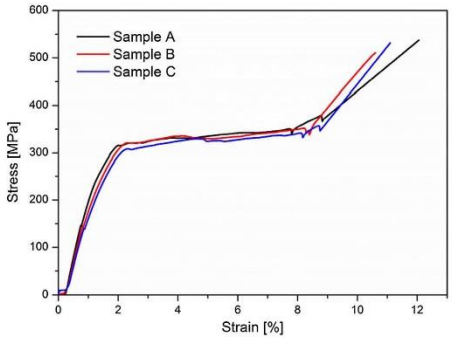

Fig. 2. Tensile tests of the analyzed laser welded NiTi samples.

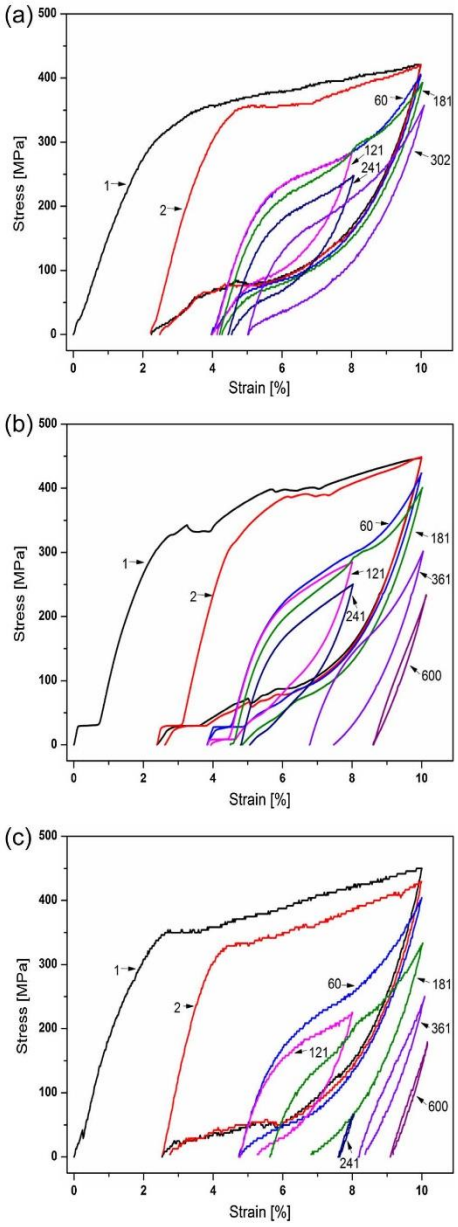

Fig. 3. Cycling tests for: (a) sample A; (b) sample B; (c) sample C.

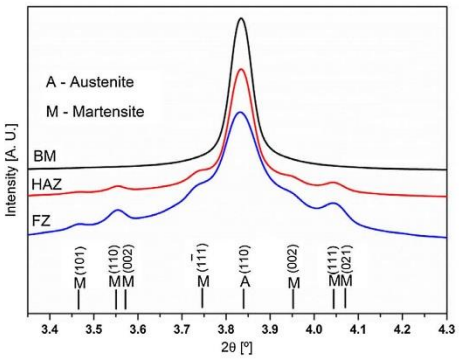

Fig. 4. Diffractograms of the base material (BM), heat affected zone (HAZ) and fusion zone (FZ) of sample B. For each identified phase, austenite (A) and martensite (M), the (*hkl*) family plane is evidenced.

It must be noticed the great resistance of the samples when subjected to load/unload cycling with very large alternating strains (8%/10%). In particular, samples B and C were seen to stand the entire programmed cycling test without breaking.

In all samples, the superelastic plateau on the first cycle occurs at about 350 MPa, similar to those of the base material. Also, samples B and C were cycled up to 600 times, at a stress level 110–130 MPa below their UTS, without rupture. In sample B a very small plateau at low stress was detected in the initial stage of the cycling protocol which is attributed to the presence of residual R-phase. However, with the prosecution of the cyclic solicitation, the R-phase transformation is suppressed.

In an ideal superelastic behavior, a complete strain recovery could be obtained in NiTi SMAs for strains up to 10% [22]. However, there are tests, as well as material parameters, that give raise to a non-complete ideal superelastic behavior. For example, the temperature at which the tests are performed, the strain rate imposed [13,23], the maximum strain [24], the effect of thermo-mechanical treatments [25] and the grain size [26] are all known to affect the superelastic behavior of NiTi.

Thus, a comprehensive structural characterization of the welds was performed by X-ray diffraction using synchrotron radiation in order to get a fine spatial resolution. This study revealed a mixed microstructure in the heat affected and in the fusion zones, with both martensite and austenite, present at room temperature. Fig. 4 shows three diffractograms from spots located at three different regions of the welded material in sample B (as an example). The base material is fully austenitic at room temperature. On the other hand, the heat affected zone and the fusion zone, have both martensite and austenite at room temperature; the extension of these regions may then be associated to the existence of the martensite peaks.

Fig. 5 depicts the 3D stacking of the diffractograms for the analyzed samples, showing the extent of each region. As expected, the extension of the heat affected and the fusion zones is related to the welding parameters: higher values of heat input (power to welding speed ratio) originate larger thermal affected regions.

The very large variations of the diffraction peaks intensities observed in some diffractograms is clearly a result of coarse grain size in the heat affected zone and fusion zone.

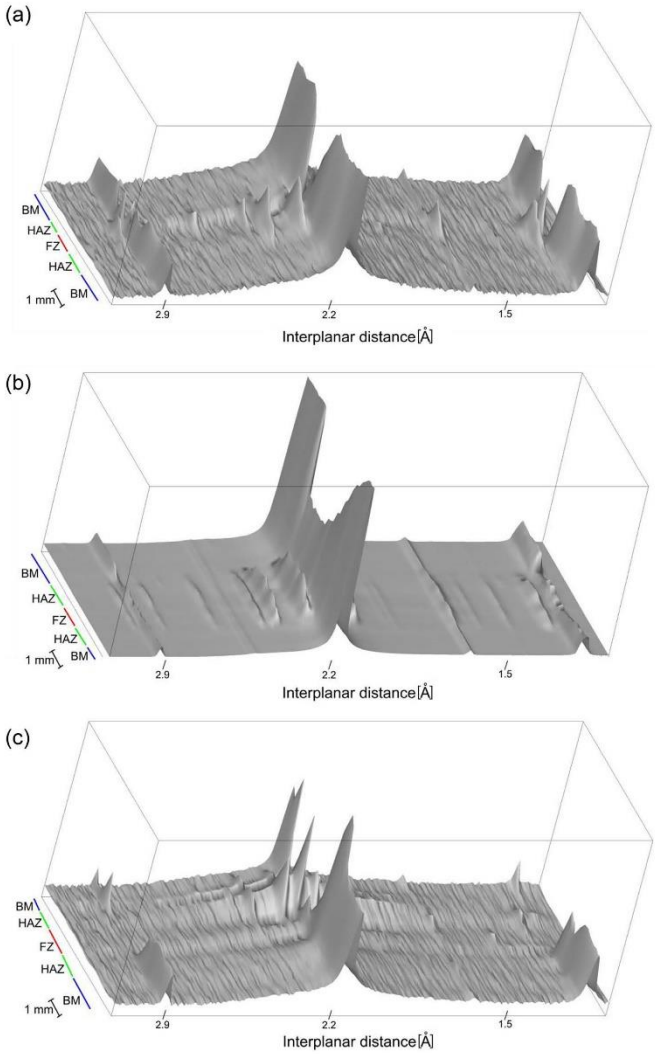

Fig. 5. Diffractograms of welded samples: (a) sample A; (b) sample B; (c) sample C. BM – Base material; HAZ – Heat affected zone; FZ – Fusion zone.

As the superelastic effect is dependent on the amount of austenite available to undergo the stress induced transformation, the presence of martensite at room temperature will have an implication on the functional behavior of the welded joints. It is expected that the superelastic recovery decreases with the increase in martensite fraction in the heat affected zone and in the fusion zone.

The presence of martensite in the heat affected zone and fusion zone of the welds brings particular features to the cyclic response of the tested materials. As the individual presence of each phase gives different contributions regarding the strain recovery upon unloading during cyclic solicitation, the presence of both phases in the welded material must be considered when analyzing the mechanical cycling tests.

It is well known that in the martensitic phase the cyclic behavior is heavily dependent on the applied strain [27,28]. In this phase, as soon as the plateau for the detwinning martensite is reached, an irrecoverable strain is expected to occur which should correspond

to the difference between the initial elastic deformation of martensite and the applied strain. However, as long as the applied stress is not enough to promote dislocation slip, a significant, if not total, recovery of the deformation can be achieved by heating the material above A_f, triggering the shape memory effect.

Tuissi et al. [5] suggested that the heat affected zone had a softening effect, lowering the stress level of the plateau in NiTi welds. Their tests were performed above the A_f temperature of the base material, but DSC analysis of the fusion zone revealed that, at testing temperatures, austenite was not yet completely transformed, having some martensite in this region. For this reason, the strain recovery of the welds was lower than that of the corresponding base material. However, the softening effect caused by the presence of martensite in the thermal affected region is evidenced in our laser welds by a significant decrease of the onset for the superelastic plateau, as the number of cycles increases.

In the present study, since there was a high strain applied to the welds, the martensite in the heat affected zone and in the fusion zone are detwinned and upon unloading a significant irrecoverable strain is observed.

The evolution of the accumulated irrecoverable strain with the number of cycles for each sample is shown in Fig. 6. It can be seen that a significant amount of accumulated irrecoverable strain occurs at the end of the first cycle of the load/unload protocol. This can be explained due to the presence of martensite in the heat affected zone and in the fusion zone of the laser welds. When compared to the reported literature on laser welding of NiTi wires, it is noticed that the accumulated irrecoverable strain is lower than in the results recorded in our plates. The main reason for this lies on the high strain applied which is considerably higher than the values reported by others [16,18,20] (ranging from 2.5% to 4% strain) and, thus, a higher irrecoverable strain is expected.

Load/unload tensile tests performed by Wada and Liu [28] on martensitic NiTi show that, for tests at 8% strain, the recoverable strain, upon unloading to zero stress, is about 1%, corresponding to the elastic deformation of martensite. Further deformation would result in dislocation slip. In our laser welds with the presence of martensite, aside from austenite, in both heat affected zone and fusion zone, the evolution of the accumulated irrecoverable strain for each sample can be explained as follows: for the sample with higher heat input, a higher amount of martensite is present, as it can be observed in the diffractograms of sample C in Fig. 5 (c). Thus, a higher irrecoverable strain will occur for this sample associated to the detwinning of the existing martensite, as well as some dislocation slip due to the high strain imposed. For the sample with lower heat input the irrecoverable strain tends to be, correspondingly, lower.

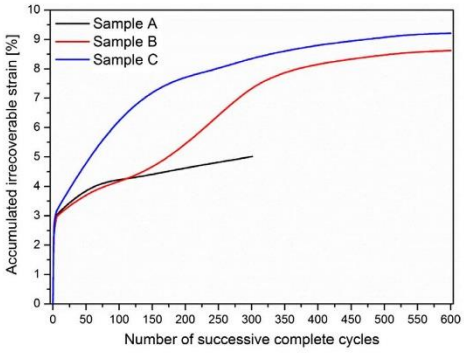

Fig. 6. Evolution of the accumulated irrecoverable strain with the number of cycles for each sample.

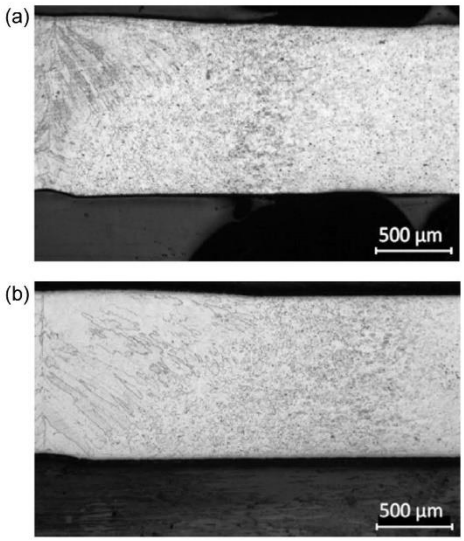

Fig. 7. Macrographs of: (a) sample A; and (b) sample C.

Miyazaki et al. [29] showed that, under superelastic cycling of NiTi, dislocations and other lattice defects are introduced during the stress induced transformation and tend to pile-up with increasing number of cycles, being responsible for the increase of the accumulated irrecoverable strain after each cycle. In our case, for the existing austenite in the welded material, it is reasonable to conclude that some of the increase in the accumulated irrecoverable strain is due to the introduction of dislocations during the stress induced transformation. These defects do not allow for the stress induced martensite to revert to austenite upon unloading, leading to a stabilization effect of martensite. This stabilized martensite does not participate in the subsequent superelastic transformation cycles as the number of cycles increases.

It is also observed that in stage 2 of the cycling tests performed (corresponding to the first set of 60 cycles at 8% strain) the superelastic plateau abruptly changed its slope as a result of the strain-hardening and the corresponding increased dislocation defects that resulted from the first set of 60 cycles at 10% strain. As the number of cycles continues, the accumulated irrecoverable strain increases up to a point where the stabilization plateau is reached, as depicted in Fig. 6 for samples B and C. The convergence to a stabilized value of the accumulated irrecoverable strain occurs almost at the same time for these two samples.

Another interesting feature that can be inferred from the mechanical tests of the welds is that all samples were mechanically tested for a significant number of cycles at stress values (110–130 MPa below) close to the ultimate tensile strength of the welds tested until rupture.

Grain size effects cannot also be neglected when looking at these results. In the fusion zone a coarse grain structure is found, as it can be seen in the macrographs of samples A and C, Fig. 7 (a) and (b), respectively. For NiTi shape memory alloys it is known that the larger the grain size, the lower the superelastic recovery is

[26]. That is, since the fusion zone and the heat affected zone have a coarser grain structure than the base material, they also contribute to the accumulated irrecoverable strain presented by the welded joint.

4. Conclusions

Mechanical behavior of laser welded superelastic NiTi plates was investigated by cyclic loading/unloading tests up to strains of 10% and 600 cycles.

This is the first study addressing mechanical cycling of welded plates at high strains and for a high number of cycles. The mechanical cycling of the laser joints was performed 110–130 MPa below the UTS of the welded joints.

It was observed that:

- The welding procedure affects the mechanical behavior of the welded plates; the higher the heat input, the more martensite is observed in the heat affected and fusion zone, and the higher the extension of these thermal affected regions.
- The extent of the heat affected zone and the fusion zone and, as a consequence, the existing martensite in these regions, affects the accumulated irrecoverable strain. The higher the extension of these regions (due to higher values of heat input), the higher the accumulated irrecoverable strain of the welds observed. Thus, a higher amount of martensite also corresponds to a higher amount of accumulated irrecoverable strain.
- Despite the presence of martensite in the heat affected zone and in the fusion zone, overall superelastic behavior of the welds was observed in all samples.
- Control of the process parameters (amount of heat input) needs to be taken into account in order to get the most adequate superelastic properties after welding. Lower heat input, thus with a lower extension of the heat affected zone and fusion zone, allows for a greater superelastic recovery, which is of significant importance for structural applications that require such functional property.

Acknowledgments

JPO and FBF acknowledge funding of CENIMAT/I3N by FEDER funds through the COMPETE 2020 Programme and National Funds through FCT – Portuguese Foundation for Science and Technology under the project UID/CTM/50025/2013. RMM acknowledges funding of UNIDEMI by FEDER funds through the COMPETE 2020 Programme and National Funds through FCT – Portuguese Foundation for Science and Technology under the project UID/EMS/00667/2013. The authors acknowledge DESY and HZG for beamtime and travel reimbursement under proposal I-20120563 EC FP7/2007-2013 grant agreement n° 312284. JPO acknowledges FCT/MCTES for funding PhD grant SFRH/BD/85047/2012.

References

[1] Es-Souni M, Es-Souni M, Fischer-Brandies H. Assessing the biocompatibility of NiTi shape memory alloys used for medical applications. Anal Bioanal Chem 2005;381(3):557–67. http://dx.doi.org/10.1007/s00216-004-2888-3.
[2] Strittmatter J, Clipa V, Gheorghita V, Gümpel P. Characterization of NiTi shape memory damping elements designed for automotive safety systems. J Mater Eng Perform 2014;23(7):2696–703. http://dx.doi.org/10.1007/s11665-014-1045-1.
[3] Chau ETF, Friend CM, Allen DM, Hora J, Webster JR. A technical and economic appraisal of shape memory alloys for aerospace applications. Mater Sci Eng, A 2006;438:589–92. http://dx.doi.org/10.1016/j.msea.2006.02.201.
[4] Eggeler G, Hornbogen E, Yawny A, Heckmann A, Wagner M. Structural and functional fatigue of NiTi shape memory alloys. Mater Sci Eng, A 2004;378(1):24–33. http://dx.doi.org/10.1016/j.msea.2003.10.327.
[5] Tuissi A, Besseghini S, Ranucci T, Squatrito F. Effect of Nd-YAG laser welding on the functional properties of the Ni–49.6 at.% Ti. Mater Sci Eng, A 1999;273–275:813–7. http://dx.doi.org/10.1016/S0921-5093(99)00422-0.
[6] Falvo A, Furgiuele F, Maletta C. Laser welding of a NiTi alloy: mechanical and shape memory behaviour. Mater Sci Eng, A 2005;412:235–40. http://dx.doi.org/10.1016/j.msea.2005.08.209.
[7] Yan XJ, Yang DZ, Liu XP. Influence of heat treatment on the fatigue life of a laser-welded NiTi alloy wire. Mater Charact 2007;58(3):262–6. http://dx.doi.org/10.1016/j.matchar.2006.05.001.
[8] Falvo A, Furgiuele F, Maletta C. Functional behaviour of a NiTi-welded joint: two-way shape memory effect. Mater Sci Eng, A 2008;481–482:647–50. http://dx.doi.org/10.1016/j.msea.2006.11.178.
[9] Vieira LA, Fernandes FMB, Miranda RM, Silva RJC, Quintino L, Cuesta A, et al. Mechanical behaviour of Nd:YAG laser welded superelastic NiTi. Mater Sci Eng, A 2011;528(16):5560–5. http://dx.doi.org/10.1016/j.msea.2011.03.089.
[10] Oliveira JP, Fernandes FMB, Schell N, Miranda RM. Shape memory effect of laser welded NiTi plates. Funct Mater Lett 2015;6:1550069. http://dx.doi.org/10.1142/S1793604715500691.
[11] Chan CW, Man HC, Yue TM. Effects of process parameters upon the shape memory and pseudo-elastic behaviors of laser-welded NiTi thin foil. Metall Mater Trans A 2011;42(8):2264–70. http://dx.doi.org/10.1007/s11661-011-0623-1.
[12] Mirshekari GR, Kermanpur A, Saatchi A, Sadrnezhaad SK, Soleymani AP. Microstructure, cyclic deformation and corrosion behavior of laser welded NiTi shape memory wires. J Mater Eng Perform 2015;24(9):3356–64. http://dx.doi.org/10.1007/s11665-015-1614-y.
[13] Nemat-Nasser S, Guo W. Superelastic and cyclic response of NiTi SMA at various strain rates and temperatures. Mech Mater 2006;38(5):463–74. http://dx.doi.org/10.1016/j.mechmat.2005.07.004.
[14] Dayananda GN, Rao MS. Effect of strain rate on properties of superelastic NiTi thin wires. Mater Sci Eng, A 2008;486(1):96–103. http://dx.doi.org/10.1016/j.msea.2007.09.006.
[15] Chan CW, Man HC, Cheng FT. Fatigue behavior of laser-welded NiTi wires in small-strain cyclic bending. Mater Sci Eng, A 2013;559:407–15. http://dx.doi.org/10.1016/j.msea.2012.08.119.
[16] Chan CW, Man HC, Yue TM. Effect of postweld heat treatment on the microstructure and cyclic deformation behavior of laser-welded NiTi-shape memory wires. Metall Mater Trans A 2012;43(6):1956–65. http://dx.doi.org/10.1007/s11661-011-1062-8.
[17] Yan XJ, Yang DZ, Qi M. Rotating–bending fatigue of a laser-welded superelastic NiTi alloy wire. Mater Charact 2006;57(1):58–63. http://dx.doi.org/10.1016/j.matchar.2005.12.009.
[18] Gugel H, Schuermann A, Theisen W. Laser welding of NiTi wires. Mater Sci Eng, A 2008;481:668–71. http://dx.doi.org/10.1016/j.msea.2006.11.179.
[19] Yan X, Ge Y. Influence of post-weld annealing on transformation behavior and mechanical properties of laser-welded NiTi alloy wires. J Mater Eng Perform 2014;23(10):3474–9. http://dx.doi.org/10.1007/s11665-014-1156-8.
[20] Hsu Y, Wang Y, Wu S, Chen C. Effect of CO_2 laser welding on the shape-memory and corrosion characteristics of TiNi alloys. Metall Mater Trans A 2001:569–76. http://dx.doi.org/10.1007/s11661-001-0073-2.
[21] Hammersley AP, Svensson SO, Hanfland M, Fitch AN, Hausermann D. Two-dimensional detector software: from real detector to idealised image or two-theta scan. High Pressure Res 1996;14(4):235–48. http://dx.doi.org/10.1080/08957959608201408.
[22] Otsuka K, Ren X. Physical metallurgy of Ti–Ni-based shape memory alloys. Prog Mater Sci 2005;50(5):511–678. http://dx.doi.org/10.1016/j.pmatsci.2004.10.001.
[23] Tobushi H, Shimeno Y, Hachisuka T, Tanaka K. Influence of strain rate on superelastic properties of TiNi shape memory alloy. Mech Mater 1998;30(2):141–50. http://dx.doi.org/10.1016/S0167-6636(98)00041-6.
[24] Lin PH, Tobushi H, Tanaka K, Hattori T, Makita M. Pseudoelastic behaviour of TiNi shape memory alloy subjected to strain variations. J Intell Mater Syst Struct 1994;5(5):694–701. http://dx.doi.org/10.1177/1045389X9400500514.
[25] Saburi T, Nenno S, Nishimoto Y, Zeniya M. Effects of thermo-mechanical treatment on the shape memory effect and the pseudoelasticity of Ti-50. 2Ni and Ti–47.5Ni–2.5Fe Alloys. J Iron Steel Inst Jpn 1986:37–44.
[26] Saburi T, Yoshida M, Nenno S. Deformation behavior of shape memory Ti–Ni alloy crystals. Scripta Metall 1984;18(4):363–6. http://dx.doi.org/10.1016/0036-9748(84)90453-8.
[27] Tan G, Liu Y, Sittner P, Saunders M. Lüders-like deformation associated with stress-induced martensitic transformation in NiTi. Scripta Mater 2004;50(2):193–8. http://dx.doi.org/10.1016/j.scriptamat.2003.09.018.
[28] Wada K, Liu Y. Shape recovery of NiTi shape memory alloy under various pre-strain and constraint conditions. Smart Mater Struct 2005;14(5):S273–86. http://dx.doi.org/10.1088/0964-1726/14/5/016.
[29] Miyazaki S, Imai T, Igo Y, Otsuka K. Effect of cyclic deformation on the pseudoelasticity characteristics of Ti–Ni alloys. Metall Trans A 1986;17(1):115–20. http://dx.doi.org/10.1007/BF02644447.

7.1.3 Martensite Stabilization During Superelastic Cycling of Laser Welded NiTi Plates

This paper was submitted and accepted in Materials Letters.

Materials Letters 171 (2016) 273–276

Contents lists available at ScienceDirect

Materials Letters

journal homepage: www.elsevier.com/locate/matlet

Martensite stabilization during superelastic cycling of laser welded NiTi plates

J.P. Oliveira [a,*], F.M. Braz Fernandes [a], N. Schell [b], R.M. Miranda [c]

[a] CENIMAT/i3N, Faculdade de Ciências e Tecnologia, Universidade Nova de Lisboa, Portugal
[b] Institute of Materials Research, Helmholtz-Zentrum Geesthacht, Max-Planck-Str. 1, D-21502 Geesthacht, Germany
[c] UNIDEMI, Faculdade de Ciências e Tecnologia, Universidade Nova de Lisboa, Portugal

ARTICLE INFO

Article history:
Received 7 November 2015
Received in revised form
17 February 2016
Accepted 21 February 2016
Available online 22 February 2016

Keywords:
NiTi shape memory alloys
Martensite stabilization
Laser welding
Phase transformation
X-ray techniques
Synchrotron radiation

ABSTRACT

Superelastic behavior of laser welded NiTi is significantly different from the original base material due to microstructural changes introduced during welding. These are responsible for a higher accumulated irrecoverable strain during mechanical cycling. In order to clarify the mechanisms responsible for the evolution of the accumulated irrecoverable strain on superelastic laser welded NiTi, detailed synchrotron X-ray diffraction analysis was performed. Welded samples were analyzed as-welded, after 4 cycles at 10% strain and after 600 cycles at 10% strain. As-welded sample had thermally stabilized martensite in the heat affected and fusion zones due to the welding procedure. It was observed that after 4 cycles, stabilization of the stress induced martensite occurred in a massive way in the thermal affected regions, due to the introduction of defects which prevented the reverse transformation upon unloading. After 600 cycles no significant changes were observed in the thermal affected regions. However, evidence of martensite stabilization in the base material, which was originally fully austenitic, near the heat affected zone was observed.

1. Introduction

Laser welding has proven to be a suitable joining technique for NiTi shape memory alloys [1–5]. The functional behavior, either by superelasticity or shape memory effect, of the laser welded NiTi joints is dependent on the laser welding procedure.

Both superelasticity and shape memory effect are affected by structural characteristics of the material, such as the martensite stabilization. Martensite stabilization can arise from either the thermal martensite [6] or from the stress-induced martensite [7]. This stabilization is usually studied separately, that is, studies are based on the stabilization of thermal martensite or in the stabilization of stress-induced martensite. In the former case, this stabilization occurs by reorientation of martensite variants [8]. In the latter case, introduction of dislocations during or after the superelastic plateau, makes the reverse transformation require an increased driving force [9]. In either case, the higher the applied stress/strain the higher should be the stabilization effect. As a consequence of this stabilization, the strain recovery after the stress-induced transformation decreases.

Recently, the present authors analyzed the functional fatigue by superelasticity in laser welded NiTi plates [10], by performing cycling tests up to 10% for a total of 600 cycles. The evolution of the accumulated irrecoverable strain was found to increase significantly at the early stages of cyclic deformation, followed by a tendency to stabilize at a fixed value. The presence, at room temperature, of both austenite and martensite in the thermal affected regions, while the base material was fully austenitic, may justify this sharp increase of the accumulated irrecoverable strain. In particular, the existing martensite in the as-welded material should have undergone detwinning during solicitation up to 10%, contributing to the irrecoverable strain of the welded joint. As for the austenite, it is expected that, aside from the introduction of dislocations which are known to occur during cyclic solicitation of NiTi [11,12], some retained martensite is found to occur due the blockage of the reverse martensitic transformation upon unloading [13,14]. In either case, the same phenomenon occurs: martensite stabilization.

In order to understand which phenomena were taking place during cyclic solicitation of these NiTi laser welds, detailed structural characterization by X-ray diffraction using synchrotron radiation was performed in three different welded NiTi joints. These samples were welded with the same parameters to keep consistency between the observed results. The use of a high energy synchrotron radiation is extremely suitable for such laser welds for two main reasons: (i) it allows a finer discretization of the

* Corresponding author.
E-mail address: jp.oliveira@campus.fct.unl.pt (J.P. Oliveira).

http://dx.doi.org/10.1016/j.matlet.2016.02.107
0167-577X/

analyzed regions due to the reduced beam spot used; (ii) it is a non-destructive technique which gives information on the microstructure of the material. In this work, stabilization of martensite (either thermal and stress-induced) is discussed based on the superelastic behavior presented by laser welded NiTi sheets complemented with synchrotron analysis performed in the welded samples after a pre-defined number of superelastic cycles.

NiTi plates, with a nominal composition of 50.8 at% Ni-49.2 at% Ti, supplied in the flat annealed condition, 1 mm thick, were used. Laser welding was performed using a DY033 Nd:YAG laser power source from Rofin-Sinar, operating in a continuous wave mode, with a gas protection of Argon injected in both face and root of the weld. The laser welding parameters for the analyzed sample in this work are as follows: power of 990 W; welding speed of 20 mm/s; heat input of 495 J/cm.

All samples were removed from the same welded plate and subjected to different mechanical solicitations: one sample as-welded (sample reference W0, where W=weld, 0=number of mechanical cycles); one sample with a total of 4 load/unload cycles up to 10% strain (sample reference W4); one sample with a total of 600 load/unload cycles up to 10% as reported in [10] (sample reference W600).

X-ray diffraction analysis, using synchrotron radiation, was performed at P07 beamline at PETRA III/DESY, with a wavelength of 0.1426 Å (87 keV). The distance between the sample and the detector was kept at 1090 mm. The beam spot dimension was of 200×100 μm. A distance of about 6 mm was probed starting in the base material going through the thermal affected regions and finishing on the other side of the base material. The distance between shots was of 200 μm. Fit2D [15] was used to analyze the raw diffraction images. X-ray diffraction was performed at room temperature as well as the cycling tests.

2. Results and discussion

The diffratograms for samples W0, W4 and W600 are depicted in Fig. 1(a), (b) and (c), respectively. For the as-welded sample W0, a clear microstructural distinction between the base material and the thermal affected regions is observed. While the base material is fully austenitic, with no evidence of martensite, the thermal affected regions present martensite with a corresponding decrease in the austenite peak intensity. The formation of this martensite is related to two distinct phenomena which occur during welding: (i) precipitation of Ni_4Ti_3 in the heat affected zone [16] and (ii) preferential Ni volatilization in the fusion zone [17].

Analyzing the superimposition of the diffractograms after 4 cycles at 10% strain (Fig. 1b), which had an accumulated irrecoverable strain of 2.85%, a notorious microstructural evolution is observed: the intensity of the martensite peaks, in the thermal affected regions, greatly increases when compared to the as-welded sample. As a result of the augmented intensity of the martensite peaks in these regions, the austenite peak intensity decreases. Additionally, the base material starts to present some evidence of martensite peaks.

After 600 mechanical cycles (Fig. 1c), there are no significant differences in the microstructure of the heat affected and fusion zones when compared to the sample cycled 4 times. Only a slight increase in the martensite peaks intensity was observed. The most significant change occurs in the base material near the heat affected zone, where martensite is clearly visible in this region. This evidence is more clear analyzing the evolution of the net height of the austenite and martensite peaks (the latter located at d=2.17 A) along the welded material, as depicted in Fig. 2.

From the analysis of the aforementioned figures, it is seen that prior to any mechanical solicitation, the welded material presents

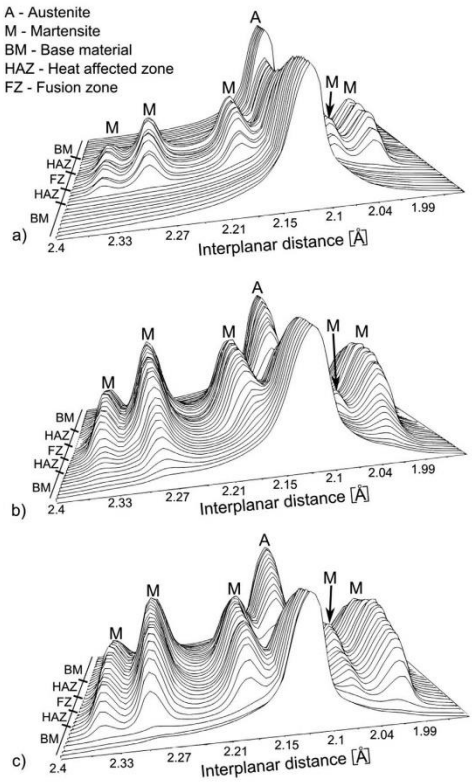

Fig. 1. Superimposition of the X-ray diffractograms for laser welded NiTi samples: (a) as-welded; (b) after 4 cycles at 10% strain; (c) after 600 cycles up to 10%. Intensity in log scale.

a mixture of both martensite and austenite in the heat affected zone and in the fusion zone. This martensite is thermally stabilized at room temperature as a consequence of the weld thermal cycle. While austenite can undergo a reversible stress-induced transformation up to 10% strain [18], the same does not occur with martensite. When in the martensitic state, any applied stress/strain after the onset of the detwinning plateau will generate a given irrecoverable strain [6]. However, it must be noticed that this deformation can be recovered by heating the material up to its A_f temperature in order to trigger the shape memory effect [19]. Cycling solicitation of these laser welds was performed up to 10% at room temperature, so, as far as thermal martensite is concerned, no recovery upon unloading would be expected.

Aside from the stabilization of thermal martensite during mechanical cycling, another martensite stabilization phenomenon occurs: stabilization of stress-induced martensite [6,20]. Delville et al. [21] showed that, during superelastic cycling of NiTi, significant accumulated irrecoverable strain could occur due to the introduction of defects along cycling. Later, Sedmak et al. [14] performed in-situ X-ray analysis using synchrotron radiation on the same material as in Delville's work. It was observed that, although the accumulated irrecoverable strain increased at each load/unload cycle, only after the 4th cycle, a clear evidence of

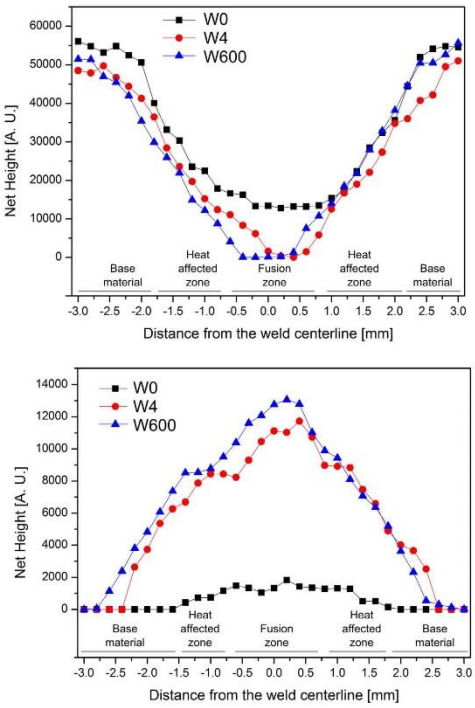

Fig. 2. Evolution of the net height from the austenite peak (top) and for the martensite peak located at d=2.17 Å (bottom) along the NiTi laser welds.

retained martensite was found. In an ideal superelastic behavior, upon unloading, stress-induced martensite would return to austenite, with no irrecoverable strain. As such, the irrecoverable strain in the early cycles was due to increasing dislocation density in the material. As residual martensite starts to accumulate (or being stabilized), build-up of the residual stress and generation of dislocations during mechanical cycling starts to decrease. In the laser welds studied in this work the same must occur: if after 4 load/unload solicitations the limit of the martensite stabilization is reached, then, after 600 cycles, no significant differences should be encountered. In fact, this can be observed comparing Fig. 1 (b) and (c). The only difference between these two Figures is that some martensite was found to be stabilized in the base material as a consequence of the cycling tests performed. However, this martensite stabilization occurs in the base material closer to the heat affected zone. As we move into the base material, far away from the fusion zone, no evidence of martensite stabilization is observed.

It must be noticed that the length of about 6 mm probed by X-ray diffraction analysis is only part of the gauge length used for the mechanical tests, which was kept at 30 mm. Nonetheless, it is evident that, within this 6 mm length, it is possible to obtain detailed information of the microstructural evolution of the welded joints as a result of the cycling tests performed. This structural information made it possible to highlight the two different mechanisms of stabilization of the martensite, which are relevant to understand the cycling behavior of the welded joints.

It is important to note that the stabilization effect can be reversed by heating the sample up to a temperature that enables the martensite to austenite transformation. After this, it is expected that the transformation temperatures decrease significantly, when compared to the stabilized material [20]. Further studies are planned to analyze the effect of an intermediate reheating on the transformation temperatures of the different regions of the laser welded NiTi plates.

3. Conclusions

Laser welding of NiTi shape memory alloys promotes the formation of martensite in the thermal affected regions, at room temperature, when the base material is fully austenitic. The reason for the occurrence of martensite is related to Ni depletion in those regions leading to an increase of the transformation temperatures. As such, the martensite of the as-welded samples is thermally stabilized. After 4 cycles at 4%, the martensite peaks intensity in the thermal affected regions increase significantly with a correspondent decrease in the superelastic recovery. The reason for the increase of the martensite peaks intensity is the stabilization of stress-induced martensite which cannot return to austenite upon unloading due to the introduction of dislocations during mechanical cycling.

After 600 mechanical cycles up to 10% strain, no significant change in the martensite peak intensity is observed in the thermal affected regions, in comparison to the sample subjected to 4 cycles. However, evidence of martensite stabilization is clearly observed in the base material closer to the heat affected zone. This change is attributed to the introduction of dislocations during the loading path, preventing full recovery by superelasticity. These results are in line with a recent publication of Sedmak et al. [14] and are of great importance, when envisaging the use of NiTi in structural or functional applications based on the superelastic effect.

Although martensite stabilization, either thermal or stress-induced, has been studied separately, to the authors' knowledge, this is the first study which evidences both types of martensite stabilization occurring within the same material during mechanical solicitation of a specific industrial application, that is, laser welding.

Acknowledgements

JPO and FBF acknowledge funding of CENIMAT/I3N by FEDER funds through the COMPETE 2020 Program and National Funds through FCT - Portuguese Foundation for Science and Technology under the project number POCI-01-0145-FEDER-007688, Reference UID/CTM/50025. RMM acknowledges funding of UNIDEMI by FEDER funds through the COMPETE 2020 Program and National Funds through FCT - Portuguese Foundation for Science and Technology under the project UID/EMS/00667/2013. The authors acknowledge DESY and HZG for beamtime and travel reimbursement under proposal I-20120563 EC FP7/2007-2013 Grant agreement no. 312284. JPO acknowledges FCT/MCTES for funding Ph.D grant SFRH/BD/85047/2012.

References

[1] A. Tuissi, S. Besseghini, T. Ranucci, F. Squatrito, M. Pozzi, Effect of Nd-YAG laser welding on the functional properties of the Ni–49.6 at%Ti, Mater. Sci. Eng. A 273–275 (1999) 813–817, http://dx.doi.org/10.1016/S0921-5093(99)00422-0.
[2] H. Gugel, A. Schuermann, W. Theisen, Laser welding of NiTi wires, Mater. Sci.

Eng. A 481–482 (2008) 668–671, http://dx.doi.org/10.1016/j.msea.2006.11.179.
[3] Y.G. Song, W.S. Li, L. Li, Y.F. Zheng, The influence of laser welding parameters on the microstructure and mechanical property of the as-jointed NiTi alloy wires, Mater. Lett. 62 (2008) 2325–2328, http://dx.doi.org/10.1016/j.matlet.2007.11.082.
[4] L.A. Vieira, F.M.B. Fernandes, R.M. Miranda, R.J.C. Silva, L. Quintino, A. Cuesta, et al., Mechanical behaviour of Nd:YAG laser welded superelastic NiTi, Mater. Sci. Eng. A 528 (2011) 5560–5565, http://dx.doi.org/10.1016/j.msea.2011.03.089.
[5] J.P. Oliveira, F.M.B. Fernandes, N. Schell, R.M. Miranda, Shape memory effect of laser welded NiTi plates, Funct. Mater. Lett. 08 (2015) 1550069, http://dx.doi.org/10.1142/S1793604715500691.
[6] G. Tan, Y. Liu, Comparative study of deformation-induced martensite stabilisation via martensite reorientation and stress-induced martensitic transformation in NiTi, Intermetallics 12 (2004) 373–381, http://dx.doi.org/10.1016/j.intermet.2003.11.008.
[7] C. Maletta, E. Sgambitterra, F. Furgiuele, R. Casati, A. Tuissi, Fatigue properties of a pseudoelastic NiTi alloy: strain ratcheting and hysteresis under cyclic tensile loading, Int. J. Fatigue 66 (2014) 78–85, http://dx.doi.org/10.1016/j.ijfatigue.2014.03.011.
[8] Y. Liu, D. Favier, Stabilisation of martensite due to shear deformation via variant reorientation in polycrystalline NiTi, Acta Mater. 48 (2000) 3489–3499, http://dx.doi.org/10.1016/S1359-6454(00)00129-4.
[9] Y. Liu, G.S. Tan, Effect of deformation by stress-induced martensitic transformation on the transformation behaviour of NiTi, Intermetallics 8 (2000) 67–75, http://dx.doi.org/10.1016/S0966-9795(99)00079-5.
[10] J.P. Oliveira, R.M. Miranda, N. Schell, F.M. Braz Fernandes, High strain and long duration cycling behavior of laser welded NiTi sheets, Int. J. Fatigue 83 (2016) 195–200, http://dx.doi.org/10.1016/j.ijfatigue.2015.10.013.
[11] A.R. Pelton, Nitinol fatigue: a review of microstructures and mechanisms, J. Mater. Eng. Perform. 20 (2011) 613–617, http://dx.doi.org/10.1007/s11665-011-9864-9.
[12] R. Delville, B. Malard, J. Pilch, P. Sittner, D. Schryvers, Transmission electron microscopy investigation of dislocation slip during superelastic cycling of Ni–Ti wires, Int. J. Plast. 27 (2011) 282–297, http://dx.doi.org/10.1016/j.ijplas.2010.05.005.
[13] A. Yawny, M. Sade, G. Eggeler, Pseudoelastic cycling of ultra-fine-grained NiTi shape-memory wires, Z. Met. 96 (2005) 608–618, http://dx.doi.org/10.3139/146.101078.
[14] P. Sedmák, P. Šittner, J. Pilch, C. Curfs, Instability of cyclic superelastic deformation of NiTi investigated by synchrotron X-ray diffraction, Acta Mater. 94 (2015) 257–270, http://dx.doi.org/10.1016/j.actamat.2015.04.039.
[15] A.P. Hammersley, S.O. Svensson, M. Hanfland, A.N. Fitch, D. Hausermann, Two-dimensional detector software: from real detector to idealised image OR two-theta scan, High. Press. Res. 14 (1996) 235–248, http://dx.doi.org/10.1080/08957959608201408.
[16] J.P. Oliveira, F.M. Braz Fernandes, R.M. Miranda, N. Schell, On the mechanisms for martensite formation in YAG laser welded austenitic NiTi, Shape Mem. Superelast. (2016), 10.1007/s40830-016-0058-z, (in press).
[17] X.J. Yan, D.Z. Yang, Corrosion resistance of a laser spot-welded joint of NiTi wire in simulated human body fluids, J. Biomed. Mater. Res. A 77 (2006) 97–102, http://dx.doi.org/10.1002/jbm.a.30378.
[18] K. Otsuka, X. Ren, Physical metallurgy of Ti–Ni-based shape memory alloys, Prog. Mater. Sci. 50 (2005) 511–678, http://dx.doi.org/10.1016/j.pmatsci.2004.10.001.
[19] C.P. Frick, A.M. Ortega, J. Tyber, A.E.M. Maksound, H.J. Maier, Y. Liu, et al., Thermal processing of polycrystalline NiTi shape memory alloys, Mater. Sci. Eng. A 405 (2005) 34–49, http://dx.doi.org/10.1016/j.msea.2005.05.102.
[20] S. Wang, K. Tsuchiya, L. Wang, M. Umemoto, Deformation mechanism and stabilization of martensite in TiNi shape memory alloy, J. Mater. Sci. Technol. 26 (2010) 936–940, http://dx.doi.org/10.1016/S1005-0302(10)60151-X.
[21] R. Delville, B. Malard, J. Pilch, P. Sittner, D. Schryvers, Microstructure Changes during non-conventional heat treatment of thin Ni–Ti wires by pulsed electric current studied by transmission electron microscopy, Acta Mater. 58 (2010) 4503–4515, http://dx.doi.org/10.1016/j.actamat.2010.04.046.

7.1.4 Shape Memory Effect of Laser Welded NiTi Plates

This paper was submitted and accepted in Functional Materials Letters.

Functional Materials Letters
Vol. 8, No. 6 (2015) 1550069 (5 pages)

DOI: 10.1142/S1793604715500691

World Scientific
www.worldscientific.com

Shape memory effect of laser welded NiTi plates

J. P. Oliveira*,§, F. M. Braz Fernandes*, N. Schell† and R. M. Miranda‡
*CENIMAT/I3N, Departamento de Ciências dos Materiais
Faculdade de Ciências e Tecnologia, FCT
Universidade Nova de Lisboa, 2829–516 Caparica, Portugal
†Institute of Materials Research, Helmholtz-Zentrum Geesthacht
Max-Planck-Str. 1, D-21502, Geesthacht, Germany
‡UNIDEMI, Departamento de Engenharia Mecânica e Industrial
Faculdade de Ciências e Tecnologia, FCT
Universidade Nova de Lisboa, 2829–516 Caparica, Portugal
§jp.oliveira@campus.fct.unl.pt

Received 15 May 2015; Accepted 26 May 2015; Published 1 July 2015

Laser welding is a suitable joining technique for shape memory alloys (SMAs). This paper reports the existence of shape memory effect (SME) on laser welded NiTi joints, subjected to bending tests, and correlates this effect with the microstructural analysis performed with X-ray diffraction (XRD). All welded samples were able to recover their initial shape after bending to 180°, which is a remarkable result for industrial applications of NiTi involving laser welding.

Keywords: NiTi; shape memory alloys; shape memory effect; X-ray diffraction; laser welding.

Equiatomic NiTi alloys exhibit a shape memory effect (SME) when deformed at a temperature below M_f, followed by heating above A_f, where M_f and A_f are the finishing temperatures of the direct (austenite to martensite) and reverse (martensite to austenite) transformations, respectively.[1] Due to the poor workability of NiTi alloys, suitable welding techniques must be used to obtain devices and components with complex geometries. However, the mechanical and functional behavior of these alloys are strongly influenced by possible thermal effects and modifications in the chemical composition associated with the welding process chosen.[2] It is well known that the transformation temperatures of NiTi shape memory alloys (SMAs) present a significant variation with the composition of their matrix.[1] Fusion welding of these alloys has been seen to exhibit this effect due to the thermal cycle imposed, which affects the existing phases and, thus, the transformation temperatures.[3,4]

Several research teams have been working in joining SMAs, however, investigations were mainly focused on wires and thin foils.[5,7]

Laser welding has been investigated in NiTi, with extensive research on the structural characterization by differential scanning calorimetry and X-ray diffraction (XRD) aiming at identifying the phase transformations and transformation temperatures.[4,8,9] Mechanical testing of welded joints has shown that these are less performing than the base material, when evaluated under tensile cycling at low strains and a reduced number of cycles.[10] Vieira *et al.* studied the superelastic mechanical behavior of laser welded plates under strains up to 8% in a total of 60 cycles.[11,12]

Limited work exists on the evaluation of SME of laser welded sheets in NiTi.[10] Considering that this functional property is of major relevance for industry, this research gap limits the scale up of the results for industrial applications requiring this joint geometry.

In this paper, we complement the study performed by Vieira *et al.*,[12] where the superelastic properties of laser welded NiTi joints were investigated. Now, our attention is focused on the SME of this laser joints, especially, how this functional effect is manifested in the fusion zone and its neighborhood. The investigations of the SME of laser welded NiTi joint reported in the literature is always concerned on the overall behavior of the material[2,10] and up to now there are no reports on the assessment of this property in the fusion

§Corresponding author.

zone and its neighborhood. It is a major concern to preserve the SME after welding due to its possible implications for specific applications.

The present study analyses and discusses the tests performed on the SME of laser welded butt joints in equiatomic NiTi plates with 0.5 mm and 1 mm thickness. The existence of a SME was observed in all samples welded with different processing conditions. These results are relevant as far as welded joints design in SMAs is concerned, aiming at their industrial applications.

NiTi plates with 50.8 at.% Ni with 0.5 mm and 1.0 mm thickness, supplied in flat annealed condition, were tested and these were superelastic at room temperature.

Laser butt welds were produced using a DY033 Nd/YAG laser power source from Rofin-Sinar, operating in the continuous wave mode with the weld beads positioned along and across the base material rolling direction to assess this effect. Laser power was varied between 790 W and 1485 W and travel speed between 20 mm/s and 70 mm/s with a focused beam diameter of 0.4 mm (Table 1). To avoid oxidation, a special chamber was used and a gas protection of argon on the top face and helium on the root, with 45 L/min and 15 L/min gas flow, respectively, was used. All samples, except sample C, were welded perpendicularly to the rolling direction. All samples were welded perpendicularly to the rolling direction, as in the previous studies[11,12] it was shown that the samples welded across the rolling direction presented better mechanical properties. Other details of the welding procedure are described in Ref. 11. Prior to the SME tests, the plates were cut into strips with a width of about 3 mm using a precision cut-off machine ATM GmbH model Brillant 221 equipped with a diamond wheel type B102 and multipurpose cutting fluid as lubricant.

The experimental procedure to evaluate the SME consisted on bending the welded samples, as presented in Fig. 1(a).[13] For this purpose, a special device, shown in Figs. 2(b) and 2(c), was designed and built in AISI 316L stainless steel allowing bending specimens up to 180° under low temperature conditions, with a curvature radius of 12.5 mm.[11]

The welded specimens were positioned in the device, dipped into a bath of liquid nitrogen (to ensure that during the bending procedure the samples were in the martensitic condition) and bent around the device. The bent samples were released at room temperature to freely recover. This procedure was repeated four times, alternating the surface of the welded plate facing the bending device, i.e., the weld face and the root were under compressive and tensile stress conditions alternatively. The permanent deformation angle, Ω, was measured under a binocular magnifier using a protractor with a resolution of 0.5°, after the specimens were in equilibrium with the room temperature (21°C). The sequence of

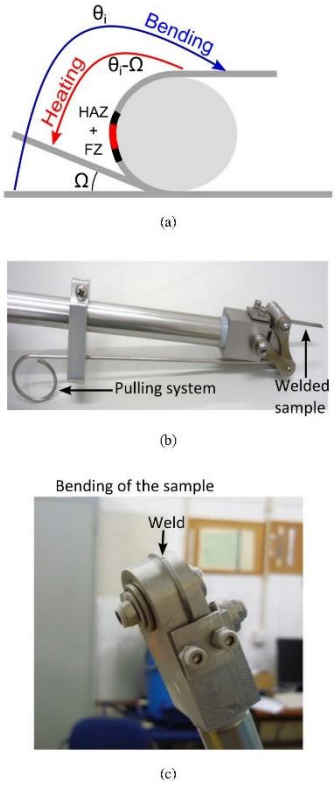

Fig. 1. (a) Schematic illustration of SME bending test; (b) device for testing; (c) detail of the sample under test.

the test is depicted in Fig. 2. All samples presented in Table 1 were subjected to the SME tests, as described previously.

As the thickness of the samples is much smaller than their length, it can be assumed that the neutral axis of the samples during bending test occurs at half thickness. Based on this assumption, the maximum strain imposed to the external face of the samples during the tests was 2% and 4%, for 0.5 mm and 1.0 mm thick samples, respectively.

XRD was carried out to identify existing phases at room temperature. Samples were analyzed in beamline P07 High Energy Materials Science (HEMS) of Petra III/DESY, using a wavelength of 0.1426 Å (energy of 87 keV) and a 2D detector (MAR 345) placed at 1.35 m from the sample. A line (perpendicular to the weld bead), 6-mm long, was probed starting in the base material, 3 mm below the center of the weld bead, going through the heat affected zone and the weld bead, and ending in the base material, 3 mm above the center of the weld

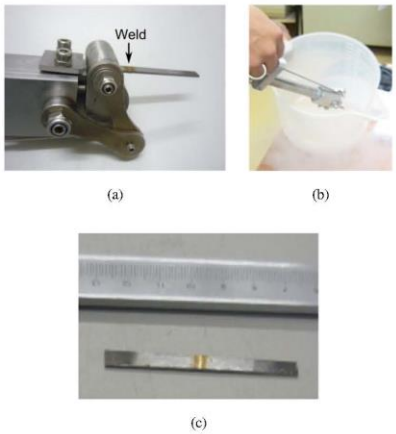

Fig. 2. Bending and free-recover method used to analyze the SME: (a) Initial shape of the sample positioned in the bending device; (b) dipping in liquid nitrogen and bending; (c) final shape after heating up to room temperature.

bead. The beam dimensions were $200 \times 100\,\mu$m, so that the larger dimension ($200\,\mu$m) was parallel to the weld bead. The distance between two consecutive spots was $200\,\mu$m. The data acquired was treated using the Fit2D program[14] in order to transform the Debye–Scherrer rings into intensity *versus* 2θ scans by integration from 0° to 360° (Phi or azimuthal angle). XRD analysis was performed in all samples.

Since the structural characterization of the welded samples showed qualitatively the same results, discussion is focused on samples A and E, i.e., on samples with 0.5 mm and 1.0 mm thickness, welded with a heat input of 158 J/cm and 743 J/cm, respectively. XRD patterns obtained in the different zones of the welds are depicted in Fig. 3 and show the existence of austenite in the base material of both samples. The fusion zone and the heat affected zone exhibit a coarse grain structure with austenite and martensite.

The recoverable deformation of martensite is known to be an anisotropic process, which behaves differently from tension to compression.[15] It is also known that the ability of martensite to recover its initial shape through SME varies

Table 1. Welding parameters for the analyzed samples.

Sample reference	Power (W)	Travel speed (mm/s)	Heat input (J/cm)	Plate thickness (mm)
A	790	50	158	0.5
B	858	70	122	
C	910	25	364	
D	990	25	396	1
E	1485	20	743	

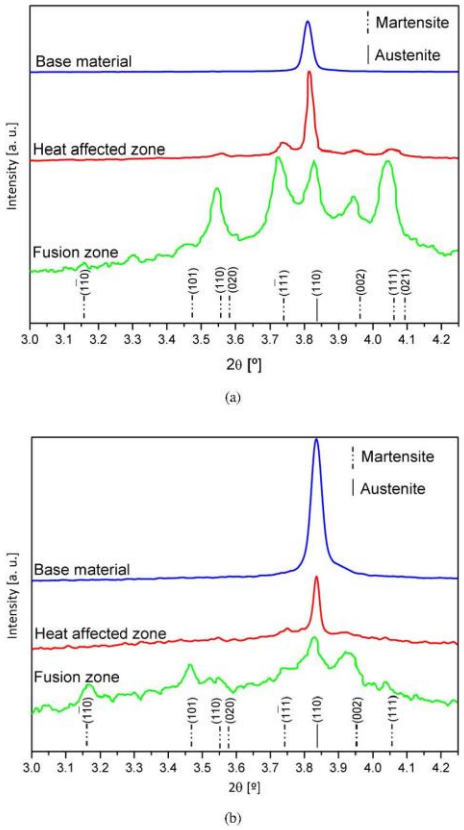

Fig. 3. XRD patterns for the base material (BM), the heat affected zone (HAZ) and the fusion zone (FZ) of samples A (a) and E (b).

between 8% and 10%.[1] The SME exhibited by the welded joints was not affected by the existence of martensite in the FZ and HAZ. This shows that the remaining austenite existing at room temperature in the FZ is sufficient to contribute for the shape memory recovery of that volume fraction of the welding when it is heated up to the room temperature. From these tests, it was possible to verify that all samples were able to recover their initial shape after performing the SME tests. It is worth mentioning that all samples were able to resist to the full sequence of four times bending/recovery cycles during the SME tests, which causes an alternating tensile/compressive stresses exerted on weld bead.

During the free recovery of the samples at room temperature two different angles were measured. One, δ, related to the overall recover of the samples ("Global" angle) and

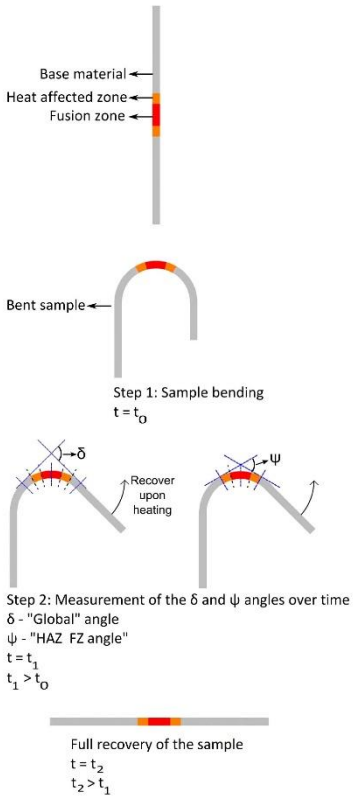

Fig. 4. Schema for determination of the angles in two different regions at three different times.

another, Ψ, related to the recover of the HAZ and FZ ("HAZ + FZ" angle). These angles were measured by taking two straight lines, tangent to the regions of interest, and determining the angle between both lines. In the δ angle case, the region of interest was in the base material approximately 5 mm away from the weld centerline where the welding procedure had no influence on the material. The macrographs of samples C and D (Fig. 5) depict that the HAZ extension ends approximately from 3.5 mm to 4.5 mm away from the weld centerline, respectively. Both regions of interest, where the recovering angles were analyzed over time, are displayed in Fig. 4.

These results, over time, for sample C (as a given example) are depicted in Fig. 6. It must be noticed that the angle measurement only started about 15 s after taking the sample out of the liquid nitrogen and placing it over a table to freely

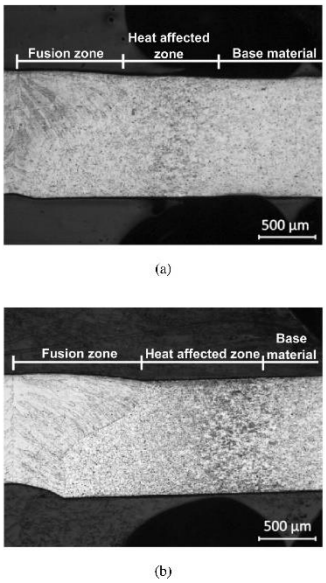

Fig. 5. Macrographs of samples: C (a) and D (b).

recover. For that reason the dashed lines represent an extrapolation of the shape memory behavior over time, taking in consideration that, immediately after the sample is removed from the liquid nitrogen, it is bent at 180° angle. It is noticed that the HAZ and FZ recover their initial shape earlier than the base material.

Scherngell *et al.*[16] studied the two way SME in NiTi alloys and found that the dislocations density introduced during the thermal training causes a rearrangement of dislocations

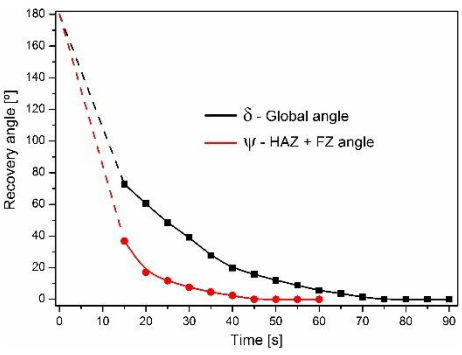

Fig. 6. Evolution of the recover angle over time for sample C.

and the introduction of new ones. It was assumed that the increased dislocation density is mostly responsible for the degradation of the recoverable strain after successive thermal/mechanical cycles. In the present work, excellent shape memory recovery — defined, in this case, as the permanent deformation angle being equal to 0° — occurred for all the samples. This may suggest that the increased dislocation density resulting from the maximum strains used (2% or 4%, for 0.5 mm and 1.0 mm, respectively) during the alternate bending is not high enough to degrade the shape recovery.

SME of different laser welded NiTis was investigated. The following conclusions can be drawn:

(1) Laser welded specimens exhibited a SME after bending up to 2% and 4%, for 0.5 mm and 1.0 mm thick samples, respectively, after four alternate bending tests.
(2) SME was observed after welding. Welds fully recovered their initial shape when the weld bead was subjected to alternating tensile/compressive stresses exerted in the welded region and its neighborhood.
(3) At room temperature, the base material had an austenitic structure, while the HAZ and FZ depicted the existence of austenite and martensite. However, this does not affect the SME recovery.

The full recovery of the initial shape of the welded samples is a remarkable result for industrial applications concerning the use of laser welding for NiTi SMAs.

Acknowledgments

The authors would like to acknowledge the funding of FCT/MCTES for the project "MICROBOND — Joining micro to small scale systems in shape memory alloys using last generation infrared lasers" (PTDC/EME-TME/100990/2008), the project Smart Composites (PTDC/CTM/66380/2006). The authors also acknowledge DESY and HZG for beamtime and travel reimbursement under proposal I-20120563 EC. JPO and FBF acknowledge funding by FEDER funds through the COMPETE 2020 Programme and National Funds through FCT — Portuguese Foundation for Science and Technology under the project UID/CTM/50025/2013. RMM acknowledges UID/EMS/00667/2013. JPO acknowledges FCT/MCTES for funding PhD grant SFRH/BD/85047/2012.

References

1. K. Otsuka and C. Wayman, *Shape Memory Materials* (Cambridge Press University, Cambridge, United Kingdom, 1999).
2. A. Falvo, F. M. Furgiuele and C. Maletta, *Mater. Sci. Eng. A* **481**, 647 (2008).
3. B. Tam, M. I. Khan and Y. Zhou, *Metallurgical Mater. Trans.* **42A**, 2166 (2011).
4. M. I. Khan and Y. Zhou, *Mater. Sci. Eng. A* **527**, 6235 (2010).
5. C. Chan, H. Man and T. Yue, *Metallurgical Mater. Trans. A* **42**, 2264 (2012).
6. A. Tuissi, S. Besseghini, T. Ranucci and F. Squatrito, *Mater. Sci. Eng. A* **273–275**, 813 (1999).
7. P. Schloßmacher and T. Haas, Laser welding of Ni-Ti shape memory alloys, *Proc. First Int. Conf. Shape Memory and Superelastic Technologies*, eds. A. Pelton, D. Hodgson and T. Duerig, California, United States of America, Vol. 85 (1994).
8. B. Tam, M. Khan and Y. Zhou, *Metallurgical Mater. Trans. A* **42**, 2166 (2011).
9. C. W. Chan and H. C. Man, *Opt. Lasers Eng.* **49**, 121 (2011).
10. A. Falvo, F. M. Furgiuele and C. Maletta, *Mater. Sci. Eng. A* **412**, 235 (2005).
11. L. A. Vieira, Laser welding of shape memory alloys, M.Sc. Thesis, Faculty of Sciences and Technology, Universidade Nova de Lisboa, Monte de Caparica (2010), (accessible on-line at http://run.unl.pt/bitstream/10362/4760/1/Vieira_2010.pdf)
12. L. A. Vieira, F. B. Fernandes, R. Miranda, R. Silva, L. Quintino, A. Cuesta and J. Ocaña, *Mater. Sci. Eng. A* **528**, 813 (2011).
13. H. Lin and S. Wu, *Scripta Metallurgica et Materialia* **26**, 59 (1992).
14. Hammersley A, FIT2D, *ESRF*, available at: http://www.esrf.eu/computing/scientific/FIT2D/.
15. Y. Liu, Detwinning process and its anisotropy in shape memory alloys, *Proc. SPIE*, eds. A. Wilson and A. Asanuma, Melbourne, Australia, Vol. 4234 (2001), p. 82.
16. H. Scherngell and A. Kneissl, *Mater. Sci. Eng. A* **273–275**, 400 (1999).

7.1.5 Residual Stress Analysis in Laser Welded NiTi Sheets Using Synchrotron X-ray Diffraction

This paper was submitted and accepted in Materials & Design

Materials and Design 100 (2016) 180–187

Contents lists available at ScienceDirect

Materials and Design

journal homepage: www.elsevier.com/locate/matdes

Residual stress analysis in laser welded NiTi sheets using synchrotron X-ray diffraction

J.P. Oliveira [a,*], F.M. Braz Fernandes [a], R.M. Miranda [b], N. Schell [c], J.L. Ocaña [d]

[a] CENIMAT/I3N, Faculdade de Ciências e Tecnologia, Universidade Nova de Lisboa, Portugal
[b] UNIDEMI, Faculdade de Ciências e Tecnologia, Universidade Nova de Lisboa, Portugal
[c] Institute of Materials Research, Helmholtz-Zentrum Geesthacht, Max-Planck-Str. 1, D-21502 Geesthacht, Germany
[d] Centro Láser UPM, Universidad Politécnica de Madrid, Edificio "La Arboleda", Ctra. Valencia, km 7,300, Campus Sur UPM, 28031 Madrid, Spain

ARTICLE INFO

Article history:
Received 26 December 2015
Received in revised form 23 March 2016
Accepted 26 March 2016
Available online 31 March 2016

Keywords:
NiTi shape memory alloys
Laser welding
Residual stress
Rietveld refinement
Synchrotron radiation

ABSTRACT

Synchrotron radiation was used for fine probing the different regions of a laser welded NiTi joint. Measurements were taken at 0.2 mm intervals, starting in the non-thermal affected material, through the heat affected zone, the fusion zone and again across the heat affected zone finishing in the base material. Along the longitudinal direction the residual stresses were found to be always tensile in the heat affected and fusion zones; along the transversal direction, an inversion of the stress states was found. The magnitude of the residual stresses was found to be more significant in the transversal direction due to constraints imposed during welding. The heat introduced during welding has a stress relief effect on the cold-rolled base material, although it does not promote any solid-state transformation. The effect of the heat input on the residual stress pattern and magnitude was identified and it was seen that high heat input leads to a higher magnitude of the residual stresses in the weld and the stress relief effect is observed over a larger extension from the weld centerline. This paper presents the first experimental study on the determination of residual stresses on laser welded NiTi shape memory alloys.

1. Introduction

NiTi shape memory alloys are stimulus-responsive materials which present both superelasticity and shape memory effect [1,2]. Laser welding of NiTi shape memory alloys has widespread rapidly over the last years. Several works report the effect of laser welding on the mechanical and functional properties of the welded joints [3–8]. It is a well-accepted fact that, after laser welding, the material presents a decrease in the mechanical properties when compared to the base material [4,9]. The presence of precipitates in the fusion zone, such as Ti_2Ni, is pointed out as a reason for the decreased in ductility of the welded material [9,10].

In fusion based welding processes, such as laser, the gradient of peak temperature followed by a variation in heating and cooling rates along a weld induces residual stresses in the weld region and its neighborhood [11,12]. The welding residual stress field depends on a variety of factors such as: material properties, welding process parameters, pre-heating temperature (if any) and dimensions of the structure to be welded as well as imposed external restrain conditions [13]. Residual stresses may give origin to distortions in the welded material, and these may cause premature failure during service [14,15].

Residual stresses can occur due to a structural mismatch or by an uneven distribution of nonelastic strains. Thermal stresses occur in welding due to a localization of the heating source which originates non uniform temperature distributions in the weld itself and surrounding medium [16]. Additionally, the molten zone shrinks during solidification and this shrinkage is constrained by the surrounding cooler material [17]. If any phase transformations, with associated volume change, occur during cooling, it is possible to compensate the tensile contraction stresses that occur in the fusion zone, provided that the phase transformation is associated with a volume expansion and not contraction.

Considering a stress-free base material it is expected that, after welding, the heat affected zone presents compressive stresses, while in the fusion zone tensile stresses should be found. This can be explained based on the "Three-bar Arrangement Theory" [18]: consider three similar metal bars, all at room temperature, connected by two rigid blocks. The bar located in the middle is heated up. However, its thermal expansion is restrained by the other two side bars. As such, compressive stresses are developed in the middle bar (while the side bars are in tension) and increase with increasing temperature. When heating stops and the middle bar is allowed to cool down, its thermal contraction is restrained again by the side bars. Then, the stress state is reversed: the middle bar is under tensile stress and the side bars under compressive stresses. Comparing to the different regions of the welded material, the middle bar acts as the fusion zone and the side bars as the heat affected zone. Fig. 1 depicts the expected residual

* Corresponding author.
E-mail address: jp.oliveira@campus.fct.unl.pt (J.P. Oliveira).

http://dx.doi.org/10.1016/j.matdes.2016.03.137
0264-1275/

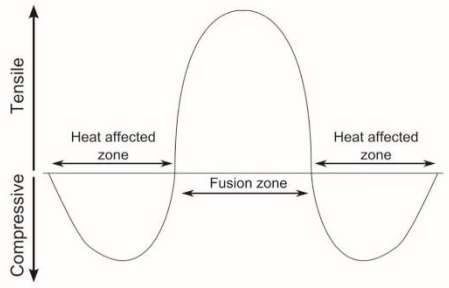

Fig. 1. Expected residual stresses in the heat affected and fusion zones after welding.

stresses in these regions of the weld. In the non-thermally affected base material the development of residual stresses is not expected.

It must be noticed that residual stresses are always present after welding. In case of large structures post-weld heat treatments are performed so that the yield stress decreases and the residual stresses left on the structure are of the order of magnitude of the yield strength of the material at the temperature of the heat treatment, decreasing their magnitude and increasing the joints mechanical performance [19,20].

Measuring residual stresses by X-ray diffraction methods is a precision reliable technique. These measurements can be performed either with laboratorial sources (low energy X-rays) or in dedicated facilities, known as storage rings, with high energy X-rays. The former are used to determine the residual stresses in a restrict thickness of the welded samples due to its low energy and, hence, its low material penetration. In opposition, in synchrotron facilities the same analysis can be performed throughout the material, as its energy is considerably higher (up to 300 keV). The use of these hard X-ray sources allows for a greater penetration in the analyzed samples, thus it is possible to work in transmission mode even when using thick samples (up to 10 mm, for example). Other advantages of the use of synchrotron radiation include the very fast acquisition time (below the millisecond range if necessary) and the ability to decrease the analyzed spot size while keeping an intense beam (high photon flux). The capabilities of using synchrotron radiation, for fine probing of materials joining was, recently, observed by Cavaleiro et al. [21] in self propagated diffusion joining of NiTi.

Although it is usual to analyze the effect of the welding process on the residual stresses of the welded joints [22–24], no such work was yet performed in laser welded NiTi shape memory alloys. As such, there is a gap in research that needs to be filled for this specific class of functional materials. Due to the intrinsic characteristics of laser welding (high energy density with reduced width of the thermally affected zones) analysis of the different regions by X-ray diffraction requires precise control of the beam dimension and its positioning in the weld. Synchrotron X-ray diffraction was carried out for such analysis, as the radiation beam is very small, has a high photon flux, and can be precisely directed to the different regions of the weld.

In this work, X-ray synchrotron radiation was used to probe laser welded NiTi samples from the base material to the fusion zone using a beam with a cross section of 200 × 200 μm. The calculation of the residual stresses was performed using Rietveld analysis with MAUD.

2. Experimental procedure

Plates 1 mm thick of 50.8Ni-Ti (at.%) shape memory alloy, supplied by Memry in the flat annealed condition, were used. To characterize the structural transformation temperatures of the base material, Differential Scanning Calorimetry (DSC) was used. The temperature range was set between −160 and 70 °C. Both cooling and heating rates

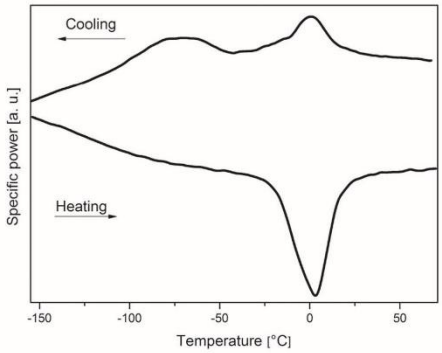

Fig. 2. DSC measurement of base material.

were set at 10 K/min. From these measurements it was confirmed that the base material was fully austenitic at room temperature (Fig. 2).

A Nd:YAG laser, operating in continuous wave mode, from Rofin Sinar was used for laser butt joining the plates. Prior to welding, the samples were cut using a precision cutting machine into 30 × 30 sq mm and cleaned with alcohol and acetone. Two welding conditions were selected and are presented in Table 1. These parameters were chosen in order to obtain full penetration joints, without defects, but with significantly different heat inputs. Argon and helium were used as shielding gases on the face and on the root, respectively, to prevent oxidation.

Microstructure of the welded joints (Fig. 3) revealed that heat affected zone was constituted by coarser equiaxed grains when compared to the base material. From the favorable oriented grains in the heat affected zone, columnar epitaxial grains grew in the fusion zone.

X-ray diffraction was performed at beamline P07 High Energy Materials Science (HEMS) of Petra III/DESY, using a wavelength of 0.1426 Å (87 keV) and a 2D detector Mar345 placed at 1.35 m from the sample. The pixel size of the detector was of 200 × 200 μm and the corresponding accuracy of the measured 2Θ angle was of 0.0084°. A probing line, perpendicular to the weld bead, started and ended in the base material, 3 mm away from the weld centerline, passing through the heat affected zone and the fusion zone.

The experimental setup using during the X-ray diffraction experiments is depicted in Fig. 4. Based on the sample orientation in terms of laboratory referential (Fig. 4), the azimuthal angle, φ, is defined as equal to 0° in the longitudinal direction of the weld bead and equal to 90° for the transversal direction (perpendicular to the weld bead).

Throughout the experiments, performed at room temperature, complete Debye-Scherrer diffraction rings were obtained (Fig. 5).

For residual stress analysis, Rietveld code implemented in MAUD [25] was used following a similar procedure as described in [26]. During Rietveld refinement, parameters such as background, intensity, profile shape, unit cell, texture and stress model were refined. For the Rietveld analysis, four austenite peaks were considered: (100), (110), (111) and (200). When both austenite and martensite were present, five additional martensite peaks were considered: (101), (110), $(1\bar{1}1)$, (020) and (211). These peaks used for Rietveld analysis are shown in Fig. 6. During

Table 1
Laser welding parameters.

Sample	Power [W]	Welding speed [mm/s]	Heat input [J/cm]
A	990	25	396
B	1485	20	743

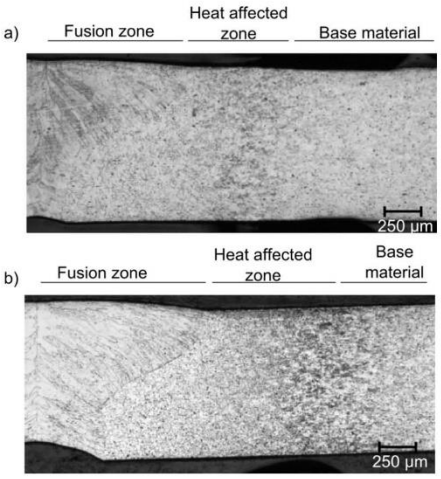

Fig. 3. Microstructure of the welded joints: a) sample A; b) sample B.

the Rietveld analysis performed in MAUD, integration in 5° steps along the azimuthal angle was performed. The mechanical properties of both phases used in the stress model are described in [27,28].

Following other authors [29] that have made similar assumptions when performing residual stress analysis using X-ray diffraction, a plane-stress condition was assumed owing to the reduced thickness of the material (1 mm).

According to the configuration used during X-ray diffraction experiments (Fig. 4), the principal directions of the system are:

- x component, along the longitudinal direction to the weld bead;
- y component, perpendicular to the weld bead;
- z component, normal to the material surface.

As a plane-stress condition is assumed, the principal stresses along the principal direction z, σ_Z, will be null, while the remaining principal stresses, σ_X and σ_Y, can be calculated through Rietveld refinement.

3. Results and discussion

Fit2D [30] was used to analyze the diffraction images in the 2Θ range from 3.4 to 4.2°. For obtaining the X-ray diffraction patterns correspondent to each analyzed spot, the raw diffraction images were integrated along the full azimuthal angle φ. As such, it was possible to perform a microstructural characterization of the existing phases in the different regions of the welds. Fig. 7 depicts the superimposition of the diffractograms obtained for samples A and B. It is observed, that, in the former, the base material was fully austenitic, but the heat affected and the fusion zones showed austenite and martensite, the latter being present at room temperature due to the welding thermal cycle. Sample B had also austenite and martensite in the thermally affected zones, but the extension of each region was slightly larger due to the higher heat input introduced in this weld.

The variation of the 2θ peak position of (110) austenite peak, which is the most intense for the NiTi system, in welds A and B, in three distinct regions of the weld (base material, heat affected and fusion zones) is depicted in Fig. 8. Fig. 8a and d, correspond to the base material and show that the 2θ position of the (110) austenite peak does not vary significantly along the azimuthal angle. However, in the heat affected zone (Fig. 8b and e) the variation is more notorious and is impaired in the fusion zone (Fig. 8c and f). It must be noticed that in the thermally affected zones a coarse grain structure is observed due to grain growth at high temperature. These coarse grains cause high intensity peaks.

After Rietveld refinement, good agreement in position, width and intensity between the calculated and experimental patterns was observed (Fig. 9), indicating a good fitting.

The calculated principal residual stresses, σ_X and σ_Y, for the welded samples are depicted in Fig. 10.

Considering both samples, the σ_X residual stress in the heat affected zone range from roughly 10 to 105 MPa, while in the fusion zone the residual stresses reach up to 135 MPa for the sample welded with the highest heat input. It can be observed an inversion of the stress state when approaching the fusion zone from the heat affected zone: the σ_Y

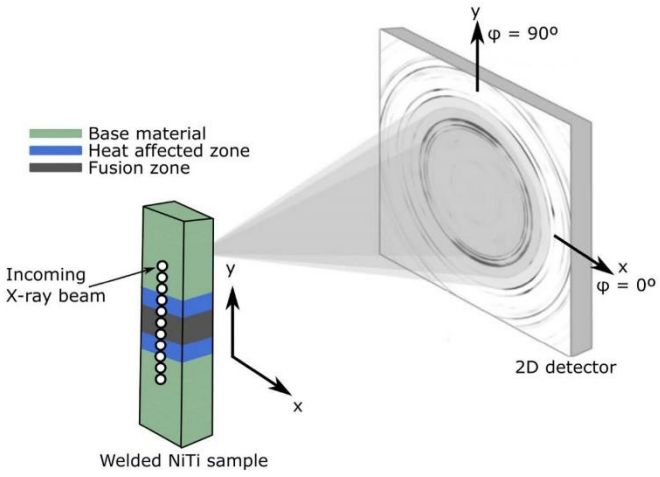

Fig. 4. Experimental setup for the X-ray diffraction experiments (not to scale): 3D schematic view.

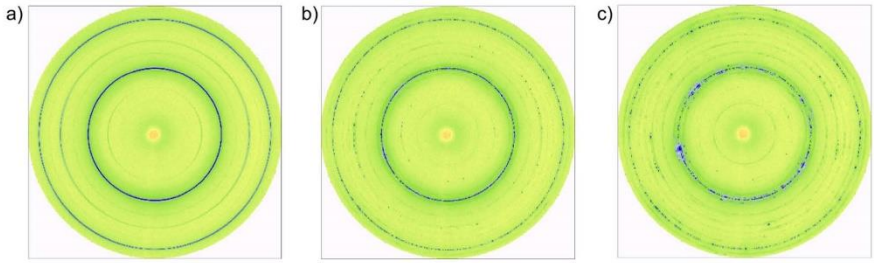

Fig. 5. Typical Debye-Scherrer rings for laser welded NiTi: a) base material, b) heat affected zone, c) fusion zone.

residual stresses are always compressive in the heat affected zone and range between 20 and 60 MPa in the fusion zone.

The inversion of the residual stress conditions in the principal directions, measured in the heat affected and fusion zones was also reported for other materials, such as steels [31]. The base material presented also residual stresses originated during its manufacturing process. It can also be observed that the distribution of the residual stresses in the material is symmetric relative to the weld centerline axis, which is characteristic of laser welding with a top hat or Gaussian beam profiles.

Comparing the residual stresses along the principal directions for the same welded sample, it can be observed that the absolute value of the residual stresses is higher along the y axis than along the x axis. This is due to the fact that, during welding, a constraint was applied along this direction in order to guarantee a good fit-up throughout the full weld length. As such, the material was not able to move freely, generating residual thermal stresses along this direction.

Of particular interest is the stress relief phenomenon observed for the principal stress σ_Y in the base material, marked in Fig. 10. Similarly, along the other principal direction (x axis), the same feature is observed. The reason for this behavior is related to the fact that, along the transversal direction (y axis), there is a decrease in the tensile stresses in the work-hardened base material. Since no distortions were observed after welding, this means that an overall equilibrium was achieved, justifying the inversion of the stress state in the base material along the longitudinal direction. In the base material, the occurrence of microstructural modifications was not expected as the maximum temperatures reached are below those needed to induce any precipitation and/or recrystallization phenomena. This stress relief of the work-hardened base material occurs in the regions that have been heated up to temperatures below 350 °C. As a consequence, the residual stresses magnitude in this region decreases due to the fusion welding process, reverting the effect of cold working without changing the grain structure of the material [32]. In the regions heated above

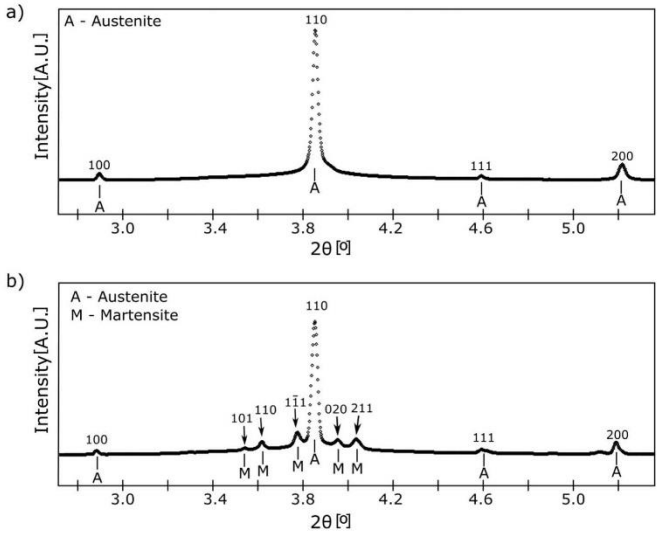

Fig. 6. Austenite (A) and martensite (M) peaks considered for Rietveld refinement: a) typical diffractogram from the base material; b) typical diffractogram from the heat affected and fusion zones.

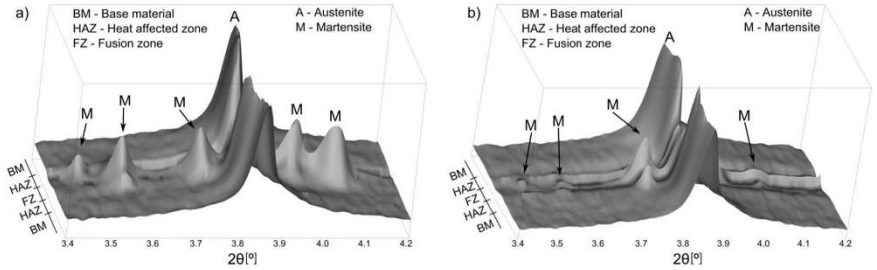

Fig. 7. 3D stacking of the diffractograms performed on laser welds: a) sample A; b) sample B.

350 °C, Ni-rich precipitates, such as Ni_4Ti_3, may be formed for time lapses in the order of a few seconds [33], increasing the transformation temperatures, thus leading to the presence of martensite at room temperature.

In order to understand the feasibility of the welding procedure to promote the aforementioned stress relief phenomenon, the peak temperatures in the base material were computed based on the 2D solution of the Rosenthal equation:

$$T - T_0 = \frac{Q}{2\pi k g} e^{(v x/2\alpha)} K0\left|\frac{v R}{2\alpha}\right|$$

where:

T, is the peak temperature at a distance x in the (x, y) plane (K);
T_0, is the room temperature (K);
Q, is the heat input (Jm^{-1}).
k, is the thermal conductivity ($W m^{-1} K^{-1}$);
g, is the plate thickness(m);
v, is the welding speed ($m s^{-1}$);
α, is the thermal diffusivity ($m^2 s^{-1}$);
K0, is a modified Bessel function of the second kind and zero order;
R, is the radial distance ($R = \sqrt{x^2+y^2}$) (m).

Both x and y directions were defined as in Fig. 4. Fig. 11, depicts the peak temperature variation as a function of the distance to the weld centerline along the y direction for welds A and B. It can be observed, that the distance from the weld centerline at which the temperature range is between 200 and 350 °C (for promoting the stress relief phenomenon), is similar to those obtained from the X-ray diffraction measurements, thus validating this assumption.

The effect of the higher heat input in sample B, gives rise to a higher magnitude of the residual stresses in the different regions of the weld (heat affected zone and fusion zone), in either the principal directions, when compared to sample A. A similar effect of the heat input on the magnitude of the residual stresses was observed by other authors [34]. This can be explained using the "Three-bar Arrangement Theory" described in the introduction.

Another interesting consequence of the higher heat input introduced in sample B is that the stress relieving phenomena in the base material occurs at a longer distance from the weld centerline, when

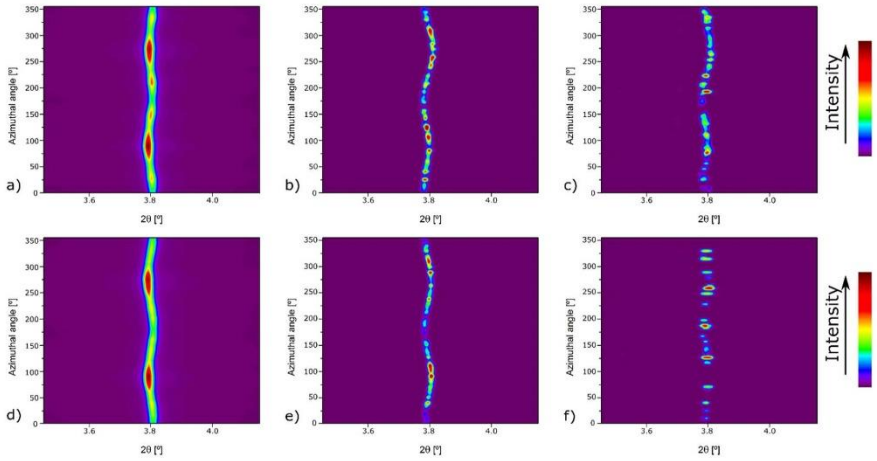

Fig. 8. Variation of the 2θ peak position of the (110) austenite peak along the azimuthal angle, φ, sample A (top) and B (bottom). a) and d) correspond to the base material; b) and e) to the heat affected zone and c) and f) to the fusion zone.

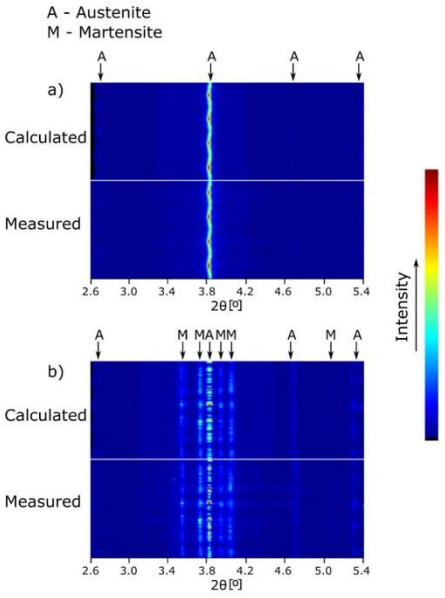

Fig. 9. Calculated and measured diffraction patterns: a) in the base material where only austenite (A) exists; b) in the fusion zone where both austenite and martensite (M) are present.

compared to sample A. This effect is evident in Fig. 10, where the stress relief phenomenon is seen to occur in a region about 0.2 mm wider than in sample A: higher heat input allows for a more extended heat propagation in the base material, which, in turn promotes the stress relieving phenomena. Additionally, the higher heat input originates a higher extension of the thermally affected regions.

From the principal stresses calculated using the Rietveld method, the von Mises stresses can also be obtained [35]. The evolution of the von Mises stresses along the welded materials is depicted in Fig. 12. In a localized narrow region of the heat affected zone, the von Mises stress reaches a maximum value of 375 MPa. Previous results [8,36] have shown that the critical stress for the martensitic transformation for laser welding of NiTi range between 335 and 375 MPa. However, in

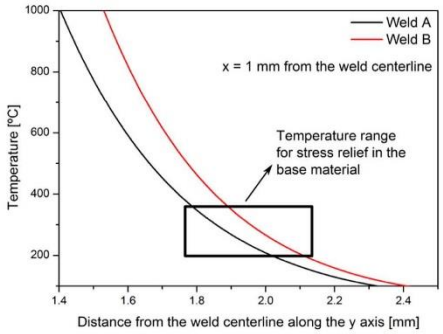

Fig. 11. Peak temperatures, from the weld centerline along the y axis, at a fixed distance of x = 1 mm from the weld centerline. The black box represents the temperature range where stress relief phenomenon may occur.

the remaining regions of the welded material the von Mises stresses are below this range.

The residual stresses were also measured for the martensite in both the heat affected and fusion zones, where this phase was observed. However, the residual stresses calculated for this phase ranged between −6 and 8 MPa, which can be negligible considering the magnitude of the residual stresses found for the austenitic phase. The reason for this to occur is related to the mechanical properties of austenitic and martensitic NiTi. The former has a higher Young's modulus than the latter. As such, the load will be predominantly transferred to the "harder" material, which is austenite in this case. Additionally, martensitic NiTi has a lower constant stress plateau than austenitic NiTi, which enables stress relaxation of the neighboring austenite. Similar behavior was also reported to occur for Cu-based shape memory alloys [37].

No distortions were observed after butt welding the NiTi plates. This is related to the fact that the global residual stresses along the material are in equilibrium.

It is possible to alter the residual stresses within a welded joint by applying proper post-weld heat treatments. The effect of different post-weld heat treatments on the distribution of the residual stresses in laser welded NiTi joints is currently under study.

4. Conclusions

The first experimental study for the determination of residual stress in laser welded NiTi shape memory alloys is presented. For this,

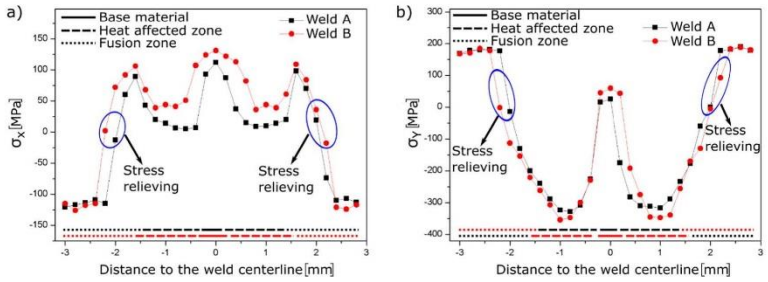

Fig. 10. Calculated residual stress for welds A and B: a) σ_X, b) σ_Y.

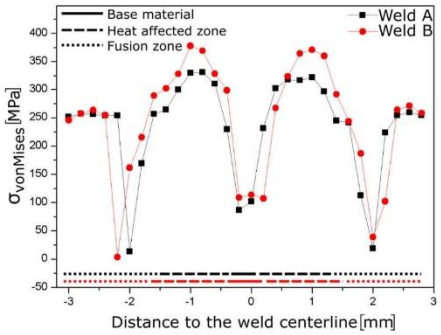

Fig. 12. von Mises stresses along the welded materials.

synchrotron radiation based X-ray diffraction was used and this data was exploited with Rietveld analysis. The following can be concluded:

- The principal stresses along the x axis were found to fall within the range of 10 to 105 MPa in the heat affected zone, while in the fusion zone they increase up to 135 MPa. The σ_Y residual stresses were found to be always compressive in the heat affected zone, while in the fusion zone there is a tensile stress state with a magnitude ranging from 20 to 60 MPa.
- The inversion of the stress states in the different regions of the weld (heat affected and fusion zones) is in good agreement with general welding thermo-mechanical analysis.
- The heat input introduced in the welds promoted stress relief phenomena on the work-hardened base material. As such, the residual stresses in this region decreased.
- Stress relieving phenomena on the base material occur at temperatures below 350 °C.
- Higher heat input originates higher magnitude of the residual stresses, in absolute modulus, in the heat affected and fusion zones.
- No distortions were observed after welding and this results from an overall near equilibrium stress state.

Acknowledgments

JPO and FBF acknowledge funding of CENIMAT/I3N by FEDER funds through the COMPETE 2020 Program and National Funds through FCT - Portuguese Foundation for Science and Technology under the project UID/CTM/50025/2013. RMM acknowledges funding of UNIDEMI by FEDER funds through the COMPETE 2020 Program and National Funds through FCT - Portuguese Foundation for Science and Technology under the project UID/EMS/00667/2013. The authors acknowledge DESY and HZG for beam time and travel reimbursement under proposal I-20120563 EC FP7/2007-2013 grant agreement no. 312284. JPO acknowledges FCT/MCTES for funding PhD grant SFRH/BD/85047/2012. The authors acknowledge useful discussions with Professor Luca Lutterotti, developer of MAUD.

References

[1] L. Sun, W.M. Huang, Z. Ding, Y. Zhao, C.C. Wang, H. Purnawali, et al., Stimulus-responsive shape memory materials: a review, Mater. Des. 33 (2012) 577–640, http://dx.doi.org/10.1016/j.matdes.2011.04.065.
[2] J.M. Jani, M. Leary, A. Subic, M.a. Gibson, A review of shape memory alloy research, applications and opportunities, Mater. Des. 56 (2014) 1078–1113, http://dx.doi.org/10.1016/j.matdes.2013.11.084.
[3] A. Tuissi, S. Besseghini, T. Ranucci, F. Squatrito, M. Pozzi, Effect of Nd-YAG laser welding on the functional properties of the Ni–49.6 at.%Ti, Mater. Sci. Eng. A 273-275 (1999) 813–817, http://dx.doi.org/10.1016/S0921-5093(99)00422-0.
[4] Y.T. Hsu, Y.R. Wang, S.K. Wu, C. Chen, Effect of CO2 laser welding on the shape-memory and corrosion characteristics of TiNi alloys, Metall. Mater. Trans. A 32 (2001) 569–576, http://dx.doi.org/10.1007/s11661-001-0073-2.
[5] A. Falvo, F.M. Furgiuele, C. Maletta, Functional behaviour of a NiTi-welded joint: two-way shape memory effect, Mater. Sci. Eng. A 481-482 (2008) 647–650, http://dx.doi.org/10.1016/j.msea.2006.11.178.
[6] H. Gugel, A. Schuermann, W. Theisen, Laser welding of NiTi wires, Mater. Sci. Eng. A 481-482 (2008) 668–671, http://dx.doi.org/10.1016/j.msea.2006.11.179.
[7] J.P. Oliveira, F.M.B. Fernandes, N. Schell, R.M. Miranda, Shape memory effect of laser welded NiTi plates, Funct. Mater. Lett. 08 (2015) 1550069, http://dx.doi.org/10.1142/S1793604715500691.
[8] J.P. Oliveira, R.M. Miranda, N. Schell, F.M. Braz Fernandes, High strain and long duration cycling behavior of laser welded NiTi sheets, Int. J. Fatigue 83 (2016) 195–200, http://dx.doi.org/10.1016/j.ijfatigue.2015.10.013.
[9] P. Schlossmacher, T. Haas, A.S. Ussler, Laser-welding of a Ni-rich TiNi shape memory alloy: mechanical behavior, J. Phys. IV 07 (1997), http://dx.doi.org/10.1051/jp4:1997539 (C5–251 – C5–256).
[10] A. Tuissi, P. Bassani, M. Gerosa, D. Mauri, M. Pini, E. Capello, et al., CO2 laser welding of NiTi/Ni-based alloys, in: A. Pelton, T. Duerig (Eds.),Proc. Int. Conf. Shape Mem. Superelastic Technol. 2004, pp. 229–238, http://dx.doi.org/10.1361/cp2003smst229.
[11] T.-L. Teng, C.-C. Lin, Effect of welding conditions on residual stresses due to butt welds, Int. J. Press. Vessel. Pip. 75 (1998) 857–864, http://dx.doi.org/10.1016/S0308-0161(98)00084-2.
[12] J. Rahman Chukkan, M. Vasudevan, S. Muthukumaran, R. Ravi Kumar, N. Chandrasekhar, Simulation of laser butt welding of AISI 316L stainless steel sheet using various heat sources and experimental validation, J. Mater. Process. Technol. 219 (2015) 48–59, http://dx.doi.org/10.1016/j.jmatprotec.2014.12.008.
[13] D. Deng, H. Murakawa, W. Liang, Numerical and experimental investigations on welding residual stress in multi-pass butt-welded austenitic stainless steel pipe, Comput. Mater. Sci. 42 (2008) 234–244, http://dx.doi.org/10.1016/j.commatsci.2007.07.009.
[14] K. Masubuchi, Analysis of Welded Structures, first ed. Pergamon Press, Oxford, 1980.
[15] Bhatti A a., Barsoum Z, Murakawa H, Barsoum I. Influence of thermo-mechanical material properties of different steel grades on welding residual stresses and angular distortion. Mater. Des. 2015;65:878–89. doi:http://dx.doi.org/10.1016/j.matdes.2014.10.019.
[16] A. Lienert, T. Siewert, S. Babu, V. Acoff, ASM Handbook, Volume 6A, Welding Fundamentals and Processes, first ed. ASM International, Ohio, 2011.
[17] R.S. Coelho, M. Corpas, J.A. Moreto, A. Jahn, J. Standfuß, A. Kaysser-Pyzalla, et al., Induction-assisted laser beam welding of a thermomechanically rolled HSLA S500MC steel: a microstructure and residual stress assessment, Mater. Sci. Eng. A 578 (2013) 125–133, http://dx.doi.org/10.1016/j.msea.2013.04.039.
[18] S. Kou, Welding Metallurgy, second ed. John Wiley & Sons, Inc., Hoboken, 2002, http://dx.doi.org/10.1002/0471434027.
[19] J.R. Cho, B.Y. Lee, Y.H. Moon, C.J. Van Tyne, Investigation of residual stress and post weld heat treatment of multi-pass welds by finite element method and experiments, J. Mater. Process. Technol. 155-156 (2004) 1690–1695, http://dx.doi.org/10.1016/j.jmatprotec.2004.04.325.
[20] A.H. Yaghi, T.H. Hyde, A.A. Becker, W. Sun, Finite element simulation of welding and residual stresses in a P91 steel pipe incorporating solid-state phase transformation and post-weld heat treatment, J. Strain Anal. Eng. Des. 43 (2008) 275–293, http://dx.doi.org/10.1243/03093247JSA372.
[21] A.J. Cavaleiro, A.S. Ramos, F.M. Braz Fernandes, N. Schell, M.T. Vieira, In situ characterization of NiTi/Ti6Al4V joints during reaction-assisted diffusion bonding using Ni/Ti multilayers, J. Mater. Eng. Perform. 23 (2014) 1625–1629, http://dx.doi.org/10.1007/s11665-014-0930-y.
[22] B. Brickstad, B.L. Josefson, A parametric study of residual stresses in multi-pass butt-welded stainless steel pipes, Int. J. Press. Vessel. Pip. 75 (1998) 11–25, http://dx.doi.org/10.1016/S0308-0161(97)00117-8.
[23] T.A. Mai, A.C. Spowage, Characterisation of dissimilar joints in laser welding of steel–kovar, copper–steel and copper–aluminium, Mater. Sci. Eng. A 374 (2004) 224–233, http://dx.doi.org/10.1016/j.msea.2004.02.025.
[24] D. Deng, H. Murakawa, Numerical simulation of temperature field and residual stress in multi-pass welds in stainless steel pipe and comparison with experimental measurements, Comput. Mater. Sci. 37 (2006) 269–277, http://dx.doi.org/10.1016/j.commatsci.2005.07.007.
[25] L. Lutterotti, S. Matthies, H.-R. Wenk, A.S. Schultz, J.W. Richardson, Combined texture and structure analysis of deformed limestone from time-of-flight neutron diffraction spectra, J. Appl. Phys. 81 (1997) 594, http://dx.doi.org/10.1063/1.364220.
[26] H.-R. Wenk, L. Lutterotti, P. Kaercher, W. Kanitpanyacharoen, L. Miyagi, R. Vasin, Rietveld texture analysis from synchrotron diffraction images. II. Complex multiphase materials and diamond anvil cell experiments, Powder Diffract. 4 (2014) 1–13, http://dx.doi.org/10.1017/S0885715614000360.
[27] P. Šittner, L. Heller, J. Pilch, C. Curfs, T. Alonso, D. Favier, Young's modulus of austenite and martensite phases in superelastic NiTi wires, J. Mater. Eng. Perform. 23 (2014) 2303–2314, http://dx.doi.org/10.1007/s11665-014-0976-x.
[28] R. Boyer, G. Welsch, E. Collings, Materials Properties Handbook: Titanium Alloys, first ed. Ohio, ASM International, 1994.
[29] A.M. Korsunsky, S.P. Collins, R. Alexander Owen, M.R. Daymond, S. Achtioui, K.E. James, Fast residual stress mapping using energy-dispersive synchrotron X-ray diffraction on station 16.3 at the SRS, J. Synchrotron Radiat. 9 (2002) 77–81, http://dx.doi.org/10.1107/S0909049502001905.
[30] A.P. Hammersley, S.O. Svensson, M. Hanfland, A.N. Fitch, D. Hausermann, Two-dimensional detector software: from real detector to idealised image or two-theta scan, High Pressure Res. 14 (1996) 235–248, http://dx.doi.org/10.1080/08957959608201408.
[31] G.A. Moraitis, G.N. Labeas, Prediction of residual stresses and distortions due to laser beam welding of butt joints in pressure vessels, Int. J. Press. Vessel. Pip. 86 (2009) 133–142, http://dx.doi.org/10.1016/j.ijpvp.2008.11.004.
[32] J.C.M. Li, Microstructure and properties of materials, World Scientific, first ed., 1996, http://dx.doi.org/10.1142/2882.
[33] A.R. Pelton, J. Dicello, S. Miyazaki, Optimisation of processing and properties of medical grade Nitinol wire, Minim. Invasive Ther. Allied Technol. 9 (2000) 107–118, http://dx.doi.org/10.3109/13645700009063057.

[34] D. Akbari, I. Sattari-Far, Effect of the welding heat input on residual stresses in butt-welds of dissimilar pipe joints, Int. J. Press. Vessel. Pip. 86 (2009) 769–776, http://dx.doi.org/10.1016/j.ijpvp.2009.07.005.
[35] X. Song, M. Xie, F. Hofmann, T.S. Jun, T. Connolley, C. Reinhard, et al., Residual stresses in linear friction welding of aluminium alloys, Mater. Des. 50 (2013) 360–369, http://dx.doi.org/10.1016/j.matdes.2013.03.051.
[36] L.A. Vieira, F.M.B. Fernandes, R.M. Miranda, R.J.C. Silva, L. Quintino, A. Cuesta, et al., Mechanical behaviour of Nd:YAG laser welded superelastic NiTi, Mater. Sci. Eng. A 528 (2011) 5560–5565, http://dx.doi.org/10.1016/j.msea.2011.03.089.
[37] J.P. Oliveira, Z. Zeng, T. Omori, N. Zhou, R.M. Miranda, F.M.B. Fernandes, Improvement of damping properties in laser processed superelastic Cu-Al-Mn shape memory alloys, Mater. Des. 98 (2016) 280–284, http://dx.doi.org/10.1016/j.matdes.2016.03.032.

7.1.6 Laser Joining of NiTi to Ti6Al4V Using a Niobium Interlayer

This paper was submitted and accepted in Acta Materialia.

Acta Materialia 105 (2016) 9–15

Contents lists available at ScienceDirect

Acta Materialia

journal homepage: www.elsevier.com/locate/actamat

Full length article

Laser joining of NiTi to Ti6Al4V using a Niobium interlayer

J.P. Oliveira [a, b, *], B. Panton [b], Z. Zeng [b, c], C.M. Andrei [d], Y. Zhou [b], R.M. Miranda [e], F.M. Braz Fernandes [a]

[a] CENIMAT/i3N, Faculdade de Ciências e Tecnologia, Universidade Nova de Lisboa, Portugal
[b] Centre for Advanced Materials Joining, University of Waterloo, Canada
[c] School of Mechanical, Electronic, and Industrial Engineering, University of Electronic Science and Technology of China, China
[d] Canadian Center for Electron Microscopy, Brockhouse Institute for Materials Research, McMaster University, Canada
[e] UNIDEMI, Faculdade de Ciências e Tecnologia, Universidade Nova de Lisboa, Portugal

ARTICLE INFO

Article history:
Received 23 October 2015
Received in revised form
27 November 2015
Accepted 10 December 2015
Available online xxx

Keywords:
NiTi
Ti6Al4V
Laser joining
Microstructure
Transmission electron microscopy

ABSTRACT

Joining NiTi to Ti6Al4V is of great interest for applications in the biomedical and aerospace fields. Despite the importance, no joining techniques have been developed that avoid the formation of brittle intermetallics to produce high strength joints. In this work, Niobium was used as an interlayer to prevent the formation of these brittle phases when joining NiTi to Ti6Al4V. The presence of this interlayer ensured that crack free welds were obtained and no brittle intermetallic compounds were observed. The Niobium interlayer was of a much higher melting temperature than the base materials so the bulk Niobium did not melt during the joining process, acting as a diffusion barrier between the NiTi and Ti6Al4V. The laser was focused on the Ti6Al4V side of the joint, which joined the Ti6Al4V and Niobium by fusion welding. At this interface a (Ti, Nb) region was formed due to dilution of the Niobium and mixing with the Ti6Al4V. At the NiTi–Nb interface a eutectic reaction was responsible for joining. Mechanical testing of the joints revealed that the minimum tensile strength matched the ultimate tensile strength of the weakest material, Niobium. These results highlight new possibilities for the use of high melting point filler materials when joining NiTi to dissimilar materials, so that the formation of undesired phases can be avoided.

1. Introduction

The functional properties of NiTi shape memory alloys (i.e. the shape memory effect and superelasticity) [1] are of significant interest in a wide range of industries including medical [2], aerospace [3] and seismic damping devices [1]. In addition to these functional properties NiTi has excellent physical properties and good resistance to fatigue [4], and corrosion [5], that increase its desirability in these applications. Titanium alloys are desired to be part of these same applications because of their remarkable strength, toughness, fatigue resistance, corrosion resistance and biocompatibility [6]. Ti6Al4V is the most widely used Ti alloy with applications found in aerospace, nuclear, civil, chemical and biomedical industries [7]. These highly versatile materials are being integrated into complex multi-component systems, in which overall system performance is optimized by tailoring individual component properties.

The manufacturing of multi-component systems often requires joining of dissimilar materials to achieve complex shapes and geometries. Direct joining of NiTi and Ti6Al4V has encountered severe problems because of differences in their physical and chemical properties [8–10]. Crystallographic mismatch between the alloys, and the formation of brittle intermetallics (i.e. Ti_2Ni, Ni_3Ti and Al_3Ti) contribute to solidification cracking and brittle failure of the joints [9–11]. Attempts have been made to minimize mixing of the alloys to avoid these brittle phases but even the low mixing and low brittle phase formation of reaction-assisted diffusion bonding was unable to avoid the brittle Ti_2Ni phase [12]. Using a braze material to stop mixing has been attempted, but the joints had poor mechanical properties [13].

The high power intensity and low heat input of laser welding has achieved successful joining where conventional joining techniques have failed. Furthermore, the rapid heating and cooling, low distortion, high accuracy and flexibility of this process are desirable for joining NiTi SMAs which are sensitive to the welding cycle [14].

* Corresponding author. CENIMAT/i3N, Faculdade de Ciências e Tecnologia, Universidade Nova de Lisboa, Portugal.
E-mail address: jp.oliveira@campus.fct.unl.pt (J.P. Oliveira).

http://dx.doi.org/10.1016/j.actamat.2015.12.021
1359-6454/

Previous investigations of dissimilar NiTi joining [15,16] offset the laser into one of the base materials to control the degree of mixing; however, the diffusion of the alloying elements was not fully stopped, so brittle intermetallics were still formed. The only reported attempt to use an interlayer to join NiTi and Ti6Al4V has been by Zoeram et al. [10] who studied the use of a Copper interlayer. Use of the Copper interlayer reduced the amount of brittle Ti_2Ni intermetallics; however, brittle Cu-based intermetallics, such as Ti_2Cu formed. These Cu-based intermetallics were found to be less brittle than the Ti_2Ni phase but they still negatively impacted the ductility of the joint.

Use of an interlayer that becomes part of the weld pool has not proven to be sufficient to inhibit the formation of brittle intermetallics when joining NiTi to dissimilar materials [17–19]. Interlayers with a higher melting point than two dissimilar base materials have proven to be successful diffusion barriers that did not allow mixing [20–22]. It is hypothesized that this method could be applied to successfully join NiTi and Ti6Al4V. Selection of an appropriate interlayer for the NiTi–Ti6Al4V joint can be determined using the following criteria:

- No brittle intermetallics are formed with either alloy;
- Crystallographically similar, and miscible with both alloys;
- No detrimental effects to system biocompatibility

With these criteria in mind Niobium was identified as a potential interlayer for the dissimilar joining of NiTi and Ti6Al4V. It is a refractory metal with a melting point of 2477 °C and, when pure, it is malleable and ductile so can conform easily to any joint configuration [23,24]. The melting point of Niobium is significantly higher than that of NiTi (1310 °C [25]) and Ti6Al4V (1660 °C [26]), so Niobium would be an excellent diffusion barrier between NiTi and Ti6Al4V; with previous proven use as a diffusion barrier between Ti and stainless steel [27]. Niobium has been successfully laser welded to Ti6Al4V [28], and joined with a eutectic reaction to NiTi [23] without the formation of brittle intermetallics, which are not present in these systems [29]. It is hypothesized that if Niobium is used as an interlayer for joining NiTi and Ti6Al4V that the laser can be offset into the Ti6Al4V so that fusion joining occurs on the Ti6Al4V–Nb side of the joint, while eutectic bonding occurs on the NiTi–Nb side of the joint. The relatively high conductivity of Niobium (52.3 m^{-1} K^{-1} [24]) to NiTi (18.0 m^{-1} K^{-1} [30]) and Ti6Al4V (6.6 m^{-1} K^{-1} [31]) would make it a good conductor of heat from the laser heated Ti side to the NiTi side and enable the eutectic reaction to form a joint.

In the current study, a Niobium interlayer was used for pulsed laser joining of NiTi to Ti6Al4V. Defect-free joints were produced, that matched the ultimate tensile strength of the Niobium interlayer.

2. Materials and methods

The NiTi shape memory alloy used in this study was purchased from Memory, had a nominal composition of 50.8 at. % Ni-49.25 at. % Ti, a thickness of 1 ± 0.05 mm, and was superelastic at room temperature. The Ti6Al4V, had a thickness of 1.1 ± 0.05 mm and was purchased from Titanium Joe. A pure Niobium interlayer (99.99 at. %) with a thickness of 50 μm, was purchased from ESPI Metals. Plates of NiTi and Ti6Al4V, with dimensions of 30 × 30 mm, were prepared using a Struers Accutom 50 precision cutting machine. The faying surfaces were ground to 1200 fine grit SiC paper to ensure proper joint fit-up and then cleaned with acetone and ethanol to completely remove impurities.

2.1. Laser welding

A Miyachi Unitek LW50A pulsed Nd:YAG laser system, with a wavelength of 1064 nm, a top-hat spatial profile and a spot size of 400 μm was used. The pulse profile had a peak power of 3.0 kW and a width of 20 ms, including a 3 ms upslope and a 15 ms downslope. The laser spot welds were overlapped by 25% to obtain a continuous weld. NiTi, Ti6Al4V, and Niobium oxidize in air and are prone to hydrogen pickup and embrittlement so a protective atmosphere is required when joining at higher temperatures. Argon was used as shielding gas at a flow rate of 0.99 m^3/h.

Preliminary welding tests were performed without filler material to determine the welding power intensity required. As expected from previous work [9], cracking upon solidification occurred due to the formation of brittle intermetallics and residual thermal stresses. In order to overcome the solidification cracking, a Niobium interlayer was introduced between the materials as a diffusion barrier. Fig. 1 depicts a schematic of the set up used for the laser welding procedure. The laser was positioned on the Ti6Al4V side of the joint (250 μm from the joint interface), so that 60% of the beam was positioned on the Ti6Al4V top surface. The Ti6Al4V was preferentially heated because NiTi suffers a degradation of properties at high temperatures. Furthermore a eutectic mixture is forms between NiTi and Niobium [32], which requires a lower amount of energy to promote joining than between the Niobium and Ti6Al4V.Finally, focusing the laser on the NiTi did not form a joint to the Ti6Al4V side.

2.2. Microstructural analysis

Transmission electron microscopy (TEM) was performed on the joint interfaces between Niobium and both base materials. Focused Ion Beam (FIB), using a Zeiss NVision 40 was used to obtain 10 × 10 μm specimens from the region of interest. TEM analysis was performed in a JEOL 2010F TEM/STEM operated at 200 kV. The electron microscope was equipped with an Oxford Inca Energy Dispersive X-ray (EDS) system and a Gatan imaging filtering (GIF) system for the acquisition of the electron energy loss spectra (EELS). Spectrum imaging technique was used to acquire an energy loss spectrum at each pixel of a selected area. Scanning TEM (STEM) EDS maps were obtained with a 1 nm probe diameter.

2.3. Mechanical testing

Test samples from the welds were prepared with an overall gauge length of 30 mm and a cross-section of 2 mm^2. Three welded specimens were analyzed. Tensile tests were performed according to the ASTM F2516-07 standard, at room temperature using an Instron model 5548 microtensile tester with an accuracy of ±0.5 μm at a displacement rate of 0.5 mm/min. Tensile strength and elongation up to fracture average values were obtained. Scanning electron microscopy (SEM) of the fracture surfaces was performed

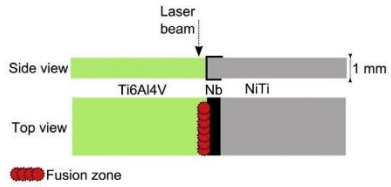

Fig. 1. Schematic of the set up used in the welding procedure.

using a Zeiss Leo 1550 Field Emission SEM with an accelerating voltage of 10 kV.

3. Results and discussion

Positioning of the laser beam on the assembly was of major importance to forming the joint. Positioning of the laser on the NiTi base material was found not to promote joining at the Ti6Al4V–Nb interface. Only with the laser focused on the Ti6Al4V side were sound joints obtained. In this configuration a good fit-up between the NiTi/Nb/Ti6Al4V was required to prevent gaps and ensure adequate heat transfer to form a joint. No joint would form if the beam was too far from the Ti6Al4V–Nb interface because insufficient heat was delivered to the NiTi–Nb side of the joint. Positioning the laser too close to the Ti6Al4V–Nb interface would also lead to no joint forming because the laser was reflected off by the Niobium interlayer.

A cross section of a weld captured during FIB milling is shown in Fig. 2. The interlayer formed defect-free interfaces with both the NiTi and the Ti6Al4V (Fig. 3). The pores observed in Fig. 2 were created during milling of the sample for transmission electron microscopy; there was no observed porosity of the specimens prior to milling. As discussed above, the laser was positioned over the Niobium and Ti6Al4V side of the joint, but the significant differences in the melting points of materials resulted in only the Ti6Al4V and NiTi melting while the bulk of the Niobium interlayer remained solid. Necking was observed in the fusion zone on the Ti6Al4V side of the joint. Similar non-symmetrical weld pools were observed during laser and electron-beam welding of Ti6Al4V to Niobium alloys [28,33]. The high melting point and thermal conductivity of the Niobium has been cited as the cause of asymmetry in weld pools. Wetting of the Niobium by the Ti6Al4V, as shown in Fig. 2, is another factor that contributed to the necking. Finally, positioning of the laser beam on the Ti6Al4V can cause a loss of material through vaporization which can also contribute to the observed necking [34].

3.1. Ti6Al4V–Nb Interface

As a result of the good wettability of the liquid Ti on the Niobium surface, the liquid phase incorporates Niobium and promotes its diffusion due to convection currents. However, as both elements have full solubility in one another, solid state diffusion of Ti into Niobium also occurs, as observed in Fig. 4. A (Ti, Nb) region formed at the interface of the Niobium interlayer and the fusion zone as shown in Fig. 4. The (Ti, Nb) region had a width of 30 nm, and additional Niobium diffused into the liquid to a distance of at least 200 nm, mixing thoroughly in the melt by convection currents and the Marangoni effect [35].

The content of Ti, Al and V in the (Ti, Nb) region decreased compared to the Ti6Al4V base material. Point EDS in the (Ti, Nb) region revealed an overall composition of 47.7Ti-46.2Nb-2.9Al-3.3V

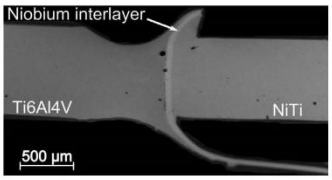

Fig. 2. Scanning electron microscopy image of the dissimilar joint.

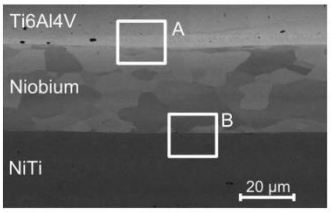

Fig. 3. Scanning electron microscopy image of the interface between the Niobium and both the Ti6Al4V and the NiTi. The white squares mark the areas prepared by FIB and used for TEM analysis, shown in Figs. 4–6.

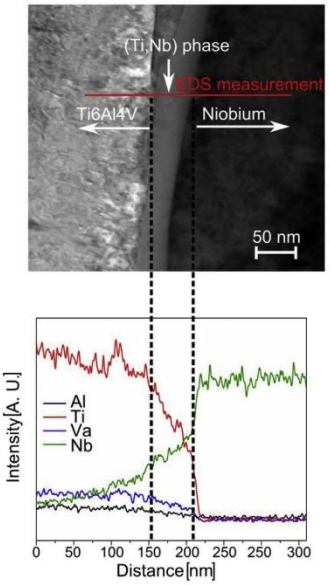

Fig. 4. Above: (Region A from Fig. 3) STEM image and EDS line scans across the Nb–Ti6Al4V interface, with the (Ti, Nb) region identified. The red line represents the EDS line scan. Below: Results for EDS line scan. (For interpretation of the references to colour in this figure legend, the reader is referred to the web version of this article.)

(in wt. %). Some TiNb-based alloys have similar compositions to this region [36,37]. The addition of Nb to these alloys results in both powerful β-stabilization and solid-solution strengthening [38]. A minimum of 36 wt. % Nb is required to stabilize the high temperature β phase at room temperature [39]. Computing the Al and Mo equivalency [39] of the (Nb,Ti) region indicated that it should be β metastable at room temperature.

Electron energy loss spectroscopy (EELS) provided a finer spatial distribution of the elements at the interface as shown in Fig. 5. The lack of mixing of Niobium with the Ti6Al4V at the Nb-fusion zone interface resulted in the (Ti, Nb) region forming. Similar segregated regions have been previously observed in dissimilar joints [14]. The mean free path of diffusion each element into a given region is limited by the temperature achieved during welding and the time

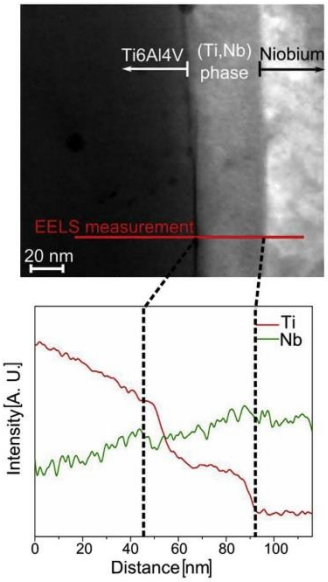

Fig. 5. Above: Region of Ti6Al4V–Nb joint interface where EELS measurements were performed. The red line represents the EELS line scan. Below: Results for EELS measurements. (For interpretation of the references to colour in this figure legend, the reader is referred to the web version of this article.)

for diffusion to occur [40]. The difference in composition and the high heating and cooling rates of the pulsed laser welding process contributed to the lack of mixing of the (Ti, Nb) region with the bulk of the fusion zone [14]. At the interface between the (Ti, Nb) region and the Niobium interlayer there was a sharp discontinuity in the Titanium spectra, which indicated no elements had diffused into the interlayer, due to the short time of the joining process.

3.2. NiTi–Nb interface

A eutectic NiTi and Niobium microstructure was observed at the NiTi–Nb interface as shown in Fig. 6 (which corresponds to insert B of Fig. 3). This microstructure was previously observed by Grummon et al. [41] when brazing NiTi to pure Niobium. It was suggested that a quasibinary eutectic isopleth exists between the intermetallic NiTi and pure Niobium [32,41]. The eutectic isotherm is 140 °C below the congruent melting temperature of NiTi (1310 °C). Spontaneous melting occurred with the pure Niobium being in intimate contact with NiTi at the high temperatures, and upon solidification two phases were formed: austenitic NiTi and bcc-Nb [42].

From the quasi-binary phase diagram it can be determined that the interface between NiTi and Niobium will spontaneously melt at temperatures above 1170 °C. It is expected that, in conditions close to equilibrium, the first liquid to form has a composition similar to the eutectic point at $Ni_{38}Ti_{36}Nb_{24}$. However, in the fast heating and cooling of pulsed laser welding the equilibrium condition does not occur [43]. In zone A of Fig. 6, was identified as the un-melted NiTi base metal. A proeutectic zone (zone B), which terminated in bulbous projections, was observed near the non-melted NiTi.

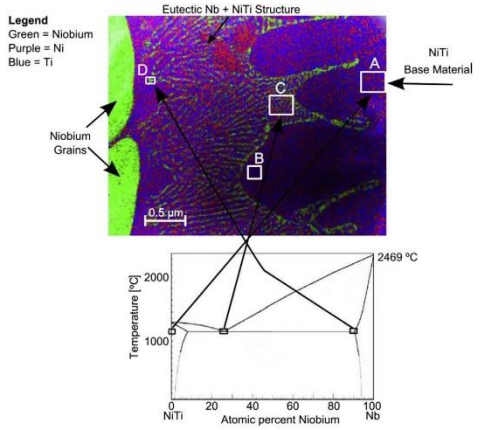

Fig. 6. EDS mapping of the NiTi–Nb interface, and a correlation of different regions with the NiTi–Nb phase diagram (adapted from Ref. [17]).

Selected area diffraction (SAD) was performed in these NiTi regions as marked in Fig. 7a). Indexing the SAD image in Fig. 7b) confirmed that these regions were the austenitic phase of NiTi.

The majority of the joint was composed of a lamellar eutectic solidification region as observed in zone C of Fig. 6. Using STEM in High Angle Annular Dark Field (HAADF) mode it was possible to distinguish between light (i.e. NiTi) and heavy (i.e. Nb) elements [44], as shown in Fig. 8. EDS mapping of these regions confirmed the dark regions were Niobium lean and the light regions were Niobium rich regions of a eutectic structure as shown in Table 1.

On the left side of Fig. 6, Niobium-rich regions were observed, which were identified as the un-melted Niobium grains. Significant grain boundary penetration around these Niobium grains is shown in Fig. 9 [45]. The faster diffusion along these paths resulted in the eutectic reaction propagating along the grain boundaries instead of through the bulk. In the Ni–W eutectic system the Tungsten has a significantly higher melting point than Nickel which resulted in grain boundary penetration of Ni–W eutectic along the W grain boundaries [46]. In the present work, similar behavior is observed by eutectic reaction of the NiTi–Nb system due to the significant difference in melting temperatures between Nb and NiTi.

Two different joining mechanisms were identified for the NiTi/Nb/Ti6Al4V joint. Fusion welding was used to join Ti6Al4V to Niobium. Niobium experienced dilution and was incorporated into the Ti6Al4V weld pool. A (Ti, Nb) region was formed upon solidification as a thin layer along the Niobium interface due to minimal mixing with the bulk fusion zone. The Niobium interlayer acted as a heat sink due to its high thermal conductivity absorbing a significant amount of energy from the Ti6Al4V side of the joint and transferring it to the NiTi side. This enabled this interface to reach temperatures of at least 1170 °C so that contact melting between NiTi and Niobium occurred and a joint between these two materials was formed. Dissimilar joint between NiTi and Ti6Al4V did not form when no interlayer was present, further suggesting that the eutectic reaction was responsible for joining at the NiTi–Nb interface. As expected from the NiTi–Nb phase diagram, no intermetallic compounds were observed in the solidified joint. The high melting point of the interlayer ensured that the bulk of the Niobium remained in the solid state during welding, successfully stopping

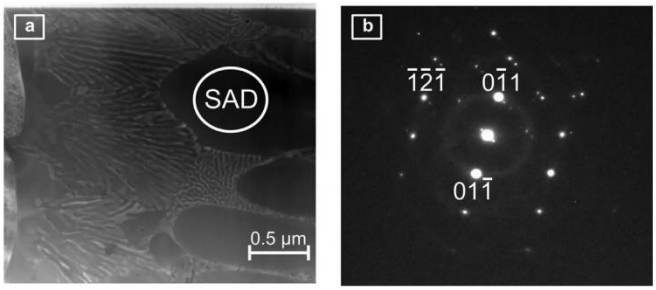

Fig. 7. a) HAADF image of the NiTi–Nb interface with a region analyzed with SAD indicated; b) Indexed SAD image of NiTi that was performed on the marked area of the NiTi region.

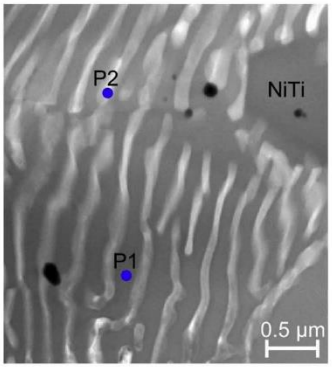

Fig. 8. HAADF image of the eutectic microstructure with EDS analysis points indicated. The black spots were identified as impurities.

Table 1
Results of EDS analysis of the eutectic NiTi + Nb structure, with positions indicated in Fig. 8.

Point	Atomic content (%)		
	Ni	Ti	Nb
P1	51.7	38.1	10.2
P2	12.5	22.8	64.7

mixture of the two base materials.

3.3. Mechanical behavior of the welded joint

Tensile tests were performed on the joints made with the Niobium interlayer, with the laser offset into the Ti6Al4V. The stress–strain curve of the welds is shown in Fig. 10. As discussed in previous sections dissimilar joints between NiTi and Ti6Al4V were not formed without the interlayer, or with the laser offset into the NiTi.

An average tensile stress of 300 MPa and an elongation to fracture near 2.0% were measured. This was a significant improvement on joints made without the interlayer, which were unable to be tested because they fractured during removal from the welding fixture. The tensile strength of pure Niobium ranges between 250 and 350 MPa, so the joint strength matched the maximum theoretical strength of the interlayer. Similar values of tensile strength were obtained by Zoeram et al. [10], despite using a Copper interlayer, which has better mechanical properties than

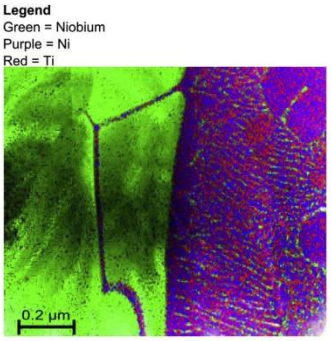

Fig. 9. –Grain boundary penetration of NiTi into the Niobium grains.

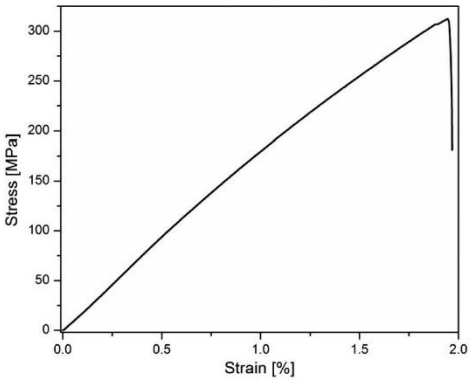

Fig. 10. Stress-strain curve of NiTi to Ti6Al4V weld with Niobium interlayer.

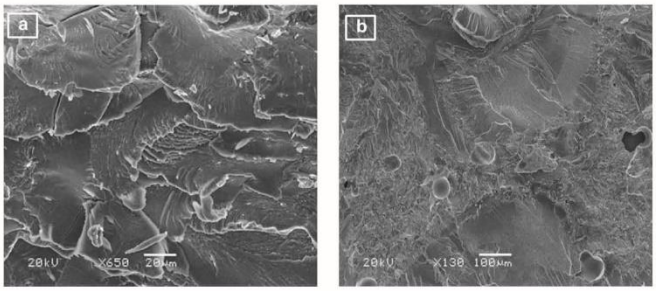

Fig. 11. Fracture surface on the Ti6Al4V side (a) and on the NiTi side (b) of the joint.

Niobium. However, the tensile strength of the Niobium interlayer joints was below the critical value for stress induced martensite formation in NiTi. The joint strength may be improved through further optimization of joining parameters including joint fit-up, laser peak power, and pulse width. This study has proven that a high melting point interlayer can be used to achieve a defect-free joint between NiTi and Ti6Al4V. If a similar interlayer was identified that had higher ultimate tensile strength, then the joint strength could be increased to accommodate the superelastic effect.

The fracture surfaces of the welded specimens exhibited mostly brittle fracture morphology from the Ti6Al4V fusion zone as shown in Fig. 11. The 50 µm thick interlayer was torn during fracture leading to the Ti6Al4V and NiTi fracture surfaces having both the fusion welded and eutectic bonded regions of the joint. The NiTi side of the joint had more ductile dimples from the eutectic phases formed, while the Ti alloy side had more brittle cleavage features from the fusion zone. Hydrogen or oxygen pick-up by the Ti6Al4V weld pool could contribute to the brittle characteristics of the fracture surfaces [47,48]. The grain boundary penetration of the Niobium interlayer by the eutectic reaction with the NiTi can reduce the ductility of this region, which can also contribute to the observed brittle crack formation [45].

4. Conclusions

Defect-free, dissimilar laser welding of NiTi to Ti6Al4V was achieved using a Niobium interlayer. This opens up the possibility to join these materials in more complex configurations. The following are the major conclusions that can be drawn from the study:

1. Niobium acted as a barrier to mixing of the two base materials, which prevented the formation of brittle intermetallics, while ensuring joining at both interfaces. Dissimilar joining between NiTi and Ti6Al4V did not occur when the interlayer was not used.
2. The average tensile strength and elongation of these interlayer joints was 300 MPa and 2%, respectively. This ultimate tensile strength matched that of the Niobium interlayer.
3. At the NiTi–Nb interface, intimate contact between NiTi and Niobium promoted joining due to a eutectic reaction.
4. At the Ti6Al4V–Nb interface, dissolution of the Niobium into the liquid Titanium occurred. A thin (Ti, Nb) region with an average chemical composition of 47.7Ti-46.2Nb-2.9Al-3.3V (in wt.%) was identified at the interface of the Niobium interlayer and the fusion zone.
5. Precise control of the position of the laser with respect to the interlayer was crucial to obtain a sound weld. If the beam was positioned far away from the interlayer, eutectic melting in the NiTi–Nb interface did not occur. When the beam was placed too close to the interlayer, no joint formed because it was reflected by the Niobium.

Acknowledgments

JPO and FMBF acknowledge funding of CENIMAT/I3N by FEDER funds through the COMPETE 2020 Programme and National Funds through FCT - Portuguese Foundation for Science and Technology under the project UID/CTM/50025/2013. RMM acknowledges funding of UNIDEMI by FEDER funds through the COMPETE 2020 Programme and National Funds through FCT - Portuguese Foundation for Science and Technology under the project UID/EMS/00667/2013. JPO acknowledges FCT/MCTES for funding PhD grant SFRH/BD/85047/2012 and stay at Waterloo University (Canada) through MIDAS Project No 612585 "MIDAS— Micro and Nanoscale Design of Thermally Actuating Systems" Marie Curie Actions, FP7-PEOPLE-2013-IRSES. Support from NSERC is also acknowledged.

References

[1] S. Saadat, J. Salichs, M. Noori, Z. Hou, H. Davoodi, I. Bar-on, Y. Suzuki, A. Masuda, An overview of vibration and seismic applications of NiTi shape memory alloy, Smart Mater Struct. 11 (2002) 218–229.
[2] S.A. Shabalovskaya, On the nature of the biocompatibility and on medical applications of NiTi shape memory and superelastic alloys, Bio-Med Mater Eng. 6 (1995) 267–289.
[3] D.J. Hartl, D.C. Lagoudas, Aerospace applications of shape memory alloys, Proc. Inst. Mech. Eng. Part G J Aerosp. Eng 221 (2007) 535–552.
[4] G. Eggeler, E. Hornbogen, A. Yawny, A. Heckmann, M. Wagner, Structural and functional fatigue of NiTi shape memory alloys, Mater Sci. Eng. A 378 (2004) 24–33.
[5] C. Trépanier, M. Tabrizian, L. Yahia, L. Bilodeau, D.L. Piron, Effect of modification of oxide layer on NiTi stent corrosion resistance, J. Biomed. Mater Res. 43 (1998) 433–440.
[6] E.O. Ezugwu, Z.M. Wang, Titanium alloys and their machinability — a review, J. Mater Process Technol. 68 (1997) 262–274.
[7] S.H. Wang, M.D. Wei, L.W. Tsay, Tensile properties of LBW welds in Ti–6Al–4V alloy at evaluated temperatures below 450 °C, Mater Lett. 57 (2003) 1815–1823.
[8] Z. Sun, J. Ion, Laser welding of dissimilar metal combinations, J. Mater Sci. 30 (1995) 4205–4214.
[9] R.M. Miranda, E. Assunção, R.J.C. Silva, J.P. Oliveira, L. Quintino, Fiber laser welding of NiTi to Ti-6Al-4V, Inter J. Adv. Manuf. Technol. (2015).
[10] A.S. Zoeram, S.A.A.A. Mousavi, Laser welding of Ti–6Al–4V to Nitinol, Mater Des. 61 (2014) 185–190.
[11] K. Otsuka, C.M. Wayman, Shape Memory Materials, Cambridge University Press, Cambridge, 1999.
[12] A.J. Cavaleiro, A.S. Ramos, F.M.B. Fernandes, N. Schell, M.T. Vieira, Situ characterization of NiTi/Ti6Al4V joints during reaction-assisted diffusion bonding using Ni/Ti multilayers, J. Mater Eng. Perform. 23 (2014) 1625–1629.

[13] L. Quintino, L. Liu, A. Hu, R.M. Miranda, Y. Zhou, Fracture analysis of Ag nanobrazing of NiTi to Ti alloy, Sold. Insp. 18 (2013) 281–286.
[14] S. Kou, Welding Metallurgy, second ed., Wiley-Interscience, New Jersey, 2003.
[15] B. Panton, A. Pequegnat, Y.N. Zhou, Dissimilar laser joining of NiTi SMA and MP35N wires, Metall. Mater Trans. A 45 (2014) 3533–3544.
[16] Z. Zeng, B. Panton, J.P. Oliveira, A. Han, N. Zhou, Dissimilar laser welding of NiTi shape memory alloy and copper, Smart Mater. Struct. 24 (2015), http://dx.doi.org/10.1088/0964-1726/24/12/125036, 125036 (8pp).
[17] H. Li, D. Sun, X. Cai, P. Dong, X. Gu, Laser welding of TiNi shape memory alloy and stainless steel using Co filler metal, Opt. Laser Technol. 45 (2013) 453–460.
[18] H.M. Li, D.Q. Sun, X.L. Cai, P. Dong, W.Q. Wang, Laser welding of TiNi shape memory alloy and stainless steel using Ni interlayer, Mater Des. 39 (2012) 285–293.
[19] H. Li, D. Sun, X. Gu, P. Dong, Z. Lv, Effects of the thickness of Cu filler metal on the microstructure and properties of laser-welded TiNi alloy and stainless steel joint, Mater Des. 50 (2013) 342–350.
[20] P. Penner, L. Liu, A. Gerlich, Y. Zhou, Dissimilar resistance spot welding of aluminum to magnesium with Zn-coated steel interlayers, Weld. J. (2014) 225–231.
[21] P. Penner, L. Liu, A. Gerlich, Y. Zhou, Feasibility study of resistance spot welding of dissimilar Al/Mg combinations with Ni based interlayers, Sci. Technol. Weld. Join. 18 (2013) 541–550.
[22] M. Sun, S.T. Niknejad, G. Zhang, M.K. Lee, L. Wu, Y. Zhou, Microstructure and mechanical properties of resistance spot welded AZ31/AA5754 using a nickel interlayer, Mater Des. 87 (2015) 905–913.
[23] F. Cardarelli, Materials Handbook: a Concise Desktop Reference, second ed., Springer, London, 2008.
[24] W.F. Gale, T.C. Totemeier, Smithells Metals Reference Book, Eighth ed., Elsevier Inc, Amsterdam, 2004.
[25] K. Otsuka, X. Ren, Physical metallurgy of Ti–Ni-based shape memory alloys, Prog. Mater Sci. 50 (2005) 511–678.
[26] A. Hasçalık, U. Çaydaş, Electrical discharge machining of titanium alloy (Ti–6Al–4V), Appl. Surf. Sci. 253 (2007) 9007–9016.
[27] S. Kundu, S. Chatterjee, Evolution of interface microstructure and mechanical properties of titanium/304 stainless steel diffusion bonded joint using Nb interlayer, ISIJ Int. 50 (2010) 1460–1465.
[28] M.J. Torkamany, F.M. Ghaini, R. Poursalehi, Dissimilar pulsed Nd:YAG laser welding of pulsed niobium to Ti–6Al–4V, Mater Des. 53 (2014) 915–920.
[29] H. Okamoto, P.R. Subramanian, L. Kacprzak, ASM Handbook, Vol. 3: Alloy Phase Diagrams, ASM International, Ohio, 1992.
[30] J. Shaw, Simulations of localized thermo-mechanical behavior in a NiTi shape memory alloy, Int. J. Plast. 16 (2000) 541–562.
[31] E.O. Ezugwu, R.B. Da Silva, J. Bonney, A.R. Machado, Evaluation of the performance of CBN tools when turning Ti–6Al–4V alloy with high pressure coolant supplies, Int. J. Mach. Tool. Manu 45 (2005) 1009–1014.
[32] D.S. Grummon, J.A. Shaw, J. Foltz, Fabrication of cellular shape memory alloy materials by reactive eutectic brazing using niobium, Mater Sci. Eng. A 438 (2006) 1113–1118.
[33] F. Franchini, P. Pierantozzi, Electron beam welding of dissimilar materials: Niobium-base alloy C-103 with titanium-base alloy Ti-6Al-4V ELI, Weld. Int. 6 (1992) 792–797.
[34] M. Jandaghi, P. Parvin, M.J. Torkamany, J. Sabbaghzadeh, Alloying element losses in pulsed Nd:YAG laser welding of stainless steel 316, J. Phys. A 41 (2008) 235503.
[35] K.C. Mills, B.J. Keene, R.F. Brooks, A. Shirali, Marangoni effects in welding, Philos Trans R Soc London, Ser. A 356 (1998) 911–926.
[36] M. Piao, S. Miyazaki, K. Otsuka, N. Nishida, Effects of Nb addition on the microstructure of Ti–Ni alloys, Mater Trans. 33 (1992) 337–345.
[37] Z.C. Liu, J.P. Lin, S.J. Li, G.L. Chen, Effects of Nb and Al on the microstructures and mechanical properties of high Nb containing TiAl base alloys, Intermetallics 10 (2002) 653–659.
[38] R. Zhang, V.L. Acoff, Processing sheet materials by accumulative roll bonding and reaction annealing from Ti/Al/Nb elemental foils, Mater Sci. Eng. A 463 (2007) 67–73.
[39] G. Welsch, R. Boyer, E.W. Collings, Materials Properties Handbook: Titanium Alloys, ASM International, Ohio, 1993.
[40] W.M. Steen, J. Mazumder, Laser Material Processing, fourth ed., Springer, London, 2010.
[41] D. Grummon, K.-B. Low, J. Foltz, J. Shaw, A new method for brazing nitinol based on the quasibinary TiNi-Nb system, in: 48th AIAA/ASME/ASCE/AHS/ASC Structures, Structural Dynamics, and Materials Conference, 2007.
[42] J. Kwo, M. Hong, S. Nakahara, Growth of rare-earth single crystals by molecular beam epitaxy: The epitaxial relationship between hcp rare earth and bcc niobium, Appl. Phys. Lett. 49 (1986) 319–321.
[43] C. Suryanarayana, Non-equilibrium Processing of Materials, Elsevier Science Ltd, Oxford, 1999.
[44] S. Van Aert, J. Verbeeck, R. Erni, S. Bals, M. Luysberg, D. Van Dyck, G. Van Tendeloo, Quantitative atomic resolution mapping using high-angle annular dark field scanning transmission electron microscopy, Ultramicroscopy 109 (2009) 1236–1244.
[45] M.C. Chaturvedi, Welding and Joining of Aerospace Materials, Woodhead Publishing Limited, Cambridge, 2012.
[46] V. Glebovsky, B. Straumal, V. Semenov, V. Sursaeva, W. Gust, Grain boundary penetration of a Ni-rich melt in tungsten polycrystals, High. Temp. Mater Process. Lond. 14 (1995) 67–73.
[47] R.R. Wang, G.E. Welsch, Joining titanium materials with tungsten inert gas welding, laser welding, and infrared brazing, J. Prosthet. Dent. 74 (1995) 521–530.
[48] X. Li, J. Xie, Y. Zhou, Effects of oxygen contamination in the argon shielding gas in laser welding of commercially pure titanium thin sheet, J. Mater Sci. 40 (2005) 3437–3443.

7.1.7 Laser Welded Superelastic Cu-Al-Mn Shape Memory Alloy Wires

This paper was submitted and accepted in Materials & Design.

Materials and Design 90 (2016) 122–128

Contents lists available at ScienceDirect

Materials and Design

journal homepage: www.elsevier.com/locate/jmad

Laser welded superelastic Cu–Al–Mn shape memory alloy wires

J.P. Oliveira [a,b,*], B. Panton [b], Z. Zeng [b,c], T. Omori [d], Y. Zhou [b], R.M. Miranda [e], F.M. Braz Fernandes [a]

[a] CENIMAT/i3N, Faculdade de Ciências e Tecnologia, Universidade Nova de Lisboa, Portugal
[b] Centre for Advanced Materials Joining, University of Waterloo, Canada
[c] School of Mechatronics Engineering, University of Electronic Science and Technology of China, China
[d] Department of Materials Science, Graduate School of Engineering, Tohoku University, Japan
[e] UNIDEMI, Faculdade de Ciências e Tecnologia, Universidade Nova de Lisboa, Portugal

ARTICLE INFO

Article history:
Received 11 August 2015
Received in revised form 20 October 2015
Accepted 23 October 2015
Available online 24 October 2015

Keywords:
Cu–Al–Mn
Shape memory alloys
Laser welding
Superelasticity

ABSTRACT

This paper presents the first study on welding of Cu-based shape memory alloys. The superelastic wires used in the investigation had a nominal composition of Cu–17Al–11.4Mn (at.%). The pulsed Nd:YAG spot welding process altered the original bamboo-like microstructure of the base metal to a fusion zone with fine equiaxed grains. Micro-load-indentation depth analysis revealed that the grain refinement increased the ductility of the fusion zone compared to the base material. Tensile tests did not show any significant difference between base material and welded specimens, with failure occurring far away from the welds in the larger grained base metal. Mechanical cycling and superelastic behavior of the welded joints showed a faster stabilization of the hysteretic response than the base material, which is beneficial for applications where energy absorption is required. The Cu–Al–Mn superelastic alloy had a very high weldability and superior properties compared to other laser welded shape memory alloys, such as NiTi.

1. Introduction

Shape memory alloys are stimulus-responsive materials which base their properties on a reversible martensitic transformation [1]. Cu-based shape memory alloys (SMAs) have higher thermal and electrical conductivity, good deformability and lower cost than the more widely used NiTi SMAs [2]. These advantages have recently motivated numerous investigations into these alloys. The Cu–Al binary system is the most important of the Cu-based SMAs because of its superior properties [3] In their investigation of the martensitic transformation of these alloys, Hultgren et al. [4] showed that the ordering reactions $\beta \rightarrow \beta_2$ (CuAl: B2, cubic) $\rightarrow \beta_1$ (Cu_3Al: DO_3, cubic), occur at low temperatures during quenching and are not suppressed by rapid cooling. For a range of compositions, the metastable β phase orders during cooling and undergoes a first-order, diffusionless, structural transition into a more closed packed phase. This is the basis for the martensitic transformation in Cu-based alloys [5]. The addition of Mn to the binary alloy was found to stabilize the bcc phase, widen the single-phase region to lower Al compositions and lower temperatures, and improve the ductility of low Al alloys by decreasing the degree of order of the system. These improvements are the basis for the superior SMA properties of the Mn alloys compared to other Cu-based SMAs [5]. Increasing either Mn or Al decreases the transformation temperatures of the alloy, with a greater sensitivity to changes in the content of the former element [6].

The effect of the Al content on the shape memory effect and superelastic properties was studied by Kainuma et al. [6,7]. Kainuma et al. [7] showed that Cu–Al–Mn SMAs with Al contents below 18 at.% exhibit good ductility and excellent cold-workability due to a lower degree of order in the Heusler ($L2_1$) β_1 parent phase. Kainuma et al. [6] studied several alloys including a Cu–Al–Mn alloy with 17 at.% Al, which is similar to the alloy used in the current study. Alloys with lower than 14 at.% Al were found to have two different parent phases: β (A2, disordered), and β_1 ($L2_1$, ordered)). Alloys with 16 and 17 at.% Al had only the latter parent phase resulting in more ideal shape memory properties. In these complex Cu–Al–Mn systems, the low temperature phase (martensite) may be of three different types: α'_1 (3R) forms with low Al content, β'_1 (18R) forms in an intermediate range and γ'_1 (2H) is predominant in higher Al content ranges.

The Cu–17Al–11Mn composition has the highest performing superelastic properties among the Cu-based SMAs, and can exceed the recoverable strain achieved in NiTi [8,9]. A comparison of the properties of Cu–17Al–11Mn SMA to the most widely used SMA NiTi is shown in Table 1. Advantages of the Cu–17A–11Mn alloy over NiTi also include a lower stress for inducing the martensite transformation, and greater thermal and electrical conductivities [2,10,11]. In addition to these superior physical properties, Cu-based SMAs are less expensive than NiTi [12]. These advantages may lead to Cu-based SMAs replacing NiTi in suitable applications.

* Corresponding author at: CENIMAT/i3N, Faculdade de Ciências e Tecnologia, Universidade Nova de Lisboa, Portugal.
E-mail address: jp.oliveira@campus.fct.unl.pt (J.P. Oliveira).

http://dx.doi.org/10.1016/j.matdes.2015.10.125
0264-1275/

Table 1
Comparison of the mechanical properties of superelastic Cu–17Al–11Mn and NiTi.

Material	Young's modulus [GPa]	Onset for stress induced transformation [MPa]	Recovery strain [%]	Work-hardening rate [GPa]	Tensile elongation [%]
Cu–17Al–11Mn	≈20 [8]	≈100 to 250 [11]	Up to 12% [8]	≈3.4 to 4.2 [11]	Up to 18 [8]
NiTi	≈70 [13]	≈350 to 600 [14,15]	Up to 9% [9]	≈3 to 15 [16]	Up to 60 [17]

Cu-based SMAs are being considered as potential lower cost alternatives to NiTi for seismic and vibrational damping applications [18,19]. After cyclic loading, conventional steel reinforcement bars often have degraded stiffness and strength, experience pinching phenomena, and large cracks form after intense earthquakes [18]. Shrestha et al. [18] showed that Cu–Al–Mn superelastic alloys provided a more stable response under cyclic loading when compared to steel. The viability for the use of the Cu–Al–Mn SMAs as solutions for these problems in structural applications was emphasized recently by Araki et al. [20] and Genkturk et al. [19]. Araki et al. [20] studied the cyclic behavior under different loading frequencies of bars of the same Cu–Al–Mn alloy investigated in the current study. The alloy had a low cyclic hardening of the stress for the martensitic transformation, which makes them promising candidates for being used in seismic applications. The same alloy was used in a study by Genkturk et al. [19] who showed that they possessed excellent superelastic properties over a range of temperatures and loading rates. However, it was noticed that stable superelasticity required precise control of the grain size and orientation. Similar dependence of the mechanical properties on the grain orientation of other Cu–Al–Mn alloys was also noted in [2,12].

The superelastic Cu–17Al–11Mn SMA is also a primary candidate for biomedical applications and is currently used for ingrown nail correction as it does not present risks to the human health [8]. Both the medical and construction fields would benefit from dissimilar joining of these materials to current alloys in these areas [21] Thus, a preliminary study envisaged to investigate the weldability of the Cu–Al–Mn alloys. Determining the weldability of the material can also increase the range of potential applications in which complex geometries of Cu–Al–Mn based components can be developed. Minimization of cost would include the minimization of Cu–Al–Mn use in a component, which would result in the weldment being a significant portion of the Cu–Al–Mn in the component. Additionally, it is important to fully characterize the effect of the weld on the superelastic properties of the material so that future components can be successfully designed. Laser welding has produced high quality joints when welding other SMAs, so it was chosen for the current investigation.

So far, no previous attempts of welding any Cu-based SMAs have been reported. In the current work laser welding of a Cu–Al–Mn SMA (superelastic at room temperature) was studied and the joints were characterized and compared to the base material.

2. Materials and methods

The Cu–17Al–11.4Mn (at.%) alloy was prepared by induction melting under an Ar atmosphere to form an ingot. This ingot was hot forged and cold drawn to make 0.500 mm wires. These wires were subjected to a solution treatment at 900 °C followed by quenching in water. The wires were subsequently aged at 200 °C to stabilize the martensitic transformation temperatures [11]. These heat treatments optimize the mechanical properties of the base material, which has a random texture [11].

The oxide layer from the final heat treatment performed on the wire was mechanically removed using 1200 fine SiC paper. The removal of the oxide layer led to a final wire diameter of 0.490 ± 0.005 mm. Prior to welding, the wires were cleaned with acetone and ethanol in order to remove any impurities that could affect the weld.

The provided material had small lot sizes. This resulted in different batches of material being used for different parts of the experiments. However, in order to keep the results consistent among themselves, a given wire (named wire 1) was used for the tensile tests and another one (named wire 2) for the mechanical cycling tests. Wire 1 was used for preparing both base material and laser welded samples for the tensile tests and wire 2 was used with the same purpose but for analyzing the cyclic behavior.

2.1. Laser welding

A Miyachi Unitek LW50A pulsed Nd:YAG laser system, with a wavelength of 1064 nm, a top-hat type spatial profile and a spot size of 600 μm was used. Argon was the shielding gas at a flow rate of 0.57 $m^3\ h^{-1}$ (20 CFH). A pulse profile with duration of 6 ms, including 1 ms upslope and 1 ms downslope was used. The welding process was developed to achieve a full penetration weld with a symmetric contour, with a minimum heat input. Bead-on-plate welds were performed with a peak power of 1.5 kW. This geometry was selected to remove the variability of joint fit-up, which was desired because this was the first investigation on the weldability of Cu-based SMAs. An in-house custom built fixture system ensured the wires were straight before welding as shown in Fig. 1.

2.2. Microstructural analysis and hardness measurements

The welded specimens were mounted in epoxy resin, mechanically polished and etched in a solution of $FeCl_3$ (10 g) + HCl (25 ml) + H_2O (100 ml) for 5 s. An Olympus BX51M optical microscope was used for microstructural observation.

Scanning Electron Microscopy (SEM) was performed using a JEOL JSM-6460SME at an acceleration voltage of 20 kV for analyzing the fracture surfaces, while Energy Dispersive Spectroscopy (EDS) was performed with an INCA energy 350 EDS microanalysis system in order to quantify the composition variations along the welded joints for comparison with the base material. Three lines located at 1/3, 1/2 and 2/3 of the wire thickness, with 12 points each, were analyzed.

Conventional hardness was performed with a micro-Vickers hardness tester, from Shimadzu Corporation, along a cross-section of the weld in order to characterize the base material and the fusion zone. A load of 300 g was used and the hold time was kept at 20 s. A total of 18 indentations were performed.

Indentation load vs indentation depth analysis was made with a Nanovea M1 hardness tester. Three sets of loads (20, 30 and 38 N) were applied in the fusion zone and in the base material. The loading/unloading rates were kept at 60, 85 and 120 N/min for 20, 30 and 38 N loads, respectively. A flat tip head with 100 μm diameter was used.

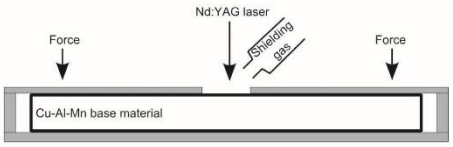

Fig. 1. Schematics of fixture, laser and shielding gas position for the welding experimental setup.

2.3. Mechanical testing

Tensile testing was performed at room temperature using an Instron model 5548 micro-tensile tester at a displacement rate of 0.5 mm/min and a measurement accuracy of ±0.5 μm, following the ASTM F2516-07 standard. The overall gauge length of the tested specimens, both base and welded material, was of 20 mm. The peak stress was measured from the tensile curves as the maximum stress achieved during the tensile test. Three samples were tested for each condition. Scanning Electron Microscopy of the fracture surfaces was observed using a Zeiss Leo 1550 Field Emission SEM with an accelerating voltage of 10 kV.

Cycling behavior of the base metal and of the welds was also analyzed. A total of 10 mechanical load/unload cycles at 5% strain were performed at a rate of 0.5 mm/min, similarly to the tensile tests.

3. Results and discussion

3.1. Microstructural and hardness characterization

The base material had a bamboo-like microstructure, with a grain size ranging from 1 to 2 mm in length (Fig. 2). This microstructure re-solidified into fine columnar and equiaxed grains in the fusion zone (Figs. 3, 4) due to the high cooling rate characteristic of laser welding [22]. The grain size in the fusion zone ranged between 15 and 80 μm (Fig. 4) which was significantly smaller than the original base material grain size. The changes in shade of the microstructure along the base material and within the fusion zone have previously been identified to be related to differences in grain orientation [11].

The high cooling rates ensured that no α-precipitates formed in the fusion zone, thereby, preserving the superelastic properties of this region. The α-precipitates do not exhibit superelasticity and their presence is known to degrade the superelastic properties of the alloy. No heat affected zone was identified in optical microscopy because the base material had previously been subjected to high temperature annealing heat treatments that resulted in a very large grain size compared to the fusion zone.

Hardness measurements were performed on a line through the base material and fusion zone as depicted in Fig. 3. A large scatter of hardness values was observed with no significant difference from the fusion zone to the base material. The Cu–Al–Mn base material average hardness was 263.9 ± 6.5 HV, while in the fusion zone this was 258.4 ± 8.1 HV. These values fall within the expected hardness range for this alloy [23]. They also confirm that there is no heat affected zone. This inability to detect a heat affected zone by either optical or hardness measurements has been previously observed by Schlobmacher et al. [24] and Hsu et al. [25] during laser welding of NiTi. This lack of heat affected zone was attributed to the effect of annealing heat treatments performed on the base material prior to welding, so the weld thermal cycle had a minimal change on the base material and no heat affected zone was noticeable.

EDS was performed on the welded joint to characterize the compositional variations along the welds and through the wire thickness, as shown in Fig. 3. No significant compositional changes were observed in the EDS results. The average compositional change in the fusion zone did not differ significantly from the base material nominal composition, as depicted in Table 2. Laser welding can change the composition of a material through vaporization, as reported for NiTi SMAs [26]; however, the parameters and single pulse used in the current process were insufficient to have any significant change on the composition of the wires.

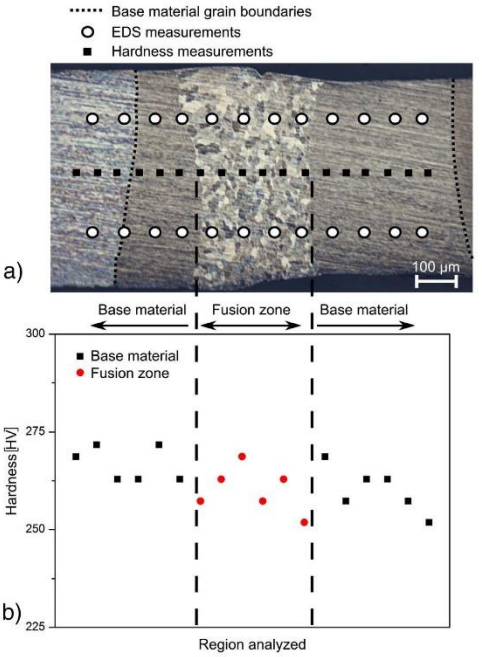

Fig. 3. a) Optical micrograph of the welded joint showing the position of EDS scan lines and hardness measurements. Three EDS line scans were performed across the cross section of the base material and fusion zone (total of 12 analyzed spots per line scan). b) Corresponding hardness values for the different regions of the welded material (total of 18 analyzed spots).

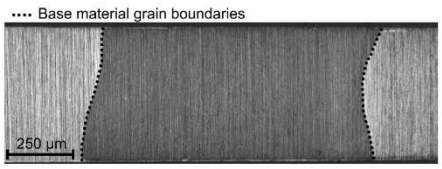

Fig. 2. Optical micrograph of the original base material.

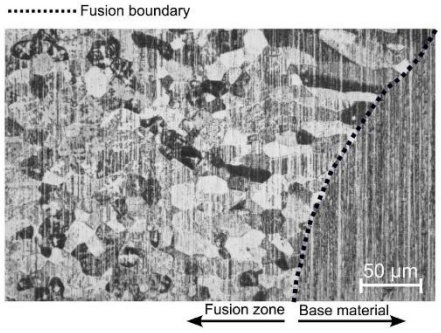

Fig. 4. Magnified view of the microstructure of the base metal and fusion zone at the fusion boundary.

Table 2
Average EDS measurements in the base material and in the fusion zone.

Region	Cu [at.%]	Al [at.%]	Mn [at.%]
Base material	72.48 ± 2.21	16.16 ± 1.89	11.37 ± 1.31
Fusion zone	71.92 ± 2.65	16.44 ± 2.31	11.64 ± 1.73

3.2. Local mechanical behavior

In order to obtain separate mechanical characterization of the fusion zone and the base material, load–displacement indentation tests were conducted. Fig. 5 depicts the plots of Load vs. Penetration depth in these regions for three sets of maximum applied loads (20, 30 and 38 N). The indenter size was 100 μm which captured either multiple grains in the fusion zone or a portion of the large base material grain in each indentation.

For applied loads of 20 and 30 N both the base material and the fusion zone exhibited the same behavior. However, for the maximum applied load of 38 N, the fusion zone had a higher penetration when compared to the base material. This increase in ductility resulted from the reduction in grain size from the bamboo-like grained base material to the fine grained fusion zone.

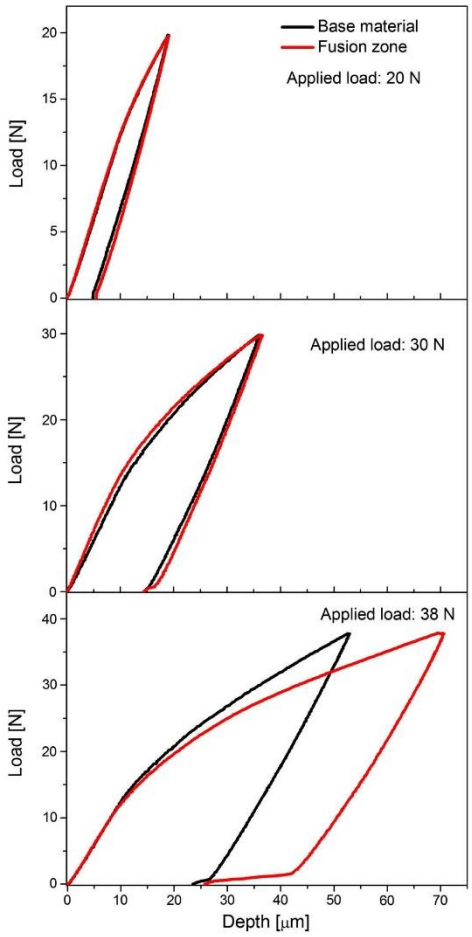

Fig. 5. Indentation curves in the fusion zone and in the base material for different applied loads.

3.3. Tensile failure and fracture analysis

Fig. 6 depicts stress–strain curves for both base material and welded wire. The tensile curves of the welds were very similar to the base material, with both materials requiring the same average stress for inducing the martensitic transformation. When welding NiTi, the most studied SMA, a decrease of the mechanical properties has been observed due to grain growth [25]. However, in the case of this Cu–Al–Mn SMA, the intentionally massive grain size of the base metal was unaffected by the welding process as previously discussed, so no significant difference was observed in the tensile behavior of the welded versus base material wires.

In superelastic Cu–Al–Mn alloys, the large grains improve the stress–strain response [11].The superelastic strain increases with the increase of grain size (d) relative to the wire diameter (D). When d/D increases, the free surface grain boundary area also increases, which drastically reduces the constraining strain imposed by the surrounding grains [11]. In the fusion zone the amount of grains was considerably higher than that in the base material, leading to an increase in the constraint of strain. However, this did not lead to any changes in the tensile properties of the welded wires.

Necking occurred in the fusion zone because of the higher ductility of this region compared to the base material. However, fracture did not occur at this necking, instead it always occurred in the coarse grained base material far away from any influence of the weld. SEM analysis of the fracture surfaces of the specimens revealed ductile fracture depicted by the dimples as shown in Fig. 7, for the welded sample. No influence of the welding process was observed on the fracture surface. Fracture along the grain boundary in the base material of the welded specimens occurred as shown in Fig. 8.

In the NiTi welds fracture occurred in the thermal affected regions [25,27,28] due to the localization of strain in the softened material. In this Cu–Al–Mn alloy, the isolation of the grain boundaries in the bamboo-like wires made them prone to localized deformation. In comparison, the fusion zone contained many grains that hindered

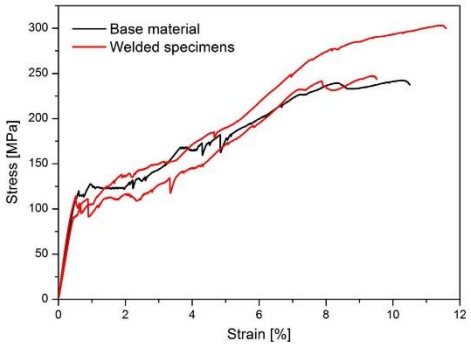

Fig. 6. Tensile tests for the base material and welded specimens.

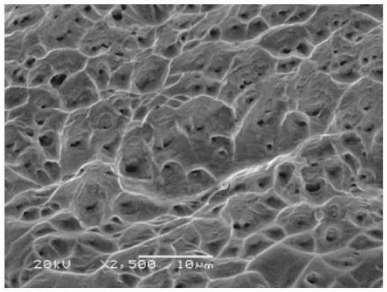

Fig. 7. Fracture surface of the welded specimen, which occurred in the base material as indicated in Fig. 8.

dislocation motion during plastic deformation. The smaller grain sizes accommodated the load such that failure did not occur in the fusion zone but rather in the base material at the isolated grain boundary.

3.4. Cyclic tensile behavior

The existence of a high density of mobile twins in the martensitic phase and mobile interfaces between the parent phase and martensite leads to internal friction [10] and a significant amount of energy can be absorbed due to this effect giving rise to high damping in SMAs. As these alloys are intended to be used in systems subjected to load variations (e.g. seismic structural applications, or medical components which move with the body) it is fundamental to understand their behavior under cyclic loading/unloading.

The cycling behavior of both base material and welded wires are shown in Fig. 9 a) and b), respectively. In these figures the start of the martensitic transformation had higher values than those in the previous tensile tests. As discussed in the experimental section, a different set of wires was used for the tensile failure, and cyclic tensile specimens. These wires may have very small variations in their composition or in the heat treatment that impacted their mechanical properties. The stress to induce the martensitic transformation is dependent on the ratio of grain size to wire diameter, and the crystallographic orientation of the grains [11]. In Cu–Al–Mn SMA alloys the transformation strain is highly dependent on the crystallographic orientation of the grains [2, 11], which affects the critical stress level for inducing the transformation following the Clausius–Clapeyron relationship [29].

Smart design based on the superelastic effect requires that cycling behavior along a given load/unload path is stabilized for a given number of cycles which depends on the application [30]. The stabilization of the superelastic effect occurs in SMAs as the microstructure evolves to inhibit dislocation motion [31]. The most significant differences between the cycling behavior of the welded and base material specimens was

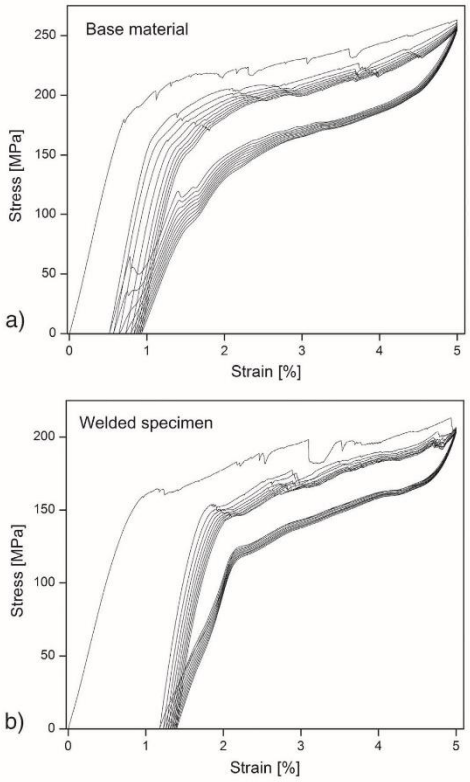

Fig. 9. Mechanical cycling behavior of: a) the base material; and b) the welded specimen.

the evolution of the irrecoverable strain after each cycle, and the hysteretic loop which gives a measure of the absorbed energy per cycle.

The irrecoverable strain after the first cycle for the base material was close to 0.5%, which is within the range of values expected from the work performed by Kainuma et al. [6]. For the welded specimens a slightly higher value for the irrecoverable strain after the first cycle was observed and this was 1.1%. The larger irrecoverable strain in the welded specimen is due to the fine grained fusion zone, which had a d/D ratio smaller than the base metal, which reduced the superelastic recovery after unloading [11]. This small d/D ratio resulted in a greater constriction of transformation which explains the larger plastic strain observed.

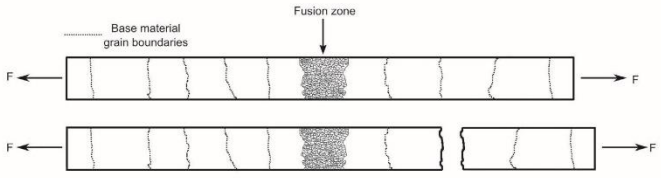

Fig. 8. Schema of the fracture along a grain boundary in the base material (not to scale).

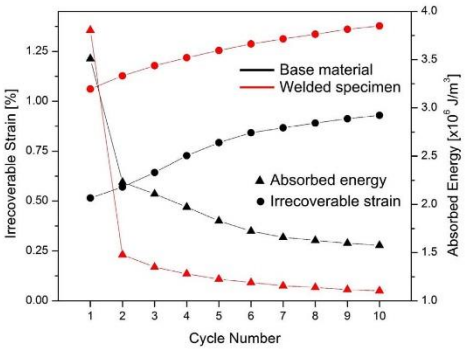

Fig. 10. Evolution of the accumulated irrecoverable strain and absorbed energy with the number of cycles for the base material and the welded specimen.

After the first cycle, the superelastic hysteretic response started to stabilize both in the base material and in the welded sample. This effect can be observed in Fig. 10 which presents the accumulation of irrecoverable strain and the energy absorbed per cycle.

Both the base metal and welded specimens converged to a stabilized superelastic response after a low number of cycles, with the latter being faster to converge than the former. This observation is of major interest when planning to design a structure using such a welded joint because it will not need a high number of mechanical cycles prior to its effective use in structural applications. The stabilized hysteretic response is obtained earlier in the welded specimen than in the base material because of the faster plastic buildup related to the constriction of transformation by the surrounding grains.

The polycrystalline wires used in this investigation had a similar cyclic deformation behavior as single crystal material studied by Kato et al. [32]. The convergence of the hysteretic response occurred in a low number of cycles, the majority of the plastic strain occurred in the first cycle and stabilized in a low number of cycles, and the critical stress for martensite formation decreased with each cycle.

4. Conclusions

This study was the first investigation of laser welding superelastic Cu–Al–Mn wire. The microstructures, hardness values and mechanical properties of welded and base metal samples were analyzed to determine the effects of welding on these shape memory alloys.

- The Cu–Al–Mn alloy had excellent weldability, which may open new possibilities for its use in civil structures and other damping applications.
- Micro-indentation load vs depth analysis showed that the finer grained fusion zone was more ductile than the bamboo-like grained base material.
- No degradation of the overall tensile properties of the welded specimens was observed when compared to the base material.
- Fracture of the welded specimens always occurred away from the fine grained fusion zone in a ductile mode in the coarse grained base material.
- Irrecoverable strains after the first mechanical cycle were of 1.1% for the welded wire and 0.5% for the base material. After the first cycle, the irrecoverable strains of both materials quickly reduced to a stabilized value.
- The pseudoelastic hysteretic response of the welded wires rapidly converged, while the base material response converged after some additional cycles.

Acknowledgments

JPO and FBF acknowledge funding of CENIMAT/i3N by FEDER funds through the COMPETE 2020 Programme and National Funds through FCT – Portuguese Foundation for Science and Technology under the project UID/CTM/50025/2013. RMM acknowledges funding of UNIDEMI by FEDER funds through the COMPETE 2020 Programme and National Funds through FCT – Portuguese Foundation for Science and Technology under the project UID/EMS/00667/2013. JPO acknowledges FCT/MCTES for funding PhD grant SFRH/BD/85047/2012 and stay at Waterloo University (Canada) through MIDAS Project No 612585 "MIDAS – Micro and Nanoscale Design of Thermally Actuating Systems" Marie Curie Actions, FP7-PEOPLE-2013-IRSES.

References

[1] L. Sun, W. Huang, Z. Ding, Y. Zhao, C. Wang, Stimulus-responsive shape memory materials: a review, Mater. Des. 33 (2012) 577–640.
[2] J.-L. Liu, H.-Y. Huang, J.-X. Xie, Superelastic anisotropy characteristics of columnar-grained Cu–Al–Mn shape memory alloys and its potential applications, Mater. Des. 85 (2015) 211–220.
[3] R. Kainuma, N. Satoh, X.J. Liu, I. Ohnuma, K. Ishida, Phase equilibria and Heusler phase stability in the Cu-rich portion of the Cu–Al–Mn system, J. Alloys Compd. 266 (1) (1998) 191–200.
[4] R.R. Hultgren, P.D. Desai, Selected thermodynamic values and phase diagrams for copper and some of its binary alloys, INCRA Monograph I Metallurgy of Copper, The International Copper Research Association, 1971.
[5] E. Obradó, C. Frontera, L. Mañosa, A. Planes, Order–disorder transitions of Cu–Al–Mn shape-memory alloys, Phys. Rev. B 58 (21) (1998) 14245–14255.
[6] R. Kainuma, S. Takahashi, K. Ishida, Thermoelastic martensite and shape memory effect in ductile Cu–Al–Mn alloys, Metall. Mater. Trans. A 27A (1996) 2187–2195.
[7] R. Kainuma, S. Takahashi, K. Ishida, Ductile shape memory alloys of the Cu–Al–Mn system, J. Phy. IV 5 (8) (1995) (C8-961-C8-966).
[8] Y. Araki, T. Endo, T. Omori, Y. Sutou, Y. Koetaka, R. Kainuma, K. Ishida, Potential of superelastic Cu–Al–Mn alloy bars for seismic applications, Earthq. Eng. Struct. Dyn. 40 (1) (2010) 107–115.
[9] M. Dolce, D. Cardone, Mechanical behaviour of shape memory alloys for seismic applications 2. Austenite NiTi wires subjected to tension, Int. J. Mech. Sci. 43 (2001) 2657–2677.
[10] K. Otsuka, C.M. Wayman, Shape Memory Materials, Cambridge University Press, Cambridge, 1999.
[11] Y. Sutou, T. Omori, K. Yamauchi, N. Ono, R. Kainuma, K. Ishida, Effect of grain size and texture on pseudoelasticity in Cu–Al–Mn-based shape memory wire, Acta Mater. 53 (15) (2005) 4121–4133.
[12] J.-L. Liu, H.-Y. Huang, J.-X. Xie, The roles of grain orientation and grain boundary characteristics in the enhanced superelasticity of Cu71.8Al17.8Mn10.4 shape memory alloys, Mater. Des. 64 (2014) 427–433.
[13] P. Sittner, L. Heller, J. Pilch, C. Curfs, T. Alonso, D. Favier, Young's modulus of austenite and martensite phases in superelastic NiTi wires, J. Mater. Eng. Perform. 23 (7) (2014) 2303–2314.
[14] D. Yang, H.C. Jiang, M.J. Zhao, L.J. Rong, Microstructure and mechanical behaviors of electron beam welded NiTi shapememory alloys, Mater. Des. 57 (2014) 21–25.
[15] S. Nemat-Nasser, W. Guo, Superelastic and cyclic response of NiTi SMA at various strain rates and temperatures, Mech. Mater. 38 (5) (2006) 463–474.
[16] S. Nemat-Nasser, J.Y. Choi, W. Guo, J.B. Isaacs, M. Taya, High strain-rate, small strain response of a NiTi shape-memory alloy, J. Eng. Mater. Technol. 127 (2005) 83–89.
[17] S. Miyazaki, Y. Kohiyama, K. Otsuka, T.W. Duerig, Effects of several factors on the ductility of the Ti–Ni alloy, Mater. Sci. Forum 56 (1990) 765–770.
[18] K.C. Shrestha, Y. Araki, T. Nagae, T. Omori, Y. Sutou, R. Kainuma, K. Ishida, Effectiveness of superelastic bars for seismic rehabilitation of clay-unit masonry walls, Earthq. Eng. Struct. Dyn. 42 (5) (2012) 725–741.
[19] B. Gencturk, Y. Araki, T. Kusama, T. Omori, R. Kainuma, F. Medina, Loading rate and temperature dependency of superelastic Cu–Al–Mn alloys, Constr. Build. Mater. 53 (2014) 555–560.
[20] Y. Araki, N. Maekawa, T. Omori, Y. Sutou, R. Kainuma, K. Ishida, Rate-dependent response of superelastic Cu–Al–Mn alloy rods to tensile cyclic loads, Smart Mater. Struct. 21 (3) (2012) 032002.
[21] S. Nag, R. Banerjee, ASM Handbook, Materials for Medical Devices, vol. 23, ASM International, Ohio, 2012.
[22] W.M. Steen, J. Mazumder, Laser Material Processing, Springer, London, 2010.
[23] Y. Sutou, N. Koeda, T. Omori, R. Kainuma, K. Ishida, Effects of aging on stress-induced martensitic transformation in ductile Cu–Al–Mn-based shape memory alloys, Acta Mater. 57 (19) (2009) 5759–5770.

[24] P. Schlossmacher, T. Haas, A. Schüssler, Laser-welding of a Ni-rich TiNi shape memory alloy: mechanical behavior, J. Phys. IV 7 (5) (1997) C5-251–C5-256.
[25] Y. Hsu, Y. Wang, S. Wu, C. Chen, Effect of CO_2 laser welding on the shape-memory and corrosion characteristics of TiNi alloys, Metall. Mater. 32A (2001) 569–579.
[26] X.-J. Yan, D.-Z. Yang, Corrosion resistance of a laser spot-welded joint of NiTi wire in simulated human body fluids, J. Biomed. Mater. Res. A 77 (2006) 97–102.
[27] A. Tuissi, S. Besseghini, T. Ranucci, F. Squatrito, M. Pozzi, Effect of Nd–YAG laser welding on the functional properties of the Ni–49.6 at.% Ti, Mater. Sci. Eng. A 273 (1999) 813–817.
[28] C.W. Chan, H.C. Man, T.M. Yue, Effect of postweld heat treatment on the microstructure and cyclic deformation behavior of laser-welded NiTi-shape memory wires, Metall. Mater. Trans. A 43 (6) (2012) 1956–1965.
[29] P. Wollants, M. De Bonte, J. Roos, Thermodynamic analysis of the stress-induced martensitic-transformation in a single-crystal, Z. Metallkd. 70 (1979) 113–117.
[30] J.M. Jani, M. Leary, A. Subic, M.A. Gibson, A review of shape memory alloy research, applications and opportunities, Mater. Des. 56 (2014) 1078–1113.
[31] S. Miyazaki, T. Imai, Y. Igo, K. Otsuka, Effect of cyclic deformation on the pseudoelasticity characteristics of Ti–Ni alloys, Metall. Trans. A 17 (1) (1986) 115–120.
[32] H. Kato, T. Ozu, S. Hashimoto, S. Miura, Cyclic stress–strain response of superelastic Cu–Al–Mn alloy single crystals, Mater. Sci. Eng. A 264 (1) (1999) 245.

7.1.8 Improvement of Damping Properties in Laser Processed Superelastic Cu-Al-Mn Shape Memory Alloys

This paper was submitted and accepted in Materials & Design.

Materials and Design 98 (2016) 280–284

Contents lists available at ScienceDirect

Materials and Design

journal homepage: www.elsevier.com/locate/matdes

Improvement of damping properties in laser processed superelastic Cu-Al-Mn shape memory alloys

J.P. Oliveira [a,b,*], Z. Zeng [b,c], T. Omori [d], N. Zhou [b], R.M. Miranda [e], F.M. Braz Fernandes [a]

[a] CENIMAT/i3N, Faculdade de Ciências e Tecnologia, Universidade Nova de Lisboa, Portugal
[b] Centre for Advanced Materials Joining, University of Waterloo, Canada
[c] School of Mechatronics Engineering, University of Electronic Science and Technology of China, China
[d] Department of Materials Science, Graduate School of Engineering, Tohoku University, Japan
[e] UNIDEMI, Faculdade de Ciências e Tecnologia, Universidade Nova de Lisboa, Portugal

ARTICLE INFO

Article history:
Received 5 February 2016
Received in revised form 4 March 2016
Accepted 7 March 2016
Available online 8 March 2016

Keywords:
Cu-Al-Mn shape memory alloys
Superelasticity
Cycling behavior
Post-weld treatment
Laser processing
Energy absorption

ABSTRACT

Cu-based shape memory alloys may be a prime candidate to replace NiTi in specific applications due to their reduced cost and excellent superelasticity. Superelastic Cu-Al-Mn alloy is currently being studied for potential applications as damping systems in seismic devices. However, joining techniques are often required to obtain complex shapes to be incorporated into multi-functional systems. In this study, the effect of post-weld laser processing was investigated in a laser welded superelastic Cu-17Al-11.4Mn (at.%) alloy and the mechanical properties were assessed. It was observed that post-weld laser processing increased the alloy tensile strength to almost the double of the as-welded material while the capability to absorb energy during mechanical cycling increased up to 1.7 times. Thus, laser processing was seen as a suitable technique to improve mechanical properties of welded CuAlMn alloys, supporting the use of these materials in applications where both strength and energy absorption are required, such as in seismic applications.

1. Introduction

Shape memory alloys are functional materials that own their properties to a reversible martensitic transformation [1]. The martensitic transformation mechanism typical of shape memory alloys is a solid-solid diffusionless transformation, which is accompanied by both micro and macroscopic deformations. These can be recovered by heating the material in an ideal reversible cycle [2].

Amongst shape memory alloys, NiTi and Cu-based alloys are the most studied ones in this peculiar class of materials [3]. The unique thermomechanical behavior of these alloys, which can present both shape memory effect and superelasticity, have made them suitable candidates for structural vibration control applications [4,5]. Despite the supremacy of NiTi which is, currently, the most used shape memory alloy for a wide range of applications [6], Cu-based shape memory alloys are emerging as potential substitutes [7]. In particular, superelastic Cu-17Al-11.4Mn (at.%) exhibits mechanical properties that are similar to those of NiTi, but has better thermal and electrical properties and is less expensive. Due to the aforementioned properties, this Cu-based alloy is currently being considered for applications in seismic devices [8]. However, it must be noticed that this material requires a precise control of grain size and orientation in order to present a stable superelastic response. Other Cu-based shape memory alloys were found to present a similar dependence [9,10].

Although the use of these materials in energy absorption applications is of great importance, it is often limited by constrains that limit their broader used. Examples of these constrains are the difficulty to obtain complex shapes and the need to integrate these materials into multi-functional systems. Welding may be a solution to both these problems: the attainment of complex shaped structures provides design flexibility; and, under suitable welding parameters, sound joints can be obtained, allowing the integration of these materials into multi-functional systems.

Recently, the effects of laser welding on the mechanical properties of superelastic Cu-17Al-11.4Mn (at.%) have been studied [11]. It was found that the tensile properties of base material and as-welded specimens were of the same order of magnitude and so, welding has no significant detrimental effect on the material. During mechanical cycling, the welds exhibited a higher irrecoverable strain than that of the base material due to the fine grain microstructure in the fusion zone, while the base material kept its original massive bamboo-like microstructure. Previous studies on the Cu-17Al-11.4Mn alloy have shown that the superelastic properties of these wires are extremely dependent on the d/D ratio (with d being the grain size and D the wire diameter): higher d/D leads to a higher strain recovery by superelasticity; lower d/D increases the critical stress for the martensitic transformation and reduces the

* Corresponding author at: CENIMAT/i3N, Faculdade de Ciências e Tecnologia, Universidade Nova de Lisboa, Portugal.
E-mail address: jp.oliveira@campus.fct.unl.pt (J.P. Oliveira).

http://dx.doi.org/10.1016/j.matdes.2016.03.032
0264-1275/

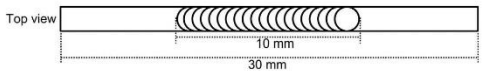

Fig. 1. Set-up for laser processing of the CuAlMn alloy (not to scale).

extension of the superelastic plateau thus, the ability to recover imposed deformation by superelasticity decreases [12].

In order to improve the mechanical properties of welded joints it is quite common to perform a post-weld processing [13,14]. The present investigation envisages to assess the effect of post-weld laser heat treatment on laser welded joints, aiming to improve the mechanical properties and damping capacity of the as-welded material for possible applications in vibration control systems and in seismic devices.

2. Experimental details

Superelastic Cu-17Al-11.4Mn (at.%), henceforward designed as CuAlMn, wires were used in this investigation. The base material ingot was prepared by induction melting under Argon atmosphere. The ingot was hot forged and cold drawn to produce wires of 0.5 mm diameter. These were repeatedly annealed at 900 °C in order to obtain large grains [15] and then water quenched after a solution heat treatment at 900 °C and subsequently aged at 200 °C in order to stabilize the martensitic transformations of the base material, which had a random texture. The oxide layer formed during these heat treatments was mechanically removed using fine SiC paper, so the final diameter of the wires was of 0.485 ± 0.005 mm. Prior to laser processing, the wires were cleaned using acetone and ethanol to avoid the existence of any impurities that could be detrimental for the processed material.

Bead on plate by laser was performed with a pulsed Nd:YAG laser system from Miyachi Unitek LW50A. The beam wavelength was of 1064 nm and a spatial profiler was used to ensure that the near-Gaussian emitted beam had a top-hat profile over the uniform-intensity circular spot with a diameter of 600 μm. A peak power of 1.5 kW and a pulse duration of 6 ms, including 1 ms upslope and 1 ms downslope, were used. Argon was used as shielding gas at a flow rate of 0.57 $m^3 h^{-1}$. These parameters were selected based on previous experiences on laser welding of superelastic CuAlMn [11].

Post-processing ran with the same equipment and laser parameters. In order to have specimens for mechanical characterization and due to constraints in the amount of available base material, laser processing was performed on the central region of the specimen in a length of about 1/3 of the total wire length, keeping the other 2/3 in the original microstructural condition.

A 10 mm length was processed in a total of 48 laser spots, with an overlap of 65% of the beam spot diameter (Fig. 1). Laser processing was performed on both the original base material samples and on previously laser welded samples, which had only one laser spot, to understand the feasibility of post-weld laser heat treatment to improve the mechanical properties of the joints.

A micro-tensile tester from Instron model 5548 was used for tensile tests to fracture. The displacement rate was set at 0.5 mm/min and the measurement accuracy was of ± 0.5 μm. The overall gauge length of the specimens was of 20 mm. The wires were mounted between the grips of the tensile machine using grinding paper (Fig. 2). This was done for two reasons: avoid the risk of slipping during the mechanical tests and to prevent excessive local deformation in the region of the wire that was in contact with the grips. Three specimens were tested for each condition (base material, as-welded, laser processed after welding and as-processed). Scanning electron microscopy (SEM) was used to analyze the fractures surface after tensile testing to fracture using a Zeiss Leo 1550 Field Emission SEM with an accelerating voltage of 10 kV.

Mechanical cycling behavior was also investigated by performing a total of 10 load/unload mechanical cycles up to 5% strain, keeping the displacement rate at 0.5 mm/min. Loading up to 5% strain was chosen in order to keep consistency with the previous study on laser welding of the superelastic CuAlMn alloy. One sample was used for each condition and these tests were performed with the same equipment as for the tensile tests to fracture.

Specimens were labeled as shown in Table 1.

Table 1
Adopted nomenclature and number of samples for each group of specimens tested.

Label	Specimen	Number of tested samples	
		Tensile tests to fracture	Cycling behavior
BM	Base material	3	1
AW	As-welded	3	1
AP	As-processed	3	1
PWP	Post-welded processing	3	1

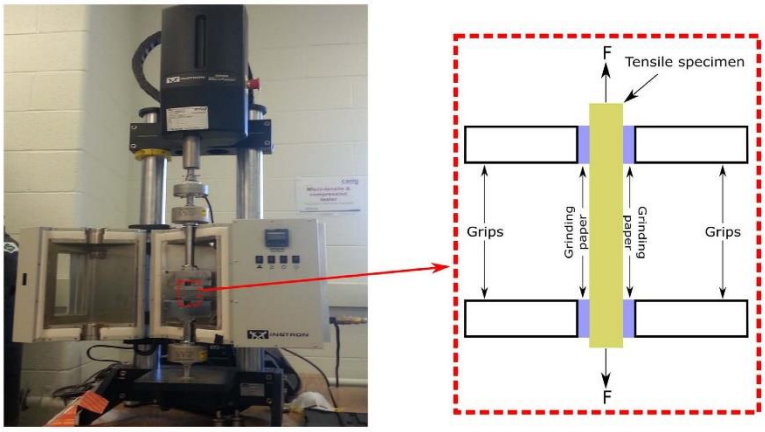

Fig. 2. Tensile equipment and schematic representation (not to scale) of the mounting of the wires for mechanical characterization.

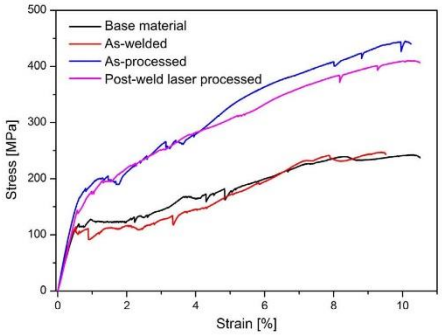

Fig. 3. Tensile curves of different tested specimens.

3. Results and discussion

This paper is intended to analyze the effect of post-weld laser processing on the as-received and as-welded superelastic CuAlMn alloy. The effect of laser welding was previously studied [11] and some of the conclusions drawn are used to understand the effect of laser processing on the mechanical properties of the welded material.

Tensile curves of the tested specimens are depicted in Fig. 3 and these include: base material, as-welded wires, post-weld laser processed and laser processed base material. The most striking observation is the significantly higher tensile strength presented by samples AP and PWP when compared to BM and AW ones. Additionally, the critical stress for the stress-induced transformation in both AP and PWP increased to about 200 MPa, while for the BM and AW samples the stress-induced transformation started at roughly 100 MPa. The reason for this significant increase in the onset stress for the martensitic transformation is related to the microstructural changes induced by laser processing in AP and PWP samples. The laser processed region showed fine grain size ranging from 15 to 80 μm (Fig. 4), similar to the microstructure in the fusion zone of the AW sample [11]. The non-processed region had a bamboo-like structure with grains of 1 to 2 mm in length, typical of this alloy. The significant increase in grain density in the laser processed material, lead to an increase in the transformation stresses. Other Cu-based shape memory alloys have been found to show a similar behavior [16]. This is related to the fact that in a more fine grained material, the grain boundaries inhibit shear between grains, pushing the stress needed to start the martensitic transformation to higher values.

From the tensile tests, it is also observed that there is no significant difference between both AP and PWP specimens, as already seen in BM and AW samples [11]. Fracture of the AP and PWP samples during tensile testing occurred in the non-processed base material, similarly to the fracture observed in the as-welded samples. As previously reported, when fracture occurred in the base material, dimples where seen on the fracture surface in a ductile-like fracture mode. For the laser welding and laser processing parameters used, no evidence of a heat affected zone was observed. This is related to the fact that the base material has a heat treatment at high temperature prior to welding in order to obtain its superelastic properties. As such, the formation of a heat affected zone adjacent to the fusion zone is inhibited.

In order to analyze the fracture surface of the processed region, another PWP sample was tested to failure, but the gauge length was set so that the fracture could just occur in the processed region. Fig. 5 depicts the fracture surface morphology of the PWP sample observed by SEM. Similarly to the fracture surfaces of all other samples, a ductile-like fracture was identified with the presence of dimples.

Laser processing replaces the bamboo structure by an equiaxed grain structure along a path where the laser impinges the material in both AP and PWP samples, thus both samples presented the same mechanical characteristics when tested to failure. In fact, the microstructure of both AP and PWP is exactly the same throughout the processed region, which justifies the same mechanical behavior observed in the two distinct samples. For this, only the cycling behavior of the PWP sample is presented and compared to the base material and the as-welded samples (Fig. 6).

Of particular interest is that the PWP sample presented a stabilized hysteretic response after the second load/unload cycle. That is, the shape of the stress-strain curve did not differ significantly from cycle number two onwards. This effect was also identified in both BM and AW samples.

Owing to the effect of laser processing on the material, it can be assumed that there are two distinct regions: the non-affected base material with a significantly large bamboo-like grain size and the processed region with micrometer sized grains. It is known that the superelasticity of the CuAlMn alloy is highly dependent on the grain size (d) and the wire diameter (D) [12]. In fact, the intentionally massive grain size of the original base material provides the best superelastic properties for this particular alloy. As such, the different regions in the laser processed sample will bring a distinct overall mechanical behavior. Fig. 7 depicts the expected mechanical behavior of the two regions: the original bamboo structure and the fine grain resulting from laser processing. The effect of smaller grain size on the Cu-Al-Mn alloy is evidenced by a raise in critical stress for the martensitic transformation. Additionally, the superelastic strain recovery of the laser processed region is lower. As such, when both the processed and non-processed regions are loaded individually, it is expected that a large (superelastic) strain will be accommodated by the bamboo-like structure, before the finer grained laser processed region starts to be strained extensively.

As a result of the lower stress for the beginning of the superelastic plateau and due to a significant ability to deform at a constant stress level, the non-processed base material will be relaxing the imposed stresses on the material.

The decrease in grain size in the laser processed zone, and thus in the overall d/D ratio in the processed material, leads to a decrease in the superelastic properties, namely by increasing the accumulated irrecoverable strain after unloading. This accumulated irrecoverable strain was found to be significantly higher for the PWP samples than for BM and AW ones (Fig. 8). This is related to the fact that a smaller d/D

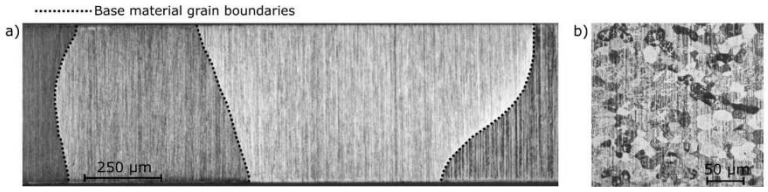

Fig. 4. Optical micrograph of base material (a) and laser processed region (b).

ratio, resulted in a more significant constriction of the transformation, thus explaining the larger plastic strain measured.

As a consequence of the significantly higher irrecoverable strain after the first load/unload cycle (Fig. 8), the ability to absorb energy (which was determined from the area inside the load/unload stress-strain curve after each full cycle) during mechanical cycling sharply decreased (Fig. 9) but remained almost constant in subsequent cycles. This means that, in the first load/unload cycle, the significantly higher ability for energy absorption exhibited by the PWP material is obtained, in part, at the expenses of a higher irrecoverable strain upon unloading. Nonetheless, the difference of the absorbed energy between PWP and BM samples is less than 10% after the 2nd cycle. Due to the higher required stress for the onset of the stress induced transformation, the PWP samples presented a higher ability for energy absorption, despite the higher irrecoverable strain during mechanical cycling, than the AW specimens. Thus, an improvement of this property was obtained after laser processing of the welded material. This means that, although laser welded superelastic CuAlMn wires present interesting properties, these can be improved by a proper post-weld processing as evidenced by this study.

If these CuAlMn alloys are intended to be used in seismic devices, the significantly high damping capacity in the first load/unload cycle is of major importance. In fact, during an earthquake, the first stroke, usually, releases the highest energy, and it tends to decrease over time in subsequent replicas. Thus, the use of laser processed CuAlMn wires could be of great importance in such applications, as they exhibit an ability to absorb higher energies than the base material in the first load/unload cycle, while in the following mechanical cycles no significant differences between the processed and non-processed materials are observed. Additionally, the ability for the PWP material for energy absorption is always higher than that of the welded material. Thus, it would be possible to obtain a complex shaped welded joints by laser with improved mechanical properties providing a post-weld laser processing is performed.

From the cycling tests, it is also observed that the onset for the stress induced transformation decreases with the number of cycles. This is known to occur for shape memory alloys due to two possible reasons: the development of defects, such as dislocations; and/or retention of martensite nuclei, which will assist the austenite to martensite transformation in the following cycles, thus, requiring lower external stresses.

Due to the occurrence of dislocation slip during the stress induced transformation, a change in the stress-strain curves during mechanical cycling of the laser processed material is observed: after the first cycle it is noticed a variation on the slope of the superelastic plateau after 3.5% strain. This variation is related to the occurrence of plastic deformation during mechanical cycling, leading to strain-hardening of the processed material. This effect is more clearly noticed in the laser processed material due to the significantly higher density of fine grains, which have a larger contribution to the plastic deformation of the material when compared to the base material or to the as-welded specimen. Other welded shape memory alloys have been found to exhibit similar behavior during mechanical cycling.

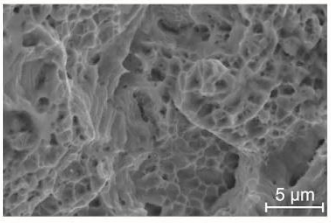

Fig. 5. Fracture surface of the post-weld laser processed (PWP) sample.

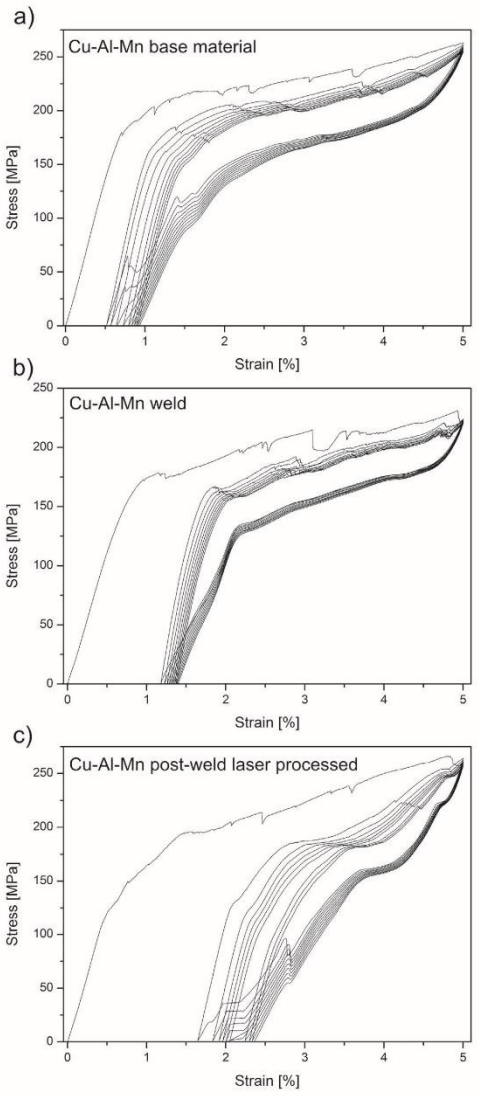

Fig. 6. Cycling behavior of: a) base material [11]; b) as-welded [11]; c) post-weld laser processed.

4. Conclusions

In this study, laser processing of superelastic CuAlMn alloy was performed after laser welding and on the base material. Laser processing was made in 1/3 of the total length of the tested specimens. Mechanical properties of the welded samples and post-welded laser processed ones was performed to evaluate the effect of post-weld laser processing and compared to the base material and as-welded material.

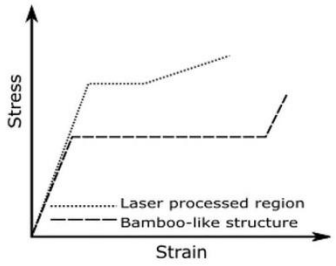

Fig. 7. Schematic representation (not to scale and with arbitrary values) of the mechanical behavior of the processed and non-processed regions.

- The tensile strength of the post-weld laser processed material increased to about twice that of both the base material and the as-welded one;
- The absorbed energy and thus the damping capacity of the post-weld laser processed material, in the first load/unload cycle increased by 1.7 times when compared to that of the original base material;
- Despite the increased irrecoverable strain during mechanical cycling, the processed material was able to show similar damping properties to those of the base material after the 2nd cycle, remaining constant in further cycling.

Therefore, the use of laser processing of these alloys may be of great interest, even when these have already subjected to welding. These results may find application in seismic applications where energy absorption is a key-factor.

Acknowledgements

JPO and FBF acknowledge funding of CENIMAT/I3N by FEDER funds through the COMPETE 2020 Programme and National Funds through FCT — Portuguese Foundation for Science and Technology under the project number 007688 Reference UID/CTM/50025. RMM acknowledge funding of UNIDEMI by FEDER funds through the COMPETE 2020 Programme and National Funds through FCT — Portuguese Foundation for Science and Technology under the project POCI-01-0145-FEDER-007688, Reference UID/CTM/50025. JPO acknowledges FCT/MCTES for funding PhD grant SFRH/BD/85047/2012 and stay at Waterloo University (Canada) through MIDAS Project No 612585 "MIDAS—Micro and Nanoscale Design of Thermally Actuating Systems" Marie Curie Actions, FP7-PEOPLE-2013-IRSES.

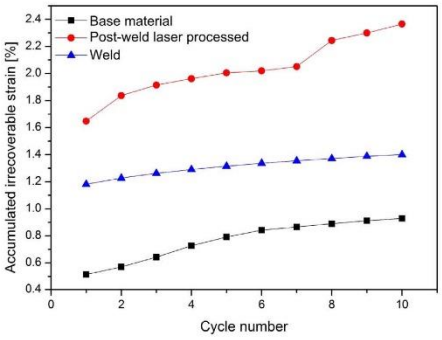

Fig. 8. Evolution of the accumulated irrecoverable strain with the number of cycles for different specimens.

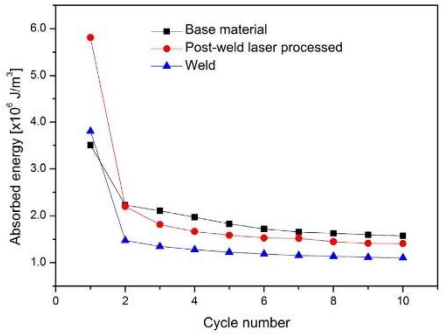

Fig. 9. Evolution of the absorbed energy with the number of cycles for different specimens.

References

[1] L. Sun, W.M. Huang, Z. Ding, Y. Zhao, C.C. Wang, H. Purnawali, et al., Stimulus-responsive shape memory materials: a review, Mater. Des. 33 (2012) 577–640, http://dx.doi.org/10.1016/j.matdes.2011.04.065.
[2] J. Ortín, A. Planes, Thermodynamics of thermoelastic martensitic transformations, Acta Metall. 37 (1989) 1433–1441, http://dx.doi.org/10.1016/0001-6160(89)90175-2.
[3] K. Otsuka, X. Ren, Physical metallurgy of Ti-Ni-based shape memory alloys, Prog. Mater. Sci. 50 (2005) 511–678, http://dx.doi.org/10.1016/j.pmatsci.2004.10.001.
[4] S. Saadat, J. Salichs, M. Noori, Z. Hou, H. Davoodi, I. Bar-on, et al., An overview of vibration and seismic applications of NiTi shape memory alloy, Smart Mater. Struct. 11 (2002) 218–229, http://dx.doi.org/10.1088/0964-1726/11/2/305.
[5] M. Dolce, D. Cardone, Mechanical behaviour of shape memory alloys for seismic applications 2. Austenite NiTi wires subjected to tension, Int. J. Mech. Sci. 43 (2001) 2657–2677, http://dx.doi.org/10.1016/S0020-7403(01)00050-9.
[6] J. Van Humbeeck, Non-medical applications of shape memory alloys, Mater. Sci. Eng. A 273–275 (1999) 134–148, http://dx.doi.org/10.1016/S0921-5093(99)00293-2.
[7] Y. Sutou, T. Omori, J.J. Wang, R. Kainuma, K. Ishida, Characteristics of Cu-Al-Mn-based shape memory alloys and their applications, Mater. Sci. Eng. A 378 (2004) 278–282, http://dx.doi.org/10.1016/j.msea.2003.12.048.
[8] Y. Araki, N. Maekawa, K.C. Shrestha, M. Yamakawa, Y. Koetaka, T. Omori, et al., Feasibility of tension braces using Cu-Al-Mn superelastic alloy bars, Struct. Control Heal. Monit. 21 (2014) 1304–1315, http://dx.doi.org/10.1002/stc.1644.
[9] J.-L. Liu, H.-Y. Huang, J.-X. Xie, The roles of grain orientation and grain boundary characteristics in the enhanced superelasticity of Cu71·8Al17·8Mn10.4 shape memory alloys, Mater. Des. 64 (2014) 427–433, http://dx.doi.org/10.1016/j.matdes.2014.07.070.
[10] S. Montecinos, Influence of microstructural parameters on damping capacity in CuAlBe shape memory alloys, Mater. Des. 68 (2015) 215–220, http://dx.doi.org/10.1016/j.matdes.2014.12.034.
[11] J.P. Oliveira, B. Panton, Z. Zeng, T. Omori, Y. Zhou, R.M. Miranda, et al., Laser welded superelastic Cu–Al–Mn shape memory alloy wires, Mater. Des. 90 (2016) 122–128, http://dx.doi.org/10.1016/j.matdes.2015.10.125.
[12] Y. Sutou, T. Omori, K. Yamauchi, N. Ono, R. Kainuma, K. Ishida, Effect of grain size and texture on pseudoelasticity in Cu–Al–Mn-based shape memory wire, Acta Mater. 53 (2005) 4121–4133, http://dx.doi.org/10.1016/j.actamat.2005.05.013.
[13] K. Elangovan, V. Balasubramanian, Influences of post-weld heat treatment on tensile properties of friction stir-welded AA6061 aluminum alloy joints, Mater. Charact. 59 (2008) 1168–1177, http://dx.doi.org/10.1016/j.matchar.2007.09.006.
[14] H. Aydin, A. Bayram, I. Durgun, The effect of post-weld heat treatment on the mechanical properties of 2024-T4 friction stir-welded joints, Mater. Des. 31 (2010) 2568–2577, http://dx.doi.org/10.1016/j.matdes.2009.11.030.
[15] T. Omori, T. Kusama, S. Kawata, I. Ohnuma, Y. Sutou, Y. Araki, et al., Abnormal grain growth induced by cyclic heat treatment, Science 80- (341) (2013) 1500–1502, http://dx.doi.org/10.1126/science.1238017.
[16] S. Montecinos, A. Cuniberti, A. Sepúlveda, Grain size and pseudoelastic behaviour of a Cu–Al–Be alloy, Mater. Charact. 59 (2008) 117–123, http://dx.doi.org/10.1016/j.matchar.2006.11.009.